



Université du Québec
à Rimouski

**DYNAMIQUE SÉDIMENTAIRE, STRATIGRAPHIE ET
PALÉOMAGNÉTISME DE LA RÉGION DU GOLFE DE SAN
JORGE, PATAGONIE, ARGENTINE, DEPUIS LA
DERNIÈRE DÉGLACIATION**

Thèse présentée
dans le cadre du programme de doctorat en océanographie
en vue de l'obtention du grade de Ph.D

PAR
© Pierre-Arnaud Desiage

Avril 2020

Composition du jury :

Urs Neumeier, président du jury, Université du Québec à Rimouski

Guillaume St-Onge, directeur de recherche, Université du Québec à Rimouski

Jean Carlos Montero Serrano, codirecteur de recherche, Université du Québec à Rimouski

Mathieu J. Duchesne, codirecteur de recherche, Commission géologique du Canada

Pierre Francus, examinateur externe, Institut National de la Recherche Scientifique

Dépôt initial le 28 novembre 2019

Dépôt final le 22 avril 2020

UNIVERSITÉ DU QUÉBEC À RIMOUSKI
Service de la bibliothèque

Avertissement

La diffusion de ce mémoire ou de cette thèse se fait dans le respect des droits de son auteur, qui a signé le formulaire « *Autorisation de reproduire et de diffuser un rapport, un mémoire ou une thèse* ». En signant ce formulaire, l'auteur concède à l'Université du Québec à Rimouski une licence non exclusive d'utilisation et de publication de la totalité ou d'une partie importante de son travail de recherche pour des fins pédagogiques et non commerciales. Plus précisément, l'auteur autorise l'Université du Québec à Rimouski à reproduire, diffuser, prêter, distribuer ou vendre des copies de son travail de recherche à des fins non commerciales sur quelque support que ce soit, y compris l'Internet. Cette licence et cette autorisation n'entraînent pas une renonciation de la part de l'auteur à ses droits moraux ni à ses droits de propriété intellectuelle. Sauf entente contraire, l'auteur conserve la liberté de diffuser et de commercialiser ou non ce travail dont il possède un exemplaire.

Salut à toi ...

And Kino drew back his arm and flung the pearl with all his might. Kino and Juana watched it go, winking and glimmering under the setting sun. [...] And the pearl lay on the floor of the sea. A crab scampering over the bottom raised a little cloud of sand, and when it settled the pearl was gone. And the music of the pearl drifted to a whisper and disappeared.

The pearl de John Steinbeck

REMERCIEMENTS

"Tout travail scientifique est une réalisation communautaire et non pas l'œuvre d'un cavalier seul. Qui sait où Darwin se serait égaré en 1837 sans Gould, sans Owen, et sans la vie scientifique très active de Londres et de Cambridge ?" Par cette citation du célèbre paléontologue Stephen J. Gould, je tiens à exprimer ma profonde gratitude à l'ensemble des personnes qui ont eu un rôle, même infime, dans mon cheminement scientifique et personnel. Si je ne peux pas remercier individuellement toutes ces personnes, j'aimerais quand-même adresser ma gratitude à quelques personnes en particulier :

Je souhaiterais en premier lieu remercier chaleureusement mon directeur de thèse Guillaume St-Onge de m'avoir offert un grand nombre d'opportunités depuis le début de mon projet de maîtrise et lors de ce doctorat. Merci de faire profiter tes étudiants des nombreuses collaborations que tu as su développer au cours de ta carrière. Ton optimisme, ton leadership et ton efficacité ont toujours été une source d'inspiration.

Je souhaiterais également remercier mon co-directeur Jean Carlos Montero Serrano avec qui j'ai développé une belle collaboration depuis le début de ce projet à Comodoro Rivadavia. Je te suis extrêmement reconnaissant d'avoir toujours pris le temps pour répondre à mes questions et dissiper mes doutes. Merci pour les (très) nombreux articles envoyés dans ma boîte courriel, j'espère encore en recevoir quand je ne serai plus ton étudiant.

Je tiens également à remercier mon co-directeur Mathieu J. Duchesne pour m'avoir accueilli pendant plusieurs semaines à la Commission Géologique du Canada à Québec et surtout de m'avoir formé aux prémisses du traitement sismique. Ce début d'expertise développée grâce à ton enseignement et nos conversations constitue un réel atout pour ma future carrière. Merci d'avoir toujours pris le temps de répondre à mes divers questionnements.

Mes remerciements vont également à Urs Neumeier et Pierre Francus pour leur participation à l'évaluation de cette thèse de doctorat.

Comment ne pas avoir une pensée amicale en terminant ce doctorat pour Alexandre Normandeau pour les nombreuses conversations scientifiques et les non-moins nombreux conseils avisés qui ont jalonné mon parcours depuis notre première expédition sur les pentes du cratère des Pingualuit. Merci également de m'avoir accueilli pendant plusieurs mois à la Commission géologique du Canada à Dartmouth.

J'aimerais également adresser une pensée particulière à mes parents en les remerciant pour leur soutien indéfectible durant mes très nombreuses années d'études. Merci de m'avoir laissé le choix.

Pour résumer simplement et poliment, un doctorat c'est long et c'est parfois pénible. Heureusement tellement de belles personnes ont émaillé mon parcours contribuant presque à transformer mes tribulations en épopées. Alors comment ne pas avoir une pensée pour tous les collocs qui sont devenus des ami(e)s et tous les ami(e)s qui sont devenu(e)s des collocs, le canapé de Charles (pré- et post-Bordeaux), l'humour d'Enrique, les gâteaux de Noémie, la douceur de vivre avec Flo et Eliott, les aventures gastronomiques avec Gab, l'éternelle "positive attitude" de Quentin B., ma "co-conspirator" Julie, les chocolatines de Quentin D, la gentillesse de Vincent et les soupers parfaits de Paul, Éva et la petite famille. Un énorme merci également à Edouard, Myriam, Arthur, Yan, Naïs, Simon, Omain, Adriana et Sarah pour les échanges, les discussions et les moments de vie dans la grotte, dans un bar, en congrès, en mission (dans un bar ...). Un merci tout spécial à ma grande amie Audrey pour l'ensemble de sa personne. Finalement une pensée pour le *Jeannie Longo* des amis, ce diable de Pierre-Julien.

J'aimerais terminer ces remerciements par la personne la plus importante dans ma vie et qui a joué un rôle essentiel dans ce doctorat, ma femme Mélany Belzile. Tu n'as pas choisi de faire ce doctorat mais tu en as pourtant subi tous les mauvais côtés. Merci de ton amour, de ta patience (oui, oui, ta patience ...) et de ton soutien.

Moi qui n'étais pas d'ici, ces 8 années passées au Québec m'ont permis d'apprivoiser une (belle) province, un patrimoine, des gens, un pays, l'hiver ... Comme beaucoup de mes compagnons d'aventures à la tête d'hexagone, je me suis arrimé, imprégné et épanoui dans le Bas-du-Fleuve pour finalement tomber en amour. A contre-cœur, je m'éloigne pour quelques saisons de ton estuaire qui est maintenant un peu le mien avec à la main la plus belle de tes fleurs de lys. Inspiré par tellement de personnes exceptionnelles qui parcourent, cultivent et enrichissent tes terres, ton savoir et ta culture, comment ne pas te vouer une reconnaissance profonde et sincère. Une gratitude qui s'accompagne malheureusement d'un arrière-goût amer car, décomplexé par le couronnement d'un enfant gâté aux idées peroxydées et englué dans un passé chimérique, tu as récemment révélé ta face la plus sombre, synonyme de peur, d'isolement, de rejet et de dénis. Québec, une trop grande poignée de tes citoyens ont oublié pour un temps que "*l'on ne connaît que les choses que l'on apprivoise*". Mais je suis confiant, Québec, je sais qu'au plus profond de toi, tu veux te laisser parler de tous les amours.

RÉSUMÉ

Ce projet de thèse a pour objectif de reconstituer la dynamique sédimentaire et géomagnétique ainsi que les variations du niveau marin dans le secteur central de la Patagonie au cours de la dernière transgression marine. Pour répondre à cet objectif, les sédiments de surface ainsi que des enregistrements sédimentaires et géophysiques prélevés dans le golfe de San Jorge (GSJ) ont été étudiés.

Dans le premier chapitre, la distribution spatiale, les mécanismes de transport et les sources potentielles des sédiments terrigènes du GSJ ont été étudiés à l'aide d'analyses de la granulométrie, de la minéralogie (fraction totale et argileuse) et de la géochimie (éléments majeurs et traces) faites sur des échantillons de surface prélevés dans le golfe et sur le plateau continental. Des échantillons terrestres et marins provenant de potentielles sources susceptibles d'alimenter le golfe ont également été prélevés en Patagonie. Les analyses minéralogiques ont permis de mettre en évidence la prédominance de la signature volcanique andine et extra-andine dans les sédiments du golfe. L'assemblage minéralogique des argiles est dominé par la smectite acheminée par le transport éolien et les apports côtiers locaux alors que les apports limités d'illite et de chlorite sont transportés dans le golfe par les courants qui remontent le plateau continental. Les assemblages minéralogiques couplés à l'utilisation du programme SedUnMix suggèrent que les sédiments de surface du GSJ proviennent à 50% d'apports océaniques/externes, à 40% des rives du golfe (érosion et ruissellement) et à 10 % du transport éolien qui achemine des poussières dans les eaux du golfe.

Dans le second chapitre, l'interprétation de plusieurs centaines de kilomètres de lignes sismiques à haute résolution, l'analyse d'archives sédimentaires prélevées dans le golfe et la construction de leurs modèles d'âge à partir de 24 datations radiocarbone ont permis de reconstituer la stratigraphie du GSJ depuis la dernière glaciation ainsi que de documenter les variations du niveau marin dans cette région. Dans le centre du golfe, les données sismiques à haute résolution (*sparker*) suggèrent l'existence d'un système de paléodrainage avec la présence de vallées et chenaux incisés qui se seraient formés et développés au cours des précédents bas niveaux marin pour ensuite être oblitérés par une succession de dépôts fluviaux et lagunaires avant la dernière transgression marine. À partir de l'interprétation lithologique couplée à une analyse multi-traceur de 4 carottes sédimentaires, quatre unités et sous-unités lithologiques ont été définies pour la séquence sédimentaire de sous-surface du golfe. Les datations radiocarbone suggèrent la mise en place de dépôts associés à des environnements subtiaux vers 14 cal ka BP dans la partie centrale du golfe. La transition vers ces conditions de sédimentation pourrait être associée à une augmentation abrupte du niveau marin dans le GSJ avant 14 cal ka BP qui pourrait être en relation avec l'impulsion de fonte 1A (MWP-1A). Finalement, les résultats de ce chapitre suggèrent que l'augmentation du

niveau marin depuis le début de la transgression marine jusqu'au milieu de l'Holocène a fortement conditionné la sédimentation dans le GSJ.

Dans le troisième chapitre, les données paléomagnétiques provenant de 4 archives sédimentaires du GSJ ont permis de documenter les variations du champ magnétique au centre de la Patagonie au cours des 14 000 dernières années. Au cours de cette étude, les paléodirections (inclinaison et déclinaison) et les paléointensités relatives ont été reconstituées à partir d'une nouvelle méthodologie de sommation des données paléomagnétiques (*stacking*) appliquée sur les différentes archives sédimentaires. Cette méthode est basée sur l'utilisation des vitesses de sédimentation ainsi que des valeurs de déviation angulaire maximum (MAD) comme facteurs de qualité. La comparaison de ces nouvelles données paléomagnétiques avec d'autres enregistrements de lacs de Patagonie et avec des modèles dipolaires globaux relève de nombreux éléments de corrélation confirmant ainsi la conformité et la qualité des enregistrements paléomagnétiques dans le GSJ. L'ensemble des résultats présentés dans ce chapitre semblent également confirmer le fort potentiel de la nouvelle méthode de *stacking* pour obtenir la meilleure qualité et la plus haute résolution de données possible parmi les archives sédimentaires disponibles pour reconstruire les enregistrements paléomagnétiques.

Au final, la contribution principale de cette thèse a été d'établir un cadre sédimentaire et stratigraphique dans le golfe de San Jorge et de documenter pour la première fois, dans ce secteur du plateau continental, la variation du niveau marin et la variabilité du champ magnétique terrestre depuis la dernière déglaciation.

Mots clés : Environnements sédimentaires, géochimie, minéralogie, sismique haute résolution, paléomagnétisme, variations du niveau marin postglaciaire, Holocène et Pléistocène tardif, Patagonie, golfe de San Jorge.

ABSTRACT

The primary goal of this thesis project is to reconstruct the sedimentary and geomagnetic dynamics as well as the sea level variations in the central sector of Patagonia during the last marine transgression. To meet this objective, surface sediments as well as sedimentary and geophysical records retrieved in the Gulf of San Jorge (GSJ) were examined.

In the first chapter, the spatial distribution, the transport processes, and the potential sources of terrigenous sediments in the GSJ were investigated using grain size analysis, mineralogy (bulk and clay), and geochemistry (major and trace elements) of surface samples collected in the Gulf and on the continental shelf. Terrestrial and marine samples from potential sediment sources for the gulf have also been collected in Patagonia. Mineralogy analyses have highlighted the predominance of the dominant volcanic signature of Patagonia in the sediments of the GSJ. The clay-mineral assemblages is dominated by smectite carried by aeolian transport and local coastal inputs, while limited inputs of illite and chlorite are transported into the gulf by the northward currents flowing along the continental shelf. Mineral assemblage coupled with the use of the SedUnMix program suggest that the origin of sediments in the GSJ is 50% from oceanic/external inputs, 40% from the inner gulf shore (erosion and runoff), and 10% from dust (i.e., aeolian transport).

In the second chapter, the interpretation of several hundred kilometers of high-resolution seismic lines, the analysis of sedimentary archives retrieved in the gulf and the development of their age model from 24 radiocarbon ages have allowed us to reconstruct the stratigraphy of the GSJ since the last glaciation as well as to document the sea level variations in this region. In the central part of the gulf, the high-resolution seismic data (sparker) suggests the existence of a paleo-fluvial network with the presence of incised valleys and channels that would have formed and developed during previous sea level lowstand and then be obliterated by a succession of riverine and lagoonal deposits before the last marine transgression. From the lithological interpretation coupled with a multi-proxy analysis of 4 sediment cores, four lithological units and sub-units were defined for the uppermost offshore sedimentary sequence of the GSJ. Radiocarbon ages suggest the settle of deposits associated with subtidal environments around 14 cal ka BP in the central part of the gulf. The transition to theses depositional envionments could be associated with an abrupt sea level rise in the GSJ before 14 cal ka BP and this could be related to the meltwater pulse 1A (MWP-1A). Finally, the results of this chapter suggest that the sea-level rise from the beginning of the marine transgression to the middle of the Holocene has highly conditioned the sedimentation in the GSJ.

In the third chapter, paleomagnetic data from four sedimentary archives of the GSJ allowed us to document the variations of the geomagnetic field in the central part of Patagonia

over the last 14,000 years. In this study, paleodirections (inclination and declination) and relative paleointensity were reconstructed using a new stacking method applied to the sedimentary archives of the gulf. This approach is based on the use of the maximum angular deviation (MAD) values and the sedimentation rates values as quality factors. The comparison of these new paleomagnetic data with other lacustrine records from Patagonia and spherical harmonic model of the geomagnetic field reveals numerous correlative features confirming the conformity and quality of paleomagnetic records in the GSJ. All the results presented in this chapter also seem to confirm the high potential of the new stacking method to obtain the highest quality and resolution of data, among the sedimentary archives available to reconstruct palaeomagnetic records.

In the end, the main contribution of this thesis was to establish a sedimentary and stratigraphic background in the Gulf of San Jorge and to document, for the first time, in this sector of the continental shelf, the sea level variation and the variability of the geomagnetic field since the last deglaciation.

Keywords: Sedimentary environments, mineralogy, geochemistry, high-resolution seismic, paleomagnetism, postglacial sea-level changes, Holocene and Late Pleistocene, Patagonia, Gulf of San Jorge.

TABLE DES MATIÈRES

REMERCIEMENTS	xii
RÉSUMÉ	xv
ABSTRACT.....	xvii
TABLE DES MATIÈRES	xix
LISTE DES TABLEAUX	xxiv
LISTE DES FIGURES	xxv
LISTE DES ABRÉVIATIONS, DES SIGLES ET DES ACRONYMES	xxxiii
INTRODUCTION GÉNÉRALE	1
LA PATAGONIE	1
MISE EN CONTEXTE DE LA SÉDIMENTATION.....	3
VARIATIONS DU NIVEAU MARIN DEPUIS LA DERNIERE GLACIATION.....	6
PALEOMAGNETISME ET ETAT DES CONNAISSANCES EN AMERIQUE DU SUD	9
OBJECTIFS	12
Objectif 1 : Sédimentation contemporaine.....	12
Objectif 2 : Stratigraphie et variations du niveau marin	13
Objectif 3 : Reconstitution paléomagnétique	14
MÉTHODOLOGIE	16
Campagnes d'échantillonnage	16
Propriétés physiques	17
Analyses granulométriques	19
Analyses minéralogiques et géochimiques	20
Mesures magnétiques et paléomagnétiques	21
Chronologie.....	23

Données géophysiques	24
ORGANISATION DE LA THÈSE	27
AUTRES RÉALISATIONS ET COLLABORATIONS	28
CHAPITRE 1 QUANTIFICATION DES SOURCES ET DES AXES DE TRANSPORT DES SEDIMENTS DE SURFACE DANS LE GOLFE DE SAN JORGE, PATAGONIE CENTRALE (ARGENTINE)	33
1.1 RÉSUMÉ EN FRANÇAIS DU PREMIER ARTICLE	33
1.2 QUANTIFYING SOURCES AND TRANSPORT PATHWAYS OF SURFACE SEDIMENTS IN THE GULF OF SAN JORGE, CENTRAL PATAGONIA (ARGENTINA).....	35
1.3 INTRODUCTION	35
1.4 STUDY AREA.....	37
1.4.1 Physical setting.....	37
1.4.2 Sedimentation.....	39
1.5 MATERIAL AND METHODS	40
1.6 RESULTS.....	41
1.6.1 Grain-size distribution	41
1.6.2 Bulk mineralogy	42
1.6.1 Elemental geochemistry	46
1.6.2 Clay mineralogy	48
1.7 SEDIMENT DISTRIBUTION, POTENTIAL SOURCE AREAS AND TRANSPORT PATHWAYS	51
1.8 SUMMARY AND CONCLUSIONS.....	55
1.9 ACKNOWLEDGMENTS	57
1.10 REFERENCES	58
1.11 SUPPLEMENTARY MATERIAL (METHODS).....	61
1.11.1 Grain-size analysis	61
1.11.2 Source samples	62
1.11.3 Bulk mineral analysis	62
1.11.4 Clay mineral analysis	63

1.11.5 Bulk elemental geochemistry.....	64
1.11.6 Statistical approach	65
1.12 SUPPLEMENTARY MATERIAL (REFERENCES)	67
1.13 SUPPLEMENTARY MATERIAL (FIGURES AND TABLES)	69
CHAPITRE 2 EVOLUTION TARDI-PLEISTOCENE ET HOLOCENE DES ENVIRONNEMENTS SEDIMENTAIRES ASSOCIEE A LA TRANSGRESSION POSTGLACIAIRE DANS LE GOLFE DE SAN JORGE, PATAGONIE CENTRALE, ARGENTINE.....	83
2.1 RÉSUMÉ EN FRANÇAIS DU DEUXIÈME ARTICLE.....	83
2.2 LATE PLEISTOCENE AND HOLOCENE EVOLUTION OF SEDIMENTARY ENVIRONMENTS ASSOCIATED WITH POSTGLACIAL TRANSGRESSION IN THE GULF OF SAN JORGE, CENTRAL PATAGONIA, ARGENTINA	85
2.3 INTRODUCTION	86
2.4 STUDY AREA	89
2.5 METHODS.....	90
2.5.1 Physical and geochemical properties of sediment cores.....	92
2.5.2 Radiocarbon dating	94
2.5.3 Geophysical surveys and data processing	97
2.6 RESULTS AND INTERPRETATIONS	97
2.6.1 Seismostratigraphy.....	97
2.6.2 Lithostratigraphy	105
2.6.3 Chronology and sedimentation rates.....	113
2.7 DISCUSSION	114
2.7.1 Sedimentary environments prior to the last marine transgression	114
2.7.2 The last marine transgression in the GSJ	118
2.8 CONCLUSIONS	122
2.9 ACKNOWLEDGMENTS.....	123
2.10 REFERENCES	124
2.11 SUPPLEMENTARY MATERIAL (FIGURES)	131

CHAPITRE 3 NOUVELLE METHODE DE Sommation POUR RECONSTRUIRE LA VARIATION SECULAIRE DU CHAMP MAGNETIQUE ET LA PALEOINTENSITE RELATIVE A HAUTE RESOLUTION EN PATAGONIE DEPUIS 14 CAL KA BP	135
3.1 RÉSUMÉ EN FRANÇAIS DU TROISIÈME ARTICLE	135
3.2 NEW STACKING METHOD TO RECONSTRUCT HIGH-RESOLUTION PALEOMAGNETIC SECULAR VARIATIONS AND RELATIVE PALEOINTENSITY IN PATAGONIA OVER THE LAST 14 KA CAL BP	137
3.3 INTRODUCTION	137
3.4 REGIONAL SETTING, STRATIGRAPHY AND SEDIMENTOLOGY	139
3.5 METHODS	141
3.5.1 Continuous magnetic measurements	143
3.5.2 Discrete magnetic measurements	144
3.5.3 Chronology	144
3.6 RESULTS	145
3.6.1 Magnetic mineralogy, concentration and grain size.....	145
3.6.2 Natural remanent magnetization	149
3.6.3 Relative palaeointensity (RPI) determination	149
3.7 PSV AND RPI STACKS	151
3.7.1 Stacking method	151
3.7.2 PSV and RPI stacks of the GSJ	155
3.8 DISCUSSION	160
3.8.1 Gulf of San Jorge PSV stack versus southern South America records	160
3.8.2 Global-scale paleomagnetic direction comparison.....	162
3.8.3 Pattern of RPI variation	165
3.9 CONCLUSIONS	166
3.10 ACKNOWLEDGMENTS	168
3.11 REFERENCES	169
3.12 SUPPLEMENTARY MATERIAL (FIGURES).....	175

CONCLUSION GÉNÉRALE.....	177
Objectif 1 : Sédimentation contemporaine.....	177
Objectif 2 : Stratigraphie et variations du niveau marin	179
Objectif 3 : Reconstitution paléomagnétique	181
Perspectives.....	182
RÉFÉRENCES BIBLIOGRAPHIQUES.....	185

LISTE DES TABLEAUX

Tableau 1: Mean grain size and End-member (EM) scores for surface sediments of the GSJ	74
Tableau 2: Mineral composition of bulk and clay fraction of sediment samples	76
Tableau 3: Chemical composition of sediment samples	78
Tableau 4: Sources contributions to surface samples	80
Tableau 5: Minerals identified in RockJock v11 (a), consolidated list of minerals (b), minerals used in SedUnMix (c), and samples associated to sources in SedUnMix (d)	82
Tableau 6: Location, water depth, length and piston cores retrieved in the GSJ during the MARGES expedition	91
Tableau 7: Radiocarbon ages from the piston cores analysed in this study. All ages were calibrated using the software CALIB version 7.1 (Stuiver and Reimer, 1993) with the Marine13 calibration curve (Reimer et al., 2013) and two different values of ΔR (0 and 200; see details in Radiocarbon dating section). Calibrated ages are presented with their minimum, maximum and median values	96
Tableau 8: Minimum (Min.), median and maximum (Max.) values of pseudo S-ratios according to the lithological units of the four sediment cores	145

LISTE DES FIGURES

Figure 1: Carte de localisation du golfe de San Jorge et des principales rivières de Patagonie	4
Figure 2: Représentation schématique de la circulation moyennée sur la colonne d'eau au large de la Patagonie. Le secteur en blanc représente le plateau continental (Matano et al., 2010)	6
Figure 3: Modèle d'évolution de l'ennoiement du golfe de San Jorge entre ~ 16 100 et 14 500 cal BP (Ponce et al., 2011).....	8
Figure 4: Distribution des enregistrements d'inclinaison, de déclinaison et d'intensité provenant d'archives sédimentaires et archéologiques (Panovska et al., 2018).....	10
Figure 5: Illustration du N/R Coriolis II lors de la mission dans le golfe de San Jorge. Exemples d'échantillonnage à l'aide du carottier à piston (haut) et d'un carottier à boîte (bas)	17
Figure 6: Localisation des échantillons de surface (A; rond orange), des carottes à gravité (B; triangle rouge), des carottes à boîte (B; rond bleu), des carottes à piston (C; rond noir) et des lignes géophysiques (C; ligne blanche) prélevées dans le golfe de San Jorge en 2014	18
Figure 7: Boucle d'hystérésis d'un matériau ferromagnétique (adapté de Maher, 2007)	23
Figure 8: Comparaison pour une même ligne <i>sparker</i> entre les données brutes et les données traitées.....	26
Figure 9: Maps of the study area with sample locations. The dots indicate surface sediment samples in the GSJ, the diamonds denote sites with surface sediment samples, as well as water column filters, and the triangles illustrate samples from potential source areas. (a) Map of Patagonia showing the main hydrodynamic circulation on the Patagonian continental shelf (gray arrows; Palma et al. 2008), simplified surface geology, and main geographic features mentioned in the text. (b-d) Bathymetric maps	

of the Gulf of San Jorge and the marine park areas. (e) Bathymetric map of the GSJ with adjacent continental margin 38

Figure 10: End-member modeling analyses (EMMA) performed on the detrital fraction of the grain-size distribution in the GSJ. (a) The grain-size distribution of the first three end-members accounts for more than 91 % of the variance. (b) Three representative unmixed grain-size distributions produced from EMMA based on the grain-size distributions of the GSJ samples (gray lines). (c-e) Log[EM3/(EM2+EM1)] end-member ratios in the GSJ and marine park areas, respectively..... 43

Figure 11: Quartz-plagioclase-clays ternary plot illustrating the relative compositions of the main minerals. The samples are illustrated according to their locations in the gulf; the northward-inner gulf to southward-outer gulf tendency is calculated from absolute latitude and longitude coordinates (excluding the park sites)..... 45

Figure 12: (a) Spatial distribution of the elemental balance for major mineral groups (i.e., $b_{\{(Quartz+Feldspars)/Clays\}}$). (b-d) Maps showing relative proportions of inner gulf coastal inputs (S1+S2; b), dust transport (S4; c) and external/oceanic contributions (S3+S5; d) to sediment mineralogical composition. The proportions in major mineral groups (quartz, feldspars and clays) of proposed sources (S1+S2, S4 and S3+S5) are presented in pie charts 47

Figure 13: (a) Si-Al-Fe abundances of marine park areas and other GSJ samples associated with mean grain size (ϕ). (b) K-Fe-Ca distribution of marine park areas and other GSJ samples, plotted together with potential source area samples, as well as surface sediment samples from the Patagonian continental shelf (Table 3). The samples are illustrated according to their location in the gulf; northward-inner gulf to southward-outer gulf tendency calculated from absolute latitude and longitude coordinates (excluding the park sites). (c) Herron (1988) geochemical classification diagram for surface sediment and water column samples of the GSJ. (d) Biplot of the PC-1 versus PC-2 generated from the log-centered transformation of major, minor and trace elements of GSJ samples, presented with map of PC-1 scores 49

Figure 14: (a-b) Ternary diagram of smectite (S), kaolinite (K), and illite + chlorite (I+C) relative concentration in samples from marine park areas, other GSJ samples, continental shelf and potential source areas. (c) Spatial distribution of $\log[S/(I+C)]$ 50

Figure 15: Schematic map of the main sedimentary regions and transport pathways identified in the Gulf of San Jorge area. The sedimentary regions were determined

according to our interpretations and previous results from Fernández et al. (2003). The bulk terrigenous inputs are illustrated with filled arrows, whereas the terrigenous clay inputs are depicted with dotted arrows. Note that the spatial distribution of the samples does not follow a regular and homogenous pattern, leading to potentially underrepresented areas.....	56
Figure 16: Spatial distribution of the mean grain-size for the surface sediments in the GSJ (a) and marine park areas (b and c).....	69
Figure 17: Spatial distribution of tephras (i.e. volcanic rhyolitic tephras) concentration in the GSJ.....	70
Figure 18: (a) Comparison of measured X-ray diffractogram and calculated best-fit curve obtained from RockJock v11 on a representative sample (BV01). The quartz and rhyolitic tephra (Hekla-4) standard used in the XRD analysis are also show for comparison. (b-c) Scanning Electron Microscopy (SEM) images of the 300-63 fraction of surface sediment sample BV01. (d) K ₂ O vs. SiO ₂ classification diagram for glass shards from BV01, BV06 and BC11 surface samples. The geochemical composition field of different volcanic provinces of the southern part of the SVZ (Carel et al., 2011 and references therein) and ashes from the 2008 Chaitén eruption (Watt et al., 2009; Ruggieri et al., 2012) are presented for comparison.....	71
Figure 19: (a) Weight % Si plotted vs. wt% quartz. (b) Weight % Ca plotted vs. wt% plagioclase. (c) Weight % Al plotted vs. wt% clays. (d) Weight % Fe plotted vs. wt% Fe-bearing + chlorite + clays	72
Figure 20: (a) Box plot illustrating the smectite (S), illite (I) and chlorite (C) relative concentration of GSJ sediment samples regarding to the RockJock and oriented mounted methods (<2 µm; MacDiff). (b) Box plot of ratios S+I/C and S/I+C showing the relative clays composition of GSJ sediment samples regarding to the RockJock and oriented mounted methods (<2 µm)	73
Figure 21: (a) Regional map showing the location of the Gulf of San Jorge in the southern part of South America. (b) Bathymetric map of the Gulf of San Jorge with position of piston cores and related box cores (black dots), as well as seismic sparker profiles (white lines) used in this study	92
Figure 22: High-resolution sparker seismic profile (section of line 008; top) with interpreted version (base) showing four seismic units and sub-units (units S0, S2, S3a and S4), incised valley (white line) as well as location of core 003PC	99

Figure 23: High-resolution sparker seismic profile (section of line 018; top) with interpreted version (base) showing six seismic units and sub-units (units S0, S1a, S1b, S2, S3a and S4), incised valleys (white lines) as well as location of core 011PC	101
Figure 24: High-resolution sparker seismic profile (section of line 003; top) with interpreted version (base) showing three seismic units and sub-units (units S0, S3b and S4)	103
Figure 25: Lithologic descriptions (Litho), photographs (Pct), CT-scan images (CT) and calibrated radiocarbon ages from piston cores retrieved in the GSJ during the MARGES expedition	107
Figure 26: Grain-size and geochemical properties, magnetic susceptibility and sedimentation rate coupled with photographs, CT-scan images, lithologic description, lithofacies and calibrated radiocarbon ages of the investigated piston cores 003PC (A), 006PC (B), 008PC (C) and 011PC (D)	109
Figure 27: Photographs of unit L2a (A), the contact between L2b and L3 (B) as well as the transition between units L3 and L4 (C) in core 003PC.....	111
Figure 28: Age-depth models for cores 006PC (A), 003PC (B), 008PC (C) and 011PC (D), generated with BACON package of the R software (Blaauw and Christen, 2011). Calibrated radiocarbon ages used in the age-depth models are presented in transparent blue excepted for the AMS ^{14}C ages from micro-fragments of algae and wood, and the age from 008PC not retained which are shown in transparent green and red, respectively. Calibrated radiocarbon dates are also illustrated with their respective conventional ages. The grey dotted lines correspond to the 95% confidence intervals and the red dotted line shows the “best” model based on the weighted mean age for each depth. Sedimentation rates are presented with the orange line excepted for the upper sections, where the age-depth models have been constructed considering the top of cores as modern ages, which are shown in dotted lines.....	117
Figure 29: Comparison between the Log (Ti/Ca) ratio values of core 003PC (red curve) with eustatic and relative sea-level curves since 20 ka BP. A 400 years running mean of Log(Ti/Ca) raw values is also presented (black curve). Selected intervals of Log(Ti/Ca) ratios (yellow curve) and median grain size (red dotted curve; ϕ) are presented superimposed over respective core photographs sections. The eustatic sea-level curves were generated from the prediction of the sea-level history using the ICE-5G model (blue curve; Peltier and Fairbanks, 2006) as well as a reconstruction from	

the Barbados coral reefs (purple curve; Abdul et al., 2016), and adapted from Jakobson et al. (2017). The estimated time intervals of MWP-1A and MWP-1B are presented with gray columns. The relative sea-level curve for the ACS (green curve) was compiled by Violante and Parker (2004) after Cavallotto et al. (1995) and Guilderson (2000).....	121
Figure 30: Scanning electron microscopy (SEM) images of the bulk fraction of sediment samples retrieved in the potential gypsum rich layer at 376 cm in 003PC. Elemental composition (weight %) of five particles (ten spectra).....	131
Figure 31: Correlation between piston (PC) and box cores (BC) using a^* for cores 003PC and 011PC, and relative content of Fe for cores 006PC and 008PC. To compensate for the absence of box core at the 003PC, this core was correlated with the closest “depth corrected” piston core, 011PC. Properties for the PC and BC are presented in black and orange, respectively, except in the case of 003PC in which 011PC is shown in orange	132
Figure 32: High-resolution sparker seismic profile (section of line 017; A) with interpreted version (B) showing six seismic units and sub-units (units S0, S1a, S1b, S2, S3a and S4) and incised valleys (white lines).....	133
Figure 33: Interpreted high-resolution sparker seismic profiles (section of lines 004bis, 012bis and 014; A, B and C) showing locations of core 001PC, 006PC and 008PC, respectively	134
Figure 34: (A) Regional map illustrating the location of the Gulf of San Jorge, as well as the paleomagnetic records discussed in this paper. From north to south, LES: Lake Escondido, LET: Lake El trébol, LCH: Lake Laguna Cháltel, LPA: Lake Laguna Potrok Aike (PASADO and SALSA projects). (B) Bathymetric map of the Gulf of San Jorge with the location of the sedimentary records used in this study	142
Figure 35: High-resolution downcore variations of the characteristic remanent magnetization (i.e., inclination and corrected declination), MAD values and magnetic properties of cores 003PC, 006PC, 008PC and 011PC. These results are presented with the lithologic descriptions and lithofacies of the four cores. The red vertical line on the inclination graphs depicts the expected inclination from the GAD model for the latitude of the coring sites. The intervals with MAD values $> 15^\circ$ are highlighted in red and the limits of the MAD values used in the stacking method (i.e., 5° , 10° and 15° , see text for details) are indicated with the red dashed lines.....	147

Figure 36: (A), (B), (C) and (D). Hysteresis loops of two typical samples for the cores 003PC, 006PC, 008PC and 011PC, respectively. (E). Day plot (Day et al., 1977) for the discrete samples retrieved in eachu-channel. The mixing reference lines for single and multi-domain (SD and MD) are from Dunlop (2002a, 2002b)	148
Figure 37: Comparison of the normalized relative paleointensity from the slope method with ARM as normalizer (left), from the average ratios of NRM/ARM (middle) and NRM/IRM (right) at 10-40 mT, coupled with the demagnetization curves for NRM, ARM and IRM (top), as well as the RPI proxy vs. its normalizer with correlation coefficients (bottom). The results are presented for cores 003PC (A), 006PC (B), 008PC (C) and 011PC (D)	153
Figure 38: Quality factors used depending on the MAD values for the construction of the PSV and RPI stacks	154
Figure 39: (A). Angular (blue curve) and moment (red curve) sensitivity function of simulated sedimentation rates. (B). Response functions of the 2G Enterprises TM SRM-755 cryogenic magnetometer used in this study at ISMER	154
Figure 40: Paleomagnetic inclination profiles of the four sediment cores, as well as the GSJ stacks. Correlative features of paleomagnetic inclination (I-A to I-G) and declination (D-A to D-G) are indicated in red. Calibrated radiocarbon ages used in the age-depth models are illustrated by sun crosses. A gray scale is used to represent the evolution of sedimentation rates in each core. The intervals with MAD values > 15° are delimited with an orange line	156
Figure 41: Paleomagnetic declination profiles of the four sediment cores, as well as the GSJ stacks. Correlative features of paleomagnetic inclination (I-A to I-G) and declination (D-A to D-G) are indicated in red. Calibrated radiocarbon ages used in the age-depth models are illustrated by sun crosses. A gray scale is used to represent the evolution of sedimentation rates in each core. The intervals with MAD values > 15° are delimited with an orange line	157
Figure 42: Relative paleointensity profiles of the four sediment cores, as well as the GSJ stack. Correlative features of relative paleointensity (R-A to R-G) are indicated in red. Calibrated radiocarbon ages used in the age-depth models are illustrated by sun crosses. A gray scale is used to represent the evolution of sedimentation rates in each core. The intervals with MAD values > 15° are delimited with an orange line.....	159

Figure 43: Comparison of paleomagnetic inclination from the GSJ stacks with southern South America paleomagnetic direction and spherical harmonic models. The regional PSV records consist of data from lakes Laguna Cháltel (dark gray; Parlermo et al., 2019), Escondido (black; Gogorza et al., 2002), El trébol (purple; Irurzun et al., 2006) and Laguna Potrok Aike (orange and light blue; PASADO and SALSA projects; Lisé-Pronovost et al., 2013; Gogorza et al., 2012). The models are represented by the CALS10k.2 spherical harmonic model (dark blue; Constable et al., 2016) and the SHA.DIF.14k model (green; Pavón-Carrasco et al., 2014). The gray shading and the dotted green lines indicate the 95% confidence interval of the GSJ stack and the SHA.DIF.14k data, respectively. Correlative features of inclination (i1 to i7) and declination (d1 to d5) are displayed in black 163

Figure 44: Comparison of paleomagnetic declination from the GSJ stacks with southern South America paleomagnetic direction and spherical harmonic models. The regional PSV records consist of data from lakes Laguna Cháltel (dark gray; Parlermo et al., 2019), Escondido (black; Gogorza et al., 2002), El trébol (purple; Irurzun et al., 2006) and Laguna Potrok Aike (orange and light blue; PASADO and SALSA projects; Lisé-Pronovost et al., 2013; Gogorza et al., 2012). The models are represented by the CALS10k.2 spherical harmonic model (dark blue; Constable et al., 2016) and the SHA.DIF.14k model (green; Pavón-Carrasco et al., 2014). The gray shading and the dotted green lines indicate the 95% confidence interval of the GSJ stack and the SHA.DIF.14k data, respectively. Correlative features of inclination (i1 to i7) and declination (d1 to d5) are displayed in black 164

Figure 45: Comparison of relative paleointensity from the GSJ stack with southern South America records and spherical harmonic models. The regional RPI records consist of data from lakes Laguna Cháltel (dark gray; Parlermo et al., 2019), Escondido (black; Gogorza et al., 2002), El trébol (purple; Irurzun et al., 2006) and Laguna Potrok Aike (orange and light blue; PASADO and SALSA projects; Lisé-Pronovost et al., 2013; Gogorza et al., 2012). The models are represented by the CALS10k.2 spherical harmonic model (dark blue; Constable et al., 2016) and the SHA.DIF.14k model (green; Pavón-Carrasco et al., 2014). The gray shading and the dotted green lines indicate the 95% confidence interval of the GSJ stack and the SHA.DIF.14k data, respectively. Correlative features of intensity (r1 to r6) are displayed in black 167

Figure 46: Anhysteretic susceptibility (k_{ARM}) vs. magnetic susceptibility (k_{LF}) biplot (King et al., 1983) used as a grain-size proxy of magnetite for the samples of cores 003PC, 006PC, 008PC and 011PC 175

Figure 47: Vector end-point diagrams (Zijderveld, 1967) of representative samples retrieved from the four sediment cores used in this study..... 176

Figure 48: Modèle schématique présentant l'évolution des environnements sédimentaires au centre du golfe de San Jorge depuis la dernière transgression marine ... 180

LISTE DES ABRÉVIATIONS, DES SIGLES ET DES ACRONYMES

ACS	<i>Argentine continental shelf</i> , plateau continental argentin
ARM	<i>anhysteretic remanent magnetisation</i> , aimantation rémanente anhystérotique
BC	<i>box corer sample</i> , échantillon de carottier à boite
BV	<i>Van Veen grab sample</i> , échantillon de benne Van Veen
CTD	<i>Conductivity temperature depth</i> , conductivité, température et profondeur
GAD	<i>geocentric axial dipole</i> , dipole axial géocentré
GSJ	<i>Gulf of San Jorge</i> , golfe de San Jorge
Hc	<i>coercive force</i> , coercivité
Her	<i>remanent coercive force</i> , coercivité rémanente
IRM	<i>isothermal remanent magnetization</i> , aimantation rémanente isothermale
ISMER	Institut des Sciences de la Mer à Rimouski
MAD	<i>maximum angular deviation</i> , déviation angulaire maximum
MARES	<i>Marine Ecosystem health of the San Jorge Gulf</i>
MARGES	<i>Marine Geology of the Gulf of San Jorge</i>
MD	<i>multidomain</i> , domaines multiples
Mr	<i>saturation remanence</i> , rémanence à saturation
Ms	<i>saturation magnetisation</i> , aimantation à saturation

MSCL	<i>multi-sensor core logger</i> , banc de mesures
MWP	<i>meltwater pulse</i> , impulsion de fonte
N/R	navire de recherche
NRM	<i>natural remanent magnetisation</i> , aimantation naturelle rémanente
PROMESSe	<i>programa multidisciplinario para el estudio del ecosistema y la geología marina del golfo San Jorge y las costas de las provincias de Chubut y Santa Cruz</i>
PSD	<i>pseudo-single domain</i> , domaine pseudo-simple
PSV	<i>paleomagnetic secular variation</i> , variation séculaire du champ magnétique
R/V	research vessel, navire de recherche
RPI	<i>relative paleointensity</i> , paléointensité relative
SAA	<i>South Atlantic Anomaly</i> , Anomalie magnétique de l'Atlantique Sud
SD	<i>single domain</i> , domaine simple
SEM	<i>scanning electron microscope</i> , microscope électronique à balayage
SIRM	<i>saturation isothermal remanent magnetization</i> , aimantation rémanente isothermale à saturation

INTRODUCTION GÉNÉRALE

Cette première partie a pour objectif d'introduire la problématique générale à l'origine de la création de ce projet de thèse. Afin de fournir un cadre régional, une description géographique sommaire de la Patagonie, qui se situe au cœur de cette thèse, sera réalisée dans un premier temps. Une revue bibliographique et une synthèse des connaissances régionales portant principalement sur le contexte sédimentaire, les variations du niveau marin et le paléomagnétisme depuis la fin du Pléistocène et lors de l'Holocène seront développées dans un second temps. À la suite de cette introduction seront présentés les objectifs de la thèse et les questions soulevées pour chacun des chapitres. La méthodologie développée pour mener à bien ce projet sera ensuite détaillée. L'organisation de la thèse et les différentes contributions et collaborations de l'auteur concluront cette section. L'introduction générale sera suivie par la présentation en anglais des trois chapitres de la thèse rédigés sous la forme d'articles scientifiques.

LA PATAGONIE

La Patagonie constitue la région située la plus au sud du continent sud-américain, s'étendant entre les latitudes 37°S et 56°S, depuis le bassin versant de la rivière Colorado jusqu'au Cap Horn. La structure géographique et géologique de la Patagonie peut être résumée par deux vastes régions distinctes, la Patagonie andine et la Patagonie extra-andine (Coronato et al., 2008). La première région qui est également appelée Cordillère de Patagonie constitue la section la plus au sud de la Cordillère des Andes, les Andes méridionales. La Patagonie andine est composée de chaînes de montagnes formées par un intense volcanisme et plutonisme et par l'activité tectonique au cours du Cénozoïque (Ramos, 2002). La Patagonie extra-andine est principalement caractérisée par des plateaux entrecoupés par des

vallées fluviales, formant de vastes plaines d'épandage fluvioglaciaire (Coronato et al., 2008). La géologie de surface de cette région est dominée par des dépôts clastiques (graviers et sables) et pyroclastiques tertiaires suivis en abondance par des roches sédimentaires et des roches ignées, du Crétacé et du Jurassique-Crétacé, respectivement (Hernández et al., 2017). Dans le secteur oriental de la région extra-andine, les vastes plateaux se jettent dans l'océan Atlantique et se connectent à la marge continentale de l'Argentine au niveau du plateau continental argentin (ACS). La surface relativement plane de l'ACS recouvre un espace d'environ $1 \times 10^6 \text{ km}^2$, s'étend sur $\sim 170 \text{ km}$ au nord de la Patagonie et peut dépasser 850 km au sud, dans le secteur des Îles Malouines (Violante et al., 2014).

La Patagonie est située à la limite de la ceinture de haute pression subtropicale où l'on retrouve l'anticyclone de Sainte-Hélène (Atlantique Sud) et l'anticyclone de l'Île de Pâques (Pacific Sud) ainsi que la zone de basse pression subpolaire. La Patagonie est ainsi localisée au cœur de la ceinture des vents d'ouest (*westerlies*) de l'Hémisphère Sud. Ces vents circonscrits sur une large bande (nord-sud) de plus de 3000 km sont particulièrement intenses en Patagonie. En effet, le sud de l'Amérique du Sud est la seule masse continentale au-delà de la latitude 44°S , à l'exception de l'Antarctique, traversée par la ceinture des vents d'ouest. La rencontre entre ces masses d'air humide et les Andes, qu'elles coupent perpendiculairement, engendre de fortes précipitations orographiques sur les flancs pacifiques de la Cordillère et une diminution abrupte des précipitations vers l'Est (Paruelo et al., 1998). Dans ce contexte, la Patagonie occidentale à l'ouest des Andes est marquée par un climat tempéré hyper-océanique (océanique avec des précipitations abondantes) contrairement à la Patagonie orientale caractérisée par un climat sec avec une faible amplitude thermique (Coronato et al., 2008). Actuellement, les vents les plus intenses sont concentrés entre les latitudes 49°S et 53°S , ce qui constitue le cœur de la ceinture des vents d'ouest (Kilian et Lamy, 2012).

MISE EN CONTEXTE DE LA SÉDIMENTATION

Localisé dans la partie centrale de la Patagonie, entre les latitudes 45°S (Cap Dos Bahías) et 47°S (Cap Tres Puntas), le golfe de San Jorge (GSJ) constitue une avancée de l'Atlantique Sud (plateau continental argentin), sur plus de 100 km de longueur et 150 km de largeur pour une superficie supérieure à 39 000 km², au sein du continent Sud-Américain (Fig. 1). Le climat semi-aride du GSJ est caractéristique de la partie orientale de la Patagonie avec des précipitations très faibles (~230 mm/an en moyenne; Aravena et Luckman, 2009). Le GSJ, qui ne possède pas d'affluents majeurs et pérennes, se trouve ainsi au centre d'un secteur côtier de plusieurs centaines de kilomètres dépourvu d'importantes rivières à l'exception de la rivière Deseado, située à quelques dizaines de kilomètres au sud du GSJ, et ayant un débit relativement modeste (5 m³/s de moyenne annuelle; Fig. 1 ; Kokot, 2004). Les principales rivières de Patagonie sont situées au nord avec les rivières Negro et Chubut (respectivement 1014 et 47 m³/s de moyenne annuelle ; Fig. 1) et au sud avec les rivières Santa Cruz et Gallegos (respectivement 750 et 15 m³/s de moyenne annuelle; Fig. 1 ; Kokot, 2004). Si actuellement les apports par les rivières ne jouent pas un rôle prépondérant sur le bilan sédimentaire au large de la Patagonie (~ 3% des apports sédimentaires terrigènes; Pierce and Siegel, 1979), en raison de leurs faibles débits (Gaiero et al., 2003; Cavallotto et al., 2011), il en était différemment au cours du Pléistocène et du dernier maximum glaciaire (LGM) où le débit de ces rivières était beaucoup plus important (Kokot, 2004). Cette différence est mise en évidence par la taille surdimensionnée de certaines vallées fluviales au regard du dynamisme actuel des rivières et par la présence au sud du plateau continental d'une grande quantité de matériel grossier qui ne pourrait pas être acheminé par les débits actuels (Violante et al., 2014). Au cours de l'Holocène, les écoulements à travers le bassin versant de l'Atlantique ont considérablement diminué alors que ceux du bassin du Pacifique ont augmenté jusqu'à inverser le rapport de force entre ces deux bassins versants (Isla et al., 2015). Par exemple, la rivière Deseado (entre 46° et 47°S) drainait au Pléistocène les eaux provenant des flancs est des glaciers du nord de la Patagonie, mais depuis la dernière glaciation, les écoulements à travers le bassin versant de cette rivière ont considérablement

baissé en raison de modifications géomorphologiques (moraines et coulées basaltiques) et des variations climatiques (McCulloch et al., 2000; Iantanos et al., 2002; Isla et al., 2015).



Figure 1: Carte de localisation du golfe de San Jorge et des principales rivières de Patagonie

L'impact des rivières sur la sédimentation dans le GSJ est en partie conditionné par la circulation sur le plateau continental argentin. Matano et al. (2010) suggèrent que la circulation sur le plateau est principalement influencée par le courant des Malouines associé à d'autres mécanismes tels que les courants d'ouest, les marées de hautes amplitudes et les décharges d'eaux de faibles salinités provenant des rivières de Patagonie et du détroit de Magellan. Le courant des Malouines constitue une subdivision dirigée vers le Nord du courant circumpolaire antarctique. Ce courant remonte ainsi à la limite du plateau continental de l'Amérique du Sud en transportant des eaux subpolaires froides et peu salées jusqu'à une latitude proche de 38°S (Fig. 2; Piola and Matano, 2001). La circulation moyenne sur le plateau est ainsi caractérisée par un écoulement important vers le nord-est avec schématiquement une structure verticale similaire à un système à deux couches avec des courants orientés vers le nord-est en surface et vers le sud-ouest dans la couche de fond (Palma et al., 2008; Matano et al., 2010). Le GSJ se trouve également à la limite d'influence de la décharge du détroit de Magellan qui longe les côtes au sud et pénètre dans le GSJ dans le secteur sud-est au niveau du cap Tres Puntas (Fernández et al., 2005; Palma et Matano, 2012).

Les caractéristiques géographiques et climatiques marquées par de vastes plaines d'épandage fluvioglaciaire faiblement recouvertes de végétation et par des conditions arides couplées avec la présence de la ceinture des vents d'ouest, confèrent à une large partie de la Patagonie des conditions optimales pour la mise en suspension et le transport d'aérosols minéraux (Prospero et al., 2002 ; Gaiero et al., 2003 ; Pye, 2015). Les poussières sont transportées sur de longues distances au cœur de l'Atlantique Sud et pourraient probablement atteindre la péninsule Antarctique (Grousset et al., 1992 ; McConnell et al., 2007 ; Crespi-Abril et al., 2016). Sur le plateau continental argentin, le transport de poussières représentent la seconde source d'apports sédimentaires devant les apports par les rivières (Gaiero et al., 2003). Dans la région du GSJ, aucune étude n'a été réalisée pour caractériser et quantifier le transport éolien malgré la localisation du golfe en plein cœur d'un secteur susceptible d'alimenter l'Atlantique Sud en aérosols minéraux (Prospero et al., 2002 ; Montes et al., 2017).

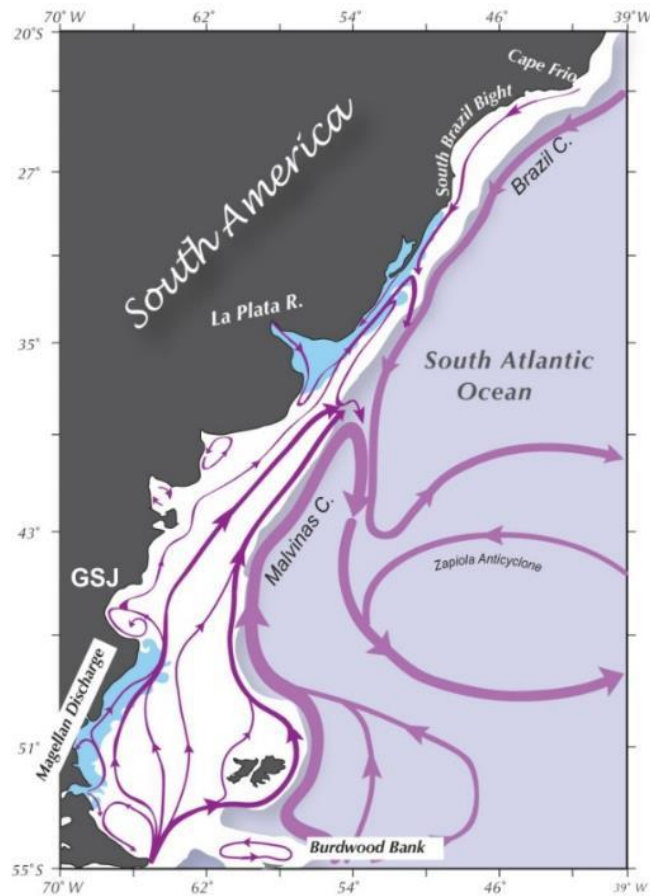


Figure 2: Représentation schématique de la circulation moyennée sur la colonne d'eau au large de la Patagonie. Le secteur en blanc représente le plateau continental (Matano et al., 2010)

VARIATIONS DU NIVEAU MARIN DEPUIS LA DERNIERE GLACIATION

Les variations climatiques au cours du Quaternaire ont également fortement influencé la morphologie et la stratigraphie du plateau continental argentin. Durant les derniers cycles glaciaires/interglaciaires, d'importantes variations eustatiques ont affecté le plateau continental avec des bas niveaux marins de plusieurs dizaines de mètres sous le niveau actuel lors des périodes froides (Rabassa, 2008). Parker et al. (1997) suggèrent la présence sur le plateau continental de quatre grands ensembles de terrasses à différentes profondeurs avec

une orientation subparallèle à la côte et principalement composés de sédiments grossiers. La formation de ces terrasses serait liée à l'action des vagues lors des périodes d'interruption ou de ralentissement de l'augmentation du niveau marin suite au dernier maximum glaciaire (~24 000 cal a BP; Rabassa, 2008; Ponce et al., 2011). Le niveau marin au cours du LGM était d'environ -105 à -120 m sous le niveau actuel (Fleming et al., 1998; Guilderson et al., 2000), une grande partie de l'ACS était alors émergée formant d'immenses plaines similaires à celles que l'on retrouve le long de la côte atlantique de la Patagonie à l'actuel (Cavallotto et al., 2011; Ponce et al., 2011). Malgré la présence d'une surface d'érosion associée à la transgression marine à la base de la séquence sédimentaire post-LGM sur une large partie de l'ACS, plusieurs témoins de cette période de bas niveau marin ont été partiellement conservés (Violante et al., 2014). Ainsi, l'identification de nombreuses vallées incisées et de chenaux lors de campagnes géophysiques, notamment au large du Río de la Plata (~35°S) et dans l'actuel estuaire de Bahía Blanca (~39°S), a permis de mettre en évidence d'anciens réseaux hydrographiques oblitérés au large du plateau continental (Violante et al., 2007; Violante et Parker, 2004 ; Giagante et al., 2011). Un modèle régional pour définir les écoulements et la configuration du réseau de drainage sur l'actuel plateau continental au cours de bas niveaux marins est proposé par Violante et al. (2014) à partir des données géophysiques disponibles.

À la fin du LGM, la phase de transgression marine postglaciaire s'est mise en place avec une remontée du niveau marin, possiblement entrecoupée par des périodes de stagnation, et l'immersion des plaines formant l'actuel plateau continental. Selon Rostami et al. (2000), l'élévation du niveau marin en Patagonie est principalement influencée par l'hydro-isostasie (subsidence du fond océanique sous l'effet de la masse d'eau provenant d'une déglaciation), par la morphologie du plateau (vaste étendue relativement plane) et par l'activité tectonique. Ponce et al. (2011), dont l'étude repose sur un modèle d'élévation du niveau marin basé sur une courbe d'élévation du niveau marin mondiale depuis le LGM proposé par Fleming et al. (1998), suggère le début de l'envahissement du GSJ par les eaux océaniques autour de 15500 - 15000 cal a BP lorsque le niveau des eaux a atteint -90 m. Un modèle de l'évolution de l'ennoiement du GSJ est également proposé par ces auteurs jusque ~ 14500 cal a BP (Fig. 3; Ponce et al., 2011). Cependant, ces datations approximatives sont

uniquement basées sur un modèle d’élévation globale dont la courbe diffère d’un modèle régional proposé par Guilderson et al. (2000). La courbe de Guilderson et al. (2000) s’appuie notamment sur 3 âges ^{14}C obtenus dans des carottes sédimentaires prélevées dans le GSJ dans les années 50 et 60 par le *Lamont-Doherty Earth Observatory*. Ces datations représentent d’ailleurs les rares informations disponibles actuellement sur la stratigraphie quaternaire du GSJ. Si de nombreux profils sismiques à haute résolution et des prélèvements de sédiments de surface et de sous-surface ont été réalisés et analysés au cours des 30 dernières années par l’*Argentine Hydrographic Survey* (e.g., Parker et al., 1997, 2008; Violante et Parker, 2004), afin notamment d’étudier les évolutions morpho-sédimentaires quaternaires du plateau, dans le secteur nord du plateau continental argentin, il n’existe actuellement aucune donnée sismique à haute résolution des séquences quaternaires dans les autres secteurs du plateau continental argentin (Violante et al., 2014).

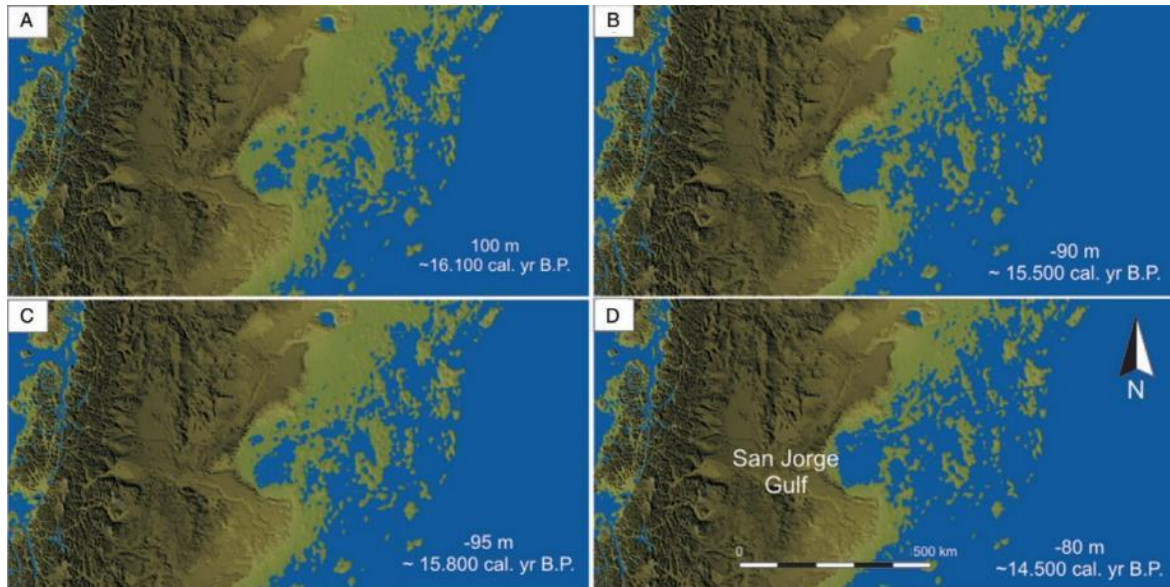


Figure 3: Modèle d’évolution de l’ennoiement du golfe de San Jorge entre ~ 16 100 et 14 500 cal BP (Ponce et al., 2011)

En l’absence d’archives sédimentaires marines disponibles dans la région du golfe de San Jorge, de nombreuses études se sont concentrées sur l’étude des crêtes de plage et des terrasses marines pour reconstituer les variations du niveau marin au cours de l’Holocène

(e.g., Schellmann and Radtke, 2010; Ribolini et al., 2011; Zanchetta et al., 2012, 2014; Bini et al., 2017). Selon les travaux de synthèses réalisés par Schellmann and Radtke (2010), le niveau marin aurait dépassé le niveau actuel autour de 8600 cal a BP et le maximum de la transgression aurait été atteint entre 7400 et 6600 cal a BP avec un niveau marin relatif compris entre 2 et 4 m au-dessus du niveau marin actuel. Après cette période, le littoral du GSJ a connu une diminution progressive et discontinue du niveau marin relatif avec plusieurs phases caractérisées par des changements de vitesse d’abaissement du niveau marin relatif (Zanchetta et al., 2012, 2014; Bini et al., 2017).

PALEOMAGNETISME ET ETAT DES CONNAISSANCES EN AMERIQUE DU SUD

Le champ magnétique terrestre est la résultante d’une dynamo auto-entretenue dans le noyau externe générée par des mouvements de convection de fluides composés de fer et de nickel. Le champ magnétique peut-être observé à n’importe quel point à la surface de la Terre sous la forme d’un vecteur caractérisé par une direction (inclinaison et déclinaison) et une magnitude proportionnelle à l’intensité. La déclinaison représente l’angle entre les méridiens géographique et magnétique et l’inclinaison, l’angle entre la résultante du champ magnétique et l’horizontale. Au cours du temps, l’intensité du champ magnétique et la position des pôles magnétiques ont connu des variations à des échelles allant d’une année à plusieurs millions d’années (Dormy et al., 2000; Stoner et St-Onge, 2007; Tauxe, 2010). Le paléomagnétisme constitue l’étude des variations du champ magnétique enregistrées dans les matériaux géologiques (e.g., les sédiments lacustres ou marins) contenant des minéraux ferrimagnétiques. Les modèles d’évolution du champ magnétique reposent ainsi sur des observations satellitaires ou des enregistrements paléomagnétiques provenant d’archives géologiques (e.g., sédiments et coulées de lave) et archéologiques, et dans de nombreux cas d’une compilation des deux (e.g., Korte et al., 2011; Constable et al., 2016; Pavón-Carrasco et al., 2014). Cependant, une des principales limites des interpolations des variations du champ magnétique générées dans ces modèles est la grande disparité géographique des

enregistrements paléomagnétiques disponibles. En effet, le nombre d'études paléomagnétiques réalisées dans l'hémisphère Sud s'avère extrêmement limité en comparaison des travaux effectués dans l'Hémisphère Nord (Fig. 4; Korte et al., 2005, 2011 ; Panovska, 2018).

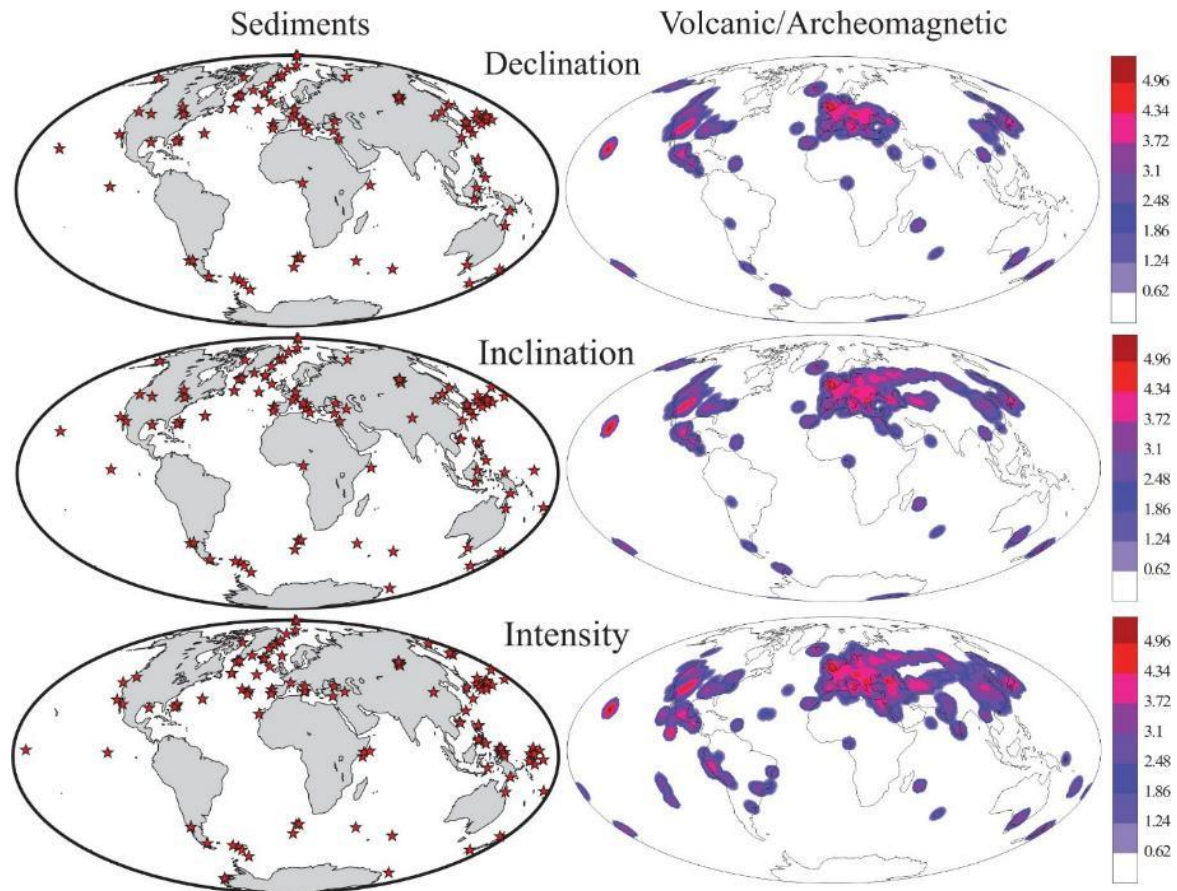


Figure 4: Distribution des enregistrements d'inclinaison, de déclinaison et d'intensité provenant d'archives sédimentaires et archéologiques (Panovska et al., 2018)

Une des premières études paléomagnétique réalisée en Amérique du Sud a été conduite par Creer et al. (1983) dans trois lacs du nord-ouest de la Patagonie ($\sim 41^\circ\text{S}$, 71.5°O ; les lacs Brazo Campanario, Morenito et El Trébol). Les sédiments des lacs Morenito et El Trébol, ainsi que d'un lac voisin (Lac Escondido), ont continué à être étudiés au cours des dernières années (e.g., Gogorza et al., 2000, 2002, 2004, 2006; Irurzun et al., 2008, 2009). Ces travaux ont permis de mettre en évidence l'enregistrement, dans les séquences

sédimentaires, des paléointensités relatives et des variations séculaires du champ magnétique depuis la dernière glaciation (~ 24 000 dernières années). Au cours des dernières années, un nouveau lac a été investigué au sud de la Patagonie, le lac Laguna Potrok Aike (e.g., Gogorza et al., 2011, 2012; Lisé-Pronovost et al., 2013). Lisé-Pronovost et al. (2013) présentent des enregistrements des variations de paléointensité relative et de paléodirections (déclinaison et inclinaison) depuis 51 200 cal a BP. Les résultats de cette étude indiquent notamment l'enregistrement, dans ce secteur de la Patagonie, de variations globales, les excursions géomagnétiques de Laschamp et Mono Lake à 41 000 et 32 000 cal a BP, respectivement (Singer, 2014). De plus, Lisé-Pronovost et al. (2013) présentent des variations régionales du champ magnétique terrestre, plus particulièrement la diminution de la paléointensité et changement des paléodirections vers 46 000 cal a BP également observés dans l'Atlantique Sud et au large du Chili (Stoner et al., 2002; Lund et al., 2006). À partir d'archives sédimentaires couvrant les 5000 dernières années et prélevées dans des lacs au sud de la Patagonie, Carmen et Laguna Cháltel, Gogorza et al. (2018) et Palermo et al. (2019) ont mis en évidence une bonne corrélation entre les enregistrements des variations de paléointensité relative ainsi que de paléodirection (inclinaison et déclinaison) et les enregistrements paléomagnétiques provenant d'autres secteurs au sud de l'Amérique du Sud. L'observation d'un synchronisme entre des événements géomagnétiques majeurs, précédemment constaté par Lisé-Pronovost et al. (2013) à partir des archives plus anciennes du lac Laguna Potrok Aike, constitue selon les auteurs une perspective prometteuse pour établir un modèle régional de la variation séculaire du champ magnétique terrestre et ainsi alimenter les modèles globaux.

Par ailleurs, malgré la faible quantité d'informations disponible dans l'Hémisphère Sud, des données provenant d'observations satellitaires et des modèles ont toutefois permis de mettre de l'avant le développement d'une importante anomalie magnétique depuis les derniers siècles, l'anomalie magnétique de l'Atlantique Sud. Cette anomalie magnétique, qui migre depuis environ 400 ans de l'Afrique vers l'Amérique du Sud, est caractérisée par les plus faibles valeurs de champ magnétique mesurées à la surface de la Terre (Pinto et al., 1992; Heitzler, 2002). Les conséquences de cette anomalie sont nombreuses, par exemple

l'anomalie magnétique de l'Atlantique Sud génère des erreurs dans les mesures des instruments d'orbitographie et de positionnement utilisant le principe de l'effet Doppler embarqués dans les satellites (Lemoine et Capdeville, 2006). En Patagonie, Palermo et al. (2019) discutent de la possibilité d'avoir enregistré cette anomalie magnétique dans les sédiments des lacs Laguna Cháltel et Laguna Potrok Aike (Gogorza et al., 2012) sous la forme d'une décroissance marquée des valeurs de paléointensité relative au cours des 500 dernières années. Cette tendance a précédemment été observée en Amérique du Sud dans des archives archéologiques provenant de la région de Buenos Aires (Goguitchaichvili et al., 2012, 2015).

OBJECTIFS

L'objectif principal de cette thèse de doctorat est de reconstituer la dynamique sédimentaire et géomagnétique ainsi que les variations du niveau marin dans le secteur central de la Patagonie au cours de la dernière transgression marine à partir d'enregistrements sédimentaires et géophysiques du golfe de San Jorge. Dans cette optique, cette thèse s'appuie sur trois objectifs spécifiques qui forment les trois chapitres de la thèse et qui ont été discutés sous la forme d'articles scientifiques.

Objectif 1 : Sédimentation contemporaine

Le premier objectif spécifique de cette thèse est de **comprendre la dynamique sédimentaire récente et d'identifier les sources de la sédimentation terrigène dans le GSJ** en utilisant la distribution granulométrique et la composition minéralogique (fraction totale et argileuse) et géochimiques (éléments majeurs et traces) des sédiments de surface. En effet, l'étude des propriétés géochimiques et minéralogiques des sédiments terrigènes de surface est couramment utilisée dans de nombreuses régions du globe pour identifier les sources sédimentaires (e.g., Mer Jaune et mer de Chine : Lim et al., 2006; Xu et al., 2009; Arctique : Viscosi-Shirley et al., 2003; Gamboa et al., 2017; Bassin de Cariaco : Elmore et

al., 2009 ; Bout-Roumazeilles et al., 2013). Sur le plateau continental argentin, l'ensemble des études utilisant les propriétés géochimiques et minéralogiques des sédiments de surface ont été réalisées en relation avec la décharge du Rio de La Plata (Campos et al., 2008) ou le long de la marge continentale (Peschick et al., 1996; Razik et al., 2015). Dans cette dernière, la minéralogie des argiles est utilisée comme indicateur pour identifier l'origine des sédiments ainsi que les conditions climatiques (altérations physiques ou chimiques; e.g., Peschick et al., 1996; Campos et al., 2008). Sur le plateau continental argentin, la composition en argiles serait principalement influencée par les apports de chlorite transportés par le courant circumpolaire antarctique et par les apports de smectite et chlorite acheminés depuis les massifs andins par les rivières de Patagonie (Peschick et al., 1996; Gaiero et al., 2004). De plus, dans une étude où sont compilées les compositions en éléments majeurs et traces ainsi que les compositions isotopiques (Sr et Nd) de matériels patagoniens récents (échantillons de sols, de sédiments de rivières et de poussières), Gaiero et al. (2007) suggèrent une signature chimique et isotopique relativement uniforme des sédiments récents influencée par le volcanisme andin. Ainsi, le premier objectif devrait permettre de répondre aux questions suivantes : Quelles sont les sources et les mécanismes de transport à l'origine des sédiments du golfe de San Jorge ? En l'absence d'apports directs par des rivières, les apports éoliens peuvent-ils être la principale source de sédiments terrigènes ? L'influence prédominante du volcanisme andin sur les signatures minéralogiques et géochimiques des sédiments est-elle préjudiciable pour la différentiation des sources et des mécanismes de transport sédimentaire sur le plateau continental ?

Objectif 2 : Stratigraphie et variations du niveau marin

Le GSJ fait partie d'un large bassin sédimentaire, le bassin du golfe de San Jorge, exploité dans le secteur terrestre pour ses réserves en hydrocarbures. De nombreuses études sismiques et stratigraphiques ont permis de caractériser l'architecture et les diverses propriétés des roches sédimentaires qui composent ce bassin (Fitzgerald et al., 1990; Sylwan, 2001). Cependant les dépôts quaternaires restent relativement peu documentés en raison de l'absence d'études sismiques et stratigraphiques à haute résolution dans ce secteur. De plus,

l'évolution des environnements sédimentaires et de la chronologie de la transgression marine suite au LGM sur le plateau continental argentin conserve de nombreuses interrogations. En effet, si de nombreuses études, portant notamment sur l'investigation des paléo-rivages, ont permis de mieux comprendre les variations du niveau marin depuis le milieu de l'Holocène sur le plateau continental et dans le GSJ (e.g., Cavallotto et al., 2004; Schellmann and Radtke, 2010; Violante et al., 2014; Bini et al., 2017), la reconstitution des changements du niveau marin avant cette période demeure complexe en raison de l'absence d'archives sédimentaires datées (Violante et Parker, 2004). En périphérie du GSJ, aucune investigation n'a été menée pour déterminer la chronologie et le déroulement de la transgression marine à l'exception du modèle de Ponce et al. (2011) et de la courbe du niveau marin régional proposée par Guilderson et al. (2000). Dans ce contexte, le deuxième objectif spécifique de cette étude est de **reconstituer la stratigraphie du golfe de San Jorge depuis la dernière glaciation afin de documenter les variations du niveau marin dans cette région** à l'aide des interprétations seismo-stratigraphiques couplées à l'analyse des éléments majeurs et traces des séries sédimentaires du golfe au cours de la dernière transgression marine. En s'appuyant sur l'analyse des données sismiques à haute résolution (i.e., étincelleur) et des enregistrements sédimentaires récoltés dans le GSJ couplées à la réalisation d'un cadre chronostratigraphique, l'objectif 2 devrait permettre de répondre aux questions suivantes : Quelle est l'évolution des environnements sédimentaires depuis le début de la transgression marine dans le GSJ ? Quel est le scénario et la chronologie de la dernière transgression marine dans le golfe de San Jorge ? Des reliques des périodes de bas niveau marin, telles que des vallées incisées, peuvent-elles être identifiées dans le GSJ ?

Objectif 3 : Reconstitution paléomagnétique

Le troisième objectif spécifique de cette thèse est de **reconstituer la variabilité du champ magnétique terrestre dans la partie centrale de la Patagonie** à partir d'archives sédimentaires du GSJ et à l'aide d'une nouvelle méthode de sommation (*stacking*) des données. En effet, l'étude de l'aimantation rémanente des sédiments marins et lacustres constitue un excellent procédé pour reconstituer la variation du champ magnétique terrestre

au cours des temps géologiques (Tauxe et al., 1993). Pour s'assurer de la qualité et de la viabilité des enregistrements paléomagnétiques, de nombreuses études, notamment en Patagonie (e.g., Lisé-Pronovost et al., 2013; Gogorza et al., 2018; Palermo et al., 2019), présentent une comparaison et une corrélation des paléodirections (inclinaison et déclinaison) et des paléointensités relatives avec des données provenant de la même région mais également avec des modèles globaux de variations du champ dipolaire (e.g., CALS10k.2; Constable et al., 2016). À partir de l'analyse paléomagnétique des sédiments du golfe de San Jorge couplée à la mise-en-place d'une nouvelle méthode de *stacking* s'appuyant sur des facteurs de qualité des données ainsi qu'à la comparaison des résultats avec des données régionales et des modèles globaux, l'objectif 3 devrait permettre de répondre aux questions suivantes : Les sédiments du golfe de San Jorge sont-ils de qualité suffisante pour reconstituer un enregistrement paléomagnétique viable ? Est-ce que les changements de paléointensité relative et de paléodirection peuvent être corrélés aux enregistrements paléomagnétiques de Patagonie et aux modèles globaux de variations du champ magnétique terrestre ? La nouvelle méthodologie de *stacking* permet-elle d'optimiser la construction d'un enregistrement paléomagnétique à partir de plusieurs archives sédimentaires ? Les données paléomagnétiques ont-elles permis d'enregistrer l'anomalie magnétique de l'Atlantique Sud ?

MÉTHODOLOGIE

Campagnes d'échantillonnage

Cette thèse de doctorat fait partie d'un vaste projet multidisciplinaire, le projet PROMESse (PROgramme Multidisciplinaire de recherche en océanographie pour l'étude de l'Écosystème et de la géologie marine du golfe San Jorge et de la région côtière des provinces de Chubut et Santa Cruz) dirigée par l'ISMER et le Conseil national argentin de recherche en sciences et techniques (CONICET) visant à étudier le golfe de San Jorge (St-Onge et Ferreyra, 2018). L'ensemble des données du golfe de San Jorge utilisées pour ce projet ont été récoltés au cours de la mission MARGES (*MARine GEology sedimentology, stratigraphy, basin architecture and paleoceanography of the San Jorge Gulf*). La mission s'est déroulée dans le GSJ et sur le plateau continental à bord du N/R Coriolis II du 17 février au 4 mars 2014 (Fig. 5). Cette expédition a permis de récolter 55 échantillons de sédiments de surface (benne Van Veen), 8 carottes à boîte (Fig. 5), 9 carottes à gravité et 5 carottes à piston ainsi qu'environ 2000 km de lignes géophysiques (Fig. 6). L'échantillonnage des sédiments de surface a été complété par 8 échantillons prélevés lors d'une première mission réalisée du 29 janvier au 15 février et axé sur des analyses biologiques, physiques et chimiques sur le golfe et le plateau continental (MARES). Cette mission a également permis d'obtenir 22 échantillons d'eau de mer prélevés à la surface et proche du fond à 11 sites dans le GSJ. Ces échantillons ont été filtrés et stockés sous forme de filtres. De plus, 13 échantillons terrestres et de rivières ont été prélevés en août 2016 en Patagonie par le professeur Augusto Crespi-Abril; 9 d'entre eux ont été récoltés sur les rives du GSJ, 2 à l'embouchure des rivières Chubut et Deseado et 2 dans la région de Bajo de Sarmiento située à l'ouest du golfe de San Jorge. Un échantillon de sédiment de surface provenant du détroit de Magellan, prélevé dans une carotte (MD07-3131) de l'expédition PACHIDERME à bord du N/R Marion Dufresne II en février 2017, a également été analysé dans le cadre du premier chapitre de cette thèse. L'ensemble de ces échantillons ont été entièrement ou partiellement utilisés pour répondre aux différents objectifs de cette thèse.



Figure 5: Illustration du N/R Coriolis II lors de la mission dans le golfe de San Jorge. Exemples d'échantillonnage à l'aide du carottier à piston (haut) et d'un carottier à boîte (bas)

Propriétés physiques

Les carottes sédimentaires prélevées dans le GSJ ont été passées aux rayons-X à l'aide du tomodensitomètre de l'ISMER. Cependant, les résultats n'étant pas assez probants en raison de la nature des sédiments présents dans les carottes, ces derniers ont été passés dans le tomodensitomètre du Laboratoire multidisciplinaire de tomodensitométrie pour les ressources naturelles et le génie civil (INRS-ETE). Les rayons-X, générés par une source de l'instrument, sont atténués en traversant l'échantillon (sédiments) et l'intensité du signal atténué est mesurée par des détecteurs. La source et les détecteurs effectuent une rotation autour de la carotte ce qui permet d'analyser les carottes dans toutes les directions de l'espace (coupes longitudinales et transversales; Crémer et al., 2000). Cet instrument permet ainsi d'imager la variation des structures sédimentaires et de déterminer, en première approximation, la densité des sédiments sans ouvrir les carottes (e.g., St-Onge et al., 2007).

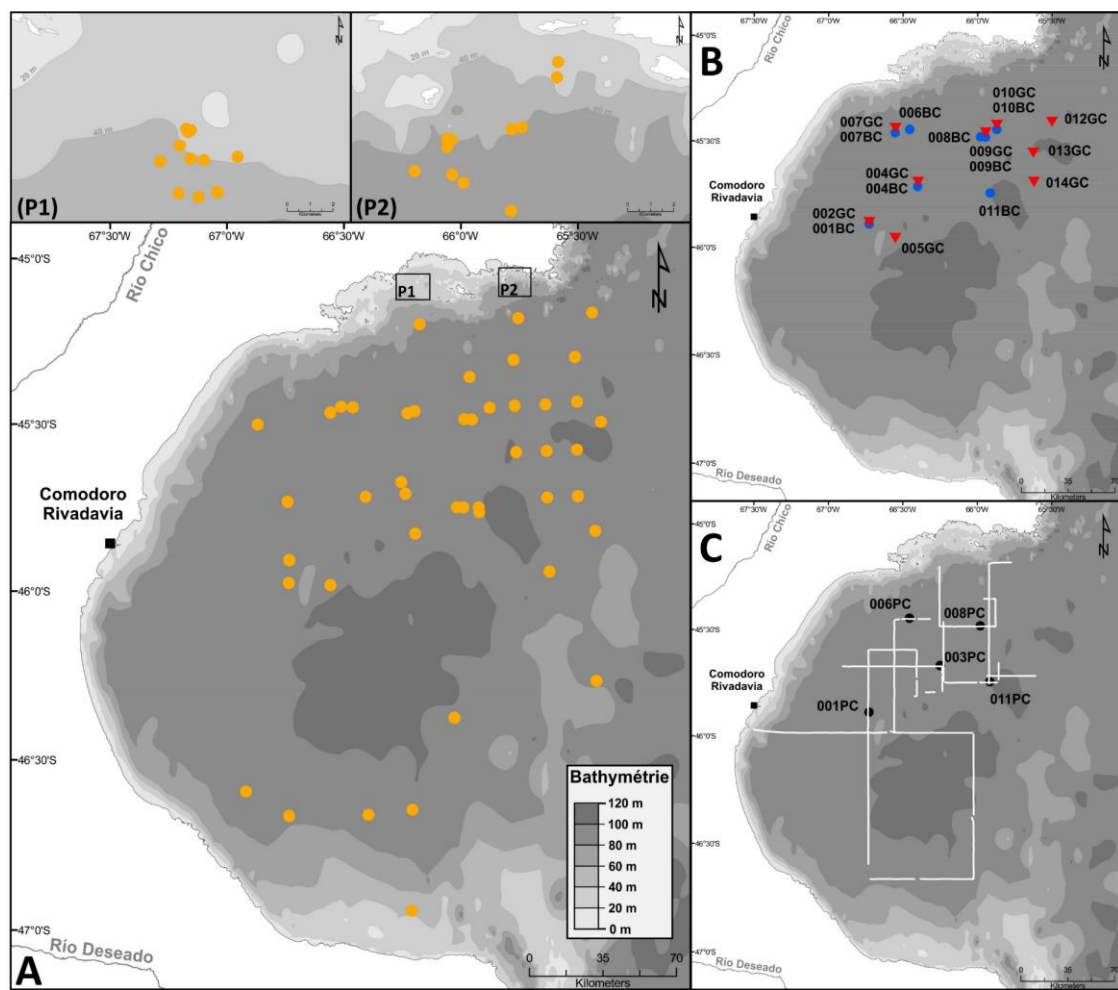


Figure 6: Localisation des échantillons de surface (A; rond orange), des carottes à gravité (B; triangle rouge), des carottes à boîte (B; rond bleu), des carottes à piston (C; rond noir) et des lignes géophysiques (C; ligne blanche) prélevées dans le golfe de San Jorge en 2014

Au laboratoire de géologie marine de l'ISMER, l'ensemble des carottes entières (*whole core*) ont ensuite été analysées sur un banc de mesure MSCL développé par GEOTEK. Ces analyses ont permis d'obtenir la vitesse des ondes de compression (p), la résistivité électrique, la densité (par atténuation des rayonnements gamma) et la susceptibilité magnétique à un intervalle de 1 cm. Les carottes ont ensuite été ouvertes longitudinalement à l'aide d'un banc de découpe pour donner deux demi-sections identiques : les sections "travail" et "archives". Les sections archives ont été photographiées à haute résolution (Geoscan IV), décrites puis archivées. Lors de description, la texture (taille des grains), la couleur des sédiments (échelle

de Munsell), les déformations dans la carotte, la présence de structures (e.g., laminations, coquilles, bioturbation, contact érosif, etc.) ont été observées, notées et dessinées. La section travail a quant à elle été utilisée pour une nouvelle série d'analyses sur le banc MSCL : la réflectance par spectrophotométrie (Minolta CM-2600d), la susceptibilité magnétique à haute résolution (senseur ponctuel) et la composition chimique par fluorescence X (XRF; St-Onge et al., 2007). Ces analyses ont été effectuées à une résolution de 1 cm pour les carottes à gravité et à piston et tous les 0.5 cm pour les carottes à boîte. Suite à l'analyse de l'ensemble des données, un protocole d'échantillonnage des sections travail a été décidé. Dans un premier temps, des u-channels ont été prélevés dans la partie centrale de 4 carottes boîtes (01BC, 06BC, 08BC et 11BC), d'une carotte à gravité (005GC) et de l'ensemble des carottes à piston (001PC, 003PC, 006PC, 008PC et 011PC) pour les analyses paléomagnétiques subséquentes. Par la suite, des prélèvements de sédiments d'au moins 10 g tous les 1 cm dans les 15 premiers cm et un échantillon à 20 cm ont été réalisés dans les carottes à gravité et les carottes boîtes pour des analyses de ^{210}Pb . Les carottes à piston ont été échantillonnées tous les 8 cm avec des prélèvements d'au moins 30 g pour des analyses granulométriques et géochimiques. Les sections correspondant à la base des carottes 003PC, 006PC et 008PC ont par la suite été rééchantillonnées à tous les 4 cm. Des prélèvements de coquilles et de matière organique ont également été effectués pour des datations ^{14}C (voir section chronologie).

Analyses granulométriques

Les analyses granulométriques ont été réalisées sur l'ensemble des échantillons de surface et sur les échantillons prélevés tous les 4 et 8 cm dans les carottes à piston. Les données de minéralogie et les éléments majeurs et traces des carottes n'ont pas été utilisées pour cette thèse, mais seront discutés dans de futurs travaux dans le GSJ. Les analyses granulométriques des échantillons des sédiments de surface et des carottes ont été effectuées sur la fraction détritique. Afin d'isoler cette fraction, la matière organique et les carbonates biogéniques ont été supprimés des échantillons avec 10 ml de peroxyde (30%) et 10 ml d'acide chlorhydrique (HCl; 0.5 M), respectivement. La déflocculation des échantillons a été réalisée sans ajout de produits chimiques, uniquement à l'aide de rinçages répétés avec de

l'eau distillée (Montero-Serrano et al., 2009). Les analyses granulométriques ont été effectuées à l'aide du Beckman Coulter Particle Size Analyser LS 13 320 de l'ISMER. Les données ont été analysées avec le logiciel GRADISTAT pour obtenir les différentes caractéristiques statistiques des sédiments selon la méthode des moments géométriques (Blott et Pye, 2001). L'algorithme de modélisation par mélange des pôles (EMMA; Dietze et al. 2012) a été utilisé afin d'extraire les distributions granulométriques significatives (*end-members*, EM) et ainsi isoler et estimer les processus (i.e., conditions de transport) liés à la distribution granulométrique des EM.

Analyses minéralogiques et géochimiques

Les analyses minéralogiques ont été réalisées sur l'ensemble des échantillons de surface et sur les échantillons prélevés tous les 4 et 8 cm dans les carottes à piston. Les données de minéralogie des carottes n'ont pas été utilisées pour cette thèse, mais seront discutées dans de futurs travaux sur le GSJ. Préalablement aux analyses minéralogiques, la fraction détritique a également été isolée en suivant le même protocole que pour la granulométrie. Les sédiments sont ensuite broyés à l'aide d'un microniseur (McCrone) et de 5 ml d'éthanol pendant une dizaine de minutes jusqu'à obtenir un mélange homogène constitué de grains <10 µm. Le mélange est séché dans une étuve à 60°C pendant 48h puis broyé à nouveau dans un mortier en agate pour éviter des agrégations de particules fines suite au séchage. Les échantillons en poudre sont chargés dans des supports et analysés par diffraction des rayons X (XRD) à l'aide du diffractomètre PANalytical X'Pert Powder. Cet instrument est équipé d'un tube de cuivre, fonctionnant à 45 kV et 40 mA, et d'un monochromateur en graphite. Les échantillons sont mesurés entre 5° et 65° 2θ avec un pas de 0.02° 2θ et un temps d'analyse de 2 secondes par étape. La quantification des principaux éléments minéralogiques est obtenue en traitant les données provenant du diffractomètre à l'aide du programme macro Excel Rockjock v11 (Ebel, 2003). Les données minéralogiques et géochimiques ont été analysées par approche statique avec, notamment, des analyses en composantes principales à l'aide du logiciel CoDaPack (Thió-Henestrosa and Martín-Fernández, 2005). De plus, le programme SedUnMixMC (Andrews et Eberl, 2012) a été

utilisé afin de déterminer la contribution de sources potentielles de sédiments pour chacun des échantillons. Pour plus de détails sur la méthode de quantification, l'analyse statistique et la stratégie développée avec le logiciel SedUnMixMC, le lecteur est prié de se référer au chapitre 1.

La minéralogie de la fraction argileuse fait référence à la minéralogie des phyllosilicates compris dans la fraction de la taille des argiles (généralement les grains inférieurs à 2 µm). Les minéraux argileux ont été identifiés par diffraction des rayons X suivant le protocole établi par Bout-Roumazeilles et al. (1999). La méthode d'analyse et de quantification des argiles est détaillée dans le chapitre 1.

Les compositions en éléments majeurs (Al, Si, Ti, Mg, Ca, K, Fe, Mn, P) et traces (notamment, V, Cr, Zn, Sr, Zr) des échantillons des sédiments de surface et des carottes ont été analysées avec le spectromètre de fluorescence X à dispersion d'énergie (EDXRF) à l'ISMER. Les données obtenues pour les échantillons des carottes complètent les éléments majeurs et traces (Ti, Fe, Co, Mn, Ni, Cu, Zn, As, Rb Sr, Ba) fournis par le senseur de fluorescence X du MSCL. De plus, l'analyse de la composition élémentaire des filtres et de téphras, qui ont été isolés des sédiments de surface du GSJ, a été réalisée à l'ISMER par Claude Belzile à l'aide d'un spectromètre à rayons X à dispersion d'énergie couplé à un microscope électronique à balayage. Les méthodes d'analyse de la composition chimique des sédiments sont présentées en détail dans le chapitre 1.

Mesures magnétiques et paléomagnétiques

L'ensemble des analyses présentées dans cette section ont été réalisées à partir des u-channels mesurés à l'aide du magnétomètre cryogénique (SRM-755 de 2G Entreprises) de l'ISMER. Dans un premier temps, l'aimantation naturelle rémanente (NRM) est mesurée en appliquant un champ magnétique alternatif (AF) de démagnétisation (variation du champ de 0 à 80 mT avec un pas de 5 mT). Pour mesurer l'aimantation rémanente anhystrétique (ARM), un champ magnétique alternatif de démagnétisation est appliqué (jusqu'à 100 mT) et couplé à un champ magnétique continu (DC) de même ordre de grandeur que celui du

champ magnétique terrestre (0.05 mT). Une aimantation rémanente isotherme (IRM) et une aimantation isotherme à saturation (SIRM) sont ensuite induites à 300 mT et 950 mT, respectivement, en utilisant un module d'induction de. Les U-channels ont ensuite été démagnétisés et mesurés selon les mêmes étapes que pour la NRM et ARM.

Les variations d'inclinaison et de déclinaison ont ensuite été calculées à partir de l'intervalle d'aimantation rémanente caractéristique (ChRM) en utilisant une analyse en composante principale (PCA) des données de démagnétisation calculée à l'aide d'un tableur développé par Mazaud (2005). Afin de valider la fiabilité des valeurs d'orientation, la déviation maximum angulaire (MAD, Kirschvink, 1980) est utilisée et sa valeur doit-être inférieure à 5° (Stoner et St-Onge, 2007). Les ratios de NRM/ARM et NRM/IRM ont également été déterminés pour obtenir la paléointensité relative (RPI; Tauxe, 1993). La reconstitution des valeurs de RPI à partir de sédiments doit être validée à l'aide de plusieurs critères spécifiques (Tauxe, 1993; Stoner et St-Onge, 2007) : (1) L'aimantation rémanente doit être portée par des grains pseudo-monodomaines (PSD) de magnétite, (2) les variations de concentration en grains magnétiques ne doivent pas varier de plus d'un ordre de grandeur, (3) le traceur de paleointensité ne doit pas être cohérent avec le traceur de la concentration en minéraux magnétiques utilisé pour le normaliser, (4) le ChRM doit être stable et à composante unique.

Pour déterminer ces critères, les propriétés d'hystérésis ont été mesurées sur des échantillons de sédiment à l'aide d'un magnétomètre à gradient alternatif (MicroMag 2900 de Princeton Measurement Corporation). Lors de cette expérimentation, le magnétomètre induit des variations du champ magnétique et mesure le degré d'aimantation des grains magnétiques de l'échantillon (Fig. 7). Au début de l'expérience, aucun champ magnétique n'est appliqué, puis un champ magnétique est induit en constante augmentation. Les grains ferrimagnétiques s'aimantent jusqu'à atteindre leur (degré) maximum d'aimantation. À partir de ce moment l'augmentation du champ magnétique n'aura plus d'influence sur leur aimantation (aimantation de saturation, Ms ; Fig. 7). Le champ est ensuite abaissé pour devenir nul, puis atteindre des valeurs négatives, les caractéristiques d'aimantation vont alors

être modifiées jusqu'à s'inverser. Les grains seront alors démagnétisés pour une certaine valeur de champ appliqué : cette étape permet de mesurer la coercivité des minéraux magnétiques (H_c). Cette expérimentation permet également d'estimer l'aimantation rémanente (subsistant en l'absence de champ appliqué, M_{rs}) et la coercivité rémanente (le champ nécessaire pour ramener M_{rs} à 0, H_{cr}). La forme de la boucle d'hystérésis et les différentes propriétés associées aux états d'aimantation (M_s , M_{rs} , H_c et H_{cr}) permettent d'obtenir des informations sur la minéralogie magnétique, la taille et le domaine des grains magnétiques (monodomaine, pseudo-monodomaine ou multidomaine; Day et al., 1977; Tauxe et al., 1996).

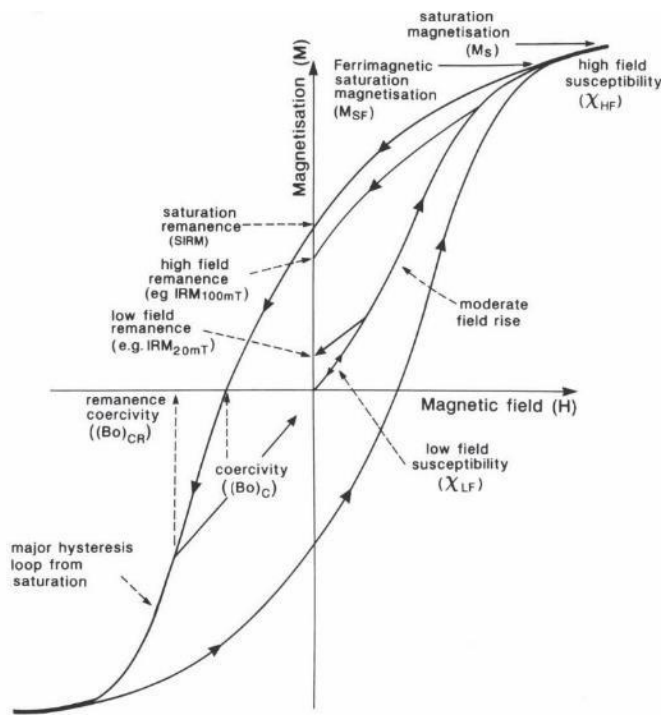


Figure 7: Boucle d'hystérésis d'un matériau ferromagnétique (adapté de Maher, 2007)

Chronologie

La datation radiocarbone (^{14}C) par accélérateur de particule (AMS, Accelerator Mass Spectrometry) a permis d'obtenir les âges absolus de 22 coquilles prélevées dans une carotte à gravité (005GC) et 5 carottes à piston (voir chapitre 2). Les échantillons ont été envoyés au

laboratoire de radiochronologie du Centre d'études nordiques de l'Université Laval où ils ont été préparés. Les préparations ont ensuite été envoyées au laboratoire W.M. Keck de l'Université de Californie à Irvine qui dispose d'un accélérateur de particule pour la datation radiocarbone. Deux échantillons composés de microfragments d'algues et de bois ont également été datés avec la même technique au Laboratoire des sciences du climat et de l'environnement en France. Les âges radiocarbones ont été calibrés en utilisant le logiciel CALIB 7.1 (Stuiver and Reimer, 1993) et la courbe « Marine13 » (Reimer et al. 2013). La méthodologie détaillée pour la reconstitution des modèles d'âges ainsi que la justification des âges réservoirs sont présentées dans le chapitre 2.

L'analyse du ^{210}Pb par spectrométrie α , à partir de la mesure de l'activité du ^{210}Po , afin d'estimer les vitesses de sédimentation et la datation des sédiments de sous-surface (~ 15 premiers cm) de quatre carottes boîtes (01BC, 06BC, 08BC et 11BC) et d'une carotte à gravité (005GC) a été réalisée au laboratoire de radiochronologie du Geotop à l'Université du Québec à Montréal (UQAM) à l'aide d'un spectromètre alpha de type EGG-Ortec. Au vu des résultats non-concluants obtenus (i.e., pas de décroissance radioactive - sédiments possiblement trop anciens) pour les sédiments de sous-surface de ces 5 carottes, les analyses au ^{210}Pb n'ont pas été utilisées dans cette thèse.

Données géophysiques

Au cours de la mission MARGES à bord du N/R Coriolis II, deux types de source d'émission ont été utilisées pour la campagne de sismique-réflexion, un chirp et un *sparker* (étincelleur). L'échosondeur de type chirp génère des ondes sonores FM (modulation de fréquence) à partir de 9 transducteurs qui servent à la fois d'émetteur et de récepteur. Au cours de la mission dans le GSJ, les données ont été acquises en utilisant l'onde acoustique (pulse) Hull_2_12_20FM (modulation de fréquence de 2 à 12 kHz) à une fréquence de 1 Hz. L'acquisition a été effectuée à l'aide de la version 2.1 du logiciel Edgetech Discover X-Star.

Le sparker utilisé au cours de la mission était un SQUID 2000 de la société Applied Acoustics. Dans le golfe, la fréquence de tir était de 1 Hz et l'énergie fournie afin de générer

l’impulsion était de 1000 J pour les 10 premières lignes et de 1500 J (maximum) pour les lignes suivantes. La réception du signal acoustique a été réalisée à l’aide d’une flûte mono-canal de 50 m de longueur composée de 12 hydrophones espacés de 0.25 m. La digitalisation et l’enregistrement des données ont été réalisés à l’aide d’un module d’acquisition CODA. Cet instrument permet de convertir le signal analogique reçu par la flûte en signal numérique pour le traitement informatique.

Lors de l’acquisition, les données sismiques provenant de l’échosondeur ont été enregistrées au format de la compagnie (.jsf). Ces fichiers ont ensuite été convertis au format .sgy (SEG-Y, Society of Exploration Geophysicists ; Hagelund et Levin, 2017). Les coordonnées géographiques des profils ont été converties en UTM en utilisant une routine MATLAB. À l’exception de la correction de l’effet de houle, aucun traitement jugé concluant n’a été appliqué sur les données de l’échosondeur.

Durant la mission, les lignes de l’étinceleur ont préalablement été converties du format .cod (format de la compagnie du CODA) à un format standard .sgy et les coordonnées géographiques ont également été modifiées de secondes d’arc à UTM. Dans le cadre du cours Nouveaux développements en océanographie réalisé à la Commission géologique du Canada à Québec sous la supervision de mon co-directeur Mathieu Duschesne, un protocole de traitement des données de l’étinceleur a été établi. Ce protocole, effectué essentiellement avec le logiciel de traitement des données sismiques VISTA (Schlumberger), vise à supprimer ou diminuer, à un niveau acceptable pour l’interprétation, les bruits parasites et les artefacts inhérents à la sismique réflexion en milieu marin. Dans un premier temps, l’effet de houle a été supprimé à l’aide d’un mini-programme (Dejitter) qui utilise la méthode des moyennes mobiles pour effectuer un lissage des valeurs correspondant aux profondeurs de la première réflexion. Par la suite, une déconvolution stationnaire et prédictive particulière, *spiking deconvolution*, a été utilisée pour atténuer les arrivées secondaires comprises dans la signature de la source et présentes sur la trace sismique (Duchesne et al., 2007). Une méthode de filtrage fréquentiel (i.e., filtre passe-bande) qui permet de conserver un échantillon de fréquences contenant l’ensemble des fréquences du signal utiles et de rejeter les fréquences

des fréquences à l'extérieur de cette bande-passante a également été appliquée pour rehausser le rapport signal-sur-bruit. De plus, une correction de l'atténuation du signal a été effectuée à l'aide d'une fonction de traitement des amplitudes, le contrôle automatique du gain (AGC), et la cohérence des amplitudes a été améliorée à l'aide d'une fonction d'égalisation la térale des traces. Les résultats obtenus avec ce protocole sont très satisfaisants avec une atténuation importante des multiples et une forte diminution des bruits parasites permettant ainsi l'interprétation des lignes dans de meilleures conditions (Fig. 8). Les lignes de l'étinceleur et de l'échosondeur ont ensuite été importées dans IHS Kingdom pour l'interprétation.

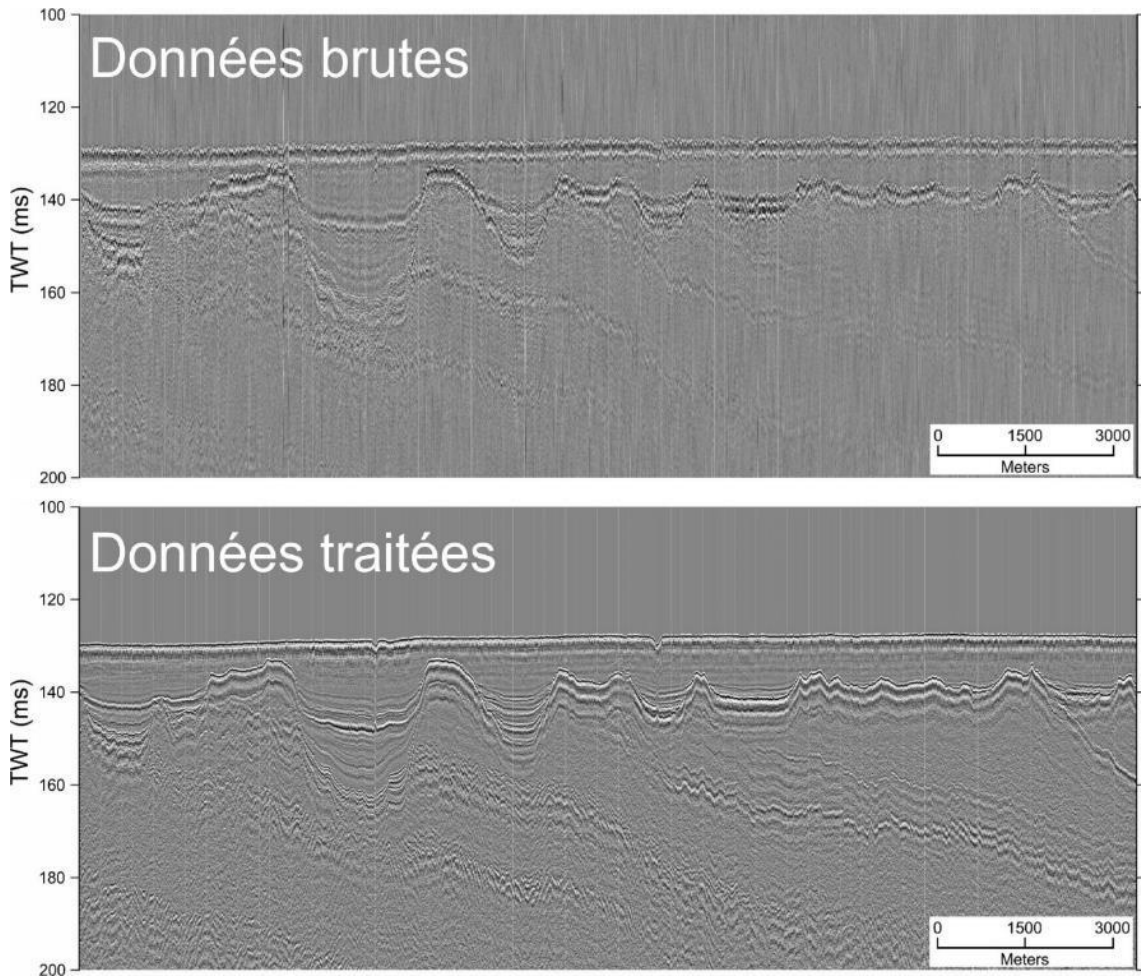


Figure 8: Comparaison pour une même ligne *sparker* entre les données brutes et les données traitées

ORGANISATION DE LA THÈSE

Cette thèse est organisée en trois chapitres rédigés sous la forme d'articles scientifiques répondant à chacun des objectifs de la thèse. Les références bibliographiques de l'introduction générale et de la conclusion générale seront présentées à la fin de la thèse alors que la bibliographie de chaque article est incluse à la fin des chapitres.

Le premier chapitre présente une description détaillée des sédiments de surface dans le golfe de San Jorge et discute des sources et des principaux modes de transport susceptibles de contribuer à la sédimentation du matériel terrigène dans le golfe. Les résultats de ce chapitre ont été publiés dans une édition spéciale de la revue *Oceanography* en décembre 2018.

Desiage, P.-A., Montero-Serrano, J.-C., St-Onge, G., Crespi-Abril, A.C., Giarratano, E., Gil, M.N., Haller, M.J., 2018. Quantifying sources and transport pathways of surface sediments in the Gulf of San Jorge, central Patagonia (Argentina). *Oceanography* 31, 92–103.

Le second chapitre décrit l'évolution des environnements sédimentaires à la suite de la dernière transgression marine dans le golfe de San Jorge. La chronologie et l'évolution des changements du niveau marin depuis l'envahissement du golfe sont également discutées. Cet article sera soumis prochainement à la revue *Continental Shelf Research*.

Desiage, P.-A., St-Onge, G., Duchesne, M.J., Montero-Serrano, J.-C., Haller, M.J. Late Pleistocene and Holocene evolution of sedimentary environments associated with postglacial transgression in the Gulf of San Jorge, central Patagonia, Argentina.

Le troisième chapitre permet de reconstituer les variations paléomagnétiques au cours des 14 000 dernières années en Patagonie à partir de 4 archives sédimentaires du GSJ et à l'aide une nouvelle méthode de *stacking*. Cet article sera soumis prochainement à la revue *Geochemistry, Geophysics, Geosystems*.

Desiage, P.-A., Philippe E., St-Onge, G., Montero-Serrano, J.-C., Haller, M.J. New stacking method to reconstruct high-resolution paleomagnetic secular variations and relative paleointensity in Patagonia over the last 14 ka cal BP.

Finalement, cette thèse est clôturée par une discussion générale abordant l'ensemble des questions scientifiques couvertes par les trois chapitres de ce projet. Au cours de cette conclusion, seront présentés les principaux résultats, la portée scientifique de ces derniers ainsi que les questionnements et les perspectives futures soulevées par cette thèse.

AUTRES RÉALISATIONS ET COLLABORATIONS

Au cours de mon doctorat, j'ai eu la chance de présenter mes travaux de recherches lors de 3 congrès internationaux (*American Geophysical Union (AGU) Fall meeting*, *International Sedimentology Congress* et *Arctic Change*), 3 congrès nationaux (GEOTOP, Québec-Océan et ACFAS) et un workshop international dans le cadre du projet PROMESse. J'ai également eu la chance de participer à deux expéditions à bord du *N/R Coriolis II*, COR1404 et COR1502, qui se sont déroulées dans le golfe de San Jorge (Patagonie) et dans le golfe du Saint-Laurent (Québec), respectivement. Lors de ces expéditions, j'étais la personne en charge des legs de nuit et j'étais responsable de l'acquisition des données géophysiques. Au cours des expéditions dans le golfe de San Jorge en 2014 et dans le golfe du Saint-Laurent en 2015, j'ai également été impliqué dans l'organisation des missions avec la conception du plan de route pour les lignes géophysiques. J'ai également eu la chance d'être sélectionné avec plusieurs étudiants internationaux pour participer à l'expédition MGL1405 sur le plateau continental au large du New Jersey à bord du *R/V Marcus G. Langseth*. Lors de cette mission, j'ai participé au déploiement et à la supervision d'un système hybride d'acquisition combinant deux flûtes sismiques de 3 km et un système de *P-cable*. J'ai aussi eu la chance de participer à une mission dans les Antilles françaises sur le *N/R Pourquoi Pas ?* dans le cadre du projet CASEIS. Mon rôle était essentiellement la collecte, la manipulation et la description des carottes sédimentaires. Finalement, l'ensemble de

l'expérience acquise lors des diverses expéditions en mer m'a permis de participer, en tant que consultant pour l'acquisition de données géophysiques, à une mission sur le *N/R Coriolis II* en 2019 pour la compagnie WSP.

Lors de mon doctorat, je me suis également impliqué dans le soutien et la formation des étudiants du laboratoire en offrant à plusieurs reprises des séminaires et des laboratoires sur la sismique marine et sur les méthodes de cartographie avec le logiciel ArcGIS, notamment. Cette implication m'a permis de collaborer plus particulièrement aux projets de trois étudiants de maîtrise et de doctorat : Yan Levesque, Naïs Sirdeys et Adriana Gamboa.

Articles

Lévesque, Y., St-Onge, G., Lajeunesse, P., **Desiage, P-A.**, and Brouard, E., 2019. Defining the maximum extent of the Laurentide Ice Sheet in home Bay cross-shelf trough during the Last Glacial episode. *Boreas*.

Gamboa, A., Montero-Serrano, J. C., St-Onge, G., Rochon, A., and **Desiage, P-A.**, 2017. Mineralogical, geochemical and magnetic signatures of surface sediments from the Canadian Beaufort Shelf and Amundsen Gulf (Canadian Arctic). *Geochemistry, Geophysics, Geosystems*, 18(2), 488-512.

Communications dans le cadre de la thèse

Desiage, P-A., St-Onge, G., Montero-Serrano, J. C., Duchesne, M.J., and Haller, M.J., 2018. Late Quaternary sediment dynamics in the Gulf of San Jorge (Patagonia). *20th International Sedimentological Congress (ISC)*, 13-17 August 2018, Québec City (QC, Canada). Affiche.

Desiage, P-A., St-Onge, G., Montero-Serrano, J. C., Duchesne, M.J., and Haller, M.J., 2017. Sedimentary environments and post-glacial evolution of the Gulf of San Jorge (Patagonia) following the Last Glacial Maximum. *Arctic Change 2017*, 11-15 December 2017, Québec City (QC, Canada). Communication orale.

Desiage, P-A., St-Onge, G., and Montero-Serrano, J. C., 2017. Influence of climatic and oceanographic variations on the sedimentation in the Gulf of San Jorge (Argentina, Central Patagonia) since the Last Glacial Maximum. *GEOTOP annual meeting*, 24-26 March 2017, Forêt Montmorency (QC, Canada). Communication orale.

Desiage, P-A., St-Onge, G. and Montero-Serrano, J. C., and Haller, M.J., 2017. Evolution of postglacial sedimentary environments in the Gulf of San Jorge. *PROMESSe project workshop*, 7-10 March 2017, Rimouski (QC, Canada). Communication orale.

Desiage, P-A., St-Onge, G., Montero-Serrano, J. C., Duchesne, M.J., and Haller, M.J., 2016. Late Pleistocene and Holocene Sea-level Variations and Post-glacial Sedimentation in the Gulf of San Jorge (Argentina, Central Patagonia). *AGU Fall Meeting*, 12-16 December 2016, San Francisco (CA, USA). Affiche.

St-Onge, G., Montero-Serrano, J. C., **Desiage, P-A.**, Gil, M.N., Giarratano, E., and Haller, M.J., 2016. Magnetic, Mineralogical, Geochemical and Sedimentological Properties of Sediments From the Gulf of San Jorge, Patagonia, Argentina. *AGU Fall Meeting*, 12-16 December 2016, San Francisco (CA, USA). Affiche.

Desiage, P-A., St-Onge, G. and Montero-Serrano, J. C., 2016. Sediment sources and dynamics in the Gulf of San Jorge, Patagonia: From the Last Glacial Maximum to the present. *GEOTOP annual meeting*, 19-20 March 2016, Montréal (QC, Canada). Communication orale.

Desiage, P-A., St-Onge, G. and Montero-Serrano, J. C., 2015. Sédimentologie et paléocéanographie du golfe San Jorge, Patagonie (Argentine). *ACFAS congress*, 25-29 May 2015, Rimouski (QC, Canada). Communication orale.

St-Onge, G., Lisé-Pronovost, A., Montero-Serrano, J. C., **Desiage, P-A.**, Haller, M.J., and scientific teams PASADO and MARGES, 2015. Variations climatiques en Patagonie au cours des derniers 51 200 ans. *ACFAS congress*, 25-29 May 2015, Rimouski (QC, Canada). Communication orale.

Desiage, P-A., St-Onge, G., Montero-Serrano, J. C., Jetté, C. and Haller, M.J., 2015. Caractérisation des sédiments de surface du Golfe de San Jorge, Patagonie, Argentine. *GEOTOP annual meeting*, 13-15 February 2015, Orford (QC, Canada). Affiche.

Communications dans le cadre de collaborations

Sirdeys, N., St-Onge, G., **Desiage, P-A.**, and Montero-Serrano, J. C., 2018. Chronostratigraphy and evidence of gas seeps in the Old Harry area, Gulf of St. Lawrence, Eastern Canada. *20th International Sedimentological Congress (ISC)*, 13-17 August 2018, Québec City (QC, Canada). Affiche.

Sirdeys, N., St-Onge, G., Montero-Serrano, J. C., and **Desiage, P-A.**, 2018. High-resolution paleoenvironmental reconstruction since the last deglaciation of the Old Harry area, Gulf of St. Lawrence. *GEOTOP annual meeting*, 21-23 March 2018, La Malbaie (QC, Canada). Communication orale.

Sirdeys, N., St-Onge, G., Montero-Serrano, J. C., Sánchez-Carnero, N., and **Desiage, P-A.**, 2017. Sedimentary processes and Quaternary stratigraphy of the Old Harry area, Gulf of St. Lawrence. *Arctic Change 2017*, 11-15 December 2017, Québec (QC, Canada). Affiche.

Gamboa, A., Montero-Serrano, J. C., St-Onge, G., Rochon, A., and **Desiage, P-A.**, 2017. Estudio de la dinámica de los sedimentos marinos en la region del mar de Beaufort – golfo de Amundsen (Ártico Canadiense) con base en indicadores magnéticos y geoquímicos. *Seminarios de Investigación-UPTOS “Clodosbalso Russián”*, 29 November 2017, Cumaná (Venezuela). Communication orale.

Sirdeys, N., St-Onge, G., Montero-Serrano, J. C., and **Desiage, P-A.**, 2017. Sedimentary processes and Quaternary stratigraphy of the Old Harry area, Gulf of St. Lawrence. *14th International symposium on Estuarine Biogeochemistry (IEBS)*, 4-7 June 2017, Rimouski (QC, Canada). Affiche.

Sirdeys, N., St-Onge, G., Montero-Serrano, J. C., and **Desiage, P-A.**, 2017. Sedimentary processes and Quaternary stratigraphy of the Old Harry area, Gulf of St. Lawrence. GEOTOP annual meeting, 24-26 March 2017, Forêt Montmorency (QC, Canada). Affiche.

Ouvrages collectifs

Nadeau, S., **Desiage, P-A.**, Beauvais, Q., Trottier, A-P., St-Onge, G., 2017. Rapport de mission FJS2017 : Chenal de navigation du Saint-Laurent. Rapport interne, 36 p.

Rémillard, A.M., **Desiage, P.-A.**, Casse, M., St-Onge, G., Montero-Serrano, J.-C. & Xie, H. 2015. Environmental conditions and dispersion processes within the Old Harry Influence Area. Université du Québec à Rimouski, Institut des sciences de la mer, expedition report, 43 p.

Normandeau, A., **Desiage, P-A.**, Clary, J., Livernoche, A., De Granpré, C., St-Onge, G., Bourgault, D., Montero Serrano, J-C., Chavane, C., Neumeier, U., Gostiaux, L., 2015. Rapport de mission COR1502 : Pointe des Monts (Estuaire du Saint-Laurent). Report submitted to NSERC, 32 p.

Rémillard, A.M., **Desiage, P.-A.**, St-Onge, G., Montero-Serrano, J.-C. & Jetté, C. 2014. Marine geology of the Gulf of San Jorge (MARGES): habitat mapping, basin architecture and stratigraphy, gas seepage, natural hazards and harmful algal blooms. Université du Québec à Rimouski, Institut des sciences de la mer, expedition report, 120 p.

CHAPITRE 1

QUANTIFICATION DES SOURCES ET DES AXES DE TRANSPORT DES SEDIMENTS DE SURFACE DANS LE GOLFE DE SAN JORGE, PATAGONIE CENTRALE (ARGENTINE)

1.1 RÉSUMÉ EN FRANÇAIS DU PREMIER ARTICLE

Situé dans la partie centrale de la Patagonie entre les latitudes 45°S et 47°S, le golfe de San Jorge (GSJ) forme un bassin semicirculaire d'environ 160 km de longueur par 250 km de largeur dénué d'affluents majeurs et pérennes. La distribution granulométrique, la composition minéralogique de la fraction brute et des argiles ainsi que l'identification des éléments majeurs et mineurs de 75 échantillons de sédiments de surface provenant du GSJ et du plateau continental adjacent ont été investigués afin de définir la distribution spatiale, le transport et les sources potentielles du matériel terrigène. Des analyses similaires ont également été effectuées sur des échantillons terrestres, marins et fluviaux, provenant de la région du GSJ et de Patagonie, afin d'affiner l'identification de l'origine des sédiments. L'assemblage minéralogique des sédiments de surface du golfe, dominé par les plagioclases, le quartz et les argiles, est principalement conditionné par la géologie associée au volcanisme continental de Patagonie. La concentration significative en particules volcanoclastiques mise en lumière par la signature minéralogique et les images de microscopie électronique à balayage des sédiments suggère une influence prédominante du volcanisme rhyolitique sur la sédimentation moderne dans le golfe. Concernant les argiles, les grandes quantités de smectite ont été acheminées dans le GSJ par le transport éolien alors que les apports d'illite et de chlorite semblent être associés aux courants remontant le plateau continental depuis le sud de la Patagonie. Finalement, les résultats de cette étude suggèrent que les sédiments de surface du GSJ proviennent à 50% d'apports externes/océaniques, à 40% des rives du golfe

suite à des mécanismes d'érosion et de ruissellement et à 10 % du transport éolien qui achemine des poussières dans les eaux du golfe.

Le premier article de cette thèse intitulé "*Quantifying sources and transport pathways of surface sediments in the Gulf of San Jorge, Central Patagonia (Argentina)*" a été écrit par moi-même sous la supervision de mon directeur Guillaume St-Onge et de mon co-directeur Jean-Carlos Montero Serrano. Pour cet article j'ai réalisé l'essentiel des analyses en laboratoire et du traitement des données en collaboration avec mon co-directeur Jean-Carlos Montero-Serrano. Des chercheurs provenant de diverses institutions en Argentine ont également été impliqués dans la production de cet article : Augusto César Crespi-Abril, Erica Giarratano, Mónica Noemí Gil et Miguel J. Haller. Augusto César Crespi-Abril a notamment réalisé l'échantillonnage de sédiments terrestres en Patagonie. Cet article a été accepté dans sa version finale le 27 juin 2018 et publié dans une édition spéciale de la revue *Oceanography* portant sur les études réalisées dans le GSJ dans le cadre du projet PROMESse.

Les résultats de cet article ont été présentés à divers niveaux d'avancements sous la forme d'une présentation orale au 83^{ème} congrès de l'Association canadienne pour le savoir (ACFAS) qui s'est déroulé à Rimouski en mai 2015 ainsi que sous la forme d'un poster lors du congrès annuel de l'union américaine de géophysique (*AGU Fall meeting*) à San Francisco (États-Unis) en décembre 2016.

1.2 QUANTIFYING SOURCES AND TRANSPORT PATHWAYS OF SURFACE SEDIMENTS IN THE GULF OF SAN JORGE, CENTRAL PATAGONIA (ARGENTINA)

The Gulf of San Jorge (GSJ) is a semicircular basin, approximately 160 km long and 250 km wide, located in the central part of Patagonia between latitudes 45° S and 47° S, and it lacks any present-day major and perennial tributaries. The grain size and bulk and clay mineralogical compositions, as well as major and minor elements of 75 surface sediment samples from the GSJ and from the adjacent continental shelf were investigated to define the spatial distribution, the transport pathways and the potential sources of terrigenous material. To better constrain the origin of sediments in the GSJ, analyses were also performed on 14 terrestrial, riverine and marine samples from potential source areas around the Gulf and Patagonia. The mineral assemblage of surface sediments in the Gulf, dominated by plagioclase, quartz and clays, is a function of the primary continental volcanic geology in Patagonia. The significant concentration of volcaniclastic particles indicated by mineralogical signatures and scanning electron microscope images of sediments suggests a substantial contribution from rhyolitic volcanism to the modern sedimentation in the Gulf. High amounts of smectite are carried into the GSJ by dust transport, whereas inputs of chlorite and illite seem to be associated with continental shelf current transport from southern Patagonia. Finally, our results suggest that the surface sediments in the GSJ are derived from 50% external/oceanic inputs, 40% inner Gulf shores (i.e., erosion and runoffs) and 10% dust (i.e., aeolian transport).

1.3 INTRODUCTION

Considered as the transition pathway between terrestrial/coastal and oceanic domains, the continental shelf is a key area for numerous and miscellaneous oceanographic processes, such as biogeochemical cycles, primary production and sediment transfer to deeper waters. Due to their shape with a partially open littoral on the ocean domain, gulfs represent suitable small-scale analog of the mechanisms occurring on the continental shelf. Furthermore, large

coastal embayments such as gulfs are often sensitive marine environments affected by human activities (e.g., fisheries and/or urban development). Located in the central part of the Argentine continental shelf (ACS), the Gulf of San Jorge (hereafter referred to as GSJ; Figure 9) is a perfect example of this dichotomy between economical-industrial development and environmental preservation. Indeed, numerous foraging and reproduction areas for marine birds and mammals coexist in the GSJ with commercial shrimp and hake fisheries, as well as terrestrial oil production.

In this strategic environmental and oceanographic context, numerous studies focusing on the grain size and mineralogical and geochemical composition of the detrital sediments over gulfs and continental shelves have been performed to determine the sources and depositional conditions and to identify the transport pathways and the regional hydrodynamics patterns (e.g., Preda and Cox, 2005; Spagnoli et al., 2008; Saukel et al., 2010). A growing number of studies also work with bulk mineralogy, clay mineralogy and elemental geochemistry to characterize the modern sedimentary processes, as well as to discriminate the provenance of terrigenous supplies (e.g., Andrews and Vogt, 2014, Gamboa et al., 2017).

On the Argentinean continental shelf and margin, the physical and chemical properties of surface and subsurface sediments have been characterized via bulk and clay mineralogy and elemental and isotopic geochemistry (e.g., Petschick et al., 1996; de Mahiques et al., 2008). All these results helped to investigate the composition and provenance of terrigenous inputs. Additionally, the chemical signatures of rivers, aeolian dust and topsoil samples have been analyzed to estimate the potential riverborne and windborne inputs to the Patagonian littoral (Gaiero et al., 2004; 2007). However, most of the coastal studies, as well as the sampling campaigns, have been conducted in the northern region of the ACS and especially in the Río de La Plata estuary at ~35° S (e.g., Nagai et al., 2014). This focus leads to a disproportionate amount of information between the north and the other coastal and inner shelf areas of Argentina.

In this study, we present the first multiproxy analysis based on grain-size distribution, bulk and clay mineralogy and elemental geochemistry (major and trace elements) of surface sediments from the GSJ. The main objectives of this study were to (1) characterize the spatial distribution of the surface sediments, and (2) define the different sources and transport processes of detrital sediment in the GSJ. Samples from potential sources areas (such as beaches, tablelands, dry-bed lakes, river mouths and oceanic environments) were also analyzed to document the relative differences between the sediment composition in the potential source areas and sediment samples from the GSJ.

1.4 STUDY AREA

1.4.1 Physical setting

The Patagonian continental shelf represents the southern part of the ACS and is delimited by the Patagonian coast from Cape Horn (55° S) nearly to the Colorado River (39° S). The hydrodynamics of the region consists of a northward (NNE) flow of subAntarctic cold water (i.e., Patagonian Current; Figure 9a) conveyed onto the shelf through the Cape Horn Current and the Malvinas Current along the continental slope (Palma et al., 2008 and references therein).

The Atlantic coast of Patagonia is therefore characterized by a dry climate (from 200 to 400 mm/yr; Coronato et al., 2008). The strongest winds are concentrated between latitudes 49° S and 53° S in the heart of the southern westerly winds belt (Kilian and Lamy, 2012). The surface hydrology consists of eight main watercourses, mostly perennial, draining toward the east from Andean headwaters to the Atlantic. Except for the Negro River in the north and the Santa Cruz River in the south, the other major watercourses have relatively limited discharge (Figure 9a; Kokot, 2004).

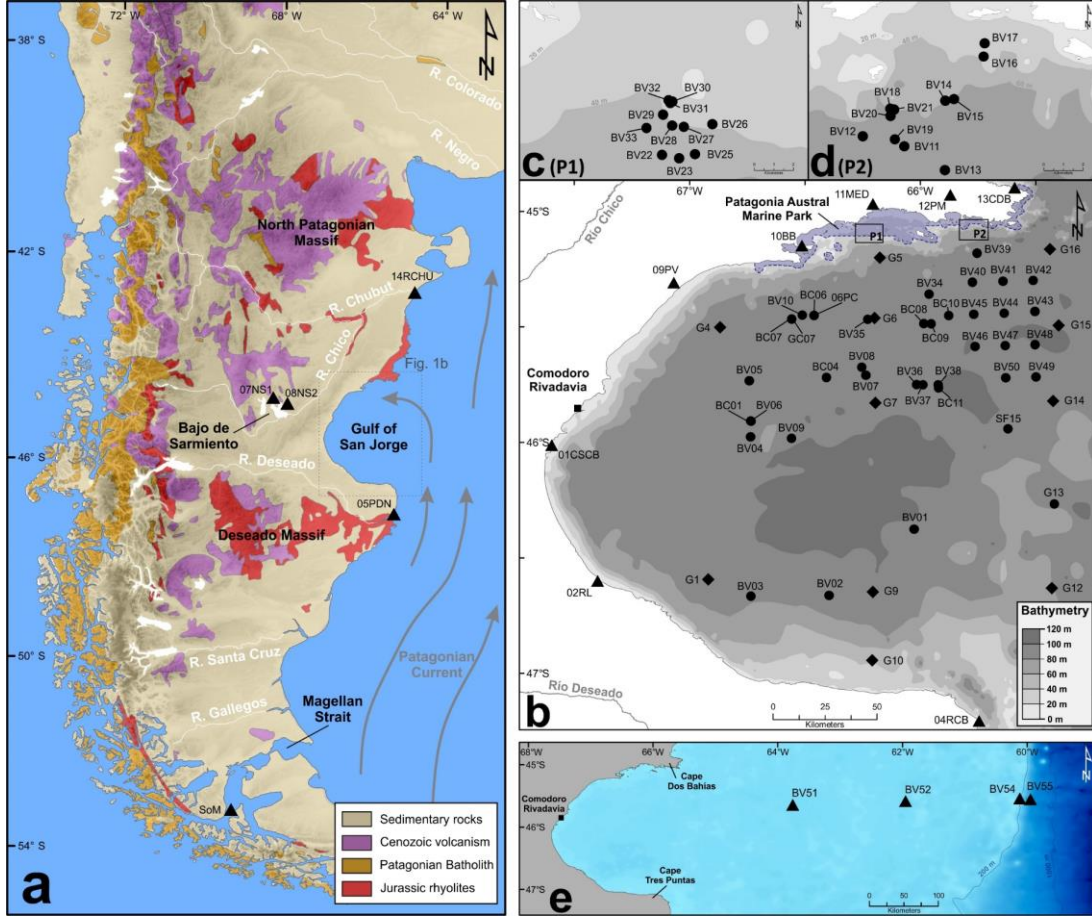


Figure 9: Maps of the study area with sample locations. The dots indicate surface sediment samples in the GSJ, the diamonds denote sites with surface sediment samples, as well as water column filters, and the triangles illustrate samples from potential source areas. (a) Map of Patagonia showing the main hydrodynamic circulation on the Patagonian continental shelf (gray arrows; Palma et al. 2008), simplified surface geology, and main geographic features mentioned in the text. (b-d) Bathymetric maps of the Gulf of San Jorge and the marine park areas. (e) Bathymetric map of the GSJ with adjacent continental margin

The GSJ is a semicircular basin located in the central part of Patagonia between latitudes 45° S (Cape Dos Bahías) and 47° S (Cape Tres Puntas; Figures 9b and e). The gulf forms an encroachment of the South Atlantic Ocean, approximately 160 km long and 250 km wide, in the heart of southern South America. The bathymetry of the basin rapidly decreases to reach the 90 m isobaths, which defines a large flat central region covering most of the surface of the gulf and corresponds to the Patagonian outer shelf (Violante et al., 2014). The

hydrodynamic and water mass origins in the gulf are related to the northward circulation on the shelf (Figure 9a; Palma et al., 2008), but the GSJ is also located at the limit of the influence of the Magellan Strait discharge flowing along the coast and entering the gulf in the southeastern sector at Cape Tres Puntas (Fernández et al., 2005).

From a geological and geographical point of view, most of the GSJ is considered as the eastern part of the San Jorge Gulf Basin, a hydrocarbon-producing basin surrounded by the North Patagonian Massif to the north, the Deseado Massif to the south and the Andes to the west (Sylwan, 2001). The presence of these two massifs is reflected in the GSJ area by the existence of Jurassic silicic volcanic rock outcrops, predominantly rhyolitic, from the Chon Aike province (Figure 9a; Pankhurst et al., 1998). The main outcrop of silicic rocks, dominated by rhyolites and ignimbrites, is located in the northeastern part of the gulf close to Cape Dos Bahías and covers the entire sector of the Patagonia Austral Marine Park (hereafter referred to as marine park; Figures 9a and b; Pankhurst et al., 1998). The tablelands of the San Jorge Gulf Basin are mainly overlain by Eocene-Miocene sedimentary rocks of the Sarmiento and Patagonia Formations (Cuitiño et al., 2015), as well as Quaternary fluvio-glacial deposits (e.g., 'Rodados Patagónicos'; Martínez and Kutschker, 2011). The tablelands reach the coast as cliffs or beach-ridge systems, generally composed of gravel and/or sand (Isla et al., 2002).

1.4.2 Sedimentation

The main suppliers of terrigenous materials to the Patagonian littoral are coastal erosion, rivers and aeolian transport, as well as transportation and redistribution of sediments from the shelf by the prevailing northward-flowing Patagonian Current. Indeed, according to Pierce and Siegel (1979) and Gaiero et al. (2003), the estimated contributions of coastal erosion, dust transport and rivers to the terrigenous sedimentary supply transferred offshore are, respectively, 56%, 41% and 3% (Violante et al., 2014). The weak proportion of sedimentary inputs on the continental shelf by the Patagonian rivers is explained by their present low flows and the low particulate loads in their downstream sectors (Gaiero et al.,

2003; Kokot, 2004). The large aeolian contribution is a combination between the strong westerly winds over the regional geomorphology and the arid climate, stimulating the resuspension and transport of surficial terrestrial sediments from Patagonian tablelands to the shelf (Crespi-Abril et al., 2018).

The Gulf does not have any present-day major and perennial tributaries likely to strongly affect the sedimentation. Furthermore, the GSJ is located in the heart of several hundred kilometers of littoral without major rivers, except for the relatively low flow of the Deseado River ($5 \text{ m}^3\text{s}^{-1}$; Kokot, 2004), reaching the ocean a few dozen kilometers south of the GSJ (Figure 9a). On the other hand, the influence of aeolian inputs has been observed in the Gulf area (Isla et al., 2002; Crespi-Abril et al., 2016) as the basin is located on the outskirts of major dust sources (Prospero et al., 2002).

1.5 MATERIAL AND METHODS

The Seventy-five marine surface samples were collected in the GSJ, as well as on the continental shelf. The sampling was performed using a Van Veen grab sampler (65 samples) and a box corer (8 samples), gravity corer (1 sample) and piston corer (1 sample) wherein the uppermost 1 cm of sediment was recovered to collect only the sediment-water interface (Figures 9b, c, d and e). These core-top sediments were found to represent modern time or at least the last decade/century in the case when the first centimeters were missing. All marine samples were recovered on board the N/R Coriolis II from January 29th to March 4th, 2014 (Leg 1: MARES and Leg 2: MARGES), as part of the PROMESSe (PROgrama Multidisciplinario para el Estudio del ecosistema y la geología marina del golfo San Jorge y las costas de las provincias de Chubut y Santa Cruz) project. Bulk and clay mineralogy and elemental geochemistry were analyzed for all samples, whereas grain size analysis was performed only on 57 samples due to the low quantity of sediments available for stations of Leg 1. The 63-300 and $<63 \mu\text{m}$ sediment fractions of three selected samples (BV01, BV06 and BC11) were also observed using a scanning electron microscope (SEM) to determine the

abundance and the geochemical characterization of volcaniclastic particles (e.g., glass shards) in marine sediments. In addition, 13 terrestrial and riverine samples as well as a marine surface sediment sample (0-2 cm sediment depth) from the Magellan Strait were also analyzed for their mineralogical and elemental geochemistry signatures (see details in the supporting information; Figures 9a and b).

To document the chemical composition and geochemical classification of suspended sediments in the water column, 22 seawater samples from 11 stations were recovered in the GSJ during the MARES cruise (Figure 9b). For each station, seawater samples were collected using Niskin bottles fixed on a CTD rosette at the sea surface (2 m depth), as well as close to the sea-floor. Between 0.5 and 1.5 L of sea water, depending on particle load, was filtered onto glass-fiber GF/F filters. The filters were stored frozen at -20 °C until their analysis.

The source samples and detailed methodology used for the analyses of grain-size, SEM, bulk and clay mineralogy, and elemental geochemistry, as well as the statistical approach are presented in the supplementary material.

1.6 RESULTS

1.6.1 Grain-size distribution

In the GSJ, the analyzed sediments are mostly fine to very fine silts, as well as very fine sands with a mean grain size (phi scale) ranging from 8.01 (very fine silt) to 3.73 (very fine sand; Figure 10b, Figure 16a and Table 1). Coarser sediments are dominant for the northern coastal sample patches (marine park area; Figures 16b and c), especially close to the Cape Dos Bahías area (P2; Figure 16c). Fine silts prevail in the north-central area of the GSJ with a finer fraction in the inner part of the gulf (Figure 16a). The mean sediment grain size measured in the GSJ for this study coincides with results obtained by Fernández et al. (2003). Furthermore, end-member modeling analysis (EMMA) provides a model with three

end-members (EM) explaining 91% of the variance in the grain size dataset (Figure 10a). Based on the grain size distributions of the three end-members (Figure 10b), EM1 represents a well-sorted distribution associated with the very fine sand fraction (mean $\sim 3.04 \phi$), EM2 shows a well-sorted distribution associated with the coarse and medium silt fractions (mean $\sim 5.29 \phi$), and EM3 represents a well-sorted distribution with main peaks corresponding to the finer grain fractions (i.e., fine silt to clay; mean $\sim 7.34 \phi$). EM1 and EM2 characterize all the samples from the park area (P1 and P2), as well as the three samples from the southern part of the gulf, and EM3 represents most of the samples from the north-central area (Table 1). Maps of the $\log[EM3/(EM2+EM1)]$ end-member ratios are used to illustrate the spatial variations of the relative proportion between very fine silt and coarse silt to identify the mechanism of transport/sources of particles in the GSJ (Figures 10c, d and e).

1.6.2 Bulk mineralogy

The most abundant minerals in the GSJ bulk sediments, identified according to the quantitative X-ray diffraction (qXRD) method developed by Eberl (2003), are quartz (14-51%), plagioclase (15-49%), clays (2-41%), amorphous silica (4.5-35.5%) and K-feldspar (2-12%). The bulk mineralogical compositions of sediments also indicate smaller proportions of pyroxene (0-2.7%), amphibole (0-1.5%), and Fe-oxides (0-0.9%; Table 2). Amorphous silica can mostly be identified as volcanic rhyolitic tephra based on the Icelandic tephra sample (Hekla-4) which is used as a mineral standard in RockJock v11 (Andrews et al., 2013). Indeed, in the XRD scans centered between 19° and 31° two-theta, the samples containing higher proportions of amorphous silica ($>10\%$; e.g., BV01; Figure 18a) present similar patterns to the standard of rhyolitic tephra (Hekla-4). Furthermore, SEM imaging of the sediments in the 63-300 μm fraction from the BV01, BV06 and BC11 sites attests to the appreciable amounts of volcaniclastic particles, which are mainly represented by highly vesicular glass shards and slightly vesicular glass shards with blocky to curviplanar shapes (Figures 18b and c). The observation of SEM images also illustrates the near absence of diatom frustules, considered as the other potential source of amorphous silica. The geochemical data in K_2O-SiO_2 of glass shards in the surface sediments confirm the rhyolitic

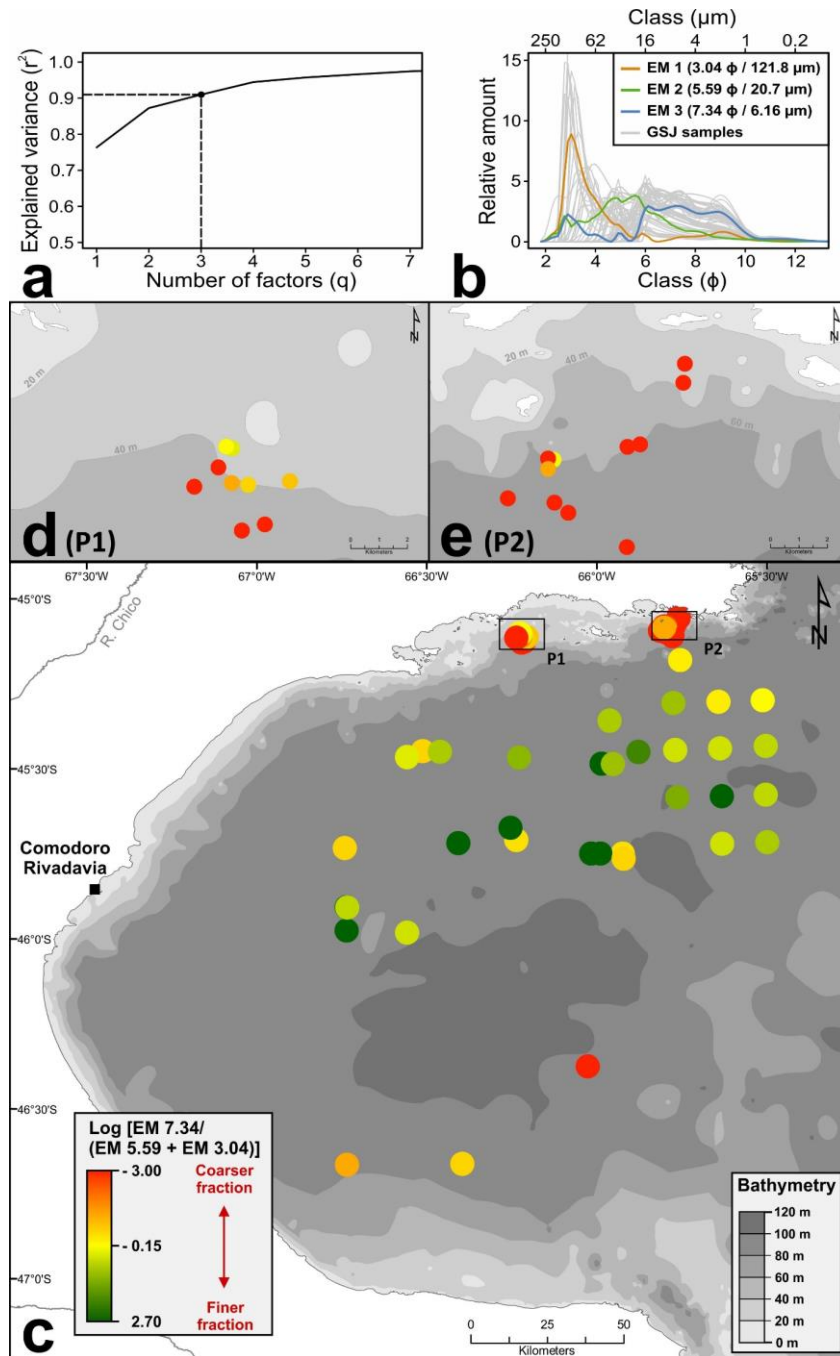


Figure 10: End-member modeling analyses (EMMA) performed on the detrital fraction of the grain-size distribution in the GSJ. (a) The grain-size distribution of the first three end-members accounts for more than 91 % of the variance. (b) Three representative unmixed grain-size distributions produced from EMMA based on the grain-size distributions of the GSJ samples (gray lines). (c-e) Log[EM3/(EM2+EM1)] end-member ratios in the GSJ and marine park areas, respectively

composition of volcaniclastic particles in surface sediments (Figure 18d). The bulk mineralogy is presented in a ternary diagram showing the three most abundant minerals (quartz, plagioclase and clays) in the GSJ samples (Figure 11). The ternary diagram also includes results from bulk mineralogy analyses of marine and terrestrial sediments from the Patagonian continental shelf, Strait of Magellan and San Jorge Gulf Basin, all representing potential source areas of sedimentary inputs in the GSJ (Figure 11). The ternary diagram reveals that the clays contents differ significantly between sediments from marine park areas and those from most of the other parts of the gulf. Indeed, the sites in the marine park areas are characterized by lower concentrations of clays (2-10.5%) with homogeneous values of quartz and plagioclase (26-42% and 34-49% respectively) in contrast with the clay contents in the other parts of the GSJ, which are higher (6-41%) with scattered values of quartz and plagioclase (14.5-51% and 16.5-37%, respectively).

To visualize the main tendencies of mineralogical enrichment in the gulf, spatial distributions of mineralogical balances for major mineral groups (i.e., $b_{\{(Quartz+Feldspars)/Clays\}}$) were conducted (Figure 12a; see statistical details in the supporting information). The results indicate higher values associated with quartz and feldspars enrichment versus clay enrichment for the marine park areas. The lower values are related to most of the other parts of the GSJ, with the exception of intermediate values for samples located in the northern and southern outer parts of the Gulf (Figure 12a).

To confirm the correct representativeness of the five-source composition, SedUnMix was run with the five sources against the source area samples previously used to define the source compositions (See details in supplementary material; Table 5). The results indicate a high proportion of sources S1, S2, S4 and S5 to the sediment composition of their respective source samples (from 65% to 100%; Table 4). The contribution of source S3 to its representative source samples is weaker (from 7% to 47%; Table 4) and proportions are mainly shared with source S5. Spatial distributions for the proportions of inner gulf coastal inputs (S1+S2), dust transport (S4) and external/oceanic contributions (S3+S5) to sediment mineralogical composition are presented respectively in Figures 12b, 12c and 12d. The

sources S1 and S2 provide a high contribution to the sediment assemblage of the coastal park areas and the NE-central part of the GSJ (>40% with mean value ~70% close to the park). The proportions of sources S1 and S2 to samples composition are comparatively low for the other sectors of the GSJ (<30%; Figure 12b). The results from Figure 12c indicate that a low to intermediate fraction of the sediment assemblage is associated with source S4 (<50%) with a distribution limited to approximately ten samples in the NW and central parts of the GSJ.

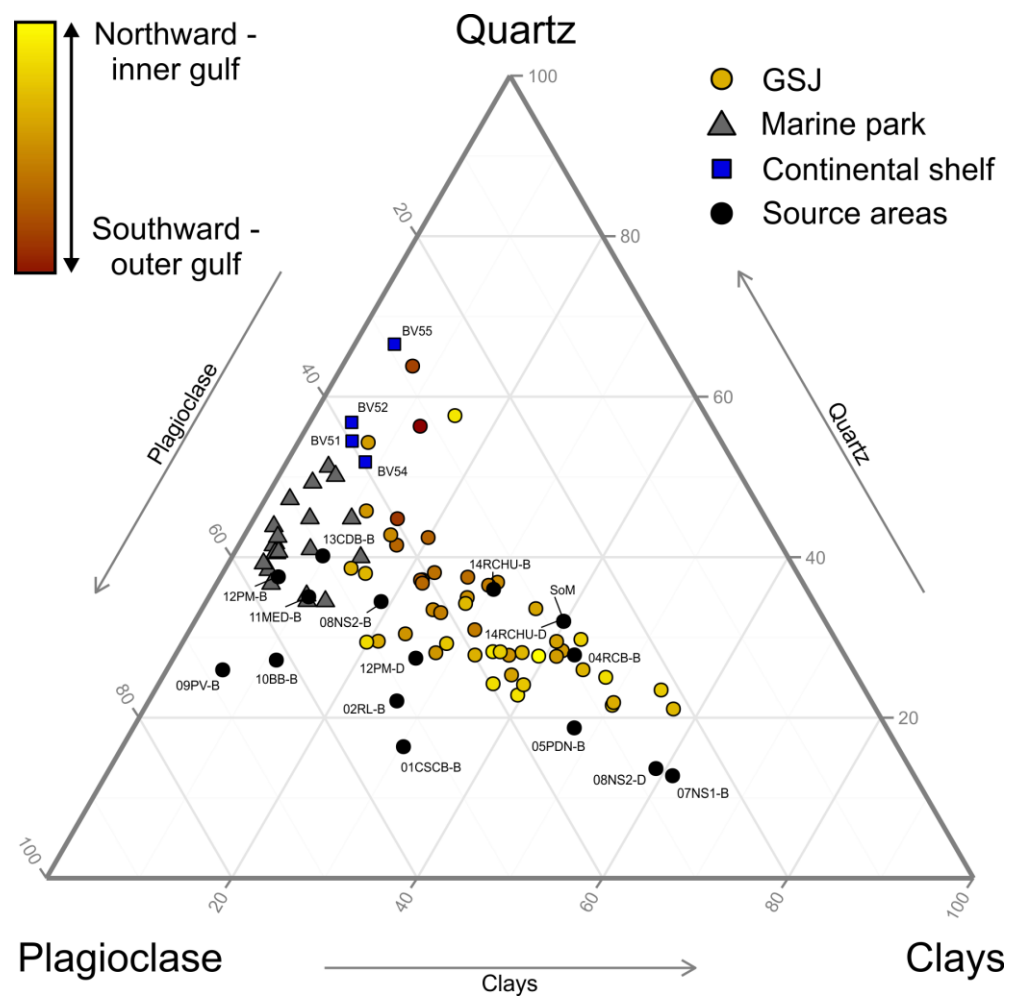


Figure 11: Quartz-plagioclase-clays ternary plot illustrating the relative compositions of the main minerals. The samples are illustrated according to their locations in the gulf; the northward-inner gulf to southward-outer gulf tendency is calculated from absolute latitude and longitude coordinates (excluding the park sites)

Nevertheless, this study focuses on the aeolian transport of silt and clay fraction particles using the < 63 µm fraction of 08NS2 and the fine dry-bedload sediment from 07NS1 as source samples to generate a dust-related source (S4) in SedUnMix. Thus, we consider only the intermediate- to long-distance aeolian transport. This bias could have led to underestimating the wind-blown “coarse” dust, which is known to be active in the region as shown by the creation and displacement of dune fields south of Comodoro Rivadavia (Montes et al., 2015). The combination of S3 and S5 represents the source with the highest contribution to the sediment composition of the Gulf, excluding the coastal park areas, especially in the central sector (from 47 to 86%), in the SW part (from 50 to 100%) and in the oceanic perimeter of the GSJ (from 56 to 100%; Figure 12d).

1.6.1 Elemental geochemistry

The major element composition of bulk sediments from the GSJ is characterized by very high proportions of SiO₂, high contents of Al₂O₃ and lower concentrations of Fe₂O₃, CaO, K₂O, MgO, TiO₂, P₂O₅ and MnO (Table 3). The minor and trace elements are dominated by Sr, Zr and V. The sediment samples are plotted in the log(SiO₂/Al₂O₃) versus log(Fe₂O₃/K₂O) classification diagram (Herron, 1988) coupled with the results of the water sample filters (surface and bottom) to compare the geochemical classification and mineralogical maturity between sediment from the seafloor and the water column (Figure 13c). The seafloor sediments and suspended sediment in the water column are geochemically classified as shale and wacke with no major distinction concerning the dispersion in the diagram of the seabed and suspended sediment samples. The ternary diagrams Al-Si-Fe and Fe-K-Ca (Figures 13a and b; see details in the supporting information) highlight the clear distinction between coastal park areas and central GSJ samples with higher relative proportions of Si (>74%; Figure 13a) and Ca (>38%; Figure 13b) in the park. The enrichment in Si seems positively correlated with coarser sediments (Figure 13a).

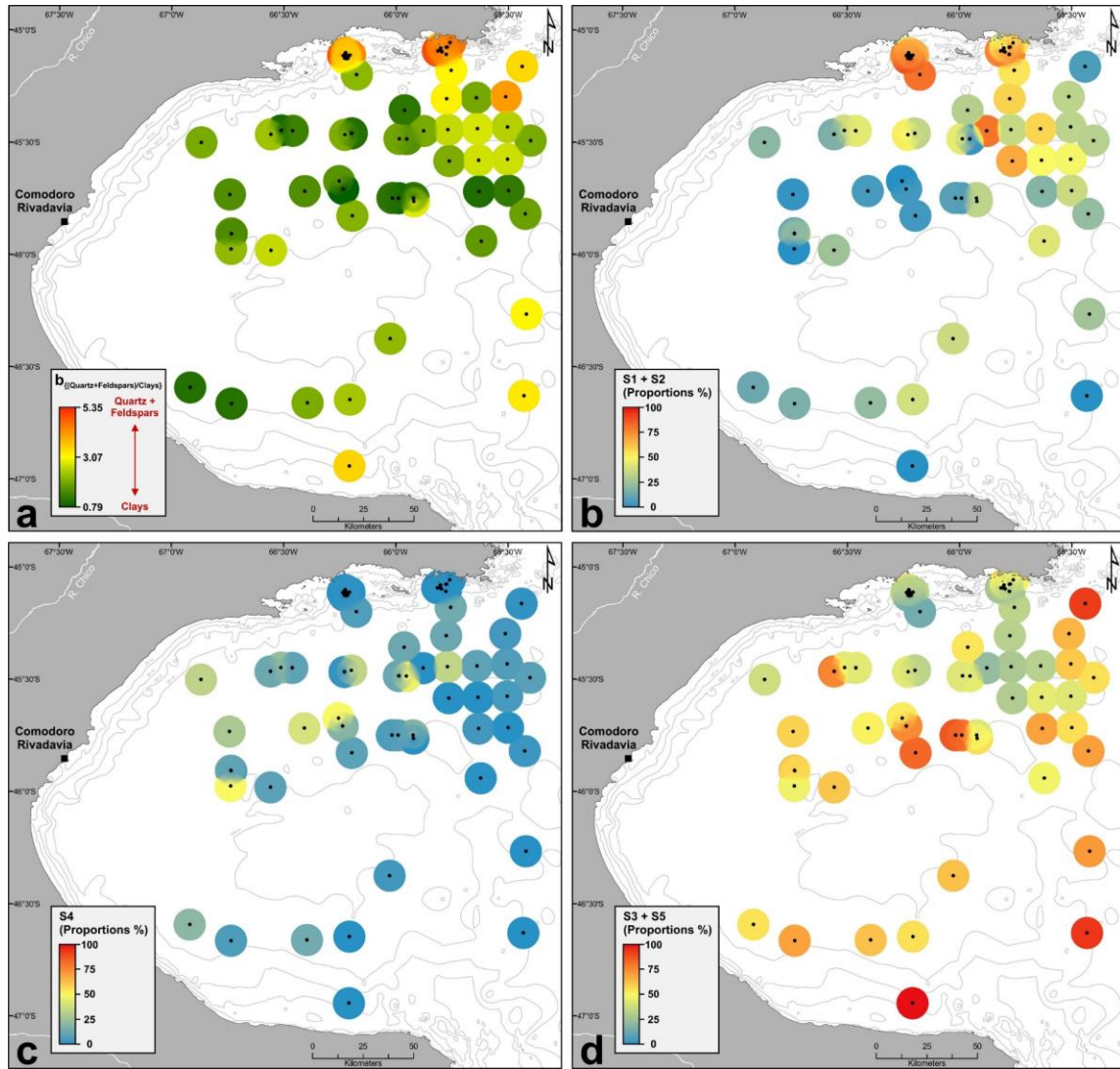


Figure 12: (a) Spatial distribution of the elemental balance for major mineral groups (i.e., $b_{\{(Quartz+Feldspars)/Clays\}}$). (b-d) Maps showing relative proportions of inner gulf coastal inputs (S1+S2; b), dust transport (S4; c) and external/oceanic contributions (S3+S5; d) to sediment mineralogical composition. The proportions in major mineral groups (quartz, feldspars and clays) of proposed sources (S1+S2, S4 and S3+S5) are presented in pie charts

We illustrate the scores from the first two principal components of the log-centered geochemical data (excluding the geochemically distinctive areas of the coastal park) as these account for more than 69% of the total variance (Figure 13d). PC-1 scores account for 53% of the total variance and appears to be positively correlated with Fe-Mg-V-LOI and negatively correlated with Ca-Si-Sr-Zr-Mn-Al-K-P. The spatial distribution of PC-1

elemental geochemical scores indicates that high values dominate the central and SW parts of the Gulf and are associated with enrichment in Fe, Mn and V in these areas (Figure 13d). These results expose a noticeable tendency similar to that of the bulk mineralogy distribution in the GSJ with higher enrichments in clays in the central and SW parts of the GSJ (Figure 13a). Limited sectors in the NE and SE parts of the GSJ, close to Capes Dos Bahias and Tres Puntas, present intermediate to low PC-1 scores (Figure 13d).

1.6.2 Clay mineralogy

The clay mineral assemblage of sediment in the gulf is highly dominated by smectite with a contribution of more than 75% for at least 85% of the samples. In contrast, chlorite, illite and kaolinite contents are rather low with average contributions close to 8%, 6.5% and 1.5%, respectively (Table 2). The relative abundances of kaolinite, smectite, and coupled illite plus chlorite (I+C) of the GSJ samples, as well as marine and terrestrial samples associated with potential source areas for sedimentary inputs in the Gulf, are plotted in a ternary diagram (Figures 14a and b). The results confirm the high proportions of smectite in GSJ sediment, especially in the coastal park areas (Figure 14b). The spatial distribution of the $\log[\text{smectite}/(\text{illite}+\text{chlorite})]$ ratios shows that the lower values occur in the southern part and oceanic perimeter of the gulf, excluding the NE sector, suggesting enrichment in I+C in these regions (Figure 14c).

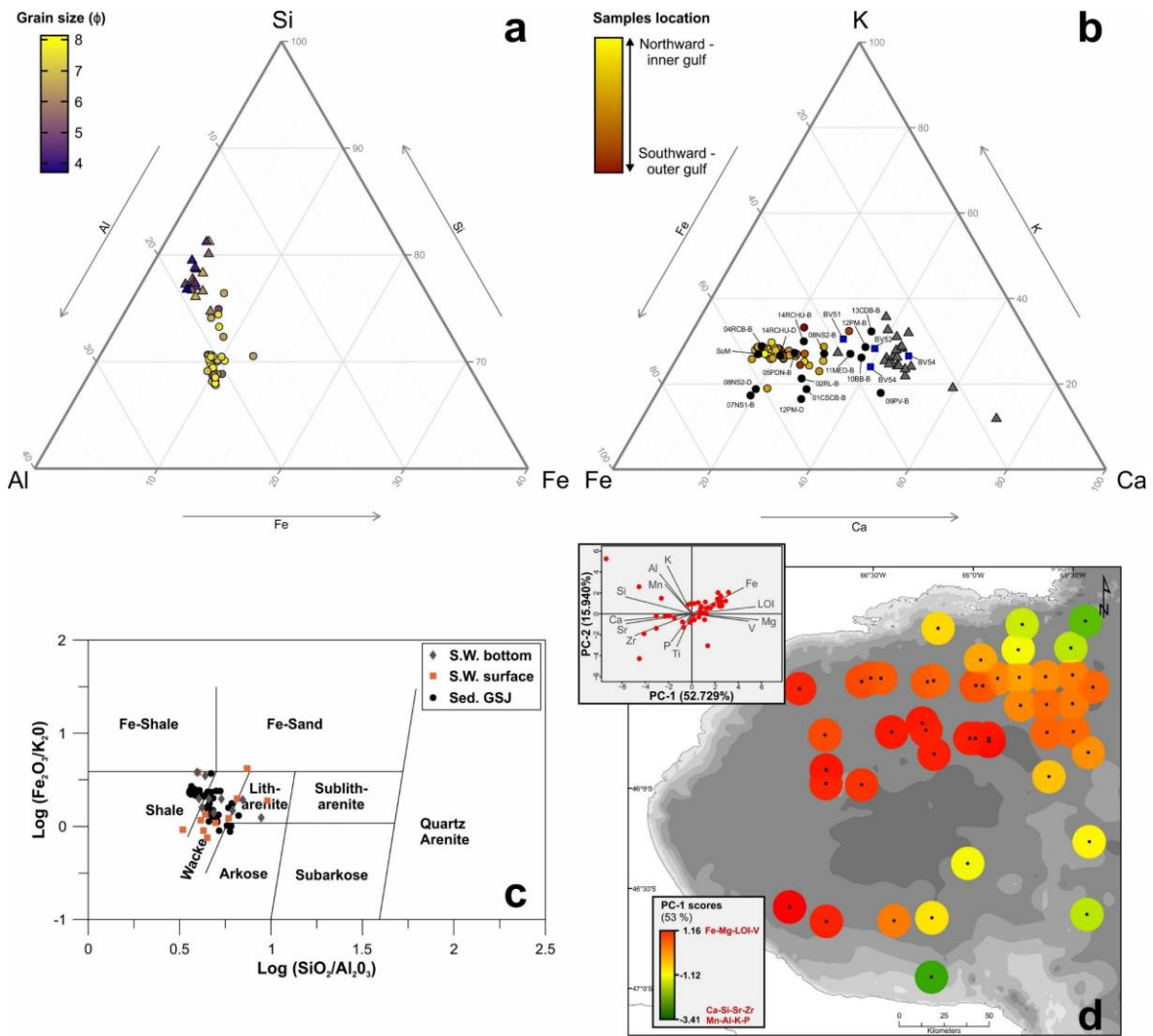


Figure 13: (a) Si-Al-Fe abundances of marine park areas and other GSJ samples associated with mean grain size (ϕ). (b) K-Fe-Ca distribution of marine park areas and other GSJ samples, plotted together with potential source area samples, as well as surface sediment samples from the Patagonian continental shelf (Table 3). The samples are illustrated according to their location in the gulf; northward-inner gulf to southward-outer gulf tendency calculated from absolute latitude and longitude coordinates (excluding the park sites). (c) Herron (1988) geochemical classification diagram for surface sediment and water column samples of the GSJ. (d) Biplot of the PC-1 versus PC-2 generated from the log-centered transformation of major, minor and trace elements of GSJ samples, presented with map of PC-1 scores

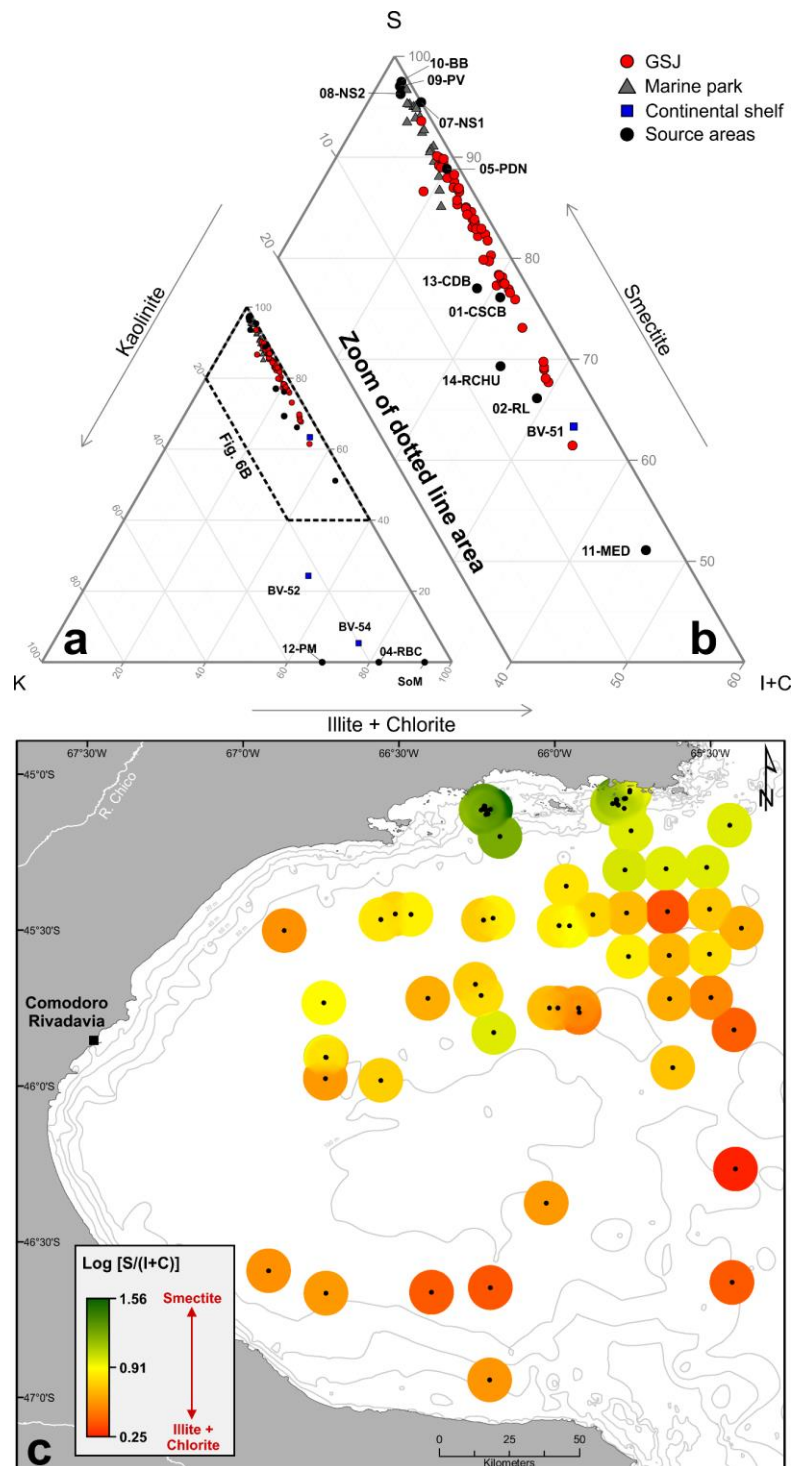


Figure 14: (a-b) Ternary diagram of smectite (S), kaolinite (K), and illite + chlorite (I+C) relative concentration in samples from marine park areas, other GSJ samples, continental shelf and potential source areas. (c) Spatial distribution of $\log[S/(I+C)]$

1.7 SEDIMENT DISTRIBUTION, POTENTIAL SOURCE AREAS AND TRANSPORT PATHWAYS

In the GSJ, the grain size analysis and distribution are used to highlight two clearly distinct sedimentary environments. The dominance of coarser sediments (i.e., very fine sand) in the northern part of the gulf in the coastal marine park areas reflects moderate- to high-energy environments (erosive environments; Fernández et al., 2003). These sediments are mainly associated with EM1, especially the sediments close to Cape Dos Bahías, and to a lesser extent with EM2. Due to the absence of riverine inputs in the GSJ, we suggest that the well-sorted fine sand EM1 can be associated with sediments derived from local erosion (i.e., beach and cliff erosion; Isla et al., 2002), and the well-sorted coarse to medium silt EM2 with wind-blown “coarse” dust from nearby sources such as dune fields on the outskirts of the GSJ (Montes et al., 2015). The second distinct sedimentary environment is observed in the central part of the gulf with fine to very fine silts corresponding to a depositional environment with low energy (Fernández et al., 2003). The sediments in this area are almost exclusively associated with EM3. The EM3 is characterized by a large dominant mode extending from medium silt to clay which could reflect a depositional environment associated with sediments transported over significant distances (e.g., currents and aeolian transport).

The bulk mineralogy, rather homogenous and dominated by plagioclase, quartz and clay minerals, is in accordance with the topsoil and riverine mineralogy from eastern Patagonia previously published in Gaiero et al. (2004). The high proportions of plagioclase and quartz reflect the dominant volcanic signature of Patagonia, mainly driven by the southern volcanic zone of the Andean Cordillera but also, to a lesser extent, by volcanic rocks erupted since the Jurassic. Indeed, numerous studies have highlighted the major influence of Andean volcanism on the mineralogical, chemical and isotopic signatures of beach, riverine and marine samples from western (Bertrand et al., 2012), as well as eastern Patagonia (Potter, 1994; Gaiero et al., 2007). The prevalence of clays in the riverine (Chubut and Deseado), as well as “Bajo de Sarmiento” samples, suggests that riverine and aeolian transport have an impact on the inputs of clays in the GSJ. According to Gaiero et al. (2004), the suspended loads of the Chubut and Deseado Rivers, likely to be partially transported to the gulf, present

the highest proportions of clay minerals in comparison to other Patagonian riverine and topsoil samples. Furthermore, the potential of wind to transport clays from dust source areas such as “Bajo de Sarmiento” (Prospero et al., 2002; Montes et al., 2017) is reinforced by the nature of the soil covering the Gulf of San Jorge Basin. Indeed, the soil is mainly composed of yermosols that are often characterized by a developed argillic (clay) B horizon with a strong ability to be eroded by wind (Gut, 2008). In the GSJ, the sediments enriched in clay minerals are located in the deep and central areas that are associated with weaker hydrodynamic conditions and identified as a depositional environment (Fernández et al., 2003). In addition, the appreciable amounts of volcaniclastic particles, identified as rhyolitic tephras (Figure 17) in the bulk mineralogical composition and observed as glass shards in SEM images of the surface sediments (Figures 18b and c), also support the aeolian and riverine transport contribution, as opposed to coastal erosion, that carries modern and past (i.e., remobilization of terrestrial tephra deposits) volcanogenic particles into the GSJ. Furthermore, the geochemical composition of glass shards suggests a dominance of rhyolitic volcaniclastic material (Figure 18d); however, the sources of recent rhyolitic products are rare in the volcanic zone close to the GSJ (i.e., Southern Volcanic Zone of the Andes), except for the Chaitén volcano in Chile (López-Escobar et al., 1993). Thus, we hypothesize that the ash plumes generated by the explosive rhyolite eruptions of Chaitén volcano and the remobilization of associated tephra deposits represent the most conclusive source of modern tephra in the GSJ.

The well-defined correlation between the grain size distribution and the bulk mineralogy, where the coarser grains are associated with clay-poor and plagioclase/quartz-rich samples (Figures 10 and 12a), highlights the presumptive impact of the grain size on the sediment mineral composition. Therefore, the bulk mineral composition of sediments in the GSJ is primarily controlled by the dominant and homogenous continental volcanic signature in Patagonia, but is also influenced by the grain size distribution.

The clay-mineral assemblages in the GSJ, highly dominated by smectite, are relatively consistent with the results reported both on the nearshore areas of Patagonia (Pierce and

Siegel, 1979) and on the continent (i.e., riverine and topsoil material; Gaiero et al., 2004). The high smectite content in the GSJ is related to the combination of two factors: (1) the potential high inputs of smectite from adjacent eastern and southern Patagonian sources (Petschick et al., 1996; Diekmann et al., 2000) and (2) the rapid gravitational settling of smectite on coastal areas compared to other clay minerals (Pierce and Siegel, 1979). Indeed, the well-crystallized smectite, as observed in the gulf (Table 2), is mostly connected to the physical weathering of Si-poor rocks, such as the basaltic and basalt-andesitic formations dominating the Cenozoic volcanism in the central part of Patagonia (Petschick et al., 1996; Corbella and Lara, 2008). Moreover, the smectite transported onto the Patagonian Shelf seems to be derived at selected locations from large morainic and glacio-fluvial Quaternary deposits (Marinoni et al., 1997). It should be noted that in the vicinity of the Gulf of San Jorge Basin, sedimentary and pyroclastic rocks represent potential sources of smectite (e.g., Las Flores Fm.; Raigemborn et al., 2009; Bajo Grande Fm; Dominguez et al., 2008). Furthermore, because of the high proportions of smectite from the “Bajo de Sarmiento” (07NS1 and 08NS2) and the Deseado River (05PDN) samples, as well as its scattered proportions in the GSJ shore samples, the clay-mineral assemblages of riverine and terrestrial samples point to riverine and aeolian transport as the main suppliers of smectite to the gulf (Figures 14a and b).

The contrast between low to moderate proportions of illite and chlorite in the GSJ and higher contents in the shelf samples shows the influence of the continental shelf inputs for these clay minerals in the gulf. The illite and chlorite are derived from Patagonian batholiths and low-grade metamorphic rocks located in Antarctica as well as in Patagonia (Petschick et al., 1996; Diekmann et al., 2000). The chlorite and illite are both transported from southern South America and the Drake Passage along the Argentinean continental shelf (Petschick et al., 1996). Once sediments are on the shelf, their redistribution and transport are controlled by the northward circulation (Palma et al., 2008). The inputs of illite and chlorite to the GSJ by the Patagonian Current flowing northward through the continental shelf from southern South America is also supported by the enrichment in I+C in the eastern and southern parts of the gulf (Figure 14c).

In addition, the concentration of kaolinite in the gulf is very low despite the numerous outcrops of rhyolites and ignimbrites in eastern Patagonia, known as potential sources of residual kaolin deposits (Dominguez et al., 2008), and despite the significant amount of kaolinite in the Las Flores Fm., which overlies tablelands in some sectors of the San Jorge Gulf Basin (Raigemborn et al., 2009). This near absence of kaolinite may be due to dilution with much higher contents of smectite, illite and chlorite.

The major and minor element composition of surface sediments seems well correlated to the mineralogical properties in the GSJ. The PC-1 scores derived from elemental geochemistry signatures shows patterns of distribution similar to those noticed in the elemental balance of major mineral groups in the gulf. The large positive PC-1 scores are associated with Fe, Mg and V in areas enriched in clays, and conversely, negative PC-1 scores are associated with Ca, Si, Sr, Zr, Mn, Al, K and P in areas enriched in quartz and feldspar (Figures 13d and 12a). Furthermore, numerous major elements reveal good correlations with various minerals identified in the gulf. For example, the major components Si, Fe and Ca are linked to the presence of quartz ($r^2 = 0.61$; Figure 19a), the sum of Fe-bearing minerals (notably, pyrite, magnetite, hematite, goethite, and maghemite) and clays ($r^2 = 0.66$; Figure 19d) and plagioclase ($r^2 = 0.77$, Figure 19b), respectively. The relation between mineralogy and major element composition supports and strengthens the use of quantitative X-ray diffraction to determine the mineralogy of sediment samples, as well as the use of SedUnMix to estimate the proportions of potential sources for the composition of surface sediments in the GSJ. Furthermore, the absence of clear differences in the geochemical classification between particles from suspended sediments from the water column and surface sediments from the same site reveals that most of the material carried towards the surface water of the gulf settle on the bottom of the GSJ (Figure 13c).

1.8 SUMMARY AND CONCLUSIONS

The investigation of grain size, bulk and clay mineralogy, and the geochemistry of surficial sediments from the GSJ was used to highlight the nature and spatial variability of surface sediments. The results reveal and allow the quantification of the numerous factors, as continental volcanism, local coastal inputs (i.e., erosion and runoff), dust and aeolian transport, hydrodynamic conditions and the northward-flowing Patagonian Current, impacting the sedimentation in the GSJ. According to our interpretation, coupled with non-linear mixing models (SedUnMix) of bulk mineralogy, we suggest that the origin of sediments in the GSJ is 50% from external/oceanic inputs, 40% from the inner gulf shores and 10% from dust (i.e., aeolian transport). In the central part of the GSJ, a region associated with a lower-energy depositional environment enriched in clays (Figure 15), the contributions of external/oceanic and dust inputs increase to 60% and 15%, respectively, whereas inner gulf shore inputs decrease to 25%. The marine park area in the northeastern part of the GSJ constitutes an erosive environment linked to high proportions of quartz, plagioclase and smectite (Figure 15) with a large contribution of the inner gulf shores (70%) to sediment composition. Furthermore, the southeastern part of the gulf can also be considered as a distinct sedimentary region enriched in quartz, illite and chlorite minerals and highly influenced by external/oceanic inputs related to the northward-flowing continental shelf current (85%; Figure 15). Finally, in the absence of current major fluvial inputs, these results highlight the combined contribution of various sediment sources and transport mechanisms that must be taken into account when investigating the recent and past sediment distribution and its interactions with biogeochemical processes in the GSJ, but also keeping in mind that fluvial inputs were significative (Kokot, 2004) during past glaciations and deglaciations following sea-level changes and glacial meltwater pulses, thus adding other possible sediment sources in the sedimentary budget during these periods.

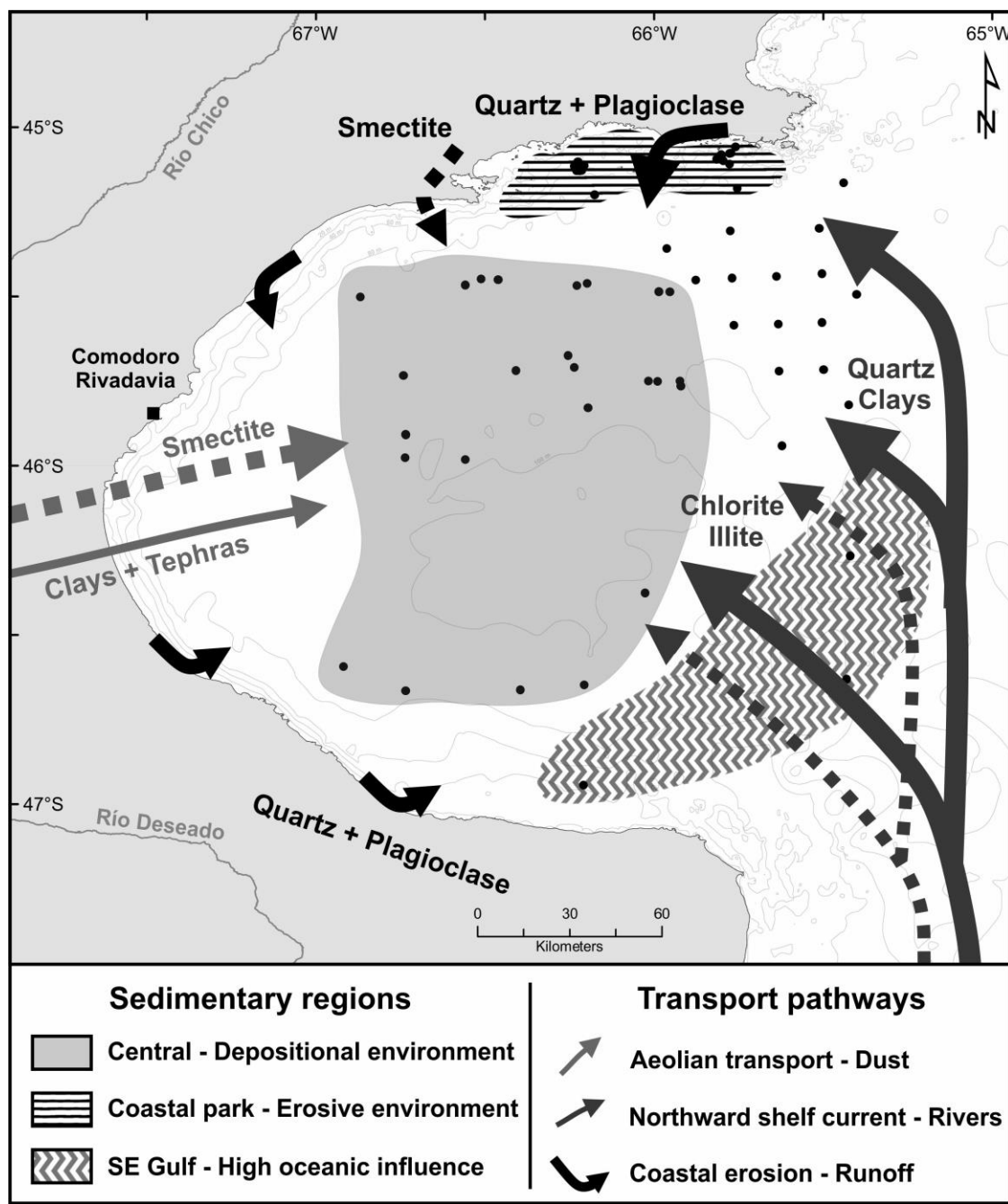


Figure 15: Schematic map of the main sedimentary regions and transport pathways identified in the Gulf of San Jorge area. The sedimentary regions were determined according to our interpretations and previous results from Fernández et al. (2003). The bulk terrigenous inputs are illustrated with filled arrows, whereas the terrigenous clay inputs are depicted with dotted arrows. Note that the spatial distribution of the samples does not follow a regular and homogenous pattern, leading to potentially underrepresented areas

1.9 ACKNOWLEDGMENTS

The authors would like to sincerely thank the captain, crew and scientific participants of the COR1404 (MARES and MARGES) expedition on board the R/V Coriolis II. Financial support for MARES and MARGES expeditions was provided by the *Ministerio de Ciencia, Tecnología e Innovación Productiva* (MINCyT), *Provincia de Chubut* and *Consejo Nacional de Investigaciones Científicas y Técnicas* (CONICET). This research was funded by the Natural Sciences and Engineering Research Council of Canada (NSERC) through Discovery grants to G. St-Onge and J.-C. Montero-Serrano and by the Fond de recherche du Québec – Nature et Technologies (FRQNT) through a team grant to G. St-Onge, J.-C. Montero-Serrano and A. Rochon. We also acknowledge the financial support of the Canadian Foundation for Innovation (CFI) and Economic Development Canada for the acquisitions of the PANalytical X-ray diffractometer (X’Pert Powder) and X-ray fluorescence (Epsilon 3-XL), respectively. We are thankful to Claude Belzile and Quentin Beauvais (UQAR-ISMER) for SEM images acquisition and technical support. Finally, we are grateful to the reviewers John T. Andrews and Federico Spagnoli for their constructive reviews.

1.10 REFERENCES

- Andrews, J., Kristjánsdóttir, G., Eberl, D., Jennings, A., 2013. A quantitative x-ray diffraction inventory of volcaniclastic inputs into the marine sediment archives off Iceland: a contribution to the Volcanoes in the Arctic System programme. *Polar Res.* 32, 11130.
- Andrews, J.T., Vogt, C., 2014. Source to sink: statistical identification of regional variations in the mineralogy of surface sediments in the western Nordic Seas (58 N–75 N; 10 W–40 W). *Mar. Geol.* 357, 151–162.
- Bertrand, S., Hughen, K.A., Sepulveda, J., Pantoja, S., 2012. Geochemistry of surface sediments from the fjords of Northern Chilean Patagonia (44–47 S): Spatial variability and implications for paleoclimate reconstructions. *Geochim. Cosmochim. Acta* 76, 125–146.
- Corbella, H., Lara, L.E., 2008. Late cenozoic quaternary volcanism in Patagonia and Tierra del Fuego. *Dev. Quat. Sci.* 11, 95–119.
- Coronato, A.M.J., Coronato, F., Mazzoni, E., Vázquez, M., 2008. The physical geography of Patagonia and Tierra del Fuego. *Dev. Quat. Sci.* 11, 13–55.
- Crespi-Abril, A.C., Montes, A.M.I., Williams, G.N., Carrasco, M.F., 2016. Uso de sensores remotos para la detección de eventos de transporte eólico de sedimentos hacia ambientes marinos en Patagonia. *Meteorologica* 41, 33–47.
- Crespi-Abril, A.C., Soria, G., De Cian, A., López-Moreno, C., 2018. Roaring forties: An analysis of a decadal series of data of dust in Northern Patagonia. *Atmos. Environ.* 177, 111–119.
- Cuitiño, J.I., Scasso, R.A., Ventura Santos, R., Mancini, L.H., 2015. Sr ages for the Chenque Formation in the Comodoro Rivadavia region (Golfo San Jorge Basin, Argentina): Stratigraphic implications. *Lat. Am. J. Sedimentol. basin Anal.* 22, 13–28.
- de Mahiques, M.M., Tassinari, C.C.G., Marcolini, S., Violante, R.A., Figueira, R.C.L., da Silveira, I.C.A., Burone, L., e Sousa, S.H. de M., 2008. Nd and Pb isotope signatures on the Southeastern South American upper margin: Implications for sediment transport and source rocks. *Mar. Geol.* 250, 51–63.
- Diekmann, B., Kuhn, G., Rachold, V., Abelmann, A., Brathauer, U., Fütterer, D.K., Gersonde, R., Grobe, H., 2000. Terrigenous sediment supply in the Scotia Sea (Southern Ocean): response to Late Quaternary ice dynamics in Patagonia and on the Antarctic Peninsula. *Palaeogeogr. Palaeoclimatol. Palaeoecol.* 162, 357–387.
- Dominguez, E., Iglesias, C., Dondi, M., 2008. The geology and mineralogy of a range of kaolins from the Santa Cruz and Chubut Provinces, Patagonia (Argentina). *Appl. Clay Sci.* 40, 124–142.
- Eberl, D.D., 2003. User guide to RockJock-A program for determining quantitative mineralogy from X-ray diffraction data. US Geological Survey. Open-File Rep. 03-78.

- Fernández, M., Carreto, J.I., Mora, J., Roux, A., 2005. Physico-chemical characterization of the benthic environment of the Golfo San Jorge, Argentina. *J. Mar. Biol. Assoc. United Kingdom* 85, 1317–1328.
- Fernández, M., Roux, A., Fernández, E., Caló, J., Marcos, A., Aldacur, H., 2003. Grain-size analysis of surficial sediments from Golfo San Jorge, Argentina. *J. Mar. Biol. Assoc. UK* 83, 1193–1197.
- Gaiero, D.M., Brunet, F., Probst, J.-L., Depetris, P.J., 2007. A uniform isotopic and chemical signature of dust exported from Patagonia: Rock sources and occurrence in southern environments. *Chem. Geol.* 238, 107–120.
- Gaiero, D.M., Depetris, P.J., Probst, J.-L., Bidart, S.M., Leleyter, L., 2004. The signature of river-and wind-borne materials exported from Patagonia to the southern latitudes: a view from REEs and implications for paleoclimatic interpretations. *Earth Planet. Sci. Lett.* 219, 357–376.
- Gaiero, D.M., Probst, J.-L., Depetris, P.J., Bidart, S.M., Leleyter, L., 2003. Iron and other transition metals in Patagonian riverborne and windborne materials: geochemical control and transport to the southern South Atlantic Ocean. *Geochim. Cosmochim. Acta* 67, 3603–3623.
- Gamboa, A., Montero-Serrano, J., St-Onge, G., Rochon, A., Desiage, P., 2017. Mineralogical, geochemical, and magnetic signatures of surface sediments from the Canadian Beaufort Shelf and Amundsen Gulf (Canadian Arctic). *Geochemistry, Geophys. Geosystems* 18, 488–512.
- Gut, B., 2008. Geology, climate and soils of Patagonia. In: *Trees in Patagonia*. Springer Science & Business Media.
- Herron, M.M., 1988. Geochemical classification of terrigenous sands and shales from core or log data. *J. Sediment. Res.* 58.
- Isla, F.I., Iantanás, N., Estrada, E., 2002. Playas reflectivas y disipativas macromareales del Golfo San Jorge, Chubut. *Rev. la Asoc. Argentina Sedimentol.* 9, 155–164.
- Kilian, R., Lamy, F., 2012. A review of Glacial and Holocene paleoclimate records from southernmost Patagonia (49–55 S). *Quat. Sci. Rev.* 53, 1–23.
- Kokot, R.R., 2004. Erosión en la costa patagónica por cambio climático. *Rev. la Asoc. Geológica Argentina* 59, 715–726.
- Marinoni, L., Setti, M., Soggetti, F., 1997. Mineralogy of sea-bottom sediments from the Strait of Magellan. *Boll. di Geofis. Teor. ed Appl.* 38, 281–292.
- Martínez, O.A., Kutschker, A., 2011. The ‘Rodados Patagónicos’ (Patagonian shingle formation) of eastern Patagonia: environmental conditions of gravel sedimentation. *Biol. J. Linn. Soc.* 103, 336–345.
- Montes, A., Rodríguez, S., San Martín, C., Allard, J., 2015. Migración de campos de dunas en cañadones costeros de Patagonia. Geomorfología e implicaciones paleoclimáticas. *Rev. Soc. Geol. España* 28, 65–76.
- Montes, A., Rodríguez, S.S., Domínguez, C.E., 2017. Geomorphology context and characterization of dunefields developed by the southern westerlies at drying Colhué Huapi shallow lake, Patagonia Argentina. *Aeolian Res.* 28, 58–70.

- Nagai, R.H., Ferreira, P.A.L., Mulkherjee, S., Martins, M. V, Figueira, R.C.L., Sousa, S.H.M., Mahiques, M.M., 2014. Hydrodynamic controls on the distribution of surface sediments from the southeast South American continental shelf between 23 S and 38 S. *Cont. Shelf Res.* 89, 51–60.
- Palma, E.D., Matano, R.P., Piola, A.R., 2008. A numerical study of the Southwestern Atlantic Shelf circulation: Stratified ocean response to local and offshore forcing. *J. Geophys. Res. Ocean.* 113.
- Pankhurst, R.J., Leat, P.T., Sruoga, P., Rapela, C.W., Márquez, M., Storey, B.C., Riley, T.R., 1998. The Chon Aike province of Patagonia and related rocks in West Antarctica: A silicic large igneous province. *J. Volcanol. Geotherm. Res.* 81, 113–136.
- Petschick, R., Kuhn, G., Gingele, F., 1996. Clay mineral distribution in surface sediments of the South Atlantic: sources, transport, and relation to oceanography. *Mar. Geol.* 130, 203–229.
- Pierce, J.W., Siegel, F.R., 1979. Suspended particulate matter on the southern Argentine shelf. *Mar. Geol.* 29, 73–91.
- Potter, P.E., 1994. Modern sands of South America: composition, provenance and global significance. *Geol. Rundschau* 83, 212–232.
- Preda, M., Cox, M.E., 2005. Chemical and mineralogical composition of marine sediments, and relation to their source and transport, Gulf of Carpentaria, Northern Australia. *J. Mar. Syst.* 53, 169–186.
- Prospero, J.M., Ginoux, P., Torres, O., Nicholson, S.E., Gill, T.E., 2002. Environmental characterization of global sources of atmospheric soil dust identified with the Nimbus 7 Total Ozone Mapping Spectrometer (TOMS) absorbing aerosol product. *Rev. Geophys.* 40, 2–31.
- Raigemborn, M., Brea, M., Zucol, A., Matheos, S., 2009. Early Paleogene climate at mid latitude in South America: Mineralogical and paleobotanical proxies from continental sequences in Golfo San Jorge basin (Patagonia, Argentina). *Geol. Acta an Int. earth Sci. J.* 7, 125–145.
- Saukel, C., Stein, R., Vogt, C., Shevchenko, V.P., 2010. Clay-mineral and grain-size distributions in surface sediments of the White Sea (Arctic Ocean): indicators of sediment sources and transport processes. *Geo-Marine Lett.* 30, 605–616.
- Spagnoli, F., Bartholini, G., Dinelli, E., Giordano, P., 2008. Geochemistry and particle size of surface sediments of Gulf of Manfredonia (Southern Adriatic sea). *Estuar. Coast. Shelf Sci.* 80, 21–30.
- Sylwan, C.A., 2001. Geology of the Golfo San Jorge Basin, Argentina. *Geología de la Cuenca del Golfo San Jorge, Argentina. J. Iber. Geol.* 27, 123–158.
- Violante, R.A., Paterlini, C.M., Marcolini, S.I., Costa, I.P., Cavallotto, J.L., Laprida, C., Dragani, W., Chapor, N.G., Watanabe, S., Totah, V., 2014. The Argentine continental shelf: morphology, sediments, processes and evolution since the Last Glacial Maximum. *Geol. Soc. London, Mem.* 41, 55–68.

1.11 SUPPLEMENTARY MATERIAL (METHODS)

Prior to the grain size, bulk mineralogical and geochemical analysis, samples (< 2 mm) were pretreated with 10 ml of hydrogen peroxide (H_2O_2 ; 30%) and 10 ml of hydrochloric acid (HCl; 0.5 N) for at least 72h to remove organic matter and carbonates sediments. Next, an aliquot of this sediment sample was ground using a micronizing mill (McCrone) and 5 ml of ethanol for approximatively 10 min until a homogenous mixture of grain < 10 μm was obtained. The mixture was oven-dried at 60 °C and ground again in an agate mortar to prevent aggregations of fine particles due to drying. Aliquots of these homogenized sediment samples were used for bulk mineralogical and geochemical analysis.

The observations of tephra using a JEOL 6460LV SEM were performed on the 300-63 μm and < 63 μm fractions of the BV01, BV06 and BC11 samples. Before sieving, the samples were pretreated with 10 ml of hydrogen peroxide (H_2O_2 ; 30%) for 24h and rinsed with distilled water at least 5 times. Finally, the samples were oven-dried at 60 °C.

1.11.1 Grain-size analysis

The grain size analysis of sediment samples was carried out on detrital fraction using a Beckman Coulter Particle Size Analyser LS 13 320 (0.04-2000 μm). Deflocculation was performed by successive washing with distilled water and the samples were mechanically shake for 12h before measurement. Grain size distribution and statistical parameters were processed with the GRADISTAT software using the geometric (μm) and logarithmic (ϕ) method of moments (Blott and Pye, 2001). The end-member modelling algorithm (EMMA; Dietze et al. 2012) was applied to the grain-size data. The EMMA algorithm is used to unmixed the original grain-size distribution (Figure 10b) in order to extract meaningful EM grain-size distributions and thus to estimate the processes (transport conditions) related to the EM grain-size distributions (Dietze et al., 2012). The characteristics and detailed procedures of the EMMA method used for this study are presented in Dietze et al. (2012) and Dietze and Dietze (2013).

1.11.2 Source samples

In order to quantify potential sources of sediment in the GSJ, 13 terrestrial and riverine samples were retrieved in August 2016 (Figures 9a and b); 9 of them were collected on the shore of the GSJ (topsoil and beach sediments), 2 at the mouths of the Chubut and Deseado Rivers (river bank and beach sediments, respectively) and 2 in the “Bajo de Sarmiento” area (topsoil sediments from dry bed of lake Colhué Huapí (NS1) and 10 km to the east of the lake, close to dune fields formed by the southern westerlies (NS2; Montes et al., 2017). A marine surface sediment sample (0-2 cm sediment depth) from the Magellan Strait was also analyzed. The latter was recovered with a CASQ gravity corer (MD07-3131) during the MD 159 PACHIDERME expedition on board R/V Marion Dufresne II (Figure 9a; February 2007).

1.11.3 Bulk mineral analysis

The random powder samples were side-loaded into the holders and analysed by X-ray diffraction (XRD) using a PANalytical X’Pert Powder diffractometer. The samples were measured between 5° and 65° 2θ in steps of 0.02° and a counting time of 2 seconds per step. Bulk mineral associations were analysed following the quantitative method developed by Eberl (2003) and Eberl and Smith (2009) and used in other Late Quaternary marine studies that deal with sediment mineralogy (e.g., Andrews et al., 2015, 2016; Andrews and Vogt 2014). For the quantification of the major mineralogical components, the XRD scans were converted into mineral weight percentages (wt.%) using the standardless option of the Excel macro-program Rockjock v11 (Eberl, 2003; Eberl and Smith, 2009). This program uses a full-pattern fitting method that permits the quantification of the whole-sediment mineralogy with an error of approximatively ±3 wt% at 50 wt% of a mineral (Eberl, 2003). To verify the quality of this fitting procedure, a degree-of-fit (DOF = minimum absolute difference) statistic was calculated between the measured and simulated XRD patterns. The DOF values obtained with our samples were satisfying. They were within a range of 0.072 to 0.442 with an average of 0.165 for the 95 samples. Polytypes of illite, smectite, plagioclase feldspars,

and K-feldspars are reported as a total amount (e.g., Andrews and Vogt, 2014; Andrews et al., 2015, 2016). This qXRD method arrived 2nd in the international “Reynolds Cup” quantitative mineral analysis competition (Omotoso et al., 2006). The calculated total mineral wt% was normalized to sum to 100%. We present the wt % data for 12 minerals (Table 2), but we focus on 11 minerals and exclude carbonates and biotite because of their restricted occurrence (Table 5).

Likewise, we used the non-linear unmixing Excel macro program SedUnMixMC (Andrews and Eberl 2012; Andrews et al., 2015, 2016) to gain a quantitative understanding of the surface changes in sediment provenance. We ran SedUnMixMC on the normalized (100%) data for the 11 key minerals (Table 5) that represented more than 99% of the overall mineral concentration in the sediment samples. SedUnMixMC allows up to six sources to be examined as potential contributors to sediment composition. Based on surface geology (e.g., Pankhurst and Rapela, 1995; Pankhurst et al., 1998; see 1.4.1) and sediment transport pathways (e.g., Matano et al., 2010; Montes et al., 2017; see 1.4.1 and 1.4.2), we suggest that the surface sediment compositions in the GSJ are potentially the mixing product of five source areas: (S1) Marine park sector (i.e., Rhyolitic rocks outcrop), (S2) Others coastal area of GSJ (i.e., Cliffs and beaches of Eocene-Miocene sedimentary rocks and/or Quaternary fluvio-glacial deposits), (S3) Rivers (i.e., Chubut and Deseado, as well as Strait of Magellan), (S4) Dust from continental Patagonia (i.e., “Bajo de Sarmiento” area), and (S5) Continental shelf (i.e., Southern South America influence and northward shelf Patagonian Current). Under this context, SedUnMix was run using 5 sources and each source is represented by 2 to 5 of the source area samples (Table 5). The samples were attributed to potential source according to their location coupled with geological and environmental context, and also with the results from the mineralogical analysis (Figure 11).

1.11.4 Clay mineral analysis

In this paper, clay minerals were quantified in the bulk sediment fraction (< 2 mm) using the Excel macro program RockJock. However, nearly all previous clay-mineral

provenance studies in the Argentinean continental shelf used oriented mounts of the <2 µm sediment fraction to identify and semi-quantify the clay-mineral abundance, notably illite, kaolinite, chlorite, and smectite (e.g., Petschick et al. 1996; Diekmann et al., 2000; Dominguez et al., 2008). Therefore, in this study, the clay-size fraction of all sediment samples was isolated and analyzed in this manner for comparison. Clay mineral associations were studied using XRD following established protocols (Bout-Roumazeilles et al., 1999). The clay-sized fraction (< 2µm) was isolated by settling according to Stoke's Law, concentrated by centrifugation and oriented on glass slides. For each samples, analyses were performed on three subsamples under different conditions: (1) untreated sample (normal run); (2) ethylene-glycol saturation applied for 12 h (glycol run); and (3) sample heated at 490 °C during 2 h (heating run). The analyses were measured on a PANalytical X'Pert Powder diffractometer, between 2.49° and 32.49° 2θ for the normal and glycol runs and between 2.49° and 14.5° 2θ for the heating run, with steps of 0.02° and a counting time of 3 seconds per step for all the runs. Semi-quantitative estimation of clay mineral abundances (smectite, illite, chlorite, kaolinite, and illite/smectite mixed layer) based on peak areas was performed using the MacDiff® 4.2.5 software (Petschick, 2000). The error on the reproducibility of measurements is estimated to be 5% for each clay mineral, as verified with analyses on replicate samples. Note that the comparison of both RockJock and oriented mounted methods yielded similar results within analytical uncertainty (Figure 20). This highlights the robustness of the qXRD method used in our study.

1.11.5 Bulk elemental geochemistry

Concentrations of 14 major and minor elements (Al_2O_3 , SiO_2 , K_2O , MgO , CaO , TiO_2 , MnO , Fe_2O_3 , P_2O_5 , Sr , V , Cr , Zn , and Zr) were measured by energy dispersive X-ray fluorescence spectrometry (EDXRF) using a PANalytical Epsilon 3-XL. Before EDXRF analysis, loss on ignition (LOI) was determined gravimetrically by heating the dried samples up to 950°C for two hours. Subsequently, the glass disks were made by melting ~ 0.6 g of samples with a mixture of lithium tetraborate and metaborate (49.75% $\text{Li}_2\text{B}_4\text{O}_7$, 49.75% LiBO_2 , and 0.5% LiBr , CLAISSE) in an automated fusion furnace (CLAISS M4 Fluxer)

prior to be analysed with the spectrometer. Acquired XRF spectra were processed with the standardless Omnia software package (PANalytical). Analytical accuracy, based on both an international standard (USGS SDC-1) as well as analysis of replicate samples, was about 1-5% for major elements and 5-10% for the other elements.

Likewise, the elemental composition analysis of filters and tephras was performed using an INCA X-sight energy dispersive X-ray spectrometer (Oxford Instruments) coupled to a JEOL 6460LV scanning electron microscope. X-ray spectra were measured from 15 randomly chosen particles for filters and 10 glass shard fragments for tephras, with two or three spectra per particle. Each spectrum was acquired for 60 (filters) and 120 (tephras) seconds of live time at an accelerating voltage of 20 kV. System quantitative optimization was made using copper as standard.

The relative proportions of the three most abundant detrital elements (Si, Al and Fe) of the GSJ samples are presented in the form of a ternary diagram with respective mean grain sizes using the phi-scale to determine the influence of grain size on major element composition. In addition, the ternary plot Fe-K-Ca was used here to understand the influence and contribution of the different sedimentary sources of Patagonia on the elemental geochemistry of sediments in the GSJ (see 1.6.2 in the main text). In this diagram the GSJ samples (excluding marine park sites) are illustrated according to their locations in the gulf.

1.11.6 Statistical approach

The mineralogical and geochemical data are of a compositional nature, that is, they are vectors of non-negative values subjected to a constant-sum constraint (usually 100%). This implies that relevant information is contained in the relative magnitudes, so statistical analysis must focus on the ratios between components (Aitchison, 1986). Under this framework, the discriminant scatter plots based on mineralogical and geochemical data were represented here as log-ratios. Note that a log-transformation will reduce the very high values and spread out the small data values and is therefore well suited for right-skewed distributions (van den Boogaart and Tolosana-Delgado, 2013). Thus, compared to the raw data, the log-

ratio scatter plots exhibit better sediment discrimination. Likewise, in order to visualize the main tendencies of mineralogical enrichment in the gulf, the spatial distribution of the major mineral groups were represented as mineralogical balances (i.e., $b_{\{(Quartz+Feldspars)/Clays\}}$). Note that mineralogical balances are log-contrasts resulting from a log-ratio of two geometric means of two non-overlapping mineralogical groups (Egozcue and Pawlowsky-Glahn, 2005). Furthermore, a principal component analysis (PCA) was performed on the elemental geochemical data set in order to highlight elemental associations with similar relative variation patterns that may be interpreted from an environmental standpoint (e.g., Montero-Serrano et al., 2010). Prior to all multivariate analyses, a log-centred (clr) transform was applied to the data (Aitchison, 1990). The clr transform is derived by dividing each variable (e.g., mineral percentage, element concentrations) by the geometric mean of the composition of the individual observations and then taking the logarithm. This operation removes statistical constraints on compositional variables, such as the constant-unit sum, and allows the valid application of classical (Euclidean) statistical methods to compositional data (Aitchison, 1990; Montero-Serrano et al., 2010). Statistical calculations were conducted with CoDaPack v2.02.04 (Thió-Henestrosa and Martín-Fernández, 2005) and “R” software using the packages “compositions” (van den Boogaart and Tolosana-Delgado, 2008) and “vegan” (Oksanen et al., 2016). Finally, the spatial interpolation of the results from bulk and clay mineralogy, and elemental geochemistry were generated using inverse distance weighting (IDW) algorithm available in ArcGIS® Spatial Analyst Tools.

1.12 SUPPLEMENTARY MATERIAL (REFERENCES)

- Aitchison, J., 1986. The statistical analysis of compositional data. Chapman and hall, London.
- Aitchison, J., 1990. Relative variation diagrams for describing patterns of compositional variability. *Math. Geol.* 22, 487–511.
- Andrews, J.T., Bjork, A.A., Eberl, D.D., Jennings, A.E., Verplanck, E.P., 2015. Significant differences in late Quaternary bedrock erosion and transport: East versus West Greenland~ 70° N—evidence from the mineralogy of offshore glacial marine sediments. *J. Quat. Sci.* 30, 452–463.
- Andrews, J.T., Eberl, D.D., 2012. Determination of sediment provenance by unmixing the mineralogy of source-area sediments: the “SedUnMix” program. *Mar. Geol.* 291, 24–33.
- Andrews, J.T., Stein, R., Moros, M., Perner, K., 2016. Late Quaternary changes in sediment composition on the NE Greenland margin (~ 73° N) with a focus on the fjords and shelf. *Boreas* 45, 381–397.
- Blott, S.J., Pye, K., 2001. GRADISTAT: a grain size distribution and statistics package for the analysis of unconsolidated sediments. *Earth Surf. Process. Landforms* 26, 1237–1248.
- Bout-Roumazeilles, V., Cortijo, E., Labeyrie, L., Debrabant, P., 1999. Clay mineral evidence of nepheloid layer contributions to the Heinrich layers in the northwest Atlantic. *Palaeogeogr. Palaeoclimatol. Palaeoecol.* 146, 211–228.
- Carel, M., Siani, G., Delpech, G., 2011. Tephrostratigraphy of a deep-sea sediment sequence off the south Chilean margin: New insight into the Hudson volcanic activity since the last glacial period. *J. Volcanol. Geotherm. Res.* 208, 99–111.
- Diekmann, B., Kuhn, G., Rachold, V., Abelmann, A., Brathauer, U., Fütterer, D.K., Gersonde, R., Grobe, H., 2000. Terrigenous sediment supply in the Scotia Sea (Southern Ocean): response to Late Quaternary ice dynamics in Patagonia and on the Antarctic Peninsula. *Palaeogeogr. Palaeoclimatol. Palaeoecol.* 162, 357–387.
- Dietze, E., Hartmann, K., Diekmann, B., Ijmker, J., Lehmkuhl, F., Opitz, S., Stauch, G., Wünnemann, B., Borchers, A., 2012. An end-member algorithm for deciphering modern detrital processes from lake sediments of Lake Donggi Cona, NE Tibetan Plateau, China. *Sediment. Geol.* 243–244, 169–180.
- Dietze, E., Wünnemann, B., Hartmann, K., Diekmann, B., Jin, H., Stauch, G., Yang, S., Lehmkuhl, F., 2013. Early to mid-Holocene lake high-stand sediments at Lake Donggi Cona, northeastern Tibetan Plateau, China. *Quat. Res.* 79, 325–336.
- Dominguez, E., Iglesias, C., Dondi, M., 2008. The geology and mineralogy of a range of kaolins from the Santa Cruz and Chubut Provinces, Patagonia (Argentina). *Appl. Clay Sci.* 40, 124–142.
- Eberl, D.D., 2003. User guide to RockJock-A program for determining quantitative mineralogy from X-ray diffraction data. US Geological Survey.

- Eberl, D.D., Smith, D.B., 2009. Mineralogy of soils from two continental-scale transects across the United States and Canada and its relation to soil geochemistry and climate. *Appl. Geochemistry* 24, 1394–1404.
- Egozcue, J.J., Pawlowsky-Glahn, V., 2005. Groups of parts and their balances in compositional data analysis. *Math. Geol.* 37, 795–828.
- Matano, R.P., Palma, E.D., Piola, A.R., 2010. The influence of the Brazil and Malvinas Currents on the southwestern Atlantic shelf circulation. *Ocean Sci.* 6, 983–995.
- Montero-Serrano, J.C., Palarea-Albaladejo, J., Martín-Fernández, J.A., Martínez-Santana, M., Gutiérrez-Martín, J.V., 2010. Sedimentary chemofacies characterization by means of multivariate analysis. *Sediment. Geol.* 228, 218–228.
- Montes, A., Rodríguez, S.S., Domínguez, C.E., 2017. Geomorphology context and characterization of dunefields developed by the southern westerlies at drying Colhué Huapi shallow lake, Patagonia Argentina. *Aeolian Res.* 28, 58–70.
- Oksanen, J., Blanchet, F.G., Kindt, R., Legendre, P., Minchin, P.R., O'Hara, R.B., Simpson, G.L., Solymos, P., Stevens, M.H.H., Wagner, H., 2016. vegan: community ecology package, version 2.4-1. See <https://cran.r-project.org/web/packages/vegan/index.html>.
- Omotoso, O., McCarty, D.K., Hillier, S., Kleeberg, R., 2006. Some successful approaches to quantitative mineral analysis as revealed by the 3rd Reynolds Cup contest. *Clays Clay Miner.* 54, 748–760.
- Pankhurst, R.J., Leat, P.T., Sruoga, P., Rapela, C.W., Márquez, M., Storey, B.C., Riley, T.R., 1998. The Chon Aike province of Patagonia and related rocks in West Antarctica: A silicic large igneous province. *J. Volcanol. Geotherm. Res.* 81, 113–136.
- Pankhurst, R.J., Rapela, C.R., 1995. Production of Jurassic rhyolite by anatexis of the lower crust of Patagonia. *Earth Planet. Sci. Lett.* 134, 23–36.
- Petschick, R., 2000. MacDiff 4.2. 5 Manual. Inst. für Geol. Univ. Erlangen Ger.
- Ruggieri, F., Fernandez-Turiel, J.L., Saavedra, J., Gimeno, D., Polanco, E., Amigo, A., Galindo, G., Caselli, A., 2012. Contribution of volcanic ashes to the regional geochemical balance: The 2008 eruption of Chaitén volcano, Southern Chile. *Sci. Total Environ.* 425, 75–88.
- Thió-Henestrosa, S., Martín-Fernández, J.A., 2005. Dealing with compositional data: the freeware CoDaPack. *Math. Geol.* 37, 773–793.
- van den Boogaart, K.G., Tolosana-Delgado, R., 2008. “Compositions”: a unified R package to analyze compositional data. *Comput. Geosci.* 34, 320–338.
- van den Boogaart, K.G., Tolosana-Delgado, R., 2013. Analyzing compositional data with R. Springer, Heidelberg-New York-Dordrecht-London, 273 pp.
- Watt, S.F.L., Pyle, D.M., Mather, T.A., Martin, R.S., Matthews, N.E., 2009. Fallout and distribution of volcanic ash over Argentina following the May 2008 explosive eruption of Chaitén, Chile. *J. Geophys. Res. Solid Earth* 114.

1.13 SUPPLEMENTARY MATERIAL (FIGURES AND TABLES)

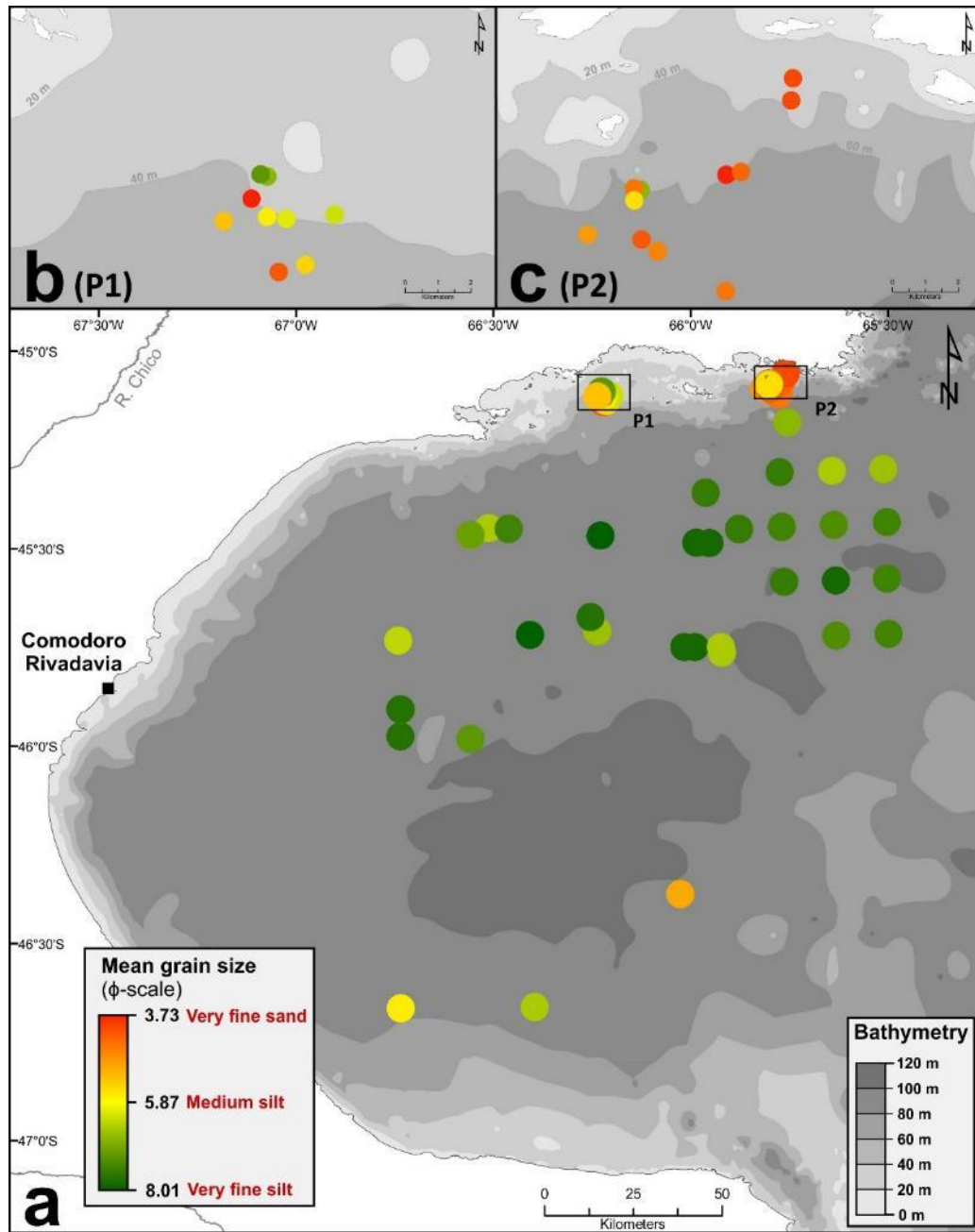


Figure 16: Spatial distribution of the mean grain-size for the surface sediments in the GSJ (a) and marine park areas (b and c)

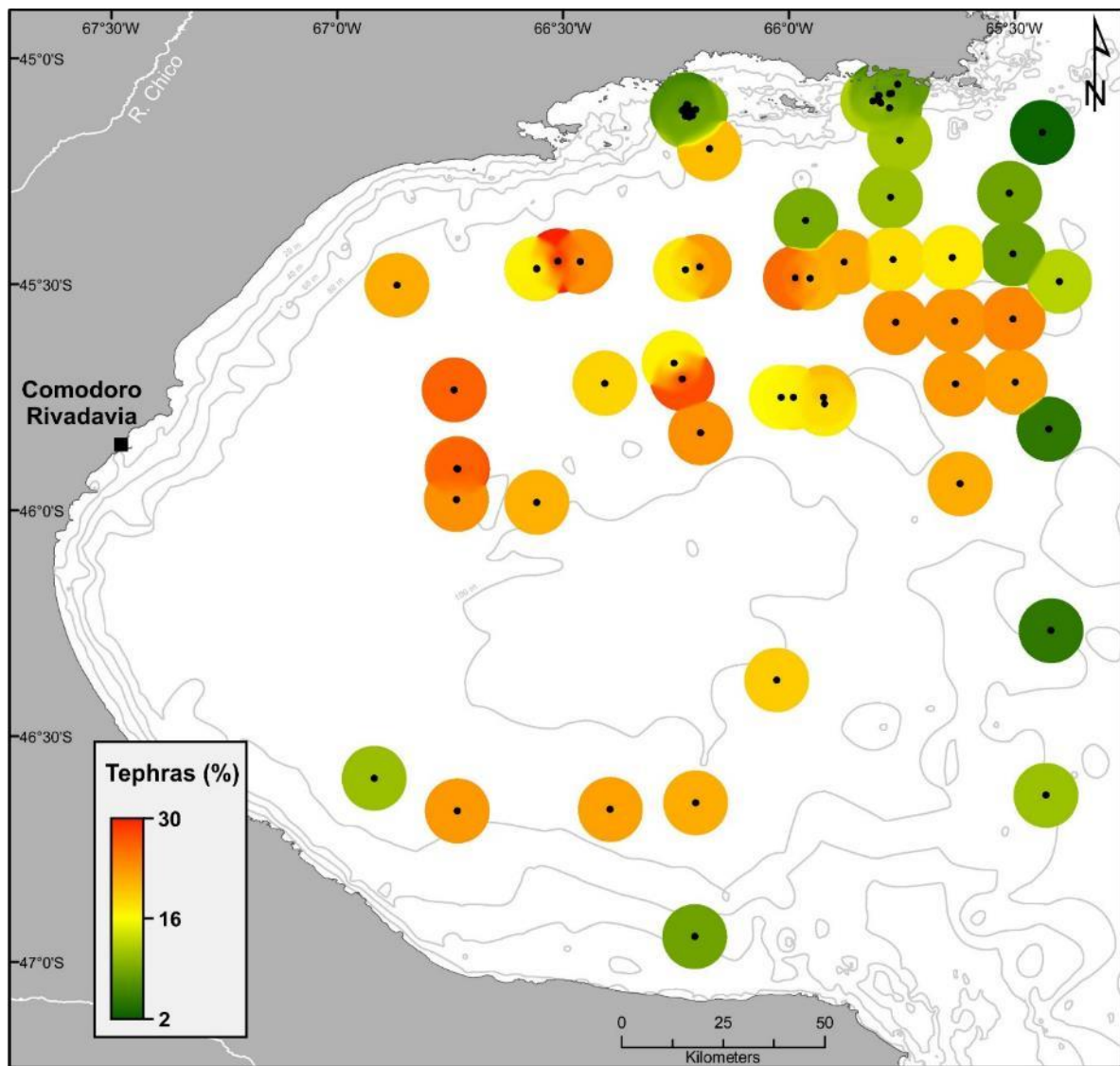


Figure 17: Spatial distribution of tephras (i.e. volcanic rhyolitic tephras) concentration in the GSJ

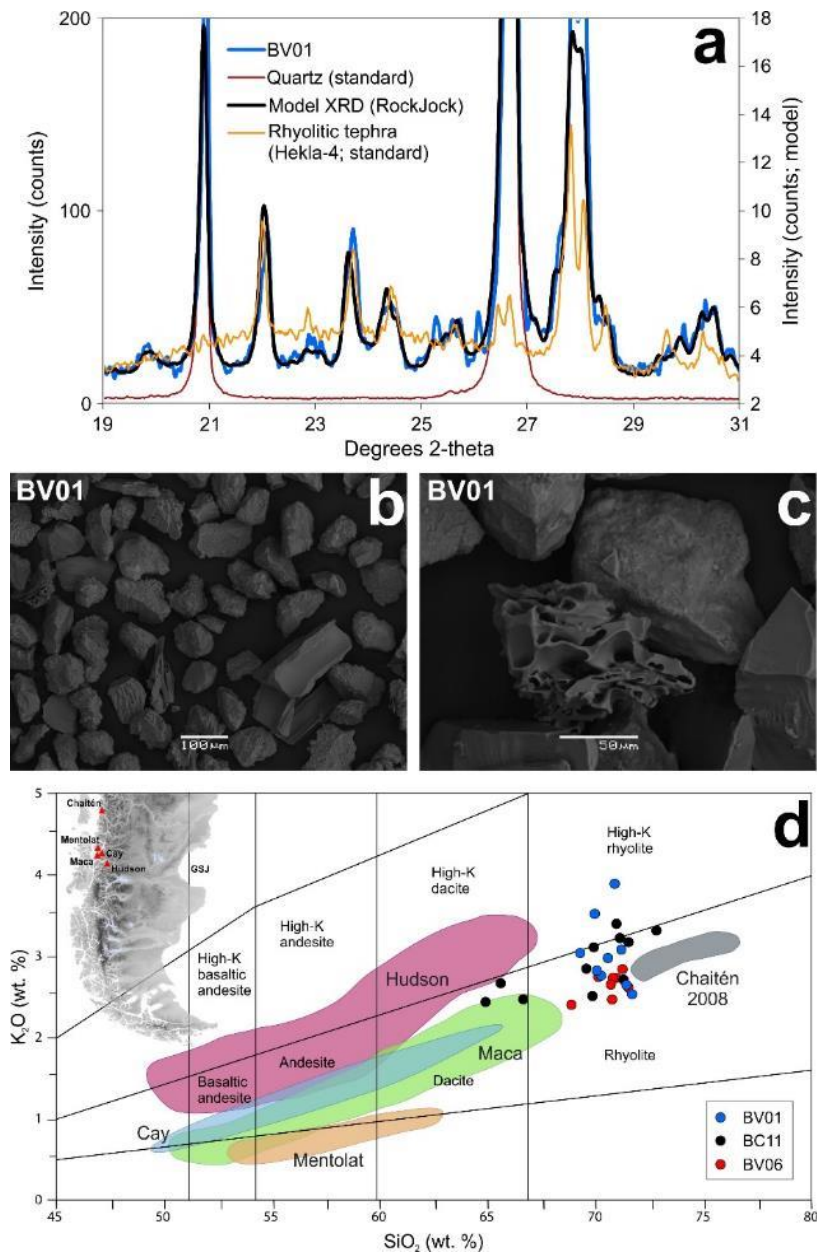


Figure 18: (a) Comparison of measured X-ray diffractogram and calculated best-fit curve obtained from RockJock v11 on a representative sample (BV01). The quartz and rhyolitic tephra (Hekla-4) standard used in the XRD analysis are also show for comparison. (b-c) Scanning Electron Microscopy (SEM) images of the 300-63 fraction of surface sediment sample BV01. (d) K₂O vs. SiO₂ classification diagram for glass shards from BV01, BV06 and BC11 surface samples. The geochemical composition field of different volcanic provinces of the southern part of the SVZ (Carel et al., 2011 and references therein) and ashes from the 2008 Chaitén eruption (Watt et al., 2009; Ruggieri et al., 2012) are presented for comparison

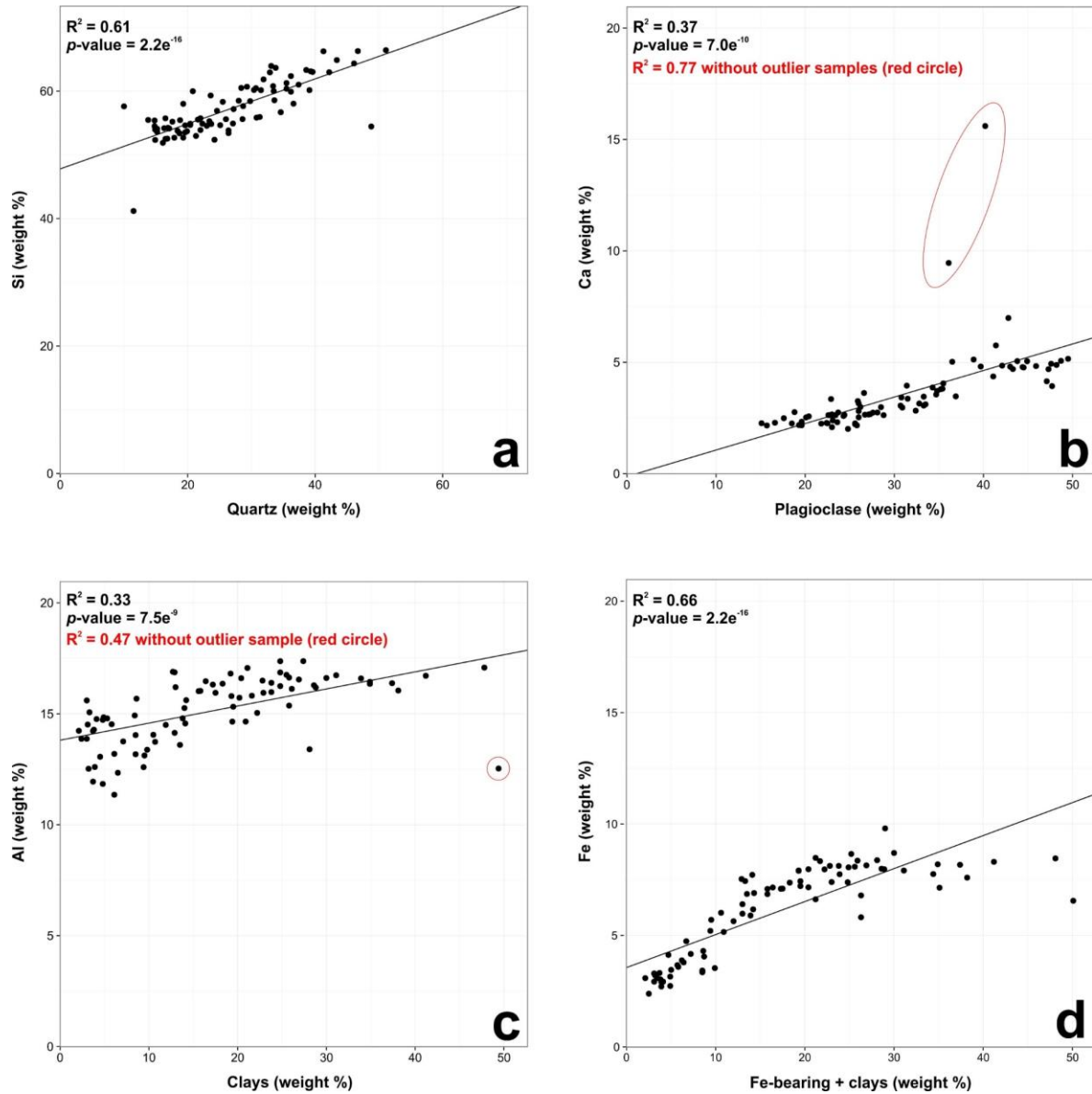


Figure 19: (a) Weight % Si plotted vs. wt% quartz. (b) Weight % Ca plotted vs. wt% plagioclase. (c) Weight % Al plotted vs. wt% clays. (d) Weight % Fe plotted vs. wt% Fe-bearing + chlorite + clays

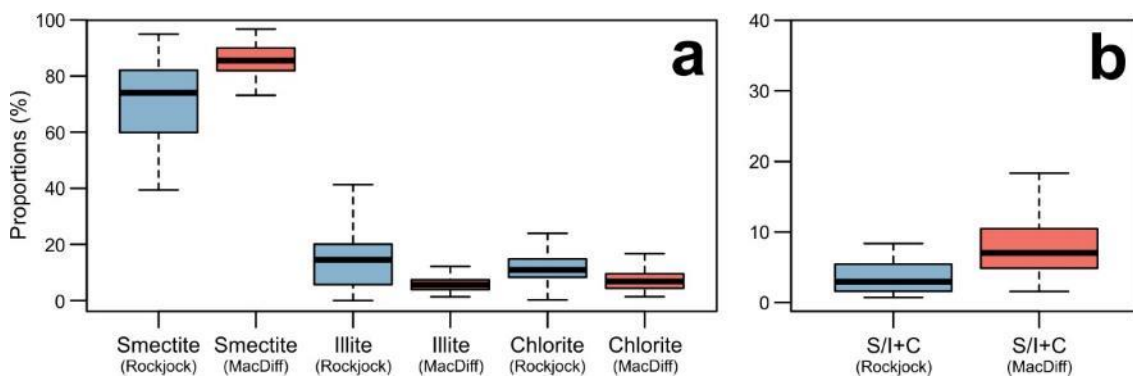


Figure 20: (a) Box plot illustrating the smectite (S), illite (I) and chlorite (C) relative concentration of GSJ sediment samples regarding to the RockJock and oriented mounted methods ($<2\text{ }\mu\text{m}$; MacDiff). (b) Box plot of ratios $\text{S}+\text{I}/\text{C}$ and $\text{S}/\text{I}+\text{C}$ showing the relative clays composition of GSJ sediment samples regarding to the RockJock and oriented mounted methods ($<2\text{ }\mu\text{m}$)

Tableau 1: Mean grain size and End-member (EM) scores for surface sediments of the GSJ

Sample	Lat.	Long.	Water depth (m)	Mean grain size	EM1 (3.04 ϕ)	EM2 (5.59 ϕ)	EM3 (7.34 ϕ)
				(ϕ -scale)	(%)		
<i>Gulf of San Jorge sediments</i>							
BV01	46°22.54'S	66°01.64'W	97	4.98	36.1	63.8	0.1
BV02	46°39.72'S	66°23.738'W	80	6.44	0.1	86.1	13.8
BV03	46°39.90'S	66°44.07'W	84	5.59	19.3	76.5	4.2
BV04	45°58.55'S	66°44.189'W	91	7.63	0.1	0.1	99.8
BV05	45°43.98'S	66°24.48'W	93	6.36	0.1	84.7	15.2
BV06	45°54.49'S	66°44.03'W	90	7.25	0.1	27.1	72.8
BV07	45°42.54'S	66°14.20'W	95	6.58	0.1	77.5	22.4
BV08	45°40.43'S	66°15.29'W	92	7.69	0.1	0.1	99.8
BV09	45°58.92'S	66°33.50'W	95	7.18	0.1	34.5	65.4
BV10	45°26.88'S	66°30.71'W	87	6.45	0.1	83.8	16.1
BV34	45°21.48'S	65°57.76'W	93	7.53	0.1	17.0	82.9
BV35	45°28.04'S	66°13.72'W	87	7.96	7.4	0.1	92.5
BV36	45°44.99'S	65°59.40'W	85	7.80	0.1	0.1	99.8
BV37	45°44.96'S	66°01.02'W	99	7.76	0.1	0.1	99.8
BV38	45°45.84'S	65°55.29'W	99	6.39	0.1	83.8	16.1
BV39	45°10.84'S	65°45.30'W	90	6.69	0.1	69.8	30.1
BV40	45°18.37'S	65°46.45'W	90	7.59	0.1	11.2	88.7
BV41	45°18.14'S	65°38.57'W	91	6.46	0.1	70.7	29.2
BV42	45°17.88'S	65°30.71'W	92	6.62	0.1	62.9	37.0
BV43	45°25.94'S	65°30.23'W	97	7.41	0.1	22.7	77.2
BV44	45°26.43'S	65°38.29'W	96	7.20	0.1	33.3	66.6
BV45	45°26.69'S	65°46.16'W	95	7.35	0.1	32.0	67.9
BV46	45°35.06'S	65°45.82'W	99	7.54	0.1	5.6	94.3
BV47	45°34.84'S	65°37.98'W	98	7.78	0.1	0.1	99.8
BV48	45°34.60'S	65°30.20'W	95	7.36	0.1	22.8	77.1
BV49	45°42.96'S	65°29.95'W	94	7.41	0.1	18.7	81.2
BV50	45°43.20'S	65°37.86'W	94	7.25	0.1	30.6	69.3
BC01	45°54.42'S	66°44.10'W	93	7.71	0.1	0.1	99.8
BC04	45°43.11'S	66°24.47'W	90	8.01	0.1	0.1	99.8
BC06	45°26.99'S	66°27.64'W	91	7.70	0.1	3.0	96.9
BC07	45°27.93'S	66°33.48'W	87	6.57	0.1	78.4	21.5
BC08	45°29.12'S	65°59.15'W	94	7.76	0.1	0.1	99.8
BC09	45°29.16'S	65°57.19'W	90	7.80	7.6	6.7	85.7
BC10	45°27.03'S	65°52.66'W	93	7.56	0.1	1.2	98.7
BC11	45°44.98'S	65°55.41'W	99	6.40	0.1	81.8	18.1
GC07	45°27.92'S	66°33.49'W	87	6.97	0.1	46.4	53.5
PC06	45°26.98'S	66°27.69'W	91	7.41	0.1	16.9	83.0
G1	46°35.61'S	66°55.18'W	88	NA	NA	NA	NA
G4	45°30.09'S	66°52.06'W	90	NA	NA	NA	NA
G5	45°11.95'S	66°10.46'W	73	NA	NA	NA	NA
G6	45°27.66'S	66°11.94'W	90	NA	NA	NA	NA
G7	45°49.68'S	66°11.80'W	100	NA	NA	NA	NA
G9	46°39.04'S	66°12.22'W	102	NA	NA	NA	NA
G10	46°56.63'S	66°12.50'W	39	NA	NA	NA	NA
G12	46°37.80'S	65°25.87'W	86	NA	NA	NA	NA
G13	46°10.03'S	65°25.18'W	89	NA	NA	NA	NA
G14	45°49.19'S	65°25.52'W	85	NA	NA	NA	NA
G15	45°29.56'S	65°24.03'W	99	NA	NA	NA	NA
G16	45°09.90'S	65°25.36'W	86	NA	NA	NA	NA
SF15	45°56.75'S	65°32.75'W	89	NA	NA	NA	NA

Patagonian Austral Interjurisdictional Marine Coastal Park sediments

BV11	45°05.89'S	65°47.75'W	67	4.61	69.3	30.6	0.1
BV12	45°05.62'S	65°48.88'W	71	4.88	36.4	63.5	0.1
BV13	45°06.549'S	65°46.63'W	65	4.38	85.3	14.6	0.1
BV14	45°04.64'S	65°46.62'W	56	3.67	99.8	0.1	0.1
BV15	45°04.60'S	65°46.38'W	50	4.29	87.7	12.2	0.1
BV16	45°03.43'S	65°45.56'W	42	3.99	97.1	2.8	0.1
BV17	45°03.06'S	65°45.53'W	32	3.96	89.1	10.8	0.1
BV18	45°04.88'S	65°48.02'W	71	6.66	0.1	57.7	42.2
BV19	45°05.70'S	65°48.00'W	64	4.17	98.4	1.5	0.1
BV20	45°04.86'S	65°48.13'W	65	4.42	72.8	27.1	0.1
BV21	45°05.05'S	65°48.12'W	70	5.46	29.8	66.0	4.2
BV22	45°07.61'S	66°13.76'W	46	NA	NA	NA	NA
BV23	45°07.71'S	66°13.28'W	49	4.09	99.6	0.3	0.1
BV24	45°07.67'S	66°13.14'W	50	NA	NA	NA	NA
BV25	45°07.59'S	66°12.84'W	52	5.41	38.2	61.7	0.1
BV26	45°06.76'S	66°12.37'W	43	6.15	0.1	88.6	11.3
BV27	45°06.84'S	66°13.16'W	44	6.08	0.1	87.4	12.5
BV28	45°06.80'S	66°13.47'W	45	5.70	16.7	78.7	4.6
BV29	45°06.51'S	66°13.72'W	45	3.73	99.8	0.1	0.1
BV30	45°06.14'S	66°13.47'W	40	6.68	7.6	36.9	55.4
BV31	45°06.19'S	66°13.53'W	36	NA	NA	NA	NA
BV32	45°06.11'S	66°13.58'W	42	7.07	0.1	58.9	41.0
BV33	45°06.87'S	66°14.18'W	46	5.26	41.1	58.8	0.1

Tableau 2: Mineral composition of bulk and clay fraction of sediment samples

Sample	Quartz	Feld.-K.	Plagio.	Pyro.	Amphi.	Fe-b.	Tephra	Diat.	A. sili.	Kaol.	Chlor.	Illite	Bioti.	Smec.	Musc.	Clays	Smec.	Illite	Chlor.	Kaol.	Smec.	Illite		
	Mineral abundance (%)																		Clay mineral composition (%)				Cristalinity*	
<i>Gulf of San Jorge sediments</i>																								
BV01	31.5	4.0	31.5	0.3	0.3	0.1	19.2	0.0	19.2	0.0	2.2	2.5	1.1	5.1	1.9	12.9	77.31	8.43	11.66	2.60	1.28	0.28		
BV02	27.2	2.8	26.0	0.2	0.0	0.1	22.0	1.7	23.7	0.3	4.8	2.7	0.0	8.0	3.6	19.4	69.00	12.15	16.17	2.68	0.94	0.26		
BV03	26.4	2.7	23.6	0.9	0.0	0.1	22.4	1.8	24.2	0.4	4.2	6.8	0.2	5.8	4.1	21.6	77.86	7.95	12.28	1.91	1.56	0.29		
BV04	16.1	3.5	15.1	0.6	0.0	0.0	23.1	3.3	26.3	0.0	3.3	10.0	0.0	21.6	2.5	37.4	77.50	8.94	11.61	1.95	1.03	0.26		
BV05	16.3	3.5	17.6	0.8	0.0	0.0	25.9	4.5	30.5	1.0	2.7	6.6	0.0	14.5	6.3	31.1	87.54	5.12	6.24	1.10	1.07	0.29		
BV06	17.1	4.3	22.4	0.0	0.0	0.1	27.8	5.8	33.6	1.2	4.0	3.0	0.0	6.5	6.5	21.1	78.37	8.30	11.44	1.89	1.07	0.27		
BV07	16.5	3.1	18.5	0.2	0.0	0.0	27.0	5.3	32.3	0.7	3.8	4.2	0.4	13.0	6.4	28.6	85.05	6.02	7.58	1.35	1.11	0.29		
BV08	15.2	2.4	15.7	0.0	0.0	0.0	16.6	8.2	24.8	0.1	3.3	7.1	0.0	24.0	6.6	41.2	83.06	6.72	8.42	1.80	1.03	0.28		
BV09	18.7	4.3	23.1	0.0	0.2	0.1	20.7	6.3	27.1	0.0	2.8	9.1	0.0	10.0	2.9	24.8	83.89	6.10	8.62	1.39	1.17	0.27		
BV10	13.8	3.1	22.8	0.0	0.0	0.1	29.2	6.4	35.6	0.9	2.2	2.7	0.3	13.9	3.9	23.8	84.59	6.44	7.83	1.13	0.98	0.26		
BV34	25.5	3.0	28.1	0.9	0.0	0.3	9.1	12.2	21.3	1.0	1.3	6.8	0.3	9.1	2.4	20.9	85.33	5.99	6.72	1.96	0.98	0.29		
BV35	18.8	4.6	27.1	0.6	0.0	0.0	17.1	12.7	29.8	0.6	1.9	6.6	0.0	7.2	2.0	18.3	83.53	6.81	8.32	1.34	0.96	0.29		
BV36	18.4	3.5	19.6	0.5	0.0	0.0	17.1	12.9	30.0	0.7	3.5	8.6	0.3	10.5	3.3	26.9	78.13	9.04	11.13	1.70	1.03	0.27		
BV37	19.3	3.1	21.8	0.0	0.0	0.1	16.2	9.6	25.8	0.8	3.8	7.0	0.0	11.9	5.3	28.8	82.18	7.08	8.96	1.77	1.14	0.30		
BV38	24.2	6.2	25.6	0.3	0.0	0.0	17.2	5.7	23.0	0.0	2.9	8.0	0.0	2.1	6.3	19.3	73.11	10.31	14.08	2.49	1.12	0.29		
BV39	28.7	7.1	35.2	0.3	0.0	0.1	11.4	5.2	16.5	0.2	1.0	1.3	0.0	7.7	1.7	11.9	89.18	3.85	5.37	1.61	1.02	0.28		
BV40	29.8	6.0	36.9	0.8	0.4	0.1	10.8	4.1	14.9	0.0	0.9	2.0	0.0	7.3	0.2	10.5	89.95	3.29	5.60	1.16	1.33	0.26		
BV41	21.6	3.6	26.6	0.8	0.0	0.9	11.9	5.9	17.8	0.0	1.1	6.3	1.0	17.9	1.7	28.1	89.44	4.22	5.24	1.10	0.99	0.28		
BV42	37.4	6.0	34.8	0.8	0.0	0.0	8.5	2.5	11.0	0.0	1.2	3.7	0.0	4.5	0.0	9.5	89.00	4.70	4.79	1.51	0.99	0.29		
BV43	34.6	6.0	33.5	0.9	0.1	0.2	8.3	2.6	10.9	0.5	1.7	4.3	0.0	5.9	0.4	12.7	82.89	6.83	8.71	1.58	0.98	0.27		
BV44	19.6	3.8	30.7	1.1	0.3	0.0	17.2	7.4	24.6	0.0	2.0	4.4	0.0	9.7	3.4	19.5	67.72	12.64	16.69	2.95	0.99	0.25		
BV45	17.6	3.3	25.9	0.8	0.0	0.2	17.9	7.8	25.7	0.0	1.9	2.9	0.0	16.5	4.8	26.1	82.37	7.62	8.97	1.04	0.99	0.29		
BV46	20.4	3.5	30.9	0.5	0.0	0.0	22.7	5.3	27.9	1.0	1.6	5.5	0.0	5.6	2.1	15.8	86.59	5.42	6.83	1.16	1.24	0.27		
BV47	22.0	4.8	27.3	0.4	0.0	0.0	22.7	5.7	28.5	0.0	2.1	5.4	0.0	4.6	4.3	16.4	81.74	6.55	10.55	1.15	1.38	0.28		
BV48	22.3	3.2	27.6	0.2	0.1	0.0	23.5	5.1	28.6	0.0	2.8	3.2	0.0	5.9	5.7	17.5	84.92	5.65	8.00	1.42	1.18	0.27		
BV49	26.0	4.0	26.7	1.3	0.0	0.2	22.0	3.5	25.5	0.8	4.2	3.1	0.4	3.1	4.0	15.6	75.92	9.23	13.14	1.70	1.06	0.28		
BV50	25.1	3.5	23.4	1.0	0.1	0.2	22.4	3.6	25.9	1.3	4.5	4.1	0.4	5.5	4.5	20.2	80.29	7.77	10.34	1.60	1.08	0.28		
BC01	17.9	6.0	16.6	0.0	0.5	0.1	24.2	7.8	32.1	1.9	3.4	5.9	0.0	9.3	5.2	25.8	90.12	3.50	5.08	1.30	1.97	0.30		
BC04	14.9	2.8	19.6	0.8	0.0	0.0	18.6	8.1	26.7	0.0	4.1	4.8	0.2	20.0	5.7	34.9	79.70	8.15	10.10	2.05	1.04	0.27		
BC06	14.9	3.5	24.4	0.3	0.7	0.0	24.9	8.6	33.5	0.7	2.1	1.7	0.2	12.1	5.4	22.2	86.99	5.34	6.21	1.46	1.07	0.29		
BC07	16.9	4.9	22.6	0.3	0.2	0.0	25.5	8.7	34.2	0.0	1.6	3.8	0.0	10.9	4.1	20.4	83.87	6.73	8.17	1.23	0.99	0.27		
BC08	16.5	3.3	23.7	0.2	1.1	0.1	25.5	9.8	35.3	0.6	1.7	2.0	0.0	9.1	5.9	19.2	85.76	5.40	7.07	1.77	1.02	0.26		
BC09	14.8	4.1	18.8	0.0	1.5	0.5	20.7	5.6	26.3	0.7	3.4	6.9	0.0	21.2	1.8	33.9	87.95	4.84	5.71	1.50	1.07	0.26		
BC10	19.9	2.9	33.3	0.2	0.3	0.1	21.4	7.2	28.6	0.6	1.7	4.0	0.0	5.1	2.7	14.2	84.33	6.75	7.31	1.61	0.99	0.27		
BC11	19.6	4.7	25.6	0.0	0.0	0.1	20.0	3.1	23.1	0.9	5.0	2.5	0.1	11.8	5.1	25.5	78.29	8.78	11.06	1.88	1.03	0.29		
GC07	48.8	4.5	22.9	0.7	0.5	0.4	8.3	0.6	8.9	1.3	1.9	4.1	0.1	4.5	1.0	12.9	88.28	4.71	6.26	0.75	1.14	0.29		
PC06	23.7	6.4	26.0	0.5	0.3	0.1	21.3	7.3	28.5	0.0	3.3	2.6	0.1	3.5	4.5	14.0	86.85	5.12	6.88	1.16	1.03	0.27		
G1	22.0	4.4	22.5	1.0	0.0	0.0	10.7	8.4	19.1	0.2	5.5	5.4	0.3	11.9	6.7	30.0	76.93	8.98	12.35	1.75	1.05	0.28		
G4	16.8	6.1	20.1	0.0	0.1	0.0	21.0	11.5	32.5	0.7	3.3	0.8	0.0	13.2	5.8	23.8	76.58	9.07	12.54	1.81	1.19	0.28		
G5	19.3	2.9	33.3	0.8	0.6	0.0	19.9	9.8	29.7	0.3	1.2	1.7	0.0	6.9	3.0	13.0	93.59	2.39	3.10	0.92	1.15	0.31		
G6	15.2	3.0	23.0	0.2	0.0	0.0	22.6	10.8	33.4	0.3	2.0	2.4	0.4	15.6	4.2	24.8	86.94	5.10	6.94	1.02	0.99	0.30		
G7	21.3	3.6	19.3	0.3	0.5	0.0	23.0	8.6	31.6	0.0	3.8	4.6	0.0	8.7	5.7	22.8	89.84	3.99	5.29	0.88	1.44	0.28		
G9	23.6	6.6	26.0	0.5	0.3	0.1	21.2	7.2	28.4	0.0	3.3	2.6	0.1	3.4	4.4	13.8	68.11	11.41	17.48	3.00	1.50	0.28		
G10	51.1	9.3	22.9	0.8	0.3	0.3	8.4	0.3	8.8	0.0	1.2	3.2	0.0	6.1	6.1	77.48	9.06	11.64	1.81	1.10	0.31			
G12	43.4	10.3	24.3	1.2	0.2	0.0	11.0	0.0	11.0	0.0	2.4	4.6	0.5	0.0	1.9	9.4	69.17	11.91	16.33	2.59	0.88	0.30		
G13	39.1	6.5	34.7	1.0	0.1	0.0	4.7	0.0	4.7	0.0	3.3	6.1	0.0	3.1	1.0	13.5	61.46	16.12	18.41	4.02	1.15	0.31		
G14	36.6	6.2	32.4	1.0	0.2	0.1	4.7	0.3	5.0	0.8	3.5	6.5	0.0	4.9	1.4	17.2	69.76	10.68	17.20	2.36	1.28	0.26		
G15	23.0	6.0	28.5	0.2	0.4	0.1	12.5	6.2	18.7	0.6	2.5	5.4	0.0	8.6	5.7	22.9	79.86	7.50	10.19	2.46	1.09	0.29		
G16	46.7	8.0	32.8	0.6	0.0	0.2	2.9	2.1	5.0	0.0	0.9	2.5	0.0	1.6	1.4	6.5	86.62	4.55	4.62	4.20	1.65	0.35		
SF15	23.4	6.6	26.2	0.5	0.3	0.1	21.0	7.2	28.2	0.1	3.3	2.6	0.1	3.6	4.4	14.1	82.93	6.77	9.20	1.10	1.15	0.32		
<i>Patagonian Austral Interjurisdictional Marine Coastal Park sediments</i>																								
BV11	31.4	6.0	42.6	1.0	0.0	0.1	15.2	0.1	15.3	0.0	0.2	1.9	0.0	1.5	0.0	3.6	91.11	3.20	4.58	1.11	1.23	0.27		
BV12	32.9	7.9	43.0	0.9	0.2	0.1	12.0	0.0	12.0	0.0	0.4	2.6	0.0	0.0	0.0	3.0	90.85	4.21	3.46	1.48	1.04	0.30		
BV13	33.6	7.2	44.4	1.5	0.8	0.1	9.3	0.0	9.3	0.0	0.5	1.4	0.0	0.1	1.0	3.0	89.23	5.39	3.95	1.44	0.91	0.33		
BV14	33.8	7.3	45.9	0.9	0.0	0.1	7.8	0.1	7.9	0.0	0.4	0.9	0.0	2.3	0.0	3.7	94.93	2.10	2.06	0.91	1.63	0.33		
BV15	35.5	8.3	43.3	2.7	0.4	0.0	7.0	0.5	7.6	0.0	0.0	1.6	0.0	0.1	0.5	2.1	88.18	4.45	5.27	2.10	0.92	0.26		
BV16	39.6	6.9	41.1	0.3	0.3	0.1	7.9	1.2	9.1	0.0</td														

BV20	41.3	12.8	35.4	0.7	0.6	0.0	5.1	0.0	5.1	0.0	0.6	2.0	0.0	0.8	0.4	3.9	90.58	3.61	4.12	1.68	1.17	0.25
BV21	38.6	11.6	36.5	1.2	0.5	0.0	6.5	1.7	8.3	0.0	0.8	2.4	0.0	0.0	0.0	3.2	90.11	3.96	4.59	1.34	1.33	0.29
BV22	27.1	4.0	42.8	0.5	0.0	0.1	11.4	5.1	16.5	0.1	0.3	3.5	0.0	4.6	0.0	8.5	95.36	1.29	2.11	1.23	1.70	0.27
BV23	28.4	6.1	43.8	0.0	0.1	0.1	9.2	3.5	12.7	0.1	1.0	1.2	0.0	5.6	0.5	8.4	93.96	2.93	1.88	1.23	0.96	0.33
BV24	33.4	3.1	49.5	0.3	0.2	0.0	7.3	1.7	9.0	0.0	0.0	1.2	0.0	1.6	1.3	4.1	56.86	17.31	25.83	0.00	0.82	0.45
BV25	30.4	5.7	47.6	0.0	0.0	0.1	8.2	3.1	11.3	0.0	0.3	2.4	0.0	1.5	0.7	4.9	94.08	2.66	2.47	0.79	0.98	0.34
BV26	31.3	8.0	38.9	0.6	0.0	0.1	9.7	5.0	14.6	0.0	0.4	3.3	0.0	2.4	0.0	6.1	95.33	1.80	1.83	1.05	1.08	0.30
BV27	30.8	6.4	35.5	0.5	0.0	0.2	10.0	5.3	15.2	0.9	0.9	4.1	0.0	4.5	0.3	10.7	96.77	1.31	1.34	0.59	1.08	0.32
BV28	36.2	7.3	39.7	0.2	0.1	0.1	7.8	3.5	11.3	0.0	0.0	2.3	0.0	1.6	0.9	4.8	93.55	1.63	2.67	2.15	1.39	0.33
BV29	33.5	3.8	48.7	0.4	0.0	0.1	7.6	2.5	10.1	0.0	0.2	2.2	0.1	0.2	0.5	3.3	86.80	7.06	3.39	2.74	1.14	0.33
BV30	26.4	5.9	40.2	0.0	1.3	0.1	2.4	5.5	7.9	0.4	0.3	3.3	0.0	5.8	0.0	9.8	92.77	3.12	3.01	1.10	0.89	0.30
BV31	28.6	4.7	41.4	0.7	0.7	0.1	8.9	7.3	16.2	0.0	0.2	3.1	0.0	2.7	1.2	7.1	95.03	2.02	2.28	0.66	1.33	0.27
BV32	39.3	9.0	34.3	0.2	0.2	0.1	6.8	4.9	11.7	0.0	0.0	2.3	0.0	1.6	1.0	4.8	94.89	2.22	2.20	0.69	1.07	0.25
BV33	35.5	3.9	44.9	0.9	0.8	0.0	6.7	3.7	10.4	0.0	0.0	2.3	0.0	0.8	0.0	3.1	92.53	4.34	1.75	1.39	0.89	0.44
<i>Patagonia continental shelf sediments (sources)</i>																						
BV51	42.2	7.8	30.8	0.7	0.8	0.2	12.8	0.0	12.8	0.0	2.4	2.1	0.0	0.0	0.0	4.5	63.34	14.13	19.56	2.97	0.98	0.28
BV52	46.1	6.2	31.4	0.7	0.5	0.0	11.1	0.0	11.2	0.0	1.1	2.1	0.0	0.0	0.5	3.7	24.33	29.96	22.85	0.58	0.29	
BV54	43.0	4.7	32.9	0.6	0.7	0.1	10.4	0.0	10.4	0.0	3.3	2.4	0.0	0.0	1.3	7.0	5.43	33.58	40.91	20.07	0.23	0.30
BV55	54.0	9.3	23.7	0.8	0.2	0.5	7.9	0.0	7.9	0.0	1.2	2.0	0.3	0.0	0.0	3.5	na	na	na	na	na	na
<i>Gulf of San Jorge shore sediments (sources)</i>																						
01CSCB-B	14.8	3.7	48.2	1.1	0.9	0.7	0.0	3.0	3.0	0.0	2.4	6.4	0.3	14.5	3.7	27.4	76.13	12.19	8.80	2.88	1.43	0.208
02RL-B	20.4	5.8	47.3	0.4	0.7	0.4	0.0	0.0	0.0	0.0	3.1	8.3	0.5	9.2	3.7	24.8	66.14	15.29	13.85	4.73	0.8	0.258
04RCB-B	24.6	5.0	25.8	0.5	0.0	0.1	0.0	5.5	5.5	1.2	3.3	13.6	0.7	12.7	6.6	38.1	0.00	49.22	32.95	17.83	nd	0.216
09PV-B	24.5	3.3	64.2	0.0	0.0	0.5	0.0	1.6	1.6	0.0	0.0	0.0	0.0	5.3	0.4	5.7	95.91	0.00	4.09	0.00	nd	nd
10BB-B	20.8	9.4	47.1	0.0	1.2	0.1	3.1	9.6	12.7	0.0	0.1	0.1	0.0	7.6	0.7	8.6	97.48	1.11	0.73	0.67	nd	0.192
11MED-B	30.4	8.9	46.6	1.1	0.2	0.2	0.0	4.1	4.1	0.0	0.4	4.3	0.0	3.1	0.0	7.8	51.10	40.13	5.87	2.90	0.18	0.355
12PM-B	31.9	9.4	47.7	1.0	0.1	0.4	0.0	4.2	4.2	0.0	0.5	1.6	0.0	2.5	0.7	5.3	0.00	45.78	22.58	31.63	nd	0.337
12PM-D	22.8	2.2	38.5	2.6	1.0	2.2	1.3	7.4	8.8	2.0	0.7	4.4	0.0	14.4	0.3	21.7	na	na	na	na	na	na
13CDB-B	35.2	10.7	43.9	1.3	0.2	0.1	0.0	0.0	0.1	0.8	2.3	0.0	3.2	2.2	8.5	77.02	9.47	9.09	4.42	nd	0.267	
<i>Bojo de sarmiento" topsoil sediments (sources)</i>																						
07NS1-B	10.0	4.3	20.4	0.6	0.0	0.3	0.0	16.5	16.5	1.6	0.7	0.0	0.0	42.4	3.1	47.8	95.40	2.45	2.15	0.00	nd	0.293
08NS2-B	28.7	9.3	38.8	1.7	0.9	0.3	0.0	4.4	4.4	0.0	0.6	3.1	0.0	10.8	1.2	15.7	96.26	0.00	2.38	1.36	1.75	nd
08NS2-D	11.5	5.3	23.0	1.4	0.0	0.7	0.0	8.7	8.7	0.0	0.2	2.1	0.1	44.9	2.1	49.4	na	na	na	na	na	na
<i>Patagonian rivers and Strait of Magellan sediments (sources)</i>																						
05PDN-B	12.3	2.5	22.1	0.0	0.0	0.0	13.5	18.1	31.6	1.2	0.6	8.3	0.0	16.6	4.4	31.2	88.86	8.68	1.36	1.10	nd	0.225
14RCHU-B	30.7	8.6	28.8	1.4	0.8	0.5	0.8	1.1	1.8	2.8	2.2	5.9	0.1	11.5	3.2	25.8	69.31	19.21	5.22	6.26	0.611	0.2
14RCHU-D	27.3	6.7	24.0	1.3	0.9	0.8	1.2	1.7	2.9	3.7	2.8	7.6	0.3	15.9	3.6	33.9	na	na	na	na	na	na
SoM	28.0	2.4	24.8	0.4	0.6	0.2	6.0	2.2	8.3	1.2	9.9	6.1	0.3	8.1	9.2	34.9	0.00	30.68	62.66	6.66	nd	0.292

na = not analysed, nd = not determined; B = bulk fraction, D = < 63µm fraction, Feld-K = Feldspath-K, Plagio. = Plagioclase, Pyro = Pyroxene, Amphi = Amphibole, Fe-b. = Fe-bearing

Diat = Diatoms, A. sili. = Amorphous Silica, Kaol. = Kaolinite, Chlор. = Chlorite, Biot. = Biotite, Smec. = Smectite, Musc. = Muscovite

*Cristalinity FWHM = Full Width at Half Maximum intensity

Tableau 3: Chemical composition of sediment samples

Sample	LOI (%)	MgO	Al ₂ O ₃	SiO ₂	P ₂ O ₅	K ₂ O	CaO	TiO ₂	Fe ₂ O ₃	MnO	V	Sr	Zr
		μg/g											
<i>Gulf of San Jorge sediments</i>													
BV01	5.7	0.8	14.2	68.5	0.4	2.3	2.5	0.7	4.5	0.1	109.5	258.8	218.0
BV02	8.5	1.4	14.7	65.1	0.6	2.5	2.1	0.7	5.5	0.1	131.8	222.2	177.7
BV03	10.4	1.7	15.9	60.8	0.4	2.5	1.7	0.8	6.3	0.1	140.8	178.3	145.9
BV04	11.9	1.7	16.5	59.1	0.5	2.7	1.7	0.8	6.2	0.1	149.4	177.4	174.7
BV05	10.4	1.7	16.8	61.7	0.5	2.6	1.9	0.8	6.0	0.1	148.4	186.5	188.3
BV06	12.0	1.9	17.2	61.7	0.5	2.7	1.7	0.8	6.5	0.1	171.1	178.2	184.0
BV07	12.3	1.9	16.4	59.8	0.5	2.6	1.7	0.8	6.1	0.1	143.8	179.3	170.0
BV08	11.6	1.9	16.8	61.0	0.6	2.6	1.6	0.8	6.3	0.1	155.6	172.1	165.5
BV09	11.2	1.8	17.0	60.8	0.5	2.7	1.8	0.8	6.1	0.1	163.7	185.2	195.6
BV10	10.8	1.7	16.1	63.2	0.4	2.5	2.0	0.8	5.9	0.1	142.2	209.6	189.9
BV34	8.2	1.0	14.7	66.4	0.5	2.1	2.0	0.7	5.0	0.0	111.4	204.2	182.1
BV35	10.4	1.5	16.5	63.1	0.5	2.5	2.0	0.8	5.6	0.0	154.5	199.9	181.7
BV36	11.9	1.7	16.6	61.2	0.4	2.7	1.6	0.8	6.2	0.1	167.5	173.1	164.7
BV37	12.5	1.9	16.3	60.0	0.5	2.6	1.7	0.8	6.1	0.1	148.8	180.4	165.7
BV38	12.4	1.7	15.9	59.6	0.4	2.6	1.7	0.8	6.0	0.1	176.8	168.5	158.5
BV39	6.5	0.6	14.6	65.7	0.5	2.1	2.8	0.7	4.3	0.0	85.8	279.4	230.7
BV40	6.7	0.6	14.1	66.5	0.5	2.0	2.6	0.8	4.6	0.1	96.3	256.2	191.4
BV41	7.4	0.7	13.5	63.2	0.7	2.0	2.7	0.8	7.5	0.0	nd	441.7	210.2
BV42	4.3	0.3	13.2	69.5	0.5	1.8	2.8	1.0	4.3	0.1	131.7	254.2	237.8
BV43	10.0	1.4	17.0	64.6	0.6	2.4	2.3	0.8	5.7	0.1	131.0	225.0	185.0
BV44	9.8	1.3	15.4	61.0	0.6	2.4	2.3	0.8	5.7	0.1	106.2	230.1	189.5
BV45	8.9	1.2	16.2	62.9	0.5	2.3	2.4	0.8	5.2	0.1	138.1	238.9	211.3
BV46	9.4	1.3	16.1	62.5	0.4	2.4	2.2	0.7	5.2	0.1	121.4	210.9	163.1
BV47	10.0	1.6	16.6	63.5	0.6	2.5	2.0	0.7	5.4	0.1	135.4	202.8	171.1
BV48	9.7	1.3	16.0	62.5	0.5	2.4	2.0	0.7	5.4	0.1	121.3	201.1	168.2
BV49	9.1	1.4	16.1	63.3	0.4	2.5	2.0	0.7	5.4	0.1	145.2	199.4	166.1
BV50	10.4	1.6	15.8	62.2	0.5	2.5	2.0	0.7	5.5	0.1	125.5	194.7	164.1
BC01	12.3	1.9	16.7	60.0	0.6	2.7	1.7	0.8	6.4	0.1	163.8	177.5	176.8
BC04	12.9	1.9	16.5	59.6	0.5	2.5	1.7	0.8	6.2	0.1	148.2	180.7	178.2
BC06	11.8	1.6	15.1	61.4	1.5	2.5	2.0	0.8	6.1	0.1	134.9	217.8	190.4
BC07	11.4	1.6	16.7	61.8	0.5	2.5	2.0	0.8	6.1	0.1	157.1	197.3	189.9
BC08	11.7	1.7	16.9	63.5	0.5	2.4	2.0	0.8	6.0	0.1	140.6	205.0	194.4
BC09	10.6	1.7	16.7	63.1	0.6	2.4	2.1	0.8	5.9	0.1	149.4	211.0	195.8
BC10	9.7	1.2	15.7	61.2	0.4	2.3	2.3	0.8	5.3	0.1	142.3	222.4	197.1
BC11	12.6	2.0	16.9	62.2	0.5	2.6	1.7	0.8	6.2	0.1	154.3	178.5	172.9
GC07	10.7	1.7	17.0	62.0	0.4	2.6	1.9	0.8	5.7	0.1	148.2	198.6	176.9
PC06	9.4	1.4	15.4	62.5	0.5	2.8	1.9	0.8	5.9	0.1	156.0	205.5	246.5
G1	13.7	2.0	16.7	61.4	0.5	2.5	1.7	0.7	6.6	0.1	144.2	169.5	138.7
G4	13.2	1.9	16.5	59.8	0.5	2.5	1.9	0.8	6.2	0.1	159.6	194.3	180.5
G5	8.7	0.8	16.3	66.1	0.4	2.1	2.6	0.7	4.9	0.0	114.3	254.1	201.7
G6	11.0	1.5	16.3	61.6	0.5	2.5	2.0	0.8	5.6	0.1	124.1	196.3	180.1
G7	11.9	2.0	16.6	60.3	0.5	2.7	1.6	0.8	6.2	0.1	152.7	172.7	175.0
G9	6.6	1.0	14.9	67.6	0.6	2.2	2.3	0.6	4.5	0.1	106.1	234.7	179.7
G10	3.6	0.2	11.4	75.7	0.4	2.2	2.5	0.5	2.9	0.1	37.1	189.3	192.3
G12	4.6	0.4	12.7	73.9	0.4	2.5	1.9	0.5	4.0	0.1	78.5	179.9	174.2
G13	4.1	0.6	13.7	68.5	0.4	2.2	2.6	0.6	5.2	0.1	119.1	249.4	159.7
G14	9.0	1.4	16.4	66.1	0.5	2.3	2.1	0.7	5.4	0.1	122.3	215.5	188.3
G15	10.3	1.4	16.0	62.1	0.5	2.4	2.2	0.8	5.6	0.1	147.4	211.8	180.9
G16	3.8	0.1	12.4	75.5	0.4	2.0	2.3	0.4	3.6	0.1	58.2	232.0	121.8
SF15	7.4	1.0	14.7	63.0	0.6	2.2	2.2	0.6	4.7	0.1	108.3	224.3	183.8
<i>Patagonian Austral Interjurisdictional Marine Coastal Park sediments</i>													
BV11	3.5	0.1	14.6	69.1	0.5	1.9	3.6	0.7	2.7	0.0	62.1	334.6	248.1
BV12	2.4	nd	15.7	71.7	0.3	2.0	3.6	0.6	2.2	0.0	43.3	333.7	191.5
BV13	2.8	nd	14.0	66.7	0.3	1.8	3.6	0.7	2.5	0.0	39.1	334.1	236.7

BV14	2.1	nd	14.3	72.5	0.3	2.0	3.6	0.6	2.3	0.0	44.8	352.5	210.4
BV15	2.6	nd	14.3	68.8	0.3	1.9	3.5	0.6	2.3	0.0	36.3	336.0	233.5
BV16	1.8	nd	14.0	71.8	0.3	2.0	3.2	0.5	1.8	0.0	24.5	316.0	176.5
BV17	na	na	na	na	na	na	na	na	na	na	na	na	na
BV18	7.1	0.2	13.3	68.2	0.4	1.9	7.0	0.6	2.6	0.0	63.5	396.0	187.3
BV19	2.2	nd	14.4	72.8	0.2	2.0	3.5	0.6	2.2	0.0	39.2	356.3	212.0
BV20	2.0	nd	12.7	75.5	0.4	2.3	2.8	0.6	2.1	0.0	28.1	248.9	214.2
BV21	3.4	nd	12.6	72.1	0.4	2.4	3.7	0.7	2.4	0.0	45.2	310.4	251.9
BV22	8.0	nd	14.1	62.5	0.4	2.0	5.2	0.6	3.3	0.0	73.6	375.4	202.5
BV23	2.4	nd	15.0	68.9	0.4	1.7	3.8	0.7	2.5	0.0	59.6	357.9	222.3
BV24	1.9	nd	14.8	69.2	0.3	1.6	3.8	0.6	2.2	0.0	32.4	366.1	207.9
BV25	3.2	nd	14.9	68.5	0.3	1.8	3.7	0.7	2.6	0.0	61.7	361.3	224.3
BV26	5.9	0.2	13.3	63.7	0.4	2.0	3.8	0.6	3.0	0.0	60.9	308.0	191.2
BV27	9.4	0.8	13.8	63.6	0.5	2.2	3.0	0.6	3.9	0.0	75.1	269.6	187.3
BV28	2.0	nd	14.8	71.0	0.4	1.8	3.6	0.7	2.4	0.0	49.3	341.1	301.7
BV29	1.8	nd	15.2	68.3	0.3	1.6	3.8	0.7	2.4	0.0	59.1	353.5	248.2
BV30	12.3	0.3	13.5	61.3	0.4	1.7	11.6	0.5	2.7	0.0	70.5	566.8	180.3
BV31	7.1	0.3	13.8	63.3	0.4	2.1	4.3	0.6	3.2	0.0	67.0	330.0	220.6
BV32	3.0	nd	11.9	71.9	0.3	2.1	2.9	0.5	2.1	0.0	44.3	277.1	163.6
BV33	2.3	nd	14.6	69.8	0.4	1.7	3.8	0.7	2.5	0.0	64.5	360.2	236.3
<i>Patagonia continental shelf sediments (sources)</i>													
BV51	3.6	0.2	13.1	71.7	0.4	2.1	2.5	0.5	3.1	0.0	63.9	248.3	125.9
BV52	3.0	0.1	12.0	73.3	0.3	1.8	2.9	0.5	2.5	0.0	44.2	251.9	125.8
BV54	2.4	0.4	12.3	66.8	0.4	1.6	3.1	0.4	2.9	0.1	42.0	302.3	125.2
BV55	3.6	nd	9.8	75.4	0.4	2.0	4.0	0.3	2.3	0.0	37.4	216.2	96.1
<i>Gulf of San Jorge shore sediments (sources)</i>													
01CSCB-B	5.2	0.9	17.7	63.0	0.0	2.0	3.7	1.0	6.5	0.1	162.8	335.7	179.7
02RL-B	4.7	1.0	17.7	63.3	0.0	2.4	3.5	0.8	6.7	0.0	173.1	296.0	140.7
04RCB-B	5.8	0.7	16.4	65.8	0.0	2.6	1.6	0.8	5.9	0.1	149.5	163.8	188.9
09PV-B	2.0	nd	17.0	67.6	0.0	1.3	4.0	1.0	3.3	0.0	81.9	398.4	227.1
10BB-B	3.2	nd	16.0	69.4	0.0	1.9	3.1	0.7	3.1	0.0	58.0	317.9	172.2
11MED-B	2.3	nd	15.7	71.2	0.0	2.0	3.0	0.7	3.4	0.0	69.1	315.8	190.1
12PM-B	1.8	nd	15.1	71.5	0.0	2.0	3.0	0.6	2.8	0.0	67.9	311.4	165.3
12PM-D	5.4	0.7	17.0	66.0	0.0	1.6	3.4	1.4	6.2	0.1	173.2	341.4	619.9
13CDB-B	2.3	0.1	15.5	72.6	0.0	2.3	3.0	0.7	2.6	0.0	52.7	285.9	275.2
<i>"Bajo de sarmiento" topsoil sediments (sources)</i>													
07NS1-B	8.4	1.2	17.5	66.6	0.0	1.5	1.9	1.0	0.1	6.5	109.0	200.9	229.7
08NS2-B	3.8	0.6	15.3	70.8	0.0	2.0	2.5	0.8	4.4	0.0	84.0	273.2	171.6
08NS2-D	9.8	0.9	12.8	47.6	0.0	1.3	1.6	0.8	5.1	0.0	104.0	155.2	249.8
<i>Patagonian rivers and Strait of Magellan sediments (sources)</i>													
05PDN-B	6.8	0.9	16.4	68.5	0.0	2.2	2.2	0.6	4.8	0.0	88.5	169.9	191.8
14RCHU-B	5.8	0.8	15.7	69.9	0.0	2.3	2.0	0.6	4.5	0.0	87.5	195.9	180.5
14RCHU-D	8.1	0.9	16.6	65.7	0.0	2.3	2.1	0.8	5.5	0.0	92.2	202.6	241.4
SoM	7.9	1.1	16.7	67.7	0.6	2.2	1.5	0.7	5.5	0.1	142.4	153.0	127.8

na = not analysed, nd = not determined; B = bulk fraction, D = < 63µm fraction

LOI= Loss On Ignition

Tableau 4: Sources contributions to surface samples

Sample	Source 1	Source 2	Source 3	Source 4	Source 5	Source 1+2	Source 3+5
	Proportions of each source (%)						
<i>Gulf of San Jorge sediments</i>							
BV01	15.5	20.5	8.1	4.3	55.0	35.9	63.2
BV02	2.0	19.5	9.6	13.6	53.2	21.6	62.7
BV03	2.4	13.5	20.6	6.2	49.6	15.8	70.2
BV04	0.0	0.0	34.8	49.7	12.3	0.0	47.1
BV05	0.1	2.2	45.5	28.5	14.1	2.3	59.5
BV06	28.6	9.4	43.3	2.7	7.6	37.9	50.9
BV07	0.4	3.6	70.3	18.1	5.8	3.9	76.0
BV08	0.0	0.0	53.0	49.5	0.0	0.0	53.0
BV09	0.2	25.1	45.3	8.8	16.1	25.3	61.4
BV10	0.5	37.0	42.3	22.6	1.4	37.5	43.7
BV34	25.9	5.2	24.6	12.6	29.9	31.2	54.5
BV35	19.8	32.2	29.4	2.6	13.4	52.0	42.8
BV36	0.2	6.6	70.2	8.8	10.6	6.8	80.8
BV37	0.0	8.6	84.0	6.1	2.8	8.6	86.8
BV38	17.7	14.7	21.0	0.0	35.1	32.5	56.2
BV39	54.5	0.4	1.9	13.3	30.6	54.9	32.5
BV40	57.7	1.3	0.4	11.9	30.9	59.0	31.3
BV41	nd	nd	nd	nd	nd	nd	nd
BV42	19.7	12.7	3.0	4.6	62.7	32.5	65.7
BV43	10.1	22.4	0.9	6.8	60.0	32.5	60.9
BV44	1.1	57.7	8.9	9.3	22.6	58.8	31.5
BV45	0.2	35.3	6.7	34.3	21.9	35.5	28.7
BV46	16.4	52.3	5.2	0.0	24.5	68.7	29.7
BV47	8.8	40.6	6.2	0.0	37.6	49.5	43.9
BV48	3.3	45.2	0.8	5.0	41.3	48.5	42.1
BV49	1.6	35.2	1.5	0.0	54.3	36.9	55.8
BV50	0.0	18.1	24.4	4.1	46.1	18.2	70.5
BC01	0.0	1.9	38.3	16.3	27.3	2.0	65.5
BC04	0.0	5.0	49.2	39.7	2.7	5.0	51.9
BC06	0.0	45.6	25.2	18.3	10.2	45.6	35.5
BC07	1.8	31.2	27.6	17.7	19.4	33.0	47.0
BC08	7.7	36.1	24.3	11.8	17.1	43.8	41.4
BC09	0.5	2.0	36.9	46.6	7.7	2.4	44.6
BC10	22.4	58.5	2.7	0.0	19.3	80.9	22.0
BC11	10.1	23.2	22.3	18.3	20.2	33.3	42.6
GC07	0.0	0.0	8.4	7.4	97.6	0.0	106.0
PC06	26.5	14.5	12.8	0.3	37.2	41.1	50.0
G1	0.0	12.5	23.6	20.2	31.7	12.6	55.4
G4	17.0	2.6	14.7	33.5	22.7	19.6	37.4
G5	49.1	32.8	4.2	6.3	9.7	81.9	13.9
G6	1.1	32.8	18.9	34.7	13.7	33.9	32.5
G7	0.3	3.4	61.9	8.8	22.2	3.7	84.1
G9	34.9	3.5	30.6	0.1	25.5	38.4	56.1
G10	0.0	0.0	4.5	0.0	100.0	0.0	104.5

G12	0.0	0.0	0.0	0.0	94.9	0.0	94.9
G13	2.4	23.3	2.0	0.1	70.1	25.7	72.1
G14	0.9	20.9	8.9	2.8	62.2	21.8	71.1
G15	1.2	30.1	18.1	8.5	38.1	31.3	56.2
G16	6.2	0.0	4.8	1.7	88.5	6.2	93.3
SF15	27.0	15.3	11.5	0.6	36.4	42.3	47.9
<i>Patagonian Austral Interjurisdictional Marine Coastal Park sediments</i>							
BV11	67.8	14.5	0.0	0.0	22.6	82.4	22.6
BV12	77.5	0.1	0.0	0.0	26.8	77.6	26.8
BV13	78.1	0.3	0.0	0.0	25.9	78.4	25.9
BV14	81.9	0.5	0.0	0.0	23.1	82.4	23.1
BV15	69.4	0.0	0.0	0.0	33.6	69.4	33.6
BV16	55.0	0.0	0.0	0.0	50.9	55.0	50.9
BV17	nd	nd	nd	nd	nd	nd	nd
BV18	40.9	0.2	1.4	5.9	51.6	41.1	53.0
BV19	71.1	7.6	0.0	0.0	26.7	78.7	26.7
BV20	29.1	0.0	0.0	0.0	67.2	29.1	67.2
BV21	37.3	1.3	0.0	0.0	60.2	38.6	60.2
BV22	73.5	15.0	0.1	1.1	16.1	88.5	16.2
BV23	78.4	9.6	0.0	3.7	13.0	88.0	13.0
BV24	nd	nd	nd	nd	nd	nd	nd
BV25	96.4	1.6	0.0	0.0	9.3	98.0	9.3
BV26	67.0	0.9	0.0	0.0	32.7	67.9	32.7
BV27	51.2	4.0	0.7	5.1	37.3	55.2	38.0
BV28	57.5	0.4	0.1	0.0	45.1	58.0	45.2
BV29	94.0	0.4	0.0	0.0	17.1	94.3	17.1
BV30	67.4	14.7	2.1	3.9	14.3	82.0	16.4
BV31	71.7	12.8	0.2	0.0	19.7	84.5	19.9
BV32	31.2	0.1	0.6	0.6	67.6	31.4	68.2
BV33	74.8	0.0	0.0	0.0	33.2	74.8	33.2

nd = not determined

Tableau 5: Minerals identified in RockJock v11 (a), consolidated list of minerals (b), minerals used in SedUnMix (c), and samples associated to sources in SedUnMix (d)

Number	(a) Mineral identified	(b) Minerals in consolidated list	Number
<i>Non-clay minerals</i>			
1	Quartz	Quartz	1
2	Kspar (ordered Microcline)	K and Na feldspar	2-6
3	Kspar (intermediate microcline)	Plagioclase	7-5
4	Kspar (sanidine)	Pyroxene	26
5	Kspar (orthoclase)	Amphibole	27
6	Kspar (anorthoclase)	Fe-bearing	16, 19-22
7	Plagioclase (albite, var. cleavelandite)	Amorphous silica	24-25
8	Plagioclase (oligoclase; Norway)	Kaolinite	28
9	Plagioclase (andesine)	Chlorite	35-37
10	Plagioclase (labradorite)	Illite	32-33
11	Plagioclase (bytownite)	Smectite	29-31, 39
12	Calcite	Muscovite	38
13	Calcite (Mg-rich)		
14	Dolomite		
15	Halite		
16	Pyrite		
17	Anhydrite		
18	Gypsum		
19	Magnetite		
20	Hematite		
21	Goethite		
22	Maghemite		
23	Anatase		
24	Tephra (Hekla)		
25	Diatoms		
26	Pyroxene (augite)		
27	Amphibole (hornblende)		
<i>Clay minerals</i>			
28	Kaolinite (disordered)		
29	Smectite (Na-Kinney montmorillonite)		
30	Smectite (Ca-Kinney montmorillonite)		
31	Smectite (hectorite)		
32	Illite (1Md)	11MED-B	
33	Illite (1M; R>3; 95%)	12PM-B	
34	Biotite (1M)	13CDB-B	Source 1 (S1)
35	Chlorite (CCa-2)	10BB-B	
36	Chlorite (Fe-rich; Tusc)	09PV-B	
37	Chlorite (Mg; Luzenac)	01CSCB-B	Source 2 (S2)
38	Muscovite (2M1)	02RL-B	
39	Rectorite (Rogue)	14RCHU-B	
		14RCHU-D	
		SoM	Source 3 (S3)
		05PDN-B	
		07NS1-B	Source 4 (S4)
		08NS2-D	
		BV51	
		BV52	Source 5 (S5)
		BV54	
		BV55	

B = bulk fraction, D = < 63µm fraction

CHAPITRE 2

EVOLUTION TARDI-PLEISTOCENE ET HOLOCENE DES ENVIRONNEMENTS SEDIMENTAIRES ASSOCIEES A LA TRANSGRESSION POSTGLACIAIRE DANS LE GOLFE DE SAN JORGE, PATAGONIE CENTRALE, ARGENTINE

2.1 RÉSUMÉ EN FRANÇAIS DU DEUXIÈME ARTICLE

Cette étude présente la première description et interprétation détaillée de la séquence sédimentaire sommitale provenant des dépôts du Pléistocène tardif et de l'Holocène dans le golfe de San Jorge (GSJ; Patagonie) afin de documenter la sédimentation dans la partie centrale du plateau continental argentin depuis le dernier maximum glaciaire. Plusieurs centaines de kilomètres de relevés sismiques à haute résolution (*sparker*) et de profileurs de sous-surface (*chirp*) ainsi que de nombreuses carottes de sédiments (carottier à boîte et à piston), recueillies à bord du N/R Coriolis II en 2014, ont été étudiées pour reconstruire la stratigraphie et l'historique de sédimentation dans le golfe. Les données *sparker* ont permis l'identification de cinq faciès sismiques, dont le socle acoustique composé de successions sédimentaires provenant du milieu du Cénozoïque et dont la surface révèle une troncature d'érosion incisée formant des vallées et des chenaux. Dans cette partie du plateau continental, ces nombreux chenaux comblés ont confirmé l'existence d'un système de paléodrainage formé au cours des précédents bas niveau marin et oblitéré par une succession de dépôts fluviaux et lagunaires avant la dernière transgression marine. Basées sur une analyse multi-traceurs de quatre carottes à piston, quatre unités et sous-unités lithologiques ont été définies pour la séquence sédimentaire de sous-surface dans la partie centrale du GSJ. L'analyse de la lithostratigraphie et des âges radiocarbones indique le début de la sédimentation subtidale à environ 14 cal ka BP dans la partie centrale du golfe. Avant le développement des conditions

subtidales, les premières étapes de l'invasion marine semblent avoir mené à la déposition d'intervalles hétérolithiques et de rythmites liées à des environnements intertidaux. Une augmentation abrupte des rapports Log(Ti/Ca) et Log(Rb/Sr) dans une couche pluricentimétrique distincte pourrait suggérer une montée rapide du niveau de la mer dans le GSJ avant ~14 cal ka BP, ce qui est compatible avec le MWP-1A. Dans l'ensemble, cette étude a mis en évidence l'impact significatif de l'augmentation du niveau marin sur la sédimentation dans le golfe, du début de l'invasion marine jusqu'au milieu de l'Holocène, ainsi que la contribution réduite, comme on le constate de nos jours, des apports fluviaux et ce à cause de la diminution progressive et du retrait du drainage glaciaire commençant avant l'Holocène.

Le second article de cette thèse intitulé "*Late Pleistocene and Holocene evolution of sedimentary environments associated with postglacial transgression in the Gulf of San Jorge, central Patagonia, Argentina*" a été rédigé par moi-même sous la supervision de mon directeur Guillaume St-Onge et de mes co-directeurs Mathieu J. Duchesne et Jean-Carlos Montero Serrano. Le professeur Miguel J. Haller a également contribué à cet article en corigeant et commentant diverses versions du manuscrit. Le traitement des données d'étinceleur, utilisées dans cette étude, a été réalisé en collaboration avec Mathieu J. Duchesne à la Commission géologique du Canada à Québec dans le cadre du cours Nouveaux développements en océanographie. J'ai réalisé l'ensemble des analyses et des interprétations présentées dans ce chapitre. Cet article sera soumis très prochainement à la revue *Continental Shelf Research*.

Les résultats de cet article ont été présentés à divers niveaux d'avancements sous la forme d'une présentation orale au congrès *Arctic Change* qui s'est déroulée à Québec en décembre 2017 ainsi que sous la forme d'une affiche scientifique lors du congrès annuel de l'union américaine de géophysique (*AGU Fall meeting*) à San Francisco (États-Unis) en décembre 2016.

2.2 LATE PLEISTOCENE AND HOLOCENE EVOLUTION OF SEDIMENTARY ENVIRONMENTS ASSOCIATED WITH POSTGLACIAL TRANSGRESSION IN THE GULF OF SAN JORGE, CENTRAL PATAGONIA, ARGENTINA

This study presents the first detailed description and interpretation of the upper sedimentary sequence of the late Pleistocene and Holocene deposits in the Gulf of San Jorge (GSJ; Patagonia) in order to document the sedimentation in the central part of the Argentine Continental Shelf (ACS) since the Last Glacial Maximum. Several hundreds of high-resolution seismic (sparker) and subbottom profiler (chirp) surveys and numerous sediment cores (box and piston cores), collected on board the R/V Coriolis II in 2014, were investigated to reconstruct the stratigraphy and depositional history in the gulf. Sparker data allowed the identification of five seismic facies, including the acoustic basement composed of mid-Cenozoic sedimentary successions and whose surface reveals incised erosional truncation forming valleys and channels. In this part of the ACS, these numerous infilled channels and valleys confirmed the existence of a paleo-fluvial network formed during previous sea-level lowstands and obliterated with a possible succession of fluvial and lagoonal/estuarine deposits prior to the last marine transgression. Based on multi-proxy analysis of four piston cores, four lithological units and sub-units were defined for the uppermost offshore sedimentary sequence in the northern-central part of the GSJ. Analysis of lithostratigraphy and radiocarbon ages indicate the onset of subtidal sedimentation at ~14 cal ka BP in the central part of the gulf. Before the development of subtidal conditions, the first steps of marine invasion seem to have led to the deposition of heterolithic beds and sedimentary rhythmites related to lagoonal/wind-tidal flat environments. An abrupt increase of Log(Ti/Ca) and Log(Rb/Sr) ratios in a distinct pluricentimetric layer could suggest a rapid sea-level rise in the GSJ prior to ~14 cal ka BP, consistent with the MWP-1A. Overall, this study highlighted the significant impact of sea-level rise on sedimentation in the gulf from the onset of marine invasion to the mid-Holocene, as well as the reduced contribution, as observed nowadays, of riverine inputs due to the progressive diminution and withdrawal of glacial drainage starting before the Holocene.

2.3 INTRODUCTION

Shaped by the succession of lowstand subaerial erosive phases and subsequent transgressive phases, continental shelves constitute privileged witnesses of the impact of sea-level variations during the Quaternary period. Over the last decades, an increasing number of paleoceanographic and marine paleoclimatic studies has focus on continental shelf records rather than deep sea archives to take advantage of the usually higher accumulation rates on the upper margin. However, several paleoceanographic and marine paleoclimatic studies on the outer shelf must settle with uncomplete or low-resolution sedimentary records associated with short time periods and abrupt events notably due to the distance to the primary sources of sediment and because of the greater sediment accumulation in the inner- and mid-shelf regions (e.g., McCave, 1972; Nittrouer and Sternberg, 1981; Crockett and Nittrouer, 2004). In this context, the sedimentary records from bays and gulfs represents preferential alternative to reconstruct late Quaternary paleoenvironments and sea-level changes in the inner part of the continental margin due to their location at the transition between inner- and mid-continental shelf, closer to sediment sources and mostly in shallow waters (Perissoratis et al., 2000; Chivas et al., 2001). Furthermore, from high- to mid-latitudes, a large part of these areas were located in the vicinity of ice sheets during glacial periods which attributed to the sedimentary archive the potential to capture the ice sheet margin fluctuations as well as the implications for regional sea-level variations (e.g., Barnhardt et al., 1995; Rémillard et al., 2017).

Developed mainly on a passive continental margin and characterised by a smooth extended surface, the Argentine Continental Shelf (ACS) was greatly affected by Quaternary sea-level variations (Rabassa et al., 2005; Rabassa, 2008; Violante et al., 2014). In this context, numerous studies have been conducted during the last decades to reconstruct the chronology of the marine transgression, as well as the relative sea-level changes following the Last Glacial Maximum (e.g., Guilderson et al., 2000; Rostami et al., 2000; Cavallotto et al., 2004; Violante and Parker, 2004; Schellmann and Radtke, 2010; Violante et al., 2014, and references therein). Based on ^{14}C dates from piston cores retrieved over the entire shelf

in 1960's, Guilderson et al. (2000) have made a post-LGM relative sea-level curve for the ACS, which was later updated and compiled by Violante and Parker (2004). This model suggests that the LGM lowermost sea-level occurred around 18 ka BP at approximately 105 m below present sea level. Then, the onset of the marine transgression resulted in a rapid sea-level rise in the early Holocene to reach a maximum sea-level between 8 and 6 ka BP, followed by a progressive fall to its present position (Cavallotto et al., 2004; Milne et al., 2005; Violante et al., 2014). However, if the mid- and late-Holocene sea-level changes on the ACS seems well documented (e.g., Cavallotto et al., 2004; Schellmann and Radtke, 2010, and references therein; Violante et al., 2014, and references therein), it appears that the reconstruction of the chronology of the transgression and the sea-level changes prior to mid-Holocene suffers from a significant lack of available sedimentological data (Violante and Parker, 2004).

In the southern part of the ACS along the Patagonia Atlantic coast, the shore of the Gulf of San Jorge (hereafter referred to as GSJ; Fig. 21) and adjacent areas provide preferential records to reconstruct Holocene sea-level history due to numerous and well preserved littoral forms (i.e., beach ridge systems, littoral terraces and valley-mouth terraces; Schellmann and Radtke, 2010). According to the synthesis work conducted by Schellmann and Radtke (2010), the sea-level rise in the middle and south Patagonia (including the GSJ region) reached the modern coastline around 8600 cal a BP and the Holocene transgression maximum lasted from 7400 to 6600 cal a BP. After this period, the coasts in the GSJ area experienced a progressive and discontinuous falling of relative sea-level characterized by several phases with different rates of relative sea-level lowering (Zanchetta et al., 2012, 2014; Bini et al., 2017). Prior to Holocene, Ponce et al. (2011), whose work is based on a model of palaeogeographical evolution of the Patagonia coast since the LGM using the global sea-level curve proposed by Fleming et al. (1998), suggest the onset of GSJ invasion by marine transgression around 15.5 cal ka BP, when the water level reached ~90 m below present sea-level. However, except for the study of Ponce et al. (2011) and the regional sea-level curve proposed by Guilderson et al. (2000), no investigation have been performed until now to

reconstruct the timing of the marine transgression prior to mid-Holocene in this sector of the ACS.

In the last 30 years, a large number of surveys and studies carried out mostly in the northern part of the shelf have contributed to identify the main features of the morphostratigraphy and sedimentary sequences of the ACS from Late Pleistocene to the Holocene marine transgression (e.g., Parker et al., 1997; Violante and Parker, 2004; Violante et al., 2014, and references therein). The sedimentary sequence related to the post-LGM times has been estimate to be thicker than 10 m in the northern part of the shelf and thinner (< 5 m) offshore Patagonia. As a large part of the ACS was subaerially exposed during the LGM, the base of the post-LGM sequence is delimited by a transgressive surface in most of the shelf (Violante and Parker, 2004; Violante et al., 2014). However, some of the pre-transgressive features have not been entirely altered by the marine transgression and, thus, numerous incised valleys and channels have been preserved in the shelf, betraying the existence of paleo-fluvial networks during lowstand phases (Violante et al., 2014). In front of the GSJ, the morphostratigraphy of the Patagonian shelf is characterized by the presence of a partially buried drainage system, as well as three terraces covered by coarse sediments and modelled during the phases of sea-level stabilization, in the post-glacial transgression between 11 and 18 ka BP (Parker et al., 1997; Violante et al., 2014).

In this study, we present the first detailed description of the upper sedimentary sequence of marine deposits in the GSJ based on high-resolution seismic stratigraphic interpretations coupled with chronostratigraphy of the post-LGM sediments and multiproxy analysis (including computerized axial tomography, magnetic susceptibility, diffuse spectral reflectance, elemental geochemistry, and grain size) from five sediment piston cores. The main objectives of this study are to (1) characterize the evolution of sedimentary environments and depositional history, as well as (2) document and discuss the chronology of the sea-level changes since the onset of the last marine transgression in the GSJ.

2.4 STUDY AREA

The GSJ forms an extension of the ACS, considered one of the largest siliciclastic shelves in the world with a width ranging between 170 and 850 km, and a total length of 2400 km. Extending along a relatively stable continental margin on most of its surface, the modelling of the shelf is mainly conditioned by sea-level fluctuations, sediment dynamics and climatic/oceanographic processes (Violante et al., 2014; Desiage et al., 2018). In the southern part of the shelf, the currents of the Patagonian section are dominated by a northward (NNE) flow of sub-Antarctic cold water conveyed onto the shelf through the Cape Horn Current, and the Malvinas Current along the continental slope (Palma et al., 2008 and references therein).

Located in the central part of Patagonia between latitudes 45°S and 47°S, the GSJ forms a semicircular basin of approximately 160 km long and 250 km wide with a surface area of 39,340 km². The bathymetry of the gulf is characterized by a rapid decrease of topography to reach the 90 m isobath which defines a large flat central region covering most of the surface of the gulf and corresponding to the Patagonian outer shelf (Violante et al., 2014). Moreover, the GSJ possesses a shallower elongated bank (~60 m) in its southern external part. The hydrodynamic and water mass characteristics are related to the northward circulation on the shelf and to the local drivers, notably tides and strong westerly winds (Palma et al., 2008). According to a high-resolution numerical model, the mean circulation corresponds to a cyclonic gyre, which is bounded to the west by an intense coastal current and to the east by the Patagonian Current, including seasonal variability (Matano and Palma, 2018). The macrotidal semidiurnal regime in the gulf is characterized by a mean tidal range of over 4 m (Isla et al., 2002).

From a geological and geographical point of view, most of the GSJ forms the eastern part of the hydrocarbon-producing San Jorge Gulf Basin which is surrounded by the Andean belt to the west, the North Patagonian Massif to the north and the Deseado Massif to the south. Covering an area of around 170 000 km² with one-third located offshore, the GSJ

basin is a dominantly extensional basin onset during Middle Jurassic in which Jurassic-Cretaceous sedimentary sequence are exploited today for oil- and gas-production (Figari et al., 1999; Sylwan, 2001). The GSJ basin is filled with Tertiary deposits mainly composed by an alternation of continental (including fluvial and lacustrine depositional environment) and marine sedimentary rocks (Sylwan, 2001; Paredes, 2002). These Tertiary formations as well as the Quaternary marine and fluvio-glacial deposits (e.g., 'Rodados Patagónicos'; Martínez and Kutschker, 2011) constitute most of the tablelands and terraces overlaying the GSJ basin. The tablelands reach the coast as cliffs or coarse-clastic beach-ridge systems (Pleistocene-Holocene), generally composed of gravel and/or sand (Isla et al., 2002; Schellmann and Radtke 2010 and references therein).

The gulf does not have any present-day major and perennial tributaries affecting significantly the sedimentation. The GSJ is located in the heart of several hundred kilometers of littoral without major rivers, except for the relatively low flow Deseado River ($5 \text{ m}^3\text{s}^{-1}$; Kokot, 2004), reaching the ocean a few dozen kilometers south of the GSJ. However, during the late Pleistocene and the early-Holocene, the streams of Patagonian Rivers, including the Deseado River, were more significant prior to the partial reversal of the Patagonian Icefield subglacial drainage from the Atlantic to the Pacific coasts (McCulloch et al., 2000; Kokot et al., 2004; Isla et al., 2015). Based on grain size, mineralogical and geochemical data as well as sediment unmixing model , Desiage et al. (2018) suggested that the origin of surface sediments in the GSJ, dominated by fine to medium silt, is 50% from external/oceanic inputs, 40% from the inner gulf shores (i.e., erosion and runoffs) and 10% from dust (i.e., aeolian transport).

2.5 METHODS

The data used in this study were collected on board the R/V Coriolis II from February 17th to March 4th during the MARGES expedition, as part of the PROMESSe (PROgrama Multidisciplinario para el Estudio del ecosistema y la geología marina del golfo San Jorge y

las costas de las provincias de Chubut y Santa Cruz) project. The geophysical survey consists in ~2000 km of high-resolution data acquired in the GSJ, mostly in the northern part, and on the shelf in front of the gulf using simultaneously or alternatively a Chirp sub-bottom profiler and a sparker (Figs. 20,21,22 and 23). Based on the seismic data analysis, five piston cores (PC; Fig. 25) and their companion trigger weight cores (TWC), ten gravity cores (GC) and eight box cores (BC) were recovered in the GSJ. This paper focus on the combined study of sparker seismic data and piston cores, with a focus on four selected cores: 003PC, 006PC, 008PC and 011PC (Figs. 20 and 25; Table 6). Only the first 230 cm of the core 006PC are used in this study because of the absence of any datable material on the lower part of the core, as well as the presence of an erosional contact dividing two distinct lithological units between the dated and the undated sections of the core. The core 001PC is partially presented but not used due to its short sedimentary record and the potentially missing several first centimeters of sediments (see details in part 2.6.3). Physical and geochemical properties of box cores were used to ensure that the top sediments in the piston cores were preserved (Fig. 31).

Tableau 6: Location, water depth, length and piston cores retrieved in the GSJ during the MARGES expedition

Core	Latitude (°S)	Longitude (°W)	Water depth (m)	Length* (cm)	Samples
COR1404-001PC	66.734	45.907	100.5	103	15
COR1404-003PC	66.255	45.6735	94	411	62
COR1404-006PC	66.461	45.45	90.5	369	62
COR1404-008PC	65.984	45.486	95	271	48
COR1404-011PC	65.924	45.75	97	406	49

* = Length of whole core measured on the vessel

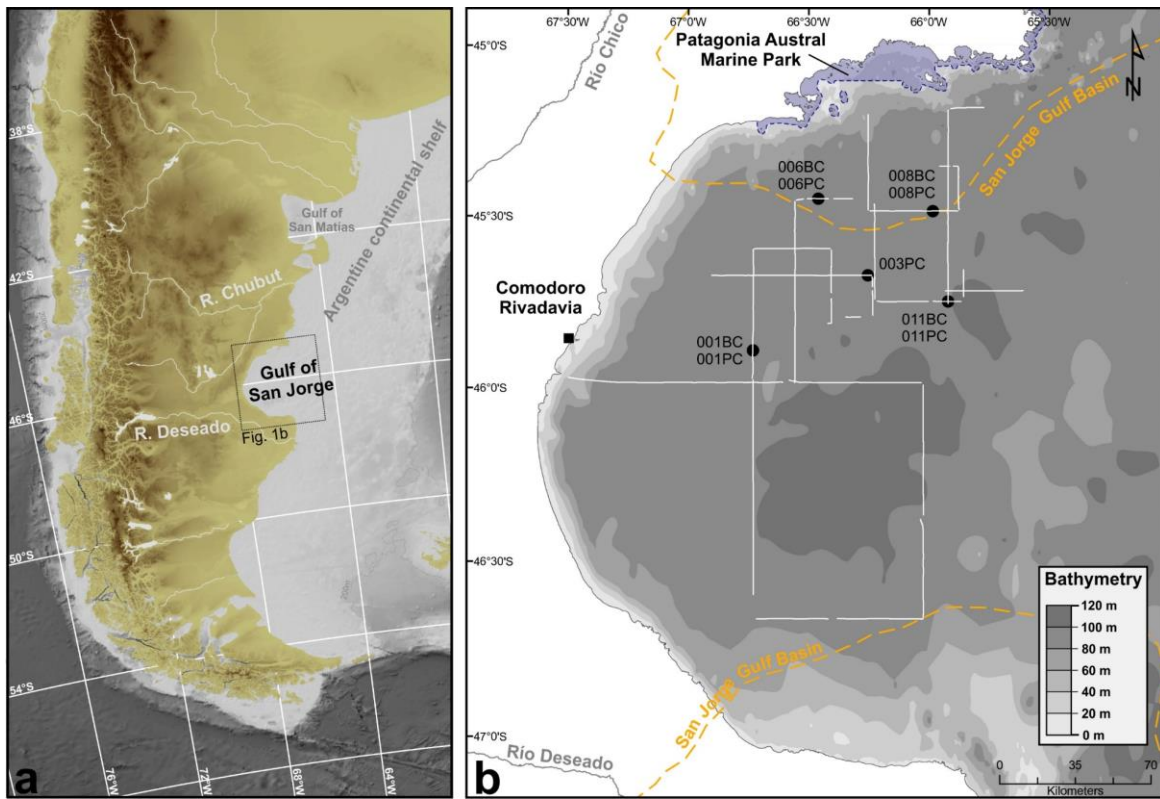


Figure 21: (a) Regional map showing the location of the Gulf of San Jorge in the southern part of South America. (b) Bathymetric map of the Gulf of San Jorge with position of piston cores and related box cores (black dots), as well as seismic sparker profiles (white lines) used in this study

2.5.1 Physical and geochemical properties of sediment cores

In the laboratory, the whole core sections were first run for the wet bulk density obtained by gamma ray attenuation and the volumetric magnetic susceptibility (k_{LF}) at 1-cm intervals using a GEOTEK Multi-Sensor Core Logger (MSCL). Digital X-ray images of sediment cores were also carried out with a CT-Scan (computerized axial tomography) at INRS-ETE (Québec City). The resulting images are displayed in greyscale representing lower and higher X-ray attenuation primarily related to bulk density (e.g., St-Onge et al., 2007, Fortin et al., 2013). The cores were then split, described and photographed (Fig. 27). Diffuse spectral reflectance measurements (sediment color) were carried out on fresh split core sections using a Minolta CM-2600d handheld spectrophotometer online with the MSCL

and then converted into the L*, a*, b* (L*: lightness; a*: green-to-red scale; b*: blue-to-yellow scale) color space of the CIE (International Commission on Illumination). Downcore element concentrations were measured at the split core surface using an Olympus Innov-X Delta Premium portable X-ray fluorescence (pXRF) mounted on the MSCL. The resolution of the magnetic susceptibility analyses were also improved with the use of a point sensor on the split core. The color reflectance, pXRF and the refined magnetic susceptibility measurements were performed at 0.5-cm and 1-cm intervals for box cores and piston cores, respectively. Prior to grain size analysis, the five piston cores were evenly sampled every 8 cm with a refined sampling at 4-cm intervals for basal sections of cores 003PC, 006PC and 008PC (total of 236 samples).

The grain size analysis of sediment samples was carried out on the detrital fraction using a Beckman Coulter LS 13 320 particle size analyser (0.04-2000 μm). Deflocculation was performed by successive washing with distilled water and the samples were mechanically shaken for 12h before measurement. Grain size distribution and statistical parameters were processed with the GRADISTAT software using the geometric (μm) and logarithmic (ϕ) method of moments (Blott and Pye, 2001).

We use the Log(Ti/Ca) and Log(Rb/Sr) ratios to monitor past changes in terrigenous detrital content relative to the marine carbonates (Blanchet et al., 2009; Tjallingii et al., 2010; Mollier-Vogel et al., 2013; Rothwell and Croudace, 2015). Indeed, the origin of Ti in sediments is commonly associated with inputs of terrigenous continental material, whereas a substantial part of Ca could be related to biogenic inputs, and so the Ti/Ca ratio can record the relative variations of terrigenous clastic inputs and marine carbonates (e.g., Tjallingii et al., 2010; Rothwell and Croudace, 2015; Li et al., 2019). Furthermore, Rb/Sr ratios can also be applied as another indicator of the relative magnitude of terrigenous clastic and biogenic inputs (Rothwell and Croudace, 2015; Li et al., 2019). Mica-enriched clay fraction is characterized by high Rb/Sr, whereas carbonate-enriched sediments by low Rb/Sr values (e.g., Zhang et al., 2015). Furthermore, the geochemical data are of a compositional nature, that is, they are vectors of non-negative values subjected to a constant-sum constraint (usually

100%). This implies that relevant information is contained in the relative magnitudes, so statistical analysis must focus on the ratios between components (Aitchison, 1986). Under this framework, the geochemical data were represented here as log-ratios. Note that a log-transformation will reduce the very high values and spread out the small data values and is therefore well suited for right-skewed distributions (van den Boogaart and Tolosana-Delgado, 2013).

The elemental composition analysis of sample 003PC-AB-376 was performed using an INCA X-sight energy dispersive X-ray spectrometer (Oxford Instruments) coupled to a JEOL 6460LV scanning electron microscope. X-ray spectra were measured from 10 randomly chosen particles, with two or three spectra per particle (Fig. 30). Each spectrum was acquired for 120 seconds of live time at an accelerating voltage of 20 kV. System quantitative optimization was made using copper as standard.

2.5.2 Radiocarbon dating

Twenty-two samples of bivalve shells (complete or fragments) from the five piston cores were dated by accelerator mass spectrometry (AMS) ^{14}C at the Keck-Carbon Cycle AMS facility (University of California, Irvine). The samples were previously prepared and pre-treated at the Radiochronology Laboratory of the Centre d'études nordiques (Laval University). Furthermore, two samples of micro-fragments of algae and wood were dated by AMS ^{14}C at the Laboratoire des sciences du climat et de l'environnement (LSCE, CNRS-CEA-UVSQ). The micro-fragments were retrieved in sieved sediment from 1 cm section of core 06PC (49-50 cm and 231-232 cm). Radiocarbon ages were calibrated using the software CALIB version 7.1 (Stuiver and Reimer, 1993) and the Marine13 calibration curve (Reimer et al., 2013). Due to the evolution of depositional environments in the sediment cores and the uncertainties about post-LGM ^{14}C -reservoir values of the extensive Atlantic coast of Argentina (Gómez et al., 2008; Schellmann and Radtke, 2010), two different values of marine regional reservoir correction (ΔR) were applied: (i) $\Delta\text{R} = 0$ as suggested and used for mollusc shells in coastal environments of the GSJ area (Cordero et al, 2003; Schellmann and Radtke,

2010); and (ii) $\Delta R = 200$ as used by Guilderson et al. (2000) on the Argentine Shelf and based on the ^{14}C reservoir value (R) of about 560 to 600 years for the Falkland current (Broecker and Olson, 1961). The conventional and calibrated ages are presented in Table 7. The calibrated ages are suggested according to their ± 2 sigma range (95% degree of confidence).

Prior to the construction of age-depth models, the correlation of the physical and geochemical parameters measured on the piston cores and their related box cores (i.e., retrieved at the same site) have been conducted to estimate the absence and the deformation of sediments at the top of piston cores (Fig. 31). To compensate for the absence of box core at the site of core 003PC as well as the overpenetration of the companion trigger weight core noticed during the expedition, this core was correlated with the closest “depth corrected” piston core 011PC. The correlation suggests that, except for core 008PC in which 2 cm are missing, no sediments were lost due to coring at the top of cores 003PC, 006PC and 011PC. The deformation of muddy sediments in the uppermost part of cores 006PC, 008PC and 011PC, related to the cumulative action of compaction and stretching during piston coring, is estimated to be approximatively 4.5 cm, 3 cm and 2 cm, respectively. According to these results, the depths of the piston cores have been adjusted and the age-depth models for cores 003PC, 006PC, 008PC and 011PC have been generated using corrected depths. Finally, no significant correlations have been found between the short piston core 001PC and the first 35 cm of 001BC which might suggest that at least 35 cm are missing at the top of 001PC. For this reason, and due to the configuration of the core and the lack of available ^{14}C dates, no age-depth model has been generated for core 001PC. According to the results of the correlations, which seem to imply that the top of the piston cores represents the actual sedimentation (i.e., no/few sediment missing), the age-depth models have been constructed considering the top of cores as modern ages.

In this paper, the corrected depths for piston cores 003PC, 006PC, 008PC and 011PC were only used for the development of age models. The “best fit” linearly interpolated age-depth models were constructed using the Bayesian statistical approach of the BACON v2.2 package of the R software (Fig. 28; Blaauw and Christen, 2011). The age-depth models were

Tableau 7: Radiocarbon ages from the piston cores analysed in this study. All ages were calibrated using the software CALIB version 7.1 (Stuiver and Reimer, 1993) with the Marine13 calibration curve (Reimer et al., 2013) and two different values of ΔR (0 and 200; see details in Radiocarbon dating section). Calibrated ages are presented with their minimum, maximum and median values

Core	Depth in core (cm)	Corrected depth	Lithology	Material	^{14}C age (uncalibrated)	^{14}C cal BP (2 sigma; $\Delta R = 0^*$)	^{14}C cal BP (2 sigma; $\Delta R = 200^*$)	Lab. ID
001PC	81		Olive gray silty clay (L4)	Shell fragment	8275 ± 25	(8698-8957) 8831	(8439-8600) 8531	UCIAMS-163922
001PC	86		Shell bed (L4)	Shell fragment	10400 ± 25	(11276-11701) 11468	(11118-11260) 11192	UCIAMS-163923
003PC	155.5	155	Olive gray silty clay (L4)	Shell fragment	6340 ± 25	(6718-6890) 6804	(6484-6651) 6574	UCIAMS-163005
003PC	210.5	210	Shell bed (L3)	Bivalve shell	10580 ± 25	(11713-12026) 11881	(11249-11660) 11415	UCIAMS-163004
003PC	275	274.5	Shell bed (L3)	Bivalve shell	11835 ± 35	(13205-13409) 13307	(12994-13253) 13133	UCIAMS-163915
003PC	296	295.5	Light olive gray clayey silt (L3)	Bivalve shell	12170 ± 25	(13482-13749) 13617	(13317-13507) 13412	UCIAMS-163000
003PC	310	309.5	Shell bed (L3)	Bivalve shell	12360 ± 30	(13719-13966) 13837	(13470-13743) 13605	UCIAMS-163914
003PC	330	329.5	Light olive gray clayey silt (L3)	Shell fragment	12210 ± 35	(13511-13803) 13667	(13334-13561) 13446	UCIAMS-163912
003PC	330	329.5	Light olive gray clayey silt (L3)	Shell fragment	12365 ± 30	(13724-13971) 13843	(13475-13749) 13611	UCIAMS-163921
006PC	13	17	Olive gray silty clay (L4)	Bivalve shell	Modern			UCIAMS-163908
006PC	146	150.5	Shell bed (L4)	Bivalve shell	10125 ± 20	(11054-11210) 11138	(10745-11028) 10888	UCIAMS-194470
006PC	204	208.5	Light olive gray clayey silt (L3)	Shell fragment	12315 ± 25	(13665-13911) 13789	(13436-13686) 13556	UCIAMS-163006
006PC	219	223.5	Shell bed (L3)	Bivalve shell	12290 ± 30	(13626-13888) 13761	(13411-13666) 13529	UCIAMS-163916
006PC	230	234.5	Light olive gray clayey silt (L3)	Shell fragment	12480 ± 30	(13834-14089) 13962	(13612-13877) 13749	UCIAMS-163019
008PC	49	47.5	Olive gray silty clay (L4)	Algae/wood micro-fragments	$2290 \pm 50^{**}$	(1772-2043) 1902	(1541-1801) 1666	GifA17577a
008PC	171	169.5	Olive gray silty clay (L4)	Shell fragment	6910 ± 20	(7367-7478) 7424	(7169-7298) 7240	UCIAMS-163913
008PC	190	188.5	Light olive gray clayey silt (L3)	Bivalve shell	9390 ± 25	(10162-10287) 10217	(9885-10124) 10004	UCIAMS-163911
008PC	200	198.5	Shell bed (L3)	Shell fragment	10470 ± 25	(11372-11828) 11621	(11166-11344) 11247	UCIAMS-163926
008PC	214	212.5	Mass wasting deposit (L3)	Shell fragment	38060 ± 400	(41417-42567) 42007	(41255-42449) 41872	UCIAMS-163920
008PC	231	229.5	Laminated clayey silt (L2b)	Wood/Algae micro-fragments	$11270 \pm 50^{**}$	(12643-12848) 12740	(12517-12706) 12609	GifA17578a
011PC	20	17	Olive gray silty clay (L4)	Bivalve shell	575 ± 20	(137-275) 219		UCIAMS-163925
011PC	334	332	Olive gray silty clay (L4)	Shell fragment	6045 ± 20	(6391-6537) 6459	(6198-6312) 6264	UCIAMS-163924
011PC	378	376	Shell bed (L3)	Bivalve shell	10605 ± 20	(11774-12045) 11923	(11289-11702) 11477	UCIAMS-163007
011PC	391	389	Light olive gray clayey silt (L3)	Shell fragment	10990 ± 25	(12473-12634) 12558	(12074-12450) 12264	UCIAMS-162999

* = calibrated with: Marine13 and CaliB, reservoir correction factor is the global mean of 400 years (Hughen et al., 2004).

** = 1 sigma

generated using a marine regional reservoir correction (ΔR) of 0 in order to compare and discuss the chronostratigraphic records previously published in the GSJ area (e.g., Schellmann and Radtke, 2010).

2.5.3 Geophysical surveys and data processing

The high-resolution sparker data were collected with an Applied Acoustics Squid 2000 sparker array shooting at an interval of 1s (~ 3 m) with an output energy between 1000 and 1500 J. The acoustic signal was recorded with a 12-element, 50-m long single channel streamer. The sparker source and the streamer were towed ~ 20 m from the stern of the ship. Sparker raw data were processed with the Schlumberger's VISTA commercial seismic processing package. The processing procedure included swell correction, Butterworth band-pass filtering, minimum-phase spiking deconvolution, scaling correction, automatic gain control and trace mixing (Duchesne and Bellefleur, 2007; Duchesne et al., 2007). The application of this processing routine allowed an effective attenuation of the artifacts related to strong secondary arrivals inherent to sparker sources (Mosher and Simpkin, 1999). However, a ringing pattern persists close to the seafloor interface with the consequence of reducing the vertical resolution as well as restricting the interpretations for the uppermost section. In addition, the seismic data were corrected for the tide using a MATLAB tide correction algorithm. The processed seismic data were then integrated and analysed with the commercial seismic and geological interpretation software IHS Kingdom. The acoustic travel times were converted into depths by using an average seismic velocity of 1480 m.s^{-1} in the water column and 1540 m.s^{-1} in the sedimentary deposits according to velocity previously used to investigate Quaternary deposits on the ACS (Kostadinoff, 1992).

2.6 RESULTS AND INTERPRETATIONS

2.6.1 Seismostratigraphy

On the basis of the analysis of high-resolution sparker and chirp seismic profiles, five seismic units, including acoustic basement, have been identified in the uppermost succession of offshore sedimentary sequence in the GSJ. The five seismic units introduced below are

labeled from the oldest to the most recent. The description and interpretation of the seismic units were performed using sparker profiles in accordance with standard procedure of seismic stratigraphy (e.g., Mitchum et al., 1977; Sangree and Widmier, 1979).

Unit S0 – Acoustic basement

The unit S0, considered in this paper as the acoustic basement, is characterised by series of high-to-moderate amplitude reflections interspersed by transparent intervals. The configuration of the seismic reflections varies from sub-parallel and wavy in the central part of the GSJ (Fig. 22) to oblique in the northern, southern and external sectors (Figs. 23 and 24). The surface of the unit is defined by a high-amplitude reflection forming alternatively smooth mounded erosional surface and irregular incised erosional truncation. This last irregular incised surface forms channels and valleys observed mainly in the central-external part of the gulf (Figs. 23 and 24). The top surface of the acoustic basement reached the seafloor and crops out at ~10 km off Comodoro Rivadavia in the western part of the GSJ as well as ~40 km off the coast of the Patagonia Austral Marine Park in the northern area.

According to the previous investigations of the terrestrial GSJ Basin stratigraphy, which are based on outcrop and wells log descriptions, as well as seismic profiles analysis, we make the hypothesis that Unit S0 is composed of mid-Cenozoic sedimentary successions, including the uppermost Santa Cruz and Chenque (Patagonia) Formations (Bellosi, 1990; Nullo and Combina, 2002; Paredes, 2002). Furthermore, similar seismostratigraphic characteristics, with a distinct discordance between Miocene and Pleistocene/Holocene deposits, have been previously observed ~500 km north of the GSJ in the gulf of San Matías (Mouzo, 2017). The unit S0 would thus correspond to the late Oligocene-Miocene marine-estuarine deposits (Chenque Formation) which are mainly composed of sandstones interbedded with claystones, transitionally overlain by fluvial-aerial deposits (Santa Cruz Formation) characterized by sandstone and claystone beds (Nullo and Combina, 2002; Paredes, 2002).

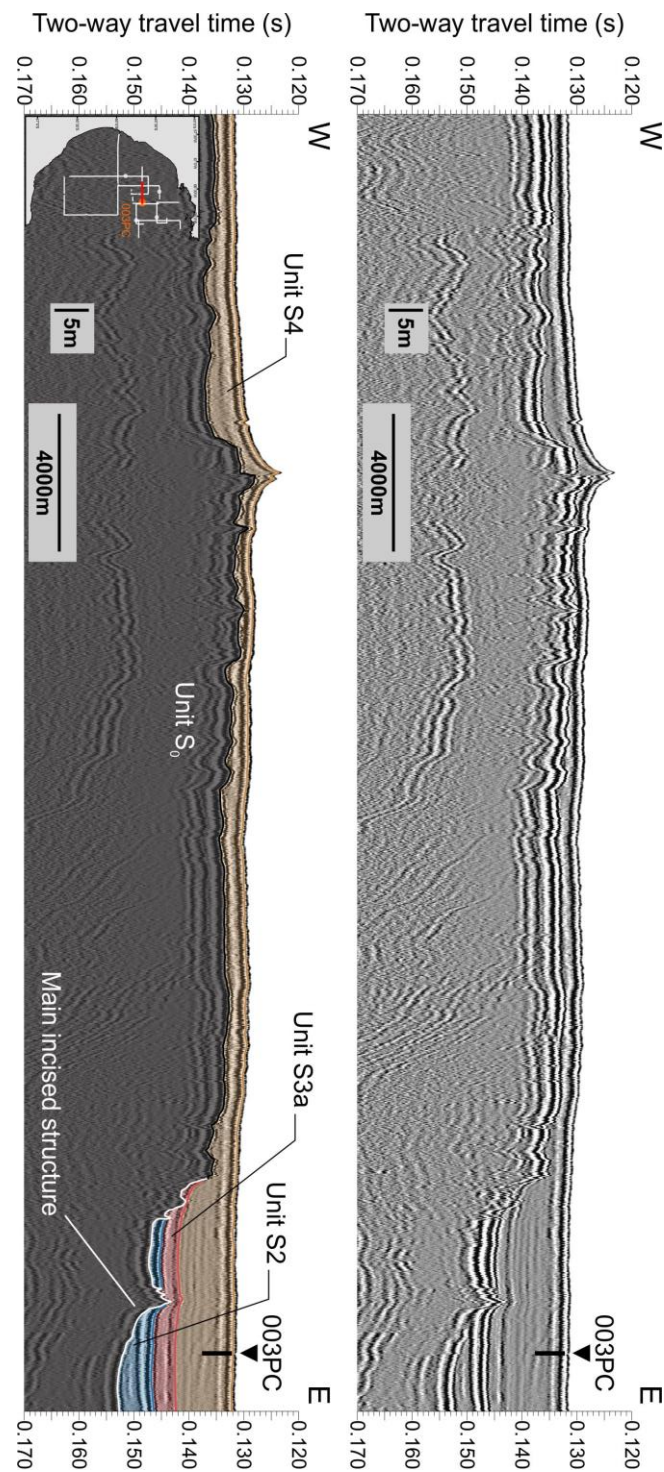


Figure 22: High-resolution sparker seismic profile (section of line 008; top) with interpreted version (base) showing four seismic units and sub-units (units S₀, S₂, S_{3a} and S₄), incised valley (white line) as well as location of core 003PC

Units S1

The units S1a and S1b were only identified on seismic lines 017, 018 (Figs. 22 and 31) and 009 filling the deepest incised structure observed in the gulf. These units are defined by high-to-low amplitude (Unit S1a) and low-to-moderate amplitudes (Unit S1b) wavy-to-parallel reflections. The geometry of these units is characterized by a divergent configuration with a combined maximum deposits thickness of ~35 m in the deepest part of the depression. Unit S1b covers unit S1a and its upper boundary corresponds to slightly irregular surface which completely bury the incised structure.

Observed in the basal part of the deepest incised structure, the acoustic configuration of unit S1a with high amplitude and confined continuous reflections suggests to reflect incised-valley fill deposits formed in sea-level lowstand conditions. The deeply incised shape of the depression, the high frequency of high amplitude and continuous reflections alternating with semitransparent and finally laminated ones, as well as the distinct onlap against the edges supports the accumulation of fluvial deposition (e.g., Dung et al., 2013; Weschenfelder et al., 2014; Yoo et al., 2016). The slightly transparent appearance with weaker reflections of S1b implies more homogenous deposits, possibly suggesting an evolution to relatively more stable environment. This transition could have been caused by the flooding of the GSJ during a marine transgression event with the establishment of shallow marine conditions coupled with low to moderate currents such as lagoonal or estuarine environments (e.g., Menier et al., 2006; Weschenfelder et al., 2014; Bae et al., 2018). The acoustic characteristics of unit S1b could also suggest some major changes in the hydrodynamic conditions of the valley's fluvial network. Indeed, it could be related to an extensive modification of the regional drainage system which could have led to the settle of a depositional environment characterized by low-to-moderate energy conditions. However, the interpretation of depositional environments of units S1 is relatively speculative and cannot be corroborated by lithostratigraphic analysis due to the absence of sediment cores intersecting the seismic units.

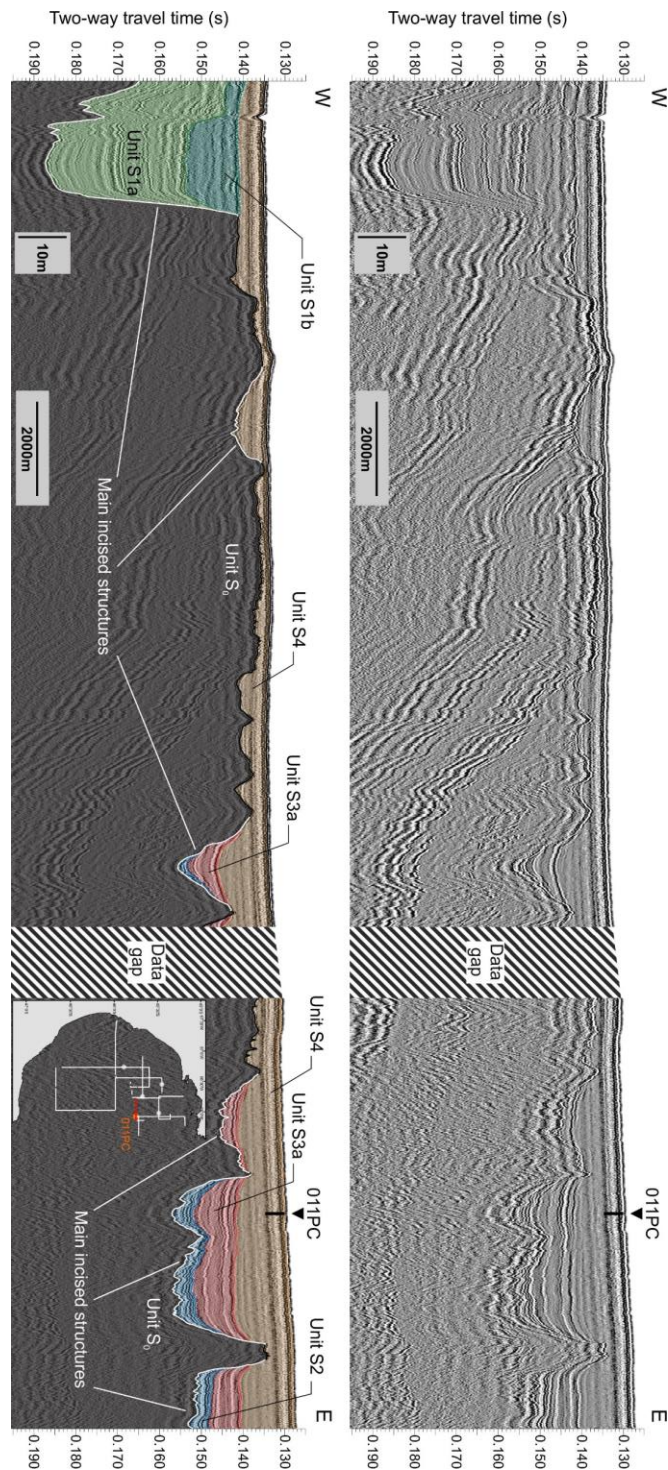


Figure 23: High-resolution sparker seismic profile (section of line 018; top) with interpreted version (base) showing six seismic units and sub-units (units S0, S1a, S1b, S2, S3a and S4), incised valleys (white lines) as well as location of core 011PC

Units S2 and S3

Unit S2 shows series of high amplitude reflections alternating with low-to-moderate amplitude reflections. The configuration is slightly wedge-shaped with confined wavy-to-sub-parallel laterally continuous reflections. The seismic terminations onlap against the incised structure walls. Its base unconformably overlies the surface of acoustic basement S0. In the gulf, unit S2 is present exclusively in the deepest incised channels and valleys, except for the depression filled by units S1, in which its maximal thickness reached ~5 m.

Units S3a and S3b are characterized by low to medium amplitude reflections and appear as semitransparent acoustic facies. The unit S3a is also observed in the deepest incised structures overlying unit S2, as well as acoustic basement S0 in shallower depressions. The configuration of the seismic reflections shows confined sub-parallel laterally continuous reflections. In the incised channels and valleys, the basal surface of S3a is concordant with S2 and when the latter is absent, S3 unconformably overlies S0. As observed for S2, the seismic terminations onlap against the incised structure walls. The thickness of this unit ranges from <1 to 10 m in these depressions. Seismic unit S3b was observed in the southern-external investigated area of the gulf where its maximal thickness can reach ~17 m at the depocenter (Fig. 24). In this sector, the slightly downlapping seismic reflections of S3b present sigmoidal configuration forming a large-scale slightly mounded (i.e., convex-upward) morphology.

The interpretation of units S2 and S3 is also based solely on the analysis of their reflection characteristics because these units have not been reached by piston cores. As for Units S1a and S1b, the aspect and configuration of units S2 and S3a observed in incised structures suggest valley fill deposits formed in sea-level lowstand or transgressive conditions. According to the high amplitude and continuous reflections alternating with semitransparent and finally laminated ones and the distinct onlap against the edges of incised structures as also described for S1a, we propose that seismic unit S2 could correspond to the filling of paleochannels by fluvial deposits (e.g., Dung et al., 2013; Weschenfelder et al., 2014; Yoo et al., 2016). The seismic unit S3a shows similar acoustic configuration with S1b,

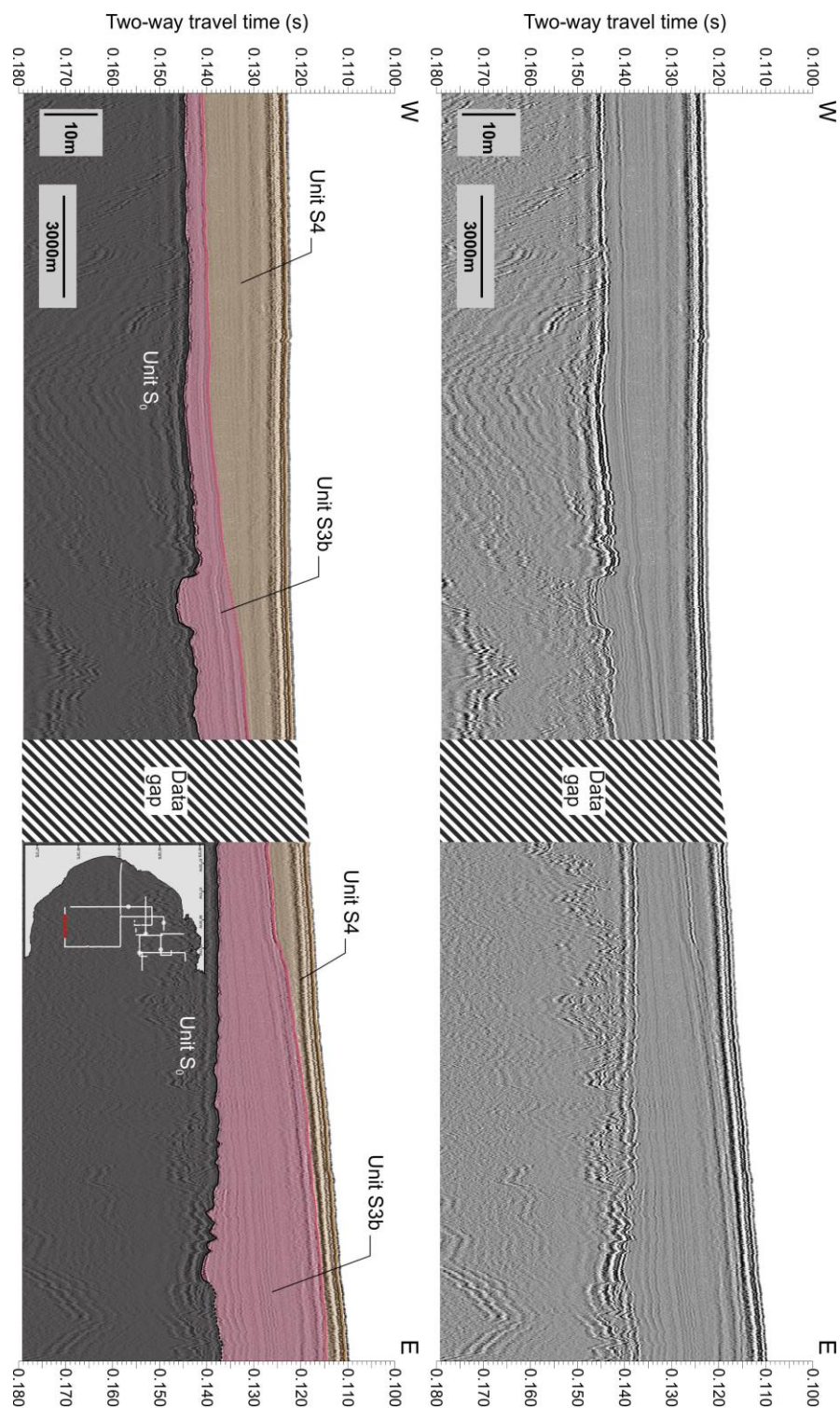


Figure 24: High-resolution sparker seismic profile (section of line 003; top) with interpreted version (base) showing three seismic units and sub-units (units S₀, S_{3b} and S₄)

characterized by low-amplitude and symmetric reflections with the onlap of seismic termination against the incised valleys walls, interpreted in this study as possible deposits formed in relatively low-to-moderate energy conditions, such as lacustrine or estuarine environments (e.g., Gilli et al., 2005; Menier et al., 2006; Bae et al., 2018).

In the south-west part of the GSJ, the limited distribution of unit S3b indicate sedimentary process only affecting this sector of the gulf. The sigmoidal configuration of medium amplitude reflections and the laterally elongated configuration of S3b advocate that the deposition of this unit was controlled by predominant hydrodynamic factors. Indeed, the deposits associated to unit S3b show similar seismic characteristics to morphological features such as large sand bodies (Dyer and Huntley, 1999; Liao et al., 2008) or shallow-water bottom current sand deposits (Viana et al., 1998) formed as a result of a strong predominant or combined currents (e.g., geostrophic, longshore and tidal currents). Furthermore, according to the bathymetry, this morphological feature seems to coincide with a shallow bank facing NNE which divides the southern part of the GSJ from the shelf (Fig. 21). The development of these deposits could thus be linked to the transport of coarse sediments by strong NE longshore current (Matano and Palma, 2018) originating from the Deseado River which is located a few dozen kilometers south of the GSJ, at a time when its flow was more significant (Kokot et al., 2004; Isla et al., 2015). However, since the unit S3b is only observed on two seismic lines intersecting perpendicularly, it appears complex to characterize and delimit it and thus to define the mechanisms behind its deposition.

Unit S4

Unit S4 is mostly semi-transparent with few low-amplitude sub-parallel reflections. In most of the GSJ, unit S4 unconformably overlies the acoustic basement S0, and occasionally, the basal surface of S4 is concordant with S3a in the deepest incised structures. In the southern-external area of the gulf, unit S4 overlies S3b and its base is characterised by onlap terminations. The surface of unit S4 corresponds to most of the present-day seafloor in the GSJ. Its thickness varies from less than 1 m to approximately 8 m in the deepest incised

valleys, but its maximum thickness is observed in the southern-external part of the GSJ where it can reach ~ 13 m.

With the exception of the acoustic basement, S4 is the only seismic unit reached by sediment cores (Figs. 21, 22 and 32). According to the lithologic and chronostratigraphic interpretation of these sedimentary records, the upper part of S4 corresponds to deposits of the last marine transgression, as well as Holocene hemipelagic sedimentation (see Section 2.6.2). However, in several sectors of the GSJ, in which more accommodation space was available, significant section of the basal part of S4 were not reached by sediment cores (Figs. 21, 22 and 23). Thus, in the absence of complete recovery of the thickest part of unit S4 with sedimentary records, it remains unclear if S4 corresponds solely to deposits settled since the last marine transgression or to deposits from older sedimentary environments such as previous Quaternary marine transgressions. Furthermore, the seismic architecture of unit S4 presents characteristics of aggradation to minor progradation even though the unit includes at least the sedimentary deposits of the last marine transgression. This could be explained by the relative equilibrium between sediment supply and eustatic sea-level changes in a passive relatively stable continental margin (Galloway, 1989). This configuration could possibly have been amplified by the shallow semi-enclosed morphology of the gulf as well as moderate sediment inputs in the GSJ during the Holocene. This low sediment input is due to the close to total absence of major perennial tributaries in this sector of Patagonia that are likely to supply the gulf with terrigenous material (McCulloch et al., 2000; Kokot et al., 2004; Isla et al., 2015; Desiage et al., 2018).

2.6.2 Lithostratigraphy

Based on multi-proxy analysis of the four piston cores 003PC, 006PC, 008PC and 011PC, four lithological units were defined for the uppermost offshore sedimentary sequence in the northern-central part of the GSJ.

Unit L1

Unit L1 is present in the basal part of core 008PC below 240 cm (Fig. 26). It is composed of well-indurated grayish brown (base) to olive gray (top) clayey silt present as angular pebbles potentially crushed by piston coring and core handling. The upper boundary of unit L1 is characterized by a sharp contact as well as 5 cm of mixed small angular pebbles and grayish brown gravelly muddy sand. A non-crushed section of unit L1 is also present in the last 13 cm of core 001PC (Fig. 25). The Log(Ti/Ca) and Log(Rb/Sr) ratios show the highest core-values in unit L1 of core 008PC, with a radical decline of values prior to the erosional contact between L1 and L2b.

Based on the indurated configuration of the sediments coupled with the seismo-stratigraphic context of cores 008PC and 001PC location, we suggest that unit L1 coincide with seismic unit S0 identified in this study as the seismic basement (Fig. 33). The high values of Log(Ti/Ca) observed in L1 indicate the predominance of detrital components over biogenic carbonate which could be interpreted as the control of sedimentation by fluvial inputs, enhanced coastal erosion of the inner gulf shores, relative sea-level rise or an increase of aeolian supply (Tjallingii et al., 2010; Rothwell and Croudace, 2015, and references therein). Furthermore, the high values of Log(Rb/Sr) could also express the significant weathering intensity occurred during the deposition of L1 (e.g., Jin et al., 2006). Unit L1 could thus correspond to late Oligocene-Miocene deposits related to marine-estuarine (Chenque Formation) or fluvial-aerial depositional environments (Santa Cruz Formation; Nullo and Combina, 2002; Paredes, 2002).

Unit L2

The thickest (64 cm) and more detailed interval of unit L2 was observed in core 003PC (Fig. 26). In this core, the unit L2 can be divided into two sub-units: the lowermost unit L2a, from 396 to 363 cm, and the uppermost unit L2b, from 363 to 332 cm. Unit L2a is composed of an interlacing of light olive gray to grayish green medium silt and light gray/bleu very-fine silt beds with thicknesses varying from mm to ~1cm. The median grain size is ranging

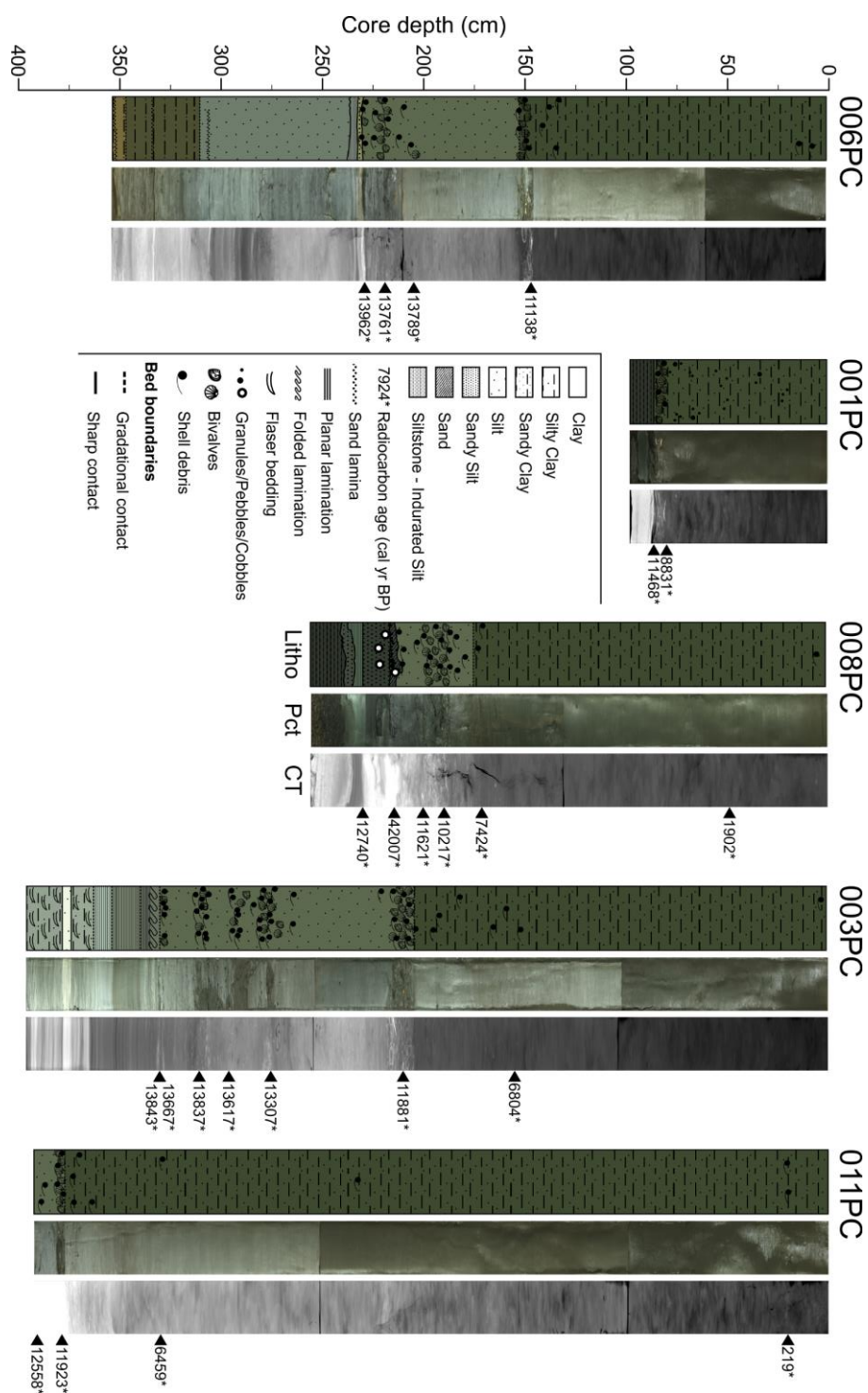


Figure 25: Lithologic descriptions (Litho), photographs (Pct), CT-scan images (CT) and calibrated radiocarbon ages from piston cores retrieved in the GSJ during the MARGES expedition

from 7.5 to 6 ϕ (Fig. 26). These wavy structures are occasionally draped by very thin (~1mm) dark gray silty-sand beds (Fig. 27A). Unit L2a is thus characterized by small-scale heterolithic bedding configuration, with multi-directional bedding pattern, interpreted as mud flasers (Fig. 27A) coupled with rare and scarcely defined ripples foresets (medium silt). Between 378 and 374 cm, unit L2a is interlayered by lighter sediments including a significant proportion of evaporite minerals (i.e., Gypsum; Fig. 27A), as suggest by SEM images and geochemical composition of sediment samples retrieved in this layer (Fig. 30). Unit L2b is composed of finely laminated clayey silt with noticeable transition of the main color from gray to olive gray at 353 cm. In unit L2b median grain size decrease with values oscillating around 7 ϕ (Fig. 26). The configuration of the unit L2b is thus described as mm-scale sub-parallel sedimentary rhythmites (Fig. 27B). The upper part of unit L2b shows soft-sediment deformation structures, defined by internally distorted and folded laminations with normal microfaults, bounded on the top by a scarcely defined contact coupled with a shell-rich bed (Fig. 27B). The boundary between sub-units L2a and L2b is gradational and the basal part of unit L2 was not recovered in core 003PC. The Ti/Al and Rb/Sr ratios display lowest core-values in unit L2a and in the basal part of L2b followed by a radical increase of values in almost 20 cm of unit L2b which coincides with the noticeable color transition of sediments starting at 353 cm (Fig. 26). A thinner section (~ 6 cm) of unit L2b with erosional upper and lower boundaries is also observed in core 008PC (Fig. 26).

The presence of heterolithic beds and sedimentary rhythmites in units L2a and L2b, with rhythmic variations in composition, color and grain-size, indicate that these units were produced under regularly repeated changes in sediment supply and physical conditions of sedimentation (Figs. 26A and 26B; Reineck and Singh, 1980). The configuration and the combined presence of these sedimentary structures seem to suggest that units L2a and L2b were formed in depositional environments tidally influenced (e.g., Hovikoski et al., 2007; Reineck and Singh, 1980; Flemming, 2012). The sedimentary facies of unit L2a with flaser structures of muddy sediments intercalated with coarser silty layers, as well as ripples of medium silt, resemble the facies of tidal flat sequences (Fig. 27A; Reineck and Singh, 1980).

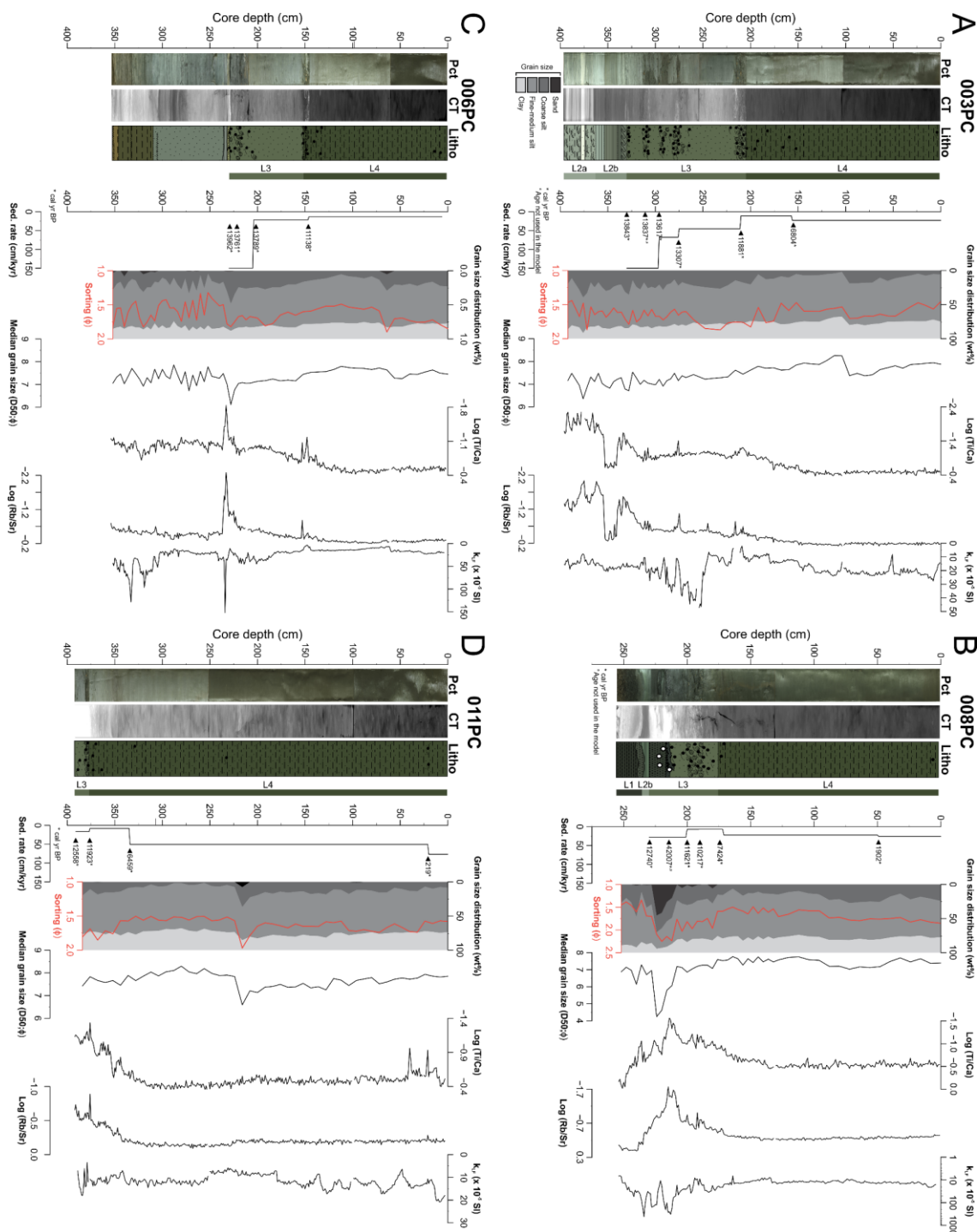


Figure 26: Grain-size and geochemical properties, magnetic susceptibility and sedimentation rate coupled with photographs, CT-scan images, lithologic description, lithofacies and calibrated radiocarbon ages of the investigated piston cores 003PC (A), 008PC (B), 006PC (C) and 011PC (D)

Furthermore, the gypsum rich layer in L2a reveals an environment favorable to evaporation with shallow waters and possibly slight freshwater inputs. Such depositional environments have been previously described and interpreted as hypersaline lagoon/marsh deposit in Holocene stratigraphic reconstruction along the coast close to the GSJ (Bahía Camarones; Zanchetta et al., 2012). The interpretation of units L2a and L2b as deposits of lagoonal/wind-tidal flat environments under semi-arid conditions is also suggested considering the lack of fossil (i.e., bivalve shells and foraminifera), as well as the presence of light olive gray and grayish green clayey bedding (Reineck and Singh, 1980 and references therein). The slightly finer-grained and sub-parallel laminations of unit L2b indicate a gradational transition to lower energetic conditions (i.e., lower velocity flows) as well as a possible decrease of tidal influences to the depositional processes. The radical increase of the Log(Ti/Ca) ratio, at the level of sediment color transition in unit L2b, points toward the increase of Ti in sediments in comparison to Ca. Considering the analogous ascent of Log(Rb/Sr) ratio, the pre-eminence of Ti could thus be interpreted as a significant increase in terrigenous inputs during the deposition of this layer. Such transitions of conditions recorded in unit L2b could suggest an abrupt evolution of depositional environment possibly related to sea-level rise or to a major change of regional drainage system leading to the increase of continental sedimentary supply (Tjallingii et al., 2010; Mollier-Vogel et al., 2013; Rothwell and Croudace, 2015; Li et al., 2019).

Units L3 and L4

The uppermost units L3 and L4 are present in each described cores (Fig. 26). Unit L3 consists of massive to crudely stratified light olive gray clayey silt with abundant and diffuse color mottles. The median grain size is ranging from 8 to 7 ϕ (Fig. 26). The sediments are extensively bioturbated with numerous bivalve shells and shell fragments including shell beds. In core 003PC, the base of unit L3 is characterized by gradational boundary with unit L2, whereas, in core 008PC, these units are divided by a sandy layer with lower and upper erosional boundaries, from 213 to 229 cm. This layer consists of very poorly sorted ($\phi > 2$) light gray sand with gravels including some well-rounded very coarse pebbles.

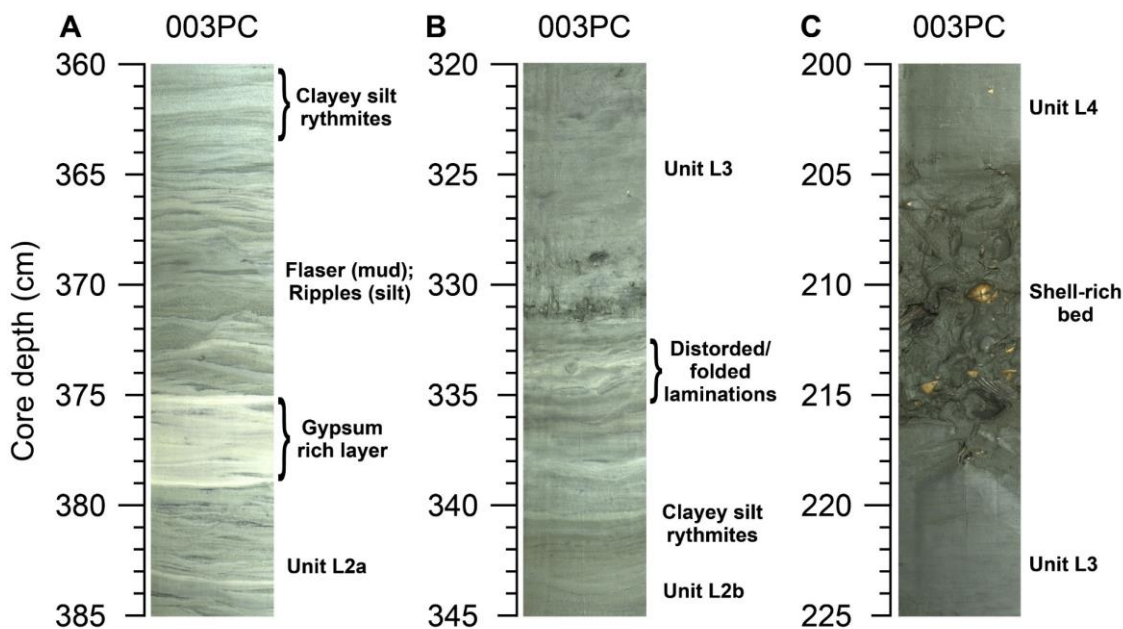


Figure 27: Photographs of unit L2a (A), the contact between L2b and L3 (B) as well as the transition between units L3 and L4 (C) in core 003PC

Unit L4 is composed of olive gray silty clay with occasional bivalve shells and shell fragments. Compared to L3, the median grain size slightly decreases to reach values closer to 8ϕ (Fig. 26). This extensively bioturbated unit shows mottled textures which are only visible on CT images. Its thickness varies from 175 cm in core 008PC to 375 cm in core 011PC. The boundary between units L3 and L4 is gradational and coupled with pluricentimetric shell bed in cores 003PC and 011PC (Fig. 27C). However, the boundary between these two units is not clearly defined in core 008PC, but could also be associated with a shell bed identified in this section of the core.

In unit L3 and L4, the Log(Ti/Ca) and Log(Rb/Sr) ratios display a relatively common pattern in every described cores with slightly increasing values in unit L3, which are significantly accentuated close to the transition between L3 and L4, and then followed by constant higher values in the upper parts of the latter unit. The magnetic susceptibility data depict progressive declining values in unit L3, as well as in the basal section of L4, and then constant lower values in the upper parts of L4, with values $< 50 \times 10^{-5}$ SI, except for the

sandy layer observed in 008PC which is characterized by an abrupt increase of magnetic susceptibility values ($> 200 \times 10^{-5}$ SI).

The abundant bioturbation structures and massive silty clay to clayey silt in units L3 and L4 denote sediments deposited under marine conditions with slow rates of sedimentation and deeper waters. The properties and configuration of L3 and L4 in cores 003PC, 006PC and 008PC suggest these units correspond to the progressive development to inner-shelf hemipelagic deposits (Reineck and Singh, 1980 and references therein). The slightly and almost steady fining-upward evolution of grain size, especially in core 003PC, coupled with the increasing values of Log(Ti/Ca) and Log(Rb/Sr) ratios in units L3 and L4, are interpreted as representing the gradual evolution towards distal and lower energetic marine conditions related to sea-level variations. In the main and upper part of L4, the relatively constant and stable physical, and geochemical proxies also suggest the development and the preservation of a marine depositional environment in the GSJ until surface sediments at the top of the cores. Furthermore, the lower and almost constant to slightly increasing values of Log(Ti/Ca) and Log(Rb/Sr) in L3 indicate a sedimentation more proximal than L4 in transition between the coastal tidally influenced environment of L2 and the marine hemipelagic environment of L4 (Fig. 26). In unit L3, the observation of several pluricentimetric shell beds, notably coupled with soft-sediment deformation structures in core 003PC, could also indicate an environment favorable to record extreme, rapid and repetitive events, such as storms waves (e.g., Aigner, 1985; Owen et al., 2011, and references therein). The formation of soft-sediment deformation structures may have numerous origins and trigger agents, for example seismic shaking, groundwater movements, tsunamis or major storms (Owen et al., 2011). However, the presence of repetitive, relatively thin and non-massive shell beds tend to favour deposits related to recurrent events like tempestites compare to hazardous and extreme events such as tsunamites (Puga-Bernabéu and Aguirre, 2017).

In both cores 003PC and 008PC, the contact between L2b and L3 is characterized as an abrupt event. However, the transition between these units doesn't seem to have been generated by the same sedimentary processes. As previously mentioned, the contact in

003PC, which consist of a shell-rich bed at the base of L3 coupled with soft-sediment deformation structures at the top of L2b, seems related to a rapid event such as storm waves. In 008PC, the transition between L2b and L3 which consists of a main layer of very poorly sorted silty sand overlaid with a thin layer of very coarse sand and fine granule with shell fragments both interlay with pluricentimetric rounded pebbles, could be associated to a more massive trigger such as a mass-wasting event in this part of the gulf. Moreover, the configuration of the retrieving sector of core 008PC on the outskirts of an incised valley could suggest possible outwash deposits related to a former drainage system discharging in the GSJ prior to marine invasion. Due to this event, a large part of sediments in units L2b and L3 could thus be missing in core 008PC.

2.6.3 Chronology and sedimentation rates

The conventional and calibrated ages are reported in Table 7. In order to compare and discuss the chronostrigraphic records previously published in the GSJ area (e.g., Schellmann and Radtke, 2010), the radiocarbon ages from our study are presented using the median of the calibrated ages with a ΔR of 0 (see details in Radiocarbon dating section). In core 003PC, the samples of isolated shell fragments or bivalve shells from the shell beds retrieved near the base of L3, yielded to ages between 13.8 and 13.6 cal ka BP. The observation of very close ages, sometimes with ages inversion, in a section of almost 30 cm, suggests an intense reworking of sediments possibly related to bioturbation as well as extreme and abrupt events such as storm waves which is also supported by the concentration of fragments and complete shells in shell beds. Similar ages from 14 to 13.8 cal ka BP have also been obtained in the basal part of the unit composed of light olive gray clayey silt (L3) in 006PC. Therefore, these ages collected at the base of L3 in 003CP, coupled with the presence of a gradational contact between L2b and L3, suggest that the transition to inner shelf hemipelagic sedimentation occurred at ~14 cal ka BP in this part of the GSJ. Ages of 11.9 and 11.6 cal ka BP from the shell beds at the transition of L3 and L4 in cores 003PC, 011PC and 008PC indicate a slight evolution of sedimentary depositional processes in the gulf from this period. In the core 006PC, a younger age, but relatively similar has also been obtained at the transition to the

olive gray silty clay unit (L4). The oldest age of 42 cal ka BP recovered in the potentially reworked deposit of L3 in 008PC is consistent with the mass-wasting origin of this deposit.

The calculated accumulation rates for sedimentary sequence covered by the age-depth models are ranging between 7 and 150 cm ka^{-1} . The highest sedimentation rates of 150 cm ka^{-1} have been calculated in cores 003PC and 006PC in the basal part of unit L3 which is characterized by several pluricentimetric shell beds and potential severe reworking. Due to the radiocarbon ages inversion in this section, the sedimentation rates have been generated using the samples retrieved at the top and at the base of the sequence of interest in cores 003PC and 006PC. According to the age-depth model from 003PC, the sedimentation rates decreased to 45 cm ka^{-1} at the top of L3. Furthermore, lower accumulation rates of 22 and 17 cm ka^{-1} have been calculated for the same sequence in cores 006PC and 011PC, respectively. After the shell bed marking the transition between L3 and L4, the sedimentation rates drop to the lowest values observed in the cores with rates not exceeding 11 cm ka^{-1} during the early Holocene. The accumulation rates then slightly increased to \sim 22 cm ka^{-1} for the mid- and late Holocene in cores 003PC and 008PC. For the same period, higher accumulation rates of \sim 50 cm ka^{-1} have been calculated for the most distal core 011PC.

2.7 DISCUSSION

2.7.1 Sedimentary environments prior to the last marine transgression

On In the continental part of the GSJ basin, numerous stratigraphic studies have shown that most of the tablelands and terraces overlaying the basin and outcropping to the surface are composed of Tertiary sedimentary formations, including the uppermost Santa Cruz and Chenque Formations, partially cover with Quaternary marine and fluvio-glacial deposits (e.g., Bellosi, 1990; Sylwan, 2001 and references therein; Isla et al., 2002; Nullo and Combina, 2002; Paredes, 2002; Martínez and Kutschker, 2011). According to the interpretation of geophysical profiles, we propose that the bedrock of the gulf, on which lies

the unconsolidated sediments, coincides with those Tertiary formation identified on land. Furthermore, the coupled analysis of sediment cores and seismic profiles suggests that the deposition of Pleistocene/Holocene occurred at the surface of these potentially mid-Cenozoic sedimentary units with a distinct discordance among those deposits as previously observed in the gulf of San Matias (Mouzo, 2017).

The numerous infilled channels and valleys incising the Tertiary deposits, observed mainly in the central part of the gulf (Figs. 21, 22 and 31), confirmed the existence of a paleo-fluvial network obliterated during the marine transgressions (Violante et al., 2014). Most of the incised channels and valleys observed in the inner portion of the gulf are extended continental shelves developed during multiple cycles of sea-level variations, primarily as a result of the erosional dynamic of rivers which are associated with a sea-level fall (Zaitlin et al., 1994). As the sea-level rose, the valleys began to be filled by sediments from numerous origins, as diverse as lagoonal to fully marine, and were remodelled during transgressive event by erosion related to tidal currents and waves among others (Zaitlin et al., 1994; Nordfjord et al., 2005; Weschenfelder et al., 2014). According to Rosgen (1994) classification, the initial river systems can be defined and characterized notably using geophysical data. This classification method accentuates the use of hydraulic parameters such as aspect ratios (e.g., width/depth ratio), sinuosity and slope, is also used to characterize buried incised valleys on the continental shelves (e.g., Nordfjord et al., 2005; Bae et al., 2018). Based solely on the wide aspect (high width/depth ratio) of the incised structures as well as the relative limited slope of the acoustic basement, it seems hazardous to define the paleo-channel type in the GSJ. Due to the small grid of seismic lines, the impossibility to use the sinuosity, which is a substantial parameter for the classification, makes the interpretation of river systems very uncertain. Furthermore, the morphology of wide and shallow channels could have been modified during transgressive phases, for example when affected by erosion of tidal currents and waves (Nordfjord et al., 2005). Thus, the relatively small grid of sparker lines collected during the expedition does not allow to capture with confidence the paleodrainage pattern and characteristics in the gulf. Nevertheless, several orientations of the incised valleys, essentially to the south and the SE, can be observed on the seismic profiles

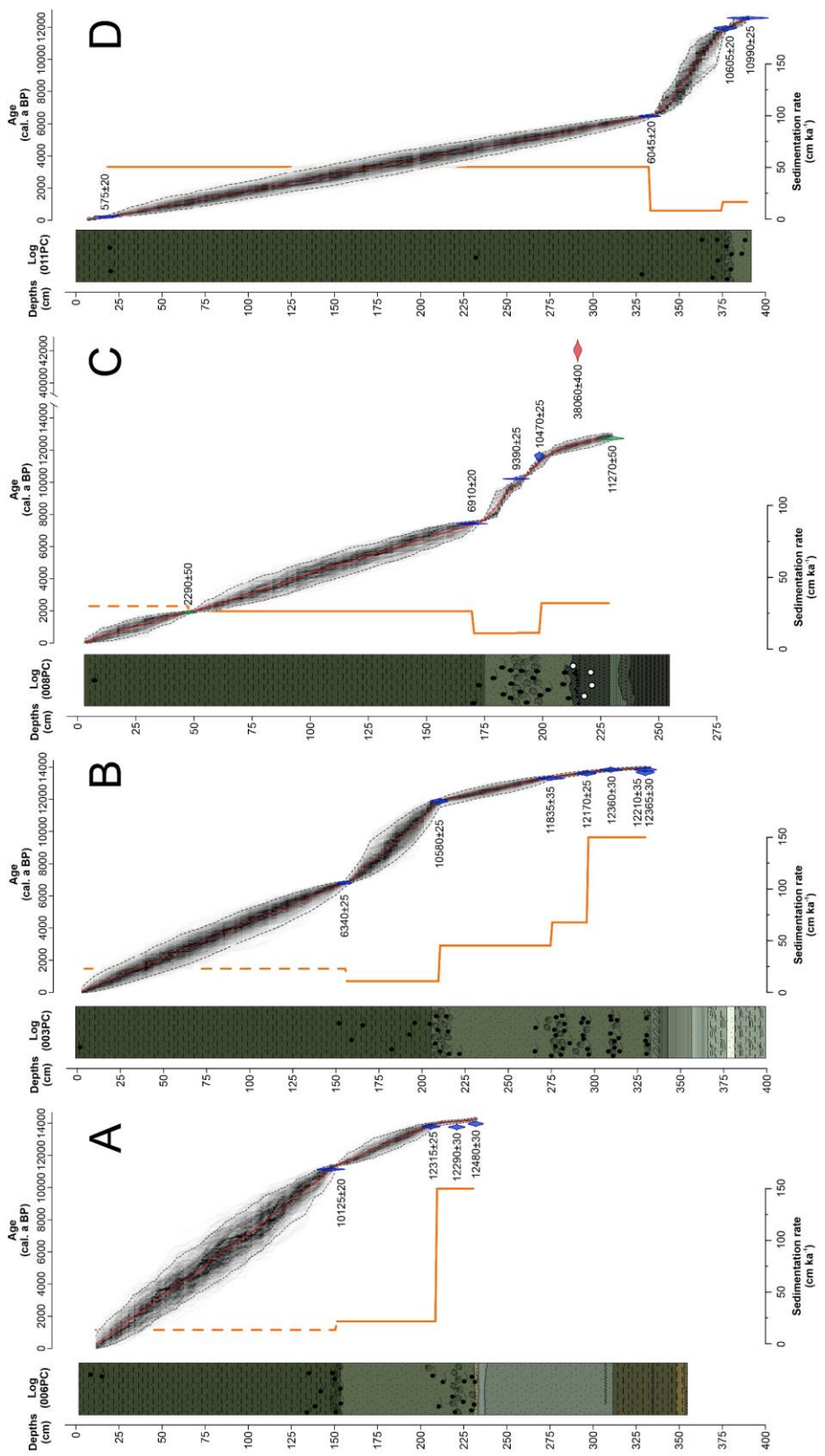


Figure 28: Age-depth models for cores 006PC (A), 003PC (B), 008PC (C) and 011PC (D), generated with BACON package of the R software (Blaauw and Christen, 2011). Calibrated radiocarbon ages used in the age-depth models are presented in transparent blue excepted for the AMS ^{14}C ages from micro-fragments of algae and wood, and the age from 008PC not retained which are shown in transparent green and red, respectively. Calibrated radiocarbon dates are also illustrated with their respective conventional ages. The grey dotted lines correspond to the 95% confidence intervals and the red dotted line shows the “best” model based on the weighted mean age for each depth. Sedimentation rates are presented with the orange line excepted for the upper sections, where the age-depth models have been constructed considering the top of cores as modern ages, which are shown in dotted lines

and that could be in agreement with a centripetal drainage in the GSJ but also to a drainage toward the outer shelf (Violante et al., 2014). In line with the interpretation of seismic units S1a, S1b, S2 and S3a, the sedimentation in the incised valleys seems to be characterized by a transition from fluvial sediments settled at the base of the incisions towards sediments settled under an environment of deposition related to lower energy conditions such as estuarine deposits. The acoustic characteristics of units S1b and S3a, coupled with the wide aspect and the almost enclosed shape of some incised structures (Figs. 22 and 31), could also indicate the conservation of a low energy environment of sedimentation during sea-level lowstand, such as lacustrine or lagoonal depositional systems. Unlike the incised valleys described in the northern part of the ACS, close to the Río de la Plata estuary, which are filled with post-LGM transgressive deposits (Violante et al., 2014 and references therein), we suggest that most of the sediment filling the paleo-channels in the GSJ, with the exception of the sediment of unit S4, were deposited during previous transgressions, subsequent sea-level highstand or lowstand. Indeed, the oldest radiocarbon ages of ~14 cal ka BP obtained at the base of unit L3 in 003PC imply a relatively short period of time between the transition to inner shelf hemipelagic sedimentation and the onset of GSJ invasion by marine transgression (i.e., ~15.5 cal ka BP; Ponce et al., 2011). This time interval does not seem sufficient, even with the maximum sediment rates of 150 cm ka^{-1} calculated for the lithological unit L3 (Fig. 28), to accumulate more than 5 m of deposits between the base of core 003PC and the top of unit S3a (Fig. 22). Furthermore, the acoustic differences between S3a and S4, as well as the slightly angular discordance between those units in the external part of the gulf (Fig. 23),

confirmed distinct depositional environments. The absence of sediment cores and radiocarbon ages retrieved in the SE part of the GSJ, do not allow to allege if unit S3b was formed during the last marine transgression or during previous ones. The morphological feature associated to unit S3b are interpreted as sand bodies or shallow-water bottom current sand deposits which are possibly related to the transport of coarse material from the Deseado River by strong longshore current during transgressive events or subsequent sea-level highstands.

2.7.2 The last marine transgression in the GSJ

During the last glacial events, the ACS was exposed forming an extensive subaerial plain (Rabassa et al., 2005). According to the sea-level curve for the ACS since the late Pleistocene proposed by Guilderson et al. (2000), the LGM lowstand was approximately 105 m below present sea level at around 18 ka (Fig. 29). The early stages of the post-LGM transgression are characterized by a rapid sea-level rise which could have led to the immersion of half the emerged shelf plain at approximately 15.3 cal ka BP (Violante and Parker, 2004; Ponce et al., 2011; Violante et al., 2014). Ponce et al. (2011) propose the onset of sea flooding in the GSJ, related to the marine transgression, between 15 and 15.5 cal ka BP, when sea level reached -90 m. This chronology could not be confirmed with the radiocarbon ages obtained in the sediment cores from the central part of the gulf used in our study (Figs. 27 and 28). Nevertheless, we propose the onset of hydrodynamic conditions favourable for inner shelf subtidal sedimentation at around 14 cal ka BP in accordance to ages collected at the base of unit L3 in cores 003PC and 006PC. Prior to this age, shallow water depositional environments related to the marine invasion of this part of the gulf were probably present, as shown by units L2a and L2b in 003PC as well as the absence of erosional contact and hiatus at the transition between L2b and L3 (i.e., soft-sediment deformation structures at the top of L2b). The lithological interpretation of units L2a and L2b at the base of 003PC suggest the presence of lagoonal/wind-tidal flat environments during this period with a progressive evolution to subtidal environment as a result of sea-level rise. From ~14 cal ka BP and the beginning of the dominance of subtidal sedimentation, the depositional

environment in the central part of the GSJ presents a progressive development towards distal and lower energetic oceanic conditions which lead to the onset of the actual marine sedimentation in the gulf. According to lithological interpretation of L3 and L4 coupled with Log(Ti/Ca) and Log(Rb/Sr) ratios, a shallow subtidal environment is maintained from ~14 to ~11.5 cal ka BP followed by a distinct evolution to marine hemipelagic environment prior to ~7 cal ka BP (Fig. 29). However, this part of the GSJ seems to expose no lithological and physical evidences of Holocene sea-level changes observed in beach ridges and littoral terraces of the gulf area (e.g., Schellmann and Radtke, 2010 and reference therein; Zanchetta et al., 2012; 2014). Nevertheless, the lithological transition between L2b and L3 in 003PC, and to a lesser extent between L3 and L4 in every piston core except 001PC, betray an evident evolution of sedimentary environments related to sea-level rise prior to the Holocene. The radiocarbon ages of ~14 cal ka BP obtained at the base of L3 suggest that the transition between this unit and L2b could be consistent with an abrupt sea-level rise event estimated between 14.1 and 13.6 ka BP (records from Barbados and Tahiti; Fairbanks, 1989; Bard et al., 1996; Peltier and Fairbanks, 2006; Fig. 29) and recently updated around 14.7 ka BP (Deschamps et al., 2012). This abrupt and global sea-level jump is associated with a brief and high-amplitude glacial discharge (deglacial meltwater pulse; MWP-1A; Fairbanks, 1989). In the second part of L2b, the abrupt increase of Log(Ti/Ca) and Log(Rb/Sr) ratios in a distinct pluricentimetric layer seems to indicate that the rapid sea-level change could have occurred prior to 14 cal ka BP in the GSJ, before the transition between L2b and L3 (Figs. 25 and 28). Evidence of MWP-1A on the ACS, occurring between 14.6 and 14 cal ka BP, have been previously highlighted by the sea-level curve proposed by Guilderson et al. (2000). The relative sea-level fluctuation curve for the ACS also presents a record of an analogous event at ~11.5 cal ka BP consistent with the MWP-1B (Fairbanks, 1989; Bard et al., 1996; Guilderson et al., 2000; Abdul et al., 2016; Fig. 29). Unfortunately, the relative sea-level curve generated by Violante and Parker (2004), compiled after the results of Guilderson et al., (2000) and Cavallotto et al. (1995), and presented in this article does not have sufficient resolution to highlight the MWP-1A and the MWP-1B (Fig. 29). Isla et al. (2013) suggest that the San Matías Gulf, located ~350 km north of the GSJ and characterized by a sill at 60

m depth, should have been flooded during the MWP-1B. In the GSJ, the slight transition of depositional conditions separating L3 and L4 and estimated between 11.9 and 11.6 cal ka BP (records from shell-rich bed; 11.1 cal ka BP in 006PC) could be correlated to the sea-level jump related to the MWP-1B. However, the slightly and constant increase of Log(Ti/Ca) and Log(Rb/Sr) ratios as well as grain size does not seem consistent with a distinct change in elemental composition and morphological characteristics of sediments related to an abrupt sea-level rise in the GSJ (Figs. 25 and 28). Indeed, if the depositional environment presents a progressive transition to the onset of marine hemipelagic conditions from ~11.5 cal ka BP in this part of the gulf, it appears highly speculative to suggest clear evidence of MWP-1B in our sedimentary records. Furthermore, the existence and intensity of MWP-1B dated between 11.1 and 11.5 ka BP (records from Barbados and Tahiti; Fairbanks, 1989; Bard et al., 1996; Abdul et al., 2016) remains controversial and disputed (e.g., Lambeck et al., 2014; Bard et al., 2016).

According to age-depth models, the sedimentation rates during the Holocene appears to be relatively low, with values ranging between 7 and 23 cm ka^{-1} , in comparison to other gulfs with close morphological and environmental conditions for which the deposition rates frequently exceed 100 cm ka^{-1} on the same period (e.g., Gulf of Cadiz, Spain; Nelson et al., 1999). The main difference between those gulfs and the GSJ is the absence of any present-day major and perennial tributaries in our sector of interest likely to affect significantly the terrigenous inputs. The preservation of this sedimentation rates throughout the Holocene in the central part of the gulf suggests that the impact of riverine inputs in sedimentary processes and the origins of terrigenous sediments during this period could be relatively close to modern ones. Moreover, the progressive diminution and withdrawal of the eastern flank of North Patagonian Ice Field through the Deseado River during early- and mid-Holocene, which could have been a potential high source of terrigenous inputs for the GSJ, could not be highlighted by the sedimentation rates and the lithological interpretation of the sediment cores. Since the eastern flank Ice Field drainage reversal toward the West, dated speculatively at 13.5 cal ka BP by McCulloch et al. (2000), and until the capture of the Deseado River by

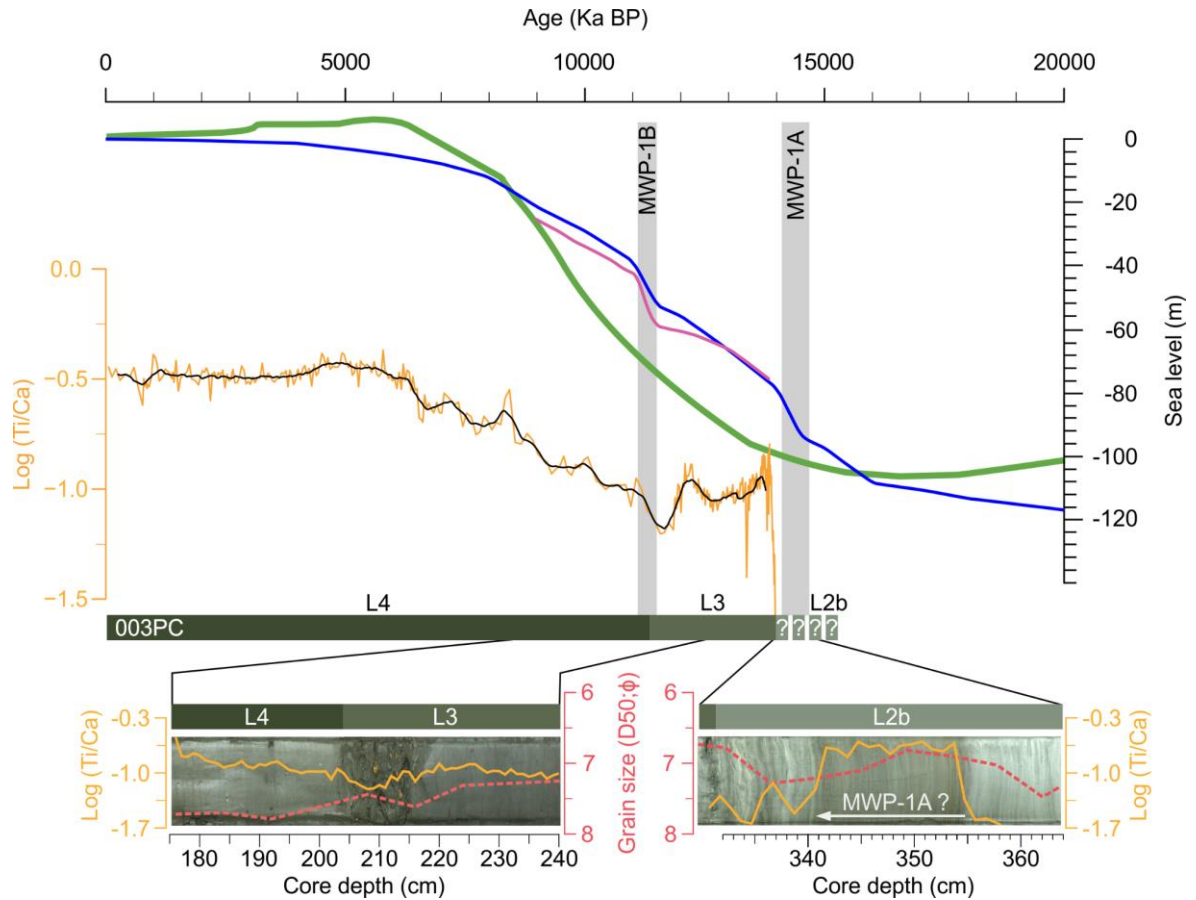


Figure 29: Comparison between the Log (Ti/Ca) ratio values of core 003PC (red curve) with eustatic and relative sea-level curves since 20 ka BP. A 400 years running mean of Log(Ti/Ca) raw values is also presented (black curve). Selected intervals of Log(Ti/Ca) ratios (yellow curve) and median grain size (red dotted curve; ϕ) are presented superimposed over respective core photographs sections. The eustatic sea-level curves were generated from the prediction of the sea-level history using the ICE-5G model (blue curve; Peltier and Fairbanks, 2006) as well as a reconstruction from the Barbados coral reefs (purple curve; Abdul et al., 2016), and adapted from Jakobson et al. (2017). The estimated time intervals of MWP-1A and MWP-1B are presented with gray columns. The relative sea-level curve for the ACS (green curve) was compiled by Violante and Parker (2004) after Cavallotto et al. (1995) and Guilderson (2000)

the Baker River, flowing into the Pacific Ocean, the discharge of the River Deseado has drastically decreased with potential resonance on sedimentation in the GSJ (Isla et al., 2013). However, the increase of Log(Ti/Ca) and Log(Rb/Sr) ratios from early Holocene displays an opposite tendency to the potential diminution of fluvio-glacial outflows through the Atlantic

coast but are consistent with the tendency of eustatic and relative sea-level curves (Fig. 29). Those results illustrate the dominant contribution of sea-level rise to the Log(Ti/Ca) and Log(Rb/Sr) ratios and thus to the terrigenous clastic inputs in the GSJ during early- to mid-Holocene. It also support the notion that with the sea level rise to its near-modern position over this period, the external/oceanic inputs, the coastal erosion of the inner gulf shores and the aeolian transport all drive the detrital input and the sediment dynamics within of the GSJ (Desiage et al., 2018). Finally, the higher sedimentation rate since mid-Holocene, observed in the most external core (i.e., $\sim 50 \text{ cm ka}^{-1}$; 011PC) seems to confirm the leading part of external/oceanic contributions to sedimentary inputs in the gulf (Desiage et al., 2018).

2.8 CONCLUSIONS

After the analysis of $\sim 2000 \text{ km}$ of high-resolution seismic profiles (sparker and chirp) as well as five piston cores, the first detailed description of the upper sedimentary sequence of the late Quaternary deposits in the GSJ was presented in this article. Five seismic facies have been defined, including the acoustic basement whose surface presents incised erosional truncation forming valleys and channels. These numerous infilled channels and valleys confirmed the existence, in this sector of the ACS, of a paleo-fluvial network obliterated with a possible succession of fluvial (S1a and S2) and lagoonal/estuarine (S1b and S3a) deposits settled during previous transgressions, subsequent sea-level highstand or lowstand.

Lithostratigraphic investigation of post-LGM depositional sequence in the gulf, illustrated by seismic unit S4, has favored the identification and description of 4 sedimentary units and sub-units. According to the lithologic and chronostratigraphic interpretation of sedimentary records, we suggest that the onset of subtidal sedimentation at around 14 cal ka BP in this part of the gulf. The evolution of hydrodynamic conditions favourable to these depositional environments could have been facilitated by an abrupt sea-level rise related to MWP-1A possibly identified in unit L2b as reported by Log(Ti/Ca) and Log(Rb/Sr) ratios. Overall, this study highlighted the significant impact of sea-level rise on sedimentation in the

gulf from the onset of marine invasion to the mid-Holocene and the reduced contribution, as observed nowadays, of riverine inputs due to the progressive diminution and withdrawal of glacial drainage starting before the Holocene. Finally, all the results presented in this paper confirmed the beginning of sea-flooding, related to the last marine transgression, prior to 14 cal ka BP as well as the establishment of modern sedimentary conditions during the mid-Holocene.

2.9 ACKNOWLEDGMENTS

The authors would like to sincerely thanks the captain, crew and scientific participants of the COR1404 (MARES and MARGES) expedition on board the R/V Coriolis II. Financial support for MARES and MARGES expeditions was provided by the Ministerio de Ciencia, Tecnología e Innovación Productiva (MINCyT), Provincia de Chubut and Consejo Nacional de Investigaciones Científicas y Técnicas (CONICET). This research was funded by the Natural Sciences and Engineering Research Council of Canada (NSERC) through Discovery grants to G. St-Onge and J.-C. Montero-Serrano and by the Fonds de recherche du Québec – Nature et Technologies (FRQNT) through a team grant to G. St-Onge, J.-C. Montero-Serrano and A. Rochon. The use of VISTA Desktop Seismic Data Processing and Kingdom Suite® software was made possible by respectively Schlumberger and IHS inc. through university partnership programs. We are thankful to Quentin Beauvais for technical support.

2.10 REFERENCES

- Abdul, N.A., Mortlock, R.A., Wright, J.D., Fairbanks, R.G., 2016. Younger Dryas sea level and meltwater pulse 1B recorded in Barbados reef crest coral *Acropora palmata*. *Paleoceanography* 31, 330–344.
- Aigner, T., 1985. Storm depositional systems: dynamic stratigraphy in modern and ancient shallow-marine sequences. *Lect. Notes Earth Sci.* Berlin Springer Verlag 3, 174 pp.
- Aitchison, J., 1986. The statistical analysis of compositional data. Chapman and hall, London.
- Bae, S.H., Kong, G.S., Lee, G.S., Yoo, D.G., Kim, D.C., 2018. Incised channel morphology and depositional fill of the paleo-Seomjin River in the continental shelf of the South Sea, Korea. *Quat. Int.* 468, 49–61.
- Bard, E., Hamelin, B., Arnold, M., Montaggioni, L., Cabioch, G., Faure, G., Rougerie, F., 1996. Deglacial sea-level record from Tahiti corals and the timing of global meltwater discharge. *Nature* 382, 241–244.
- Bard, E., Hamelin, B., Deschamps, P., Camoin, G., 2016. Comment on “Younger Dryas sea level and meltwater pulse 1B recorded in Barbados reefal crest coral *Acropora palmata*” by NA Abdul et al. *Paleoceanography* 31, 1603–1608.
- Barnhardt, W.A., Roland Gehrels, W., Kelley, J.T., 1995. Late Quaternary relative sea-level change in the western Gulf of Maine: Evidence for a migrating glacial forebulge. *Geology* 23, 317–320.
- Bellosi, E., 1990. Formación Chenque: Registro de la transgresión patagoniana (Terciario medio) de la cuenca de San Jorge, Argentina, in: *Actas 11 Congreso Geológico Argentino*, San Juan. pp. 57–60.
- Bini, M., Zanchetta, G., Ribolini, A., Salvatore, M.C., Baroni, C., Pappalardo, M., Isola, I., Isla, F.I., Fucks, E., Boretto, G., 2017. Last Interglacial Sea-level highstand deduced from notches and inner margins of marine terraces at Puerto Deseado, Santa Cruz Province, Argentina. *Geogr. Fis. e Din. Quat.* 40, 29–39.
- Blaauw, M., Christen, J.A., 2011. Flexible paleoclimate age-depth models using an autoregressive gamma process. *Bayesian Anal.* 6, 457–474.
- Blanchet, C.L., Thouveny, N., Vidal, L., 2009. Formation and preservation of greigite (Fe_3S_4) in sediments from the Santa Barbara Basin: Implications for paleoenvironmental changes during the past 35 ka. *Paleoceanogr. Paleoclimatology* 24, PA2224.
- Blott, S.J., Pye, K., 2001. GRADISTAT: a grain size distribution and statistics package for the analysis of unconsolidated sediments. *Earth Surf. Process. Landforms* 26, 1237–1248.
- Broecker, W.S., Olson, E.A., 1961. Lamont radiocarbon measurements VIII. *Radiocarbon* 3, 176–204.
- Burdige, D.J., 1993. The biogeochemistry of manganese and iron reduction in marine sediments. *Earth-Science Rev.* 35, 249–284.

- Cavallotto, J.L., Parker, G., Violante, R.A., 1995. Relative sea level changes in the Río de la Plata during the Holocene. In: 2 Annual Meeting of International Geoscience Programme 367: Late Quaternary Coastal Records of Rapid Change: Application to Present and Future Conditions. pp. 19–20.
- Cavallotto, J.L., Violante, R.A., Parker, G., 2004. Sea-level fluctuations during the last 8600 years in the de la Plata River (Argentina). *Quat. Int.* 114, 155–165.
- Chivas, A.R., García, A., van der Kaars, S., Couapel, M.J.J., Holt, S., Reeves, J.M., Wheeler, D.J., Switzer, A.D., Murray-Wallace, C. V., Banerjee, D., 2001. Sea-level and environmental changes since the last interglacial in the Gulf of Carpentaria, Australia: an overview. *Quat. Int.* 83, 19–46.
- Cordero, R.R., Panarello, H., Lanzelotti, S., Dubois, C.M.F., 2003. Radiocarbon age offsets between living organisms from the marine and continental reservoir in coastal localities of Patagonia (Argentina). *Radiocarbon* 45, 9–15.
- Crockett, J.S., Nittrouer, C.A., 2004. The sandy inner shelf as a repository for muddy sediment: an example from Northern California. *Cont. Shelf Res.* 24, 55–73.
- Croudace, I.W., Rothwell, R.G., 2015. Micro-XRF Studies of Sediment Cores: Applications of a non-destructive tool for the environmental sciences. *Developments in Paleoenvironmental Research* 17. Springer Netherlands, Dordrecht, 656 pp.
- Deschamps, P., Durand, N., Bard, E., Hamelin, B., Camoin, G., Thomas, A.L., Henderson, G.M., Okuno, J., Yokoyama, Y., 2012. Ice-sheet collapse and sea-level rise at the Bølling warming 14,600 years ago. *Nature* 483, 559–564.
- Desiage, P.-A., Montero-Serrano, J.-C., St-Onge, G., Crespi-Abril, A.C., Giarratano, E., Gil, M.N., Haller, M.J., 2018. Quantifying sources and transport pathways of surface sediments in the Gulf of San Jorge, central Patagonia (Argentina). *Oceanography* 31, 92–103.
- Duchesne, M.J., Bellefleur, G., 2007. Processing of single-channel high-resolution seismic data collected in the St. Lawrence Estuary. Current Research of the Geological Survey of Canada 2007-D1, 11pp.
- Duchesne, M.J., Bellefleur, G., Galbraith, M., Kolesar, R., Kuzmiski, R., 2007. Strategies for waveform processing in sparker data. *Mar. Geophys. Res.* 28, 153–164.
- Dung, B.V., Stattegger, K., Unverricht, D., Van Phach, P., Thanh, N.T., 2013. Late Pleistocene–Holocene seismic stratigraphy of the Southeast Vietnam shelf. *Glob. Planet. Change* 110, 156–169.
- Dyer, K.R., Huntley, D.A., 1999. The origin, classification and modelling of sand banks and ridges. *Cont. Shelf Res.* 19, 1285–1330.
- Fairbanks, R.G., 1989. A 17,000-year glacio-eustatic sea level record: influence of glacial melting rates on the Younger Dryas event and deep-ocean circulation. *Nature* 342, 637–642.
- Figari, E.G., Strelkov, E., Laffitte, G., Cid de La Paz, M.S., Courtade, S.F., Celaya, J., Vottero, A., Lafourcade, P., Martinez, R., Villar, H.J., 1999. Los sistemas petroleros de la Cuenca del Golfo San Jorge: Síntesis estructural, estratigráfica y geoquímica, in: 4 Congreso de Exploración y Desarrollo de Hidrocarburos. pp. 197–237.

- Fleming, K., Johnston, P., Zwart, D., Yokoyama, Y., Lambeck, K., Chappell, J., 1998. Refining the eustatic sea-level curve since the Last Glacial Maximum using far- and intermediate-field sites. *Earth Planet. Sci. Lett.* 163, 327–342.
- Flemming, B.W., 2012. Siliciclastic back-barrier tidal flats, in: *Principles of Tidal Sedimentology*. Springer, pp. 231–267.
- Fortin, D., Francus, P., Gebhardt, A.C., Hahn, A., Kliem, P., Lisé-Pronovost, A., Roychowdhury, R., Labrie, J., St-Onge, G., Team, T.P.S., 2013. Destructive and non-destructive density determination: method comparison and evaluation from the Laguna Potrok Aike sedimentary record. *Quat. Sci. Rev.* 71, 147–153.
- Galloway, W.E., 1989. Genetic stratigraphic sequences in basin analysis I: architecture and genesis of flooding-surface bounded depositional units. *Am. Assoc. Pet. Geol. Bull.* 73, 125–142.
- Gamboa, A., Montero-Serrano, J., St-Onge, G., Rochon, A., Desiage, P., 2017. Mineralogical, geochemical, and magnetic signatures of surface sediments from the Canadian Beaufort Shelf and Amundsen Gulf (Canadian Arctic). *Geochemistry, Geophys. Geosystems* 18, 488–512.
- Gilli, A., Anselmetti, F.S., Ariztegui, D., Beres, M., McKenzie, J.A., Markgraf, V., 2005. Seismic stratigraphy, buried beach ridges and contourite drifts: the Late Quaternary history of the closed Lago Cardiel basin, Argentina (49° S). *Sedimentology* 52, 1–23.
- Gómez, E.A., Borel, C.M., Aguirre, M.L., Martínez, D.E., 2008. Radiocarbon reservoir ages and hardwater effect for the northeastern coastal waters of Argentina. *Radiocarbon* 50, 119–129.
- Guilderson, T.P., Burckle, L., Hemming, S., Peltier, W.R., 2000. Late Pleistocene sea level variations derived from the Argentine Shelf. *Geochemistry, Geophys. Geosystems* 1.
- Hovikoski, J., Gingras, M., Räsänen, M., Rebata, L.A., Guerrero, J., Ranzi, A., Melo, J., Romero, L., del Prado, H.N., Jaimes, F., 2007. The nature of Miocene Amazonian epicontinental embayment: High-frequency shifts of the low-gradient coastline. *Geol. Soc. Am. Bull.* 119, 1506–1520.
- Isla, F.I., 2013. The flooding of the San Matías Gulf: The Northern Patagonia sea-level curve. *Geomorphology* 203, 60–65.
- Isla, F.I., Espinosa, M., Iantinos, N., 2015. Evolution of the Eastern flank of the North Patagonian Ice Field: The deactivation of the Deseado River (Argentina) and the activation of the Baker River (Chile). *Zeitschrift für Geomorphol.* 59, 119–131.
- Isla, F.I., Iantinos, N., Estrada, E., 2002. Playas reflectivas y disipativas macromareales del Golfo San Jorge, Chubut. *Rev. la Asoc. Argentina Sedimentol.* 9, 155–164.
- Jakobsson, M., Pearce, C., Cronin, T.M., Backman, J., Anderson, L.G., Barrientos, N., Björk, G., Coxall, H., De Boer, A., Mayer, L.A., 2017. Post-glacial flooding of the Bering Land Bridge dated to 11 cal ka BP based on new geophysical and sediment records. *Clim. Past* 13, 991–1005.
- Jin, Z., Cao, J., Wu, J., Wang, S., 2006. A Rb/Sr record of catchment weathering response to Holocene climate change in Inner Mongolia. *Earth Surf. Process. Landforms* J. Br. Geomorphol. Res. Gr. 31, 285–291.

- Kokot, R.R., 2004. Erosión en la costa patagónica por cambio climático. Rev. la Asoc. Geológica Argentina 59, 715–726.
- Kostadinoff, J., 1992. Estudio geofísico de la Península de Valdés y los golfos nordpatagónicos. Rev. la Asoc. Geológica Argentina 47, 229–236.
- Lambeck, K., Rouby, H., Purcell, A., Sun, Y., Cambridge, M., 2014. Sea level and global ice volumes from the Last Glacial Maximum to the Holocene. Proc. Natl. Acad. Sci. 111, 15296–15303.
- Li, J., Liu, S., Shi, X., Zhang, H., Fang, X., Cao, P., Yang, G., Xue, X., Khokiattiwong, S., Kornkanitnan, N., 2019. Sedimentary responses to the sea level and Indian summer monsoon changes in the central Bay of Bengal since 40 ka. Mar. Geol. 415, 105947.
- Liao, H.-R., Yu, H.-S., Su, C.-C., 2008. Morphology and sedimentation of sand bodies in the tidal shelf sea of eastern Taiwan Strait. Mar. Geol. 248, 161–178.
- Martínez, O.A., Kutschker, A., 2011. The ‘Rodados Patagónicos’(Patagonian shingle formation) of eastern Patagonia: environmental conditions of gravel sedimentation. Biol. J. Linn. Soc. 103, 336–345.
- Matano, R.P., Palma, E.D., 2018. Seasonal variability of the oceanic circulation in the Gulf of San Jorge, Argentina. Oceanography 31, 16–24.
- McCave, I.N., 1972. Transport and escape of fine-grained sediment from shelf areas. Shelf sediment Transp. Process pattern 225–248.
- McCulloch, R.D., Bentley, M.J., Purves, R.S., Hulton, N.R.J., Sugden, D.E., Clapperton, C.M., 2000. Climatic inferences from glacial and palaeoecological evidence at the last glacial termination, southern South America McCulloch, R. D., Bentley, M. J., Purves, R. S., Hulton, N. R. J., Sugden, D. E., & Clapperton, C. M. (2000). Climatic inferences from gl. J. Quat. Sci. 15, 409–417.
- Menier, D., Reynaud, J.-Y., Proust, J.-N., Guillocheau, F., Guennoc, P., Bonnet, S., Tessier, B., Goubert, E., 2006. Basement control on shaping and infilling of valleys incised at the southern coast of Brittany, France. SEPM Spec. Pub., Incised Valleys in time and space.
- Milne, G.A., Long, A.J., Bassett, S.E., 2005. Modelling Holocene relative sea-level observations from the Caribbean and South America. Quat. Sci. Rev. 24, 1183–1202.
- Mitchum Jr, R.M., Vail, P.R., Sangree, J.B., 1977. Seismic stratigraphy and global changes of sea level, part 6: stratigraphic interpretation of seismic reflection patterns in depositional sequences. In: Payton, C.E. (Ed.), Seismic Stratigraphy - Applications to Hydrocarbon Exploration. AAPG Memoir 26pp. 117–133.
- Mollier-Vogel, E., Leduc, G., Böschen, T., Martinez, P., Schneider, R.R., 2013. Rainfall response to orbital and millennial forcing in northern Peru over the last 18 ka. Quat. Sci. Rev. 76, 29–38.
- Mosher, D.C., Simpkin, P.G., 1999. Environmental marine Geoscience 1. Status and trends of marine high-resolution seismic reflection profiling: Data acquisition. Geosci. Canada 26, 174–188.
- Mouzo, F.H., 2017. Geología submarina del golfo norpatagónico San Matías. Rev. la Asoc. Geológica Argentina 74, 553–569.

- Nelson, C.H., Baraza, J., Maldonado, A., Rodero, J., Escutia, C., Barber Jr, J.H., 1999. Influence of the Atlantic inflow and Mediterranean outflow currents on Late Quaternary sedimentary facies of the Gulf of Cadiz continental margin. *Mar. Geol.* 155, 99–129.
- Nittrouer, C.A., Sternberg, R.W., 1981. The formation of sedimentary strata in an allochthonous shelf environment: the Washington continental shelf. *Mar. Geol.* 42, 201–232.
- Nordfjord, S., Goff, J.A., Austin Jr, J.A., Sommerfield, C.K., 2005. Seismic geomorphology of buried channel systems on the New Jersey outer shelf: assessing past environmental conditions. *Mar. Geol.* 214, 339–364.
- Nullo, F.E., Combina, A.M., 2002. Sedimentitas terciarias continentales, in: Congreso Geológico Argentino. pp. 245–258.
- Owen, G., Moretti, M., Alfaro, P., 2011. Recognising triggers for soft-sediment deformation: current understanding and future directions. *Sediment. Geol.* 235, 133–140.
- Palma, E.D., Matano, R.P., Piola, A.R., 2008. A numerical study of the Southwestern Atlantic Shelf circulation: Stratified ocean response to local and offshore forcing. *J. Geophys. Res. Ocean.* 113.
- Paredes, J.M., 2002. Asociaciones de facies y correlación de las sedimentitas de la Formación Chenque (Oligoceno-Mioceno) en los alrededores de Comodoro Rivadavia, Cuenca del Golfo San Jorge, Argentina. *Rev. la Asoc. Argentina Sedimentol.* 9, 53–64.
- Parker, G., Paterlini, M.C., Violante, R., 1997. El fondo marino.
- Peltier, W.R., Fairbanks, R.G., 2006. Global glacial ice volume and Last Glacial Maximum duration from an extended Barbados sea level record. *Quat. Sci. Rev.* 25, 3322–3337.
- Perissoratis, C., Piper, D.J.W., Lykousis, V., 2000. Alternating marine and lacustrine sedimentation during late Quaternary in the Gulf of Corinth rift basin, central Greece. *Mar. Geol.* 167, 391–411.
- Ponce, J.F., Rabassa, J., Coronato, A., Borromei, A.N.A., 2011. Palaeogeographical evolution of the Atlantic coast of Pampa and Patagonia from the last glacial maximum to the Middle Holocene. *Biol. J. Linn. Soc.* 103, 363–379.
- Puga-Bernabéu, Á., Aguirre, J., 2017. Contrasting storm-versus tsunami-related shell beds in shallow-water ramps. *Palaeogeogr. Palaeoclimatol. Palaeoecol.* 471, 1–14.
- Rabassa, J., 2008. Late cenozoic glaciations in Patagonia and Tierra del Fuego. *Dev. Quat. Sci.* 11, 151–204.
- Rabassa, J., Coronato, A.M., Salemme, M., 2005. Chronology of the Late Cenozoic Patagonian glaciations and their correlation with biostratigraphic units of the Pampean region (Argentina). *J. South Am. Earth Sci.* 20, 81–103.
- Reimer, P.J., Bard, E., Bayliss, A., Beck, J.W., Blackwell, P.G., Ramsey, C.B., Buck, C.E., Cheng, H., Edwards, R.L., Friedrich, M., 2013. IntCal13 and Marine13 radiocarbon age calibration curves 0–50,000 years cal BP. *Radiocarbon* 55, 1869–1887.

- Reineck, H.-E., Singh, I.B., 1980. Depositional sedimentary environments: with reference to terrigenous clastics. Springer-Verlag, Berlin-Heidelberg-New York, pp. 549.
- Rémillard, A.M., St-Onge, G., Bernatchez, P., Hétu, B., Buylaert, J.-P., Murray, A.S., Lajeunesse, P., 2017. Relative sea-level changes and glacio-isostatic adjustment on the Magdalen Islands archipelago (Atlantic Canada) from MIS 5 to the late Holocene. *Quat. Sci. Rev.* 171, 216–233.
- Rosgen, D.L., 1994. A classification of natural rivers. *Catena* 22, 169–199.
- Rostami, K., Peltier, W.R., Mangini, A., 2000. Quaternary marine terraces, sea-level changes and uplift history of Patagonia, Argentina: comparisons with predictions of the ICE-4G (VM2) model of the global process of glacial isostatic adjustment. *Quat. Sci. Rev.* 19, 1495–1525.
- Sangree, J.B., Widmier, J.M., 1979. Interpretation of depositional facies from seismic data. *Geophysics* 44, 131–160.
- Schellmann, G., Radtke, U., 2010. Timing and magnitude of Holocene sea-level changes along the middle and south Patagonian Atlantic coast derived from beach ridge systems, littoral terraces and valley-mouth terraces. *Earth-Science Rev.* 103, 1–30.
- St-Onge, G., Mulder, T., Francus, P., Long, B., 2007. Continuous physical properties of cored marine sediments. *Proxies Late Cenozoic Paleoceanogr.* Elsevier 63–98.
- Stuiver, M., Reimer, P.J., 1993. Extended ^{14}C data base and revised CALIB 3.0 ^{14}C age calibration program. *Radiocarbon* 35, 215–230.
- Sylwan, C.A., 2001. Geology of the Golfo San Jorge Basin, Argentina. *Geología de la Cuenca del Golfo San Jorge, Argentina. J. Iber. Geol.* 27, 123–158.
- Tjallingii, R., Stattegger, K., Wetzel, A., Van Phach, P., 2010. Infilling and flooding of the Mekong River incised valley during deglacial sea-level rise. *Quat. Sci. Rev.* 29, 1432–1444.
- van den Boogaart, K.G., Tolosana-Delgado, R., 2013. Analyzing compositional data with R. Springer, Heidelberg-New York-Dordrecht-London, 273 pp.
- Viana, A.R., Faugères, J.-C., Stow, D.A. V, 1998. Bottom-current-controlled sand deposits—a review of modern shallow-to deep-water environments. *Sediment. Geol.* 115, 53–80.
- Violante, R.A., Parker, G., 2004. The post-last glacial maximum transgression in the de la Plata River and adjacent inner continental shelf, Argentina. *Quat. Int.* 114, 167–181.
- Violante, R.A., Paterlini, C.M., Marcolini, S.I., Costa, I.P., Cavallotto, J.L., Laprida, C., Dragani, W., Chaporri, N.G., Watanabe, S., Totah, V., 2014. The Argentine continental shelf: morphology, sediments, processes and evolution since the Last Glacial Maximum. *Geol. Soc. London, Mem.* 41, 55–68.
- Weschenfelder, J., Baitelli, R., Corrêa, I.C.S., Bortolin, E.C., dos Santos, C.B., 2014. Quaternary incised valleys in southern Brazil coastal zone. *J. South Am. Earth Sci.* 55, 83–93.
- Yoo, D.-G., Chang, T.-S., Lee, G.-S., Kim, G.-Y., Kim, S.-P., Park, S.-C., 2016. Late Quaternary seismic stratigraphy in response to postglacial sea-level rise at the mid-eastern Yellow Sea. *Quat. Int.* 392, 125–136.

- Zaitlin, B.A., Dalrymple, R.W., Boyd, R., 1994. The stratigraphic organization of incised-valley systems associated with relative sea-level change. SEPM Spec. Publ. 51, 45–60.
- Zanchetta, G., Consoloni, I., Isola, I., Pappalardo, M., Ribolini, A., Aguirre, M., Fucks, E., Baneschi, I., Bini, M., Ragaini, L., 2012. New insights on the Holocene marine transgression in the Bahía Camarones (Chubut, Argentina). Ital. J. Geosci. 131, 19–31.
- Zanchetta, G., Bini, M., Isola, I., Pappalardo, M., Ribolini, A., Consoloni, I., Boretto, G., Fucks, E., Ragaini, L., Terrasi, F., 2014. Middle- to late-Holocene relative sea-level changes at Puerto Deseado (Patagonia, Argentina). The Holocene 24, 307–317.
- Zhang, Y., Chiessi, C.M., Mulitza, S., Zabel, M., Trindade, R.I.F., Holland, M.H.B.M., Dantas, E.L., Govin, A., Tiedemann, R., Wefer, G., 2015. Origin of increased terrigenous supply to the NE South American continental margin during Heinrich Stadial 1 and the Younger Dryas. Earth Planet. Sci. Lett. 432, 493–500.

2.11 SUPPLEMENTARY MATERIAL (FIGURES)

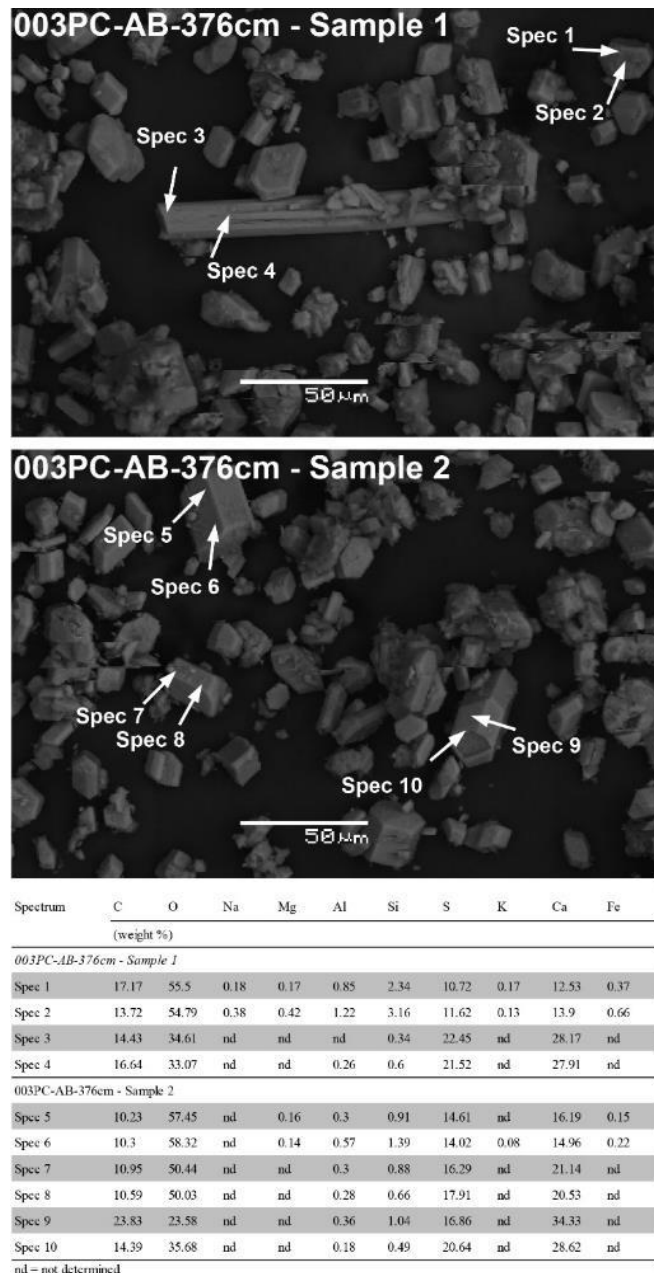


Figure 30: Scanning electron microscopy (SEM) images of the bulk fraction of sediment samples retrieved in the potential gypsum rich layer at 376 cm in 003PC. Elemental composition (weight %) of five particles (ten spectra)

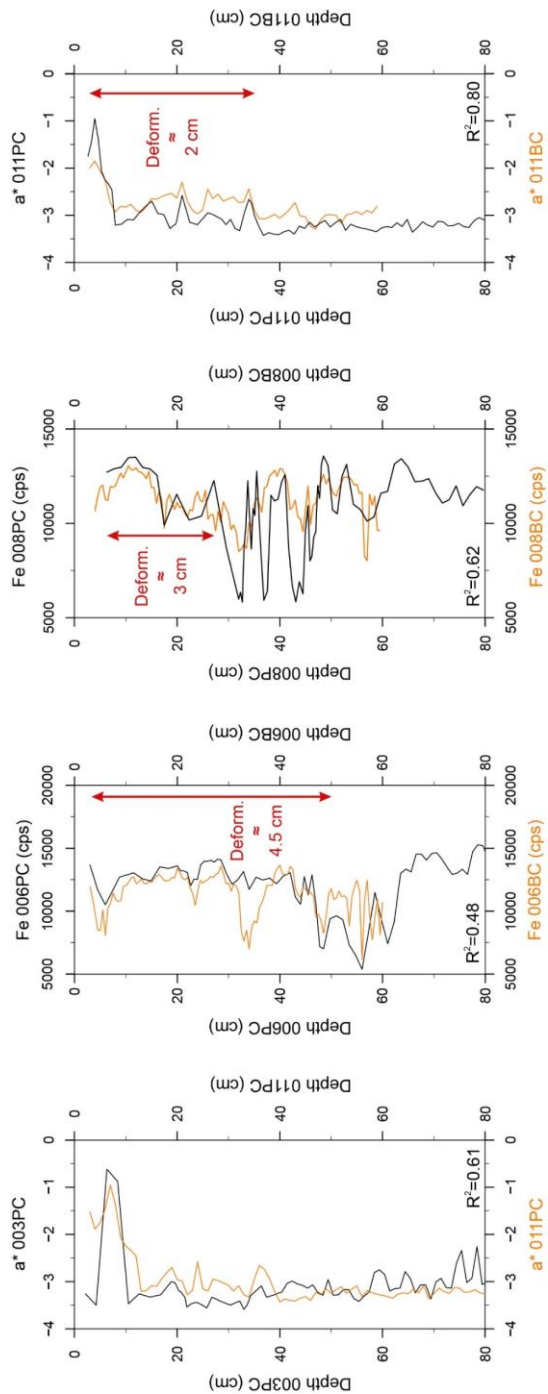


Figure 31: Correlation between piston (PC) and box cores (BC) using a^* for cores 003PC and 011PC, and relative content of Fe for cores 006PC and 008PC. To compensate for the absence of box core at the 003PC, this core was correlated with the closest “depth corrected” piston core, 011PC. Properties for the PC and BC are presented in black and orange, respectively, except in the case of 003PC in which 011PC is shown in orange

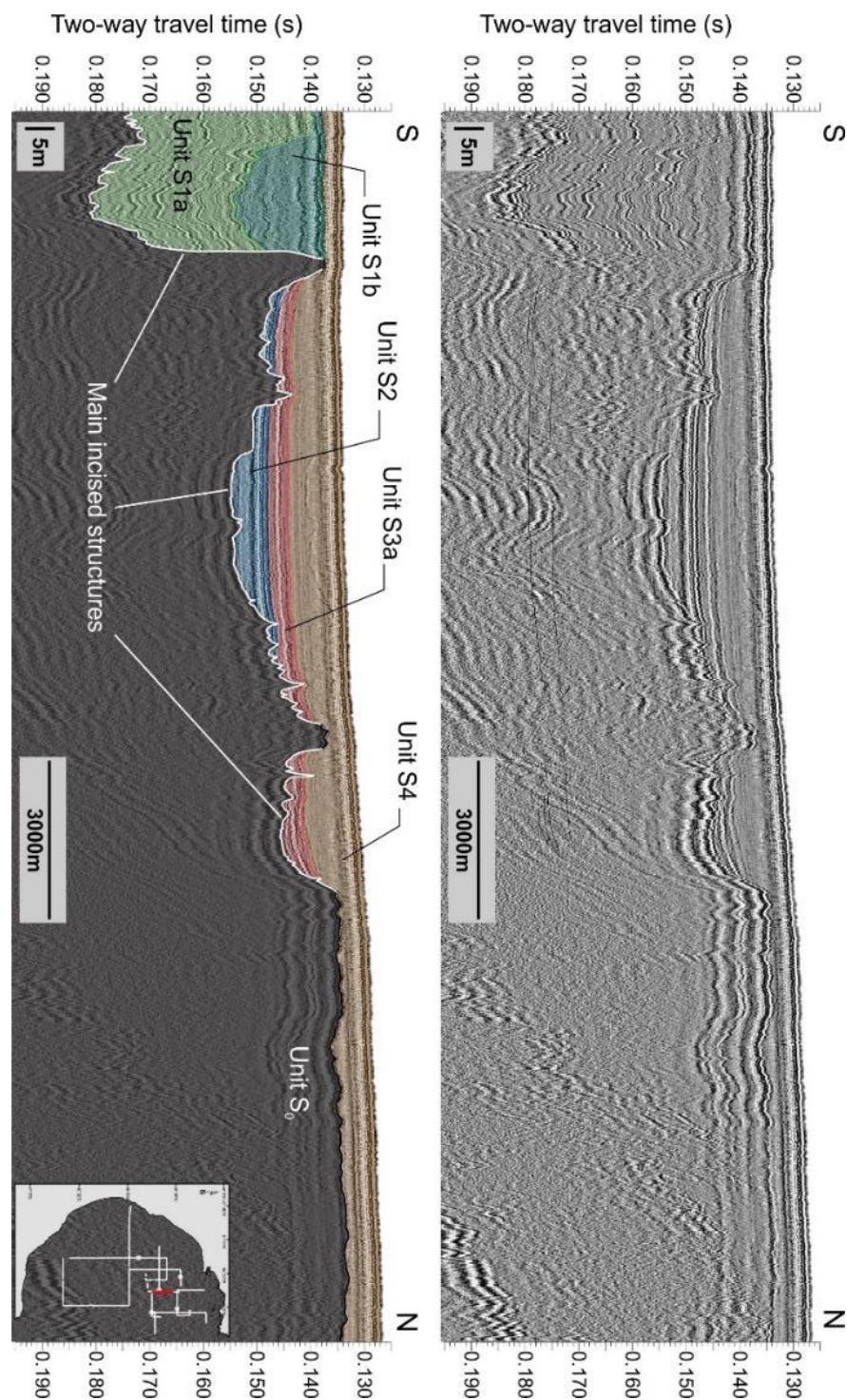


Figure 32: High-resolution sparker seismic profile (section of line 017; A) with interpreted version (B) showing six seismic units and sub-units (units S₀, S_{1a}, S_{1b}, S₂, S_{3a} and S₄) and incised valleys (white lines)

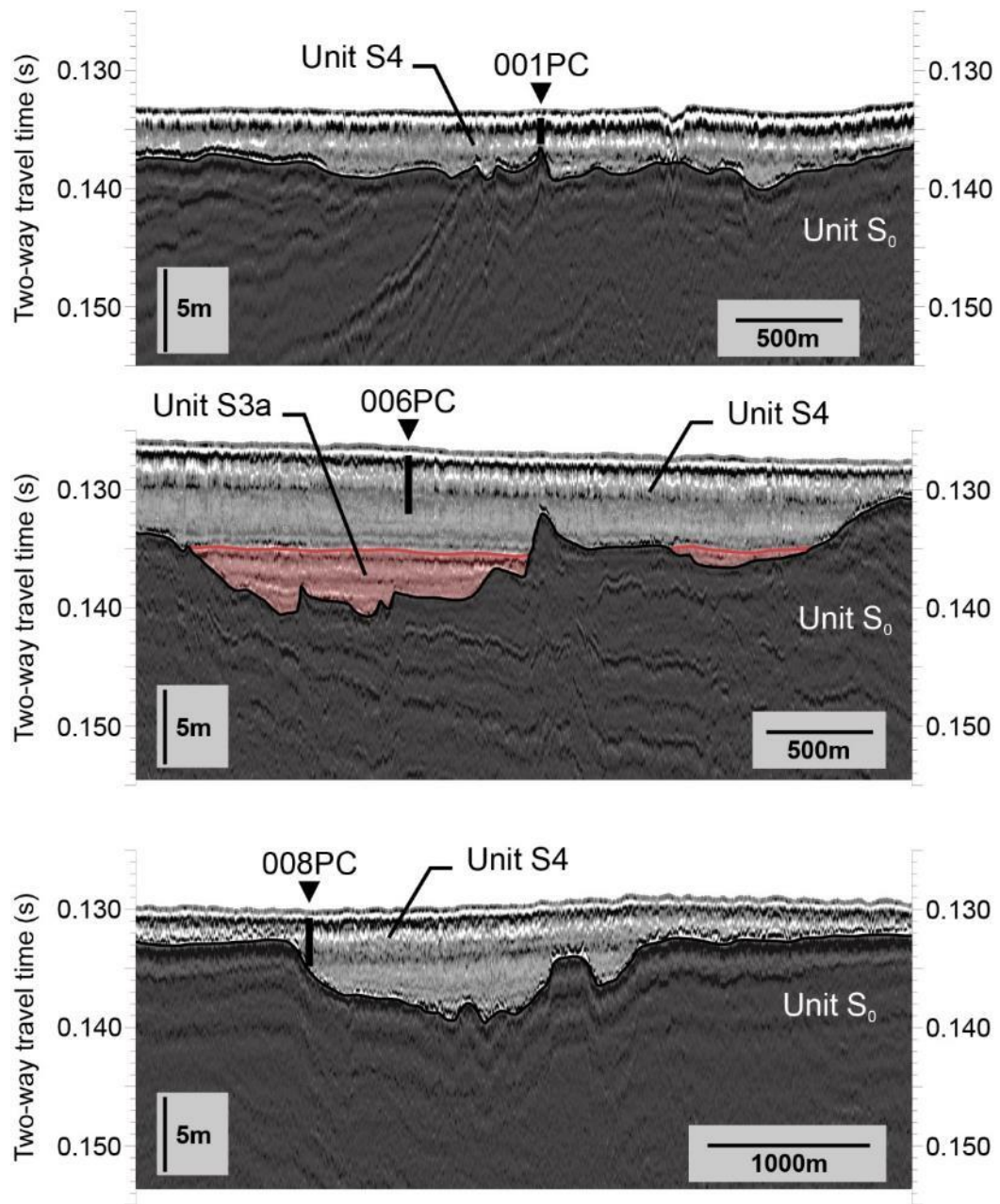


Figure 33: Interpreted high-resolution sparker seismic profiles (section of lines 004bis, 012bis and 014; A, B and C) showing locations of core 001PC, 006PC and 008PC, respectively

CHAPITRE 3

NOUVELLE METHODE DE SOMMATION POUR RECONSTRUIRE LA VARIATION SECULAIRE DU CHAMP MAGNETIQUE ET LA PALEOINTENSITE RELATIVE A HAUTE RESOLUTION EN PATAGONIE DEPUIS 14 CAL KA BP

3.1 RÉSUMÉ EN FRANÇAIS DU TROISIÈME ARTICLE

La variation séculaire du champ magnétique (PSV) et la paléointensité relative (RPI) à haute résolution ont été reconstruites pour les derniers 14 000 ans en utilisant quatre archives sédimentaires marines provenant du golfe de San Jorge en Patagonie. L'analyse des propriétés magnétiques des sédiments suggère que le signal de la rémanence est caractérisé par une aimantation à une seule composante, forte et stable, soutenue par des minéraux ferromagnétiques à faible coercivité dans le pseudo mono-domaine (PSD). Afin de respecter les caractéristiques magnétiques et lithologiques inhérentes à chaque archive sédimentaire, les enregistrements PSV et RPI du golfe ont été reconstruits en utilisant une nouvelle méthode de sommation (*stacking*) basée sur deux facteurs de qualité, les valeurs de déviation angulaire maximum (MAD) et les vitesses de sédimentation. La comparaison des nouveaux stacks de PSV et RPI avec d'autres enregistrements de lacs de Patagonie ainsi qu'avec des modèles globaux du champ magnétique utilisant des harmoniques sphériques (SHA.DIFF.14 et CALS10k.2) suggère une bonne corrélation des résultats avec une variabilité cohérente ce qui indique une capture réaliste de la dynamique géomagnétique régionale par les sédiments du GSJ. Dans l'ensemble, l'application des valeurs MAD et des taux de sédimentation comme facteurs de qualité dans la méthode de sommation semble être un moyen prometteur d'atteindre la meilleure qualité et résolution temporelle parmi les différentes archives sédimentaires disponibles.

Le troisième article de cette thèse intitulé "*New stacking method to reconstruct high-resolution paleomagnetic secular variations and relative paleointensity in Patagonia over the last 14 ka cal BP*" a été rédigé par moi-même en collaboration avec Edouard Philippe, étudiant au laboratoire au moment de réaliser cet article, et sous la supervision de mon directeur Guillaume St-Onge et de mon co-directeur Jean-Carlos Montero Serrano. La méthode de *stacking* est née d'une réflexion entre Edouard Philippe, Guillaume St-Onge et moi-même, et a été programmée par Edouard Philippe. Pour cet article j'ai réalisé l'essentiel des analyses en laboratoire et du traitement des données sous la supervision de mon directeur Guillaume St-Onge avec l'aide de Quentin Beauvais (UQAR-ISMER). Cet article sera soumis prochainement à la revue *Geochemistry, Geophysics, Geosystems*.

Les résultats préliminaires de cet article ont été présentés sous la forme d'une présentation orale lors d'un workshop international organisé pour présenter les résultats préliminaires du projet PROMESse et qui s'est déroulé à Rimouski en mars 2017.

3.2 NEW STACKING METHOD TO RECONSTRUCT HIGH-RESOLUTION PALEOMAGNETIC SECULAR VARIATIONS AND RELATIVE PALEOINTENSITY IN PATAGONIA OVER THE LAST 14 KA CAL BP

High-resolution paleomagnetic secular variation (PSV) and relative paleointensity (RPI) were reconstructed over the last 14 cal ka BP using four marine sedimentary archives from the Gulf of San Jorge in Patagonia. The analysis of sediment magnetic properties suggests that the remanence signal is characterized by a strong, stable and single component magnetization carried by low coercivity ferrimagnetic minerals in the pseudo-single domain (PSD) range. In order to respect the magnetic and lithologic characteristics inherent to each sedimentary archive, the PSV and RPI records from the gulf have been reconstructed using a new stacking approach based on two quality factors, the maximum angular deviation (MAD) values and the sedimentation rates. The comparison of the new PSV and RPI stacks with other lacustrine records from Patagonia as well as with spherical harmonic models of the geomagnetic field (SHA.DIFF.14 and CALS10k.2) suggests a good correlation with a consistent variability implying a realistic capture of the regional geomagnetic dynamics by the sediments of the GSJ. Overall, the application of the MAD values and the sedimentation rates as quality factor in the stacking method seems to be a promising way to reach the highest quality and temporal resolution available from different sedimentary archives.

3.3 INTRODUCTION

For the last thirty years, the quantitative and qualitative improvement of sediment archives have greatly contributed to reconstruct the variability of the geomagnetic field at different scales. Indeed, the sedimentary sequences, whether marine or lacustrine, can represent continuous and well-dated records suitable to establish the relative variations of the Earth's magnetic field (e.g., Tauxe, 1993; Channell et al., 2000; Valet, 2003; Stoner and St-Onge, 2007; Barletta et al., 2010). In order to characterize the evolution of the Earth's magnetic field, paleomagnetic studies work on reconstructing the geomagnetic directional

changes (declination and inclination), identified as paleomagnetic secular variations (PSV), as well as the variability of the relative paleointensity (RPI). Unfortunately, not all sedimentary sequences have the same potential to establish the variability of the geomagnetic field, and a set of assessment criteria have been proposed to evaluate their reliability (e.g., Tauxe, 1993; Opdyke and Channell, 1996; Stoner and St-Onge, 2007). Among those criteria, the maximum angular deviation (MAD) value provides a quantitative measurement of the analytical uncertainty of the calculated component magnetization, and it is used to asses the quality of magnetization (Stoner and St-Onge, 2007). Furthermore, the ability to record high-resolution paleomagnetic data is related to the sediment accumulation rate of the sedimentary sequences, as well as to the characteristics of the magnetic magnetometer, especially the width of the response function when u-channels are used (Philippe et al., 2018).

Contrary to the Northern Hemisphere mid-latitudes where most of the high-resolution paleomagnetic studies have been carried out, the Southern Hemisphere remains scarcely investigated (e.g., Korte et al., 2011; Panovaska et al., 2018). This disparity is partly explained by the dominance in Southern Hemisphere of low to intermediate sedimentation rate basins, which is a negative factor for the reconstruction of reliable high-resolution paleomagnetic data (Panovaska et al., 2018), as well as the accessibility in the absence of landmass south of 56°S, with the exception of the inhospitable Antarctic continent. In order to overcome these constraints, high-resolution paleomagnetic records of lacustrine sediments have been published in the last decades in South America, mainly in Argentina (e.g., Gogorza et al., 2002, 2004, 2006, 2012, 2018; Irurzun et al., 2006; Lisé-Pronovost et al., 2013; Palermo et al., 2019). Indeed, during the 2000s, several studies carried out in two adjoining lakes (Escondido and El Trébol), located in the northern part of Patagonia (41°S 71°W; Fig. 34), depicted the record of relative paleointensity and paleosecular variations over the last 16 cal ka BP and 21 cal ka BP, respectively (Gogorza et al., 2004, 2006; Irurzun et al., 2006). In the framework of the International Continental scientific Drilling Program (ICDP), the sediment of lake Laguna Potrok Aike, located in southern Argentina (51°S 70°W; Fig. 34) has been recently investigated for its continuous and high-resolution paleomagnetic records (e.g., Gogorza et al., 2012; Lisé-Pronovost et al., 2013). With reconstructions of relative

paleointensity and PSV over the last 51.2 cal ka BP, Lisé-Pronovost et al. (2013) has highlighted the recording on this part of Patagonia of two global variations, the Laschamp and Mono Lake geomagnetic excursions occurred around 41 cal ka BP and 33 cal ka BP, respectively (Korte et al., 2019), as well as regional variations of the geomagnetic field previously observed in records from the Southern Ocean (Atlantic, Stoner et al., (2002); Pacific, Lund et al., (2006)). In recent years, Palermo et al. (2019) has also published high-resolution paleosecular variations and normalized intensity records for the last 4.7 cal ka BP from sediment cores retrieved in the crater lake Laguna Cháltel in southeastern Patagonia (49.5°S 71°W; Fig. 34).

A large number of paleomagnetic studies defining the regional paleosecular variations and relative paleointensity use stacking methods with sediment cores retrieved from adjoining region as well as locations geographically apart (e.g., Stoner et al., 2002; Laj et al., 2004; Gogorza et al., 2006; Barletta et al., 2010; Reilly et al., 2018; Palermo et al., 2019). Unfortunately, in several studies, the stacks are generated using solely arithmetic mean of each measured values, from different sediment cores, temporally concordant without discernable consideration for properties/characteristics inherent to each sedimentary sequence. In order to strengthen the paleomagnetic reconstructions developed from stacks, we propose in this study a new stacking method using the MAD values and the sediment accumulation rates as quality factors. Based on this new stacking method, we present a paleomagnetic secular variation and relative paleointensity stack for the last 14 cal ka BP in the Atlantic region of Patagonia, generated from 4 marine sediment archives retrieved in the Gulf of San Jorge (GSJ).

3.4 REGIONAL SETTING, STRATIGRAPHY AND SEDIMENTOLOGY

Located in the central part of Patagonia between latitudes 45°S and 47°S, the GSJ forms a semicircular basin of approximately 160 km long and 250 km wide with a surface area of 39,340 km². The bathymetry of the gulf is characterized by a rapid decrease of topography

to reach the 90 m isobath which defines a large flat central region covering most of the surface of the gulf and corresponding to the Patagonian outer shelf (Violante et al., 2014). The gulf is an extension of the Patagonian continental shelf which represents the southern part of the Argentine continental shelf (ACS) and is delimited by the Patagonian coast from Cape Horn (55°S) nearly to the Colorado River (39°S). The ACS is considered one of the largest siliciclastic shelves in the world with a width ranging between 170 and 850 km, and a total length of 2400 km. The modelling of the shelf is mainly conditioned by sea-level fluctuations, sediment dynamics and climatic/oceanographic processes (Violante et al., 2014).

From geological and geographical points of view, most of the GSJ forms the eastern part of the hydrocarbon producing San Jorge Gulf Basin that is surrounded by the North Patagonian Massif to the north, the Deseado Massif to the south, and the Andes to the west (Sylwan, 2001). The tablelands of the San Jorge Gulf Basin are mainly overlain by Eocene-Miocene sedimentary rocks of the Sarmiento and Patagonia Formations (Cuitiño et al., 2015), as well as Quaternary marine and fluvio-glacial deposits (e.g., “Rodados Patagónicos”; Martínez and Kutschker, 2011).

The GSJ does not have any present-day major and perennial tributaries likely to strongly affect the sedimentation. Furthermore, the gulf is in the heart of several hundred kilometers of littoral without major rivers, except for the relatively low flow of the Deseado River ($5 \text{ m}^3 \text{ s}^{-1}$; Kokot, 2004), which reaches the ocean a few dozen kilometers south of the GSJ. In this context, Desiage et al. (2018) proposed that the origin of surface sediments in the GSJ, dominated by fine to medium silt, is 50% from external/oceanic inputs, 40% from the inner gulf shores (i.e., erosion and runoffs) and 10% from dust (i.e., aeolian transport). Based on multi-proxy analysis of the four sediment cores used in this study, four lithological units and sub-units were defined for the post-LGM sedimentary sequence in the central part of the GSJ (Desiage et al., in prep.). Two sub-units, L2a and L2b, identified solely in one piston core (003PC) depict the presence of lagoonal/wind-tidal flat environments with a progressive evolution to subtidal environment. Unfortunately, no datable material could have been retrieved in those units. The lithological interpretation of the uppermost units L3 and

L4 identified in each cores used in this study suggests progressive development from subtidal sedimentation towards distal and lower energetic oceanic conditions which lead, around 7 cal ka BP, to the onset of marine hemipelagic sedimentation close to present one in this part of the gulf. The oldest ages, used in the age-depth models, collected at the base of L3 in two sediment cores (003PC and 006PC), indicate the potential onset of this unit at ~14 cal ka BP in this part of the GSJ. The transition between L3 and L4 have been dated between 11.9 and 11.1 cal ka BP, depending of which core.

According to the results of Desiage et al. (in prep.), the calculated accumulation rates for sedimentary sequence covered by the age-depth models are ranging between 7 and 150 cm ka^{-1} . The highest sedimentation rates of 150 cm ka^{-1} have been calculated in two cores (003PC and 006PC) in the basal part of unit L3. Then, the accumulation rates observed in all cores decrease to values between 17 and 68 cm ka^{-1} prior to ~11.5 cal ka BP. The lowest sedimentation rates included between 7 and 13 cm ka^{-1} have been calculated in the basal part of L4 following by a slightly progressive increase to values between 22 and 50 cm ka^{-1} for the mid- and late Holocene.

3.5 METHODS

The sediment cores used in this study were collected on board the R/V Coriolis II from February 17th to March 4th during the MARGES expedition, as part of the PROMESSe (*PROgrama Multidisciplinario para el Estudio del ecosistema y la geología marina del golfo San Jorge y las costas de las provincias de Chubut y Santa Cruz*) project. Four piston cores (003PC, 006PC, 008PC and 011PC) retrieved in the central part of the gulf (Fig. 34B) were sampled with u-channel according to the methodology presented by Stoner and St-Onge (2007).

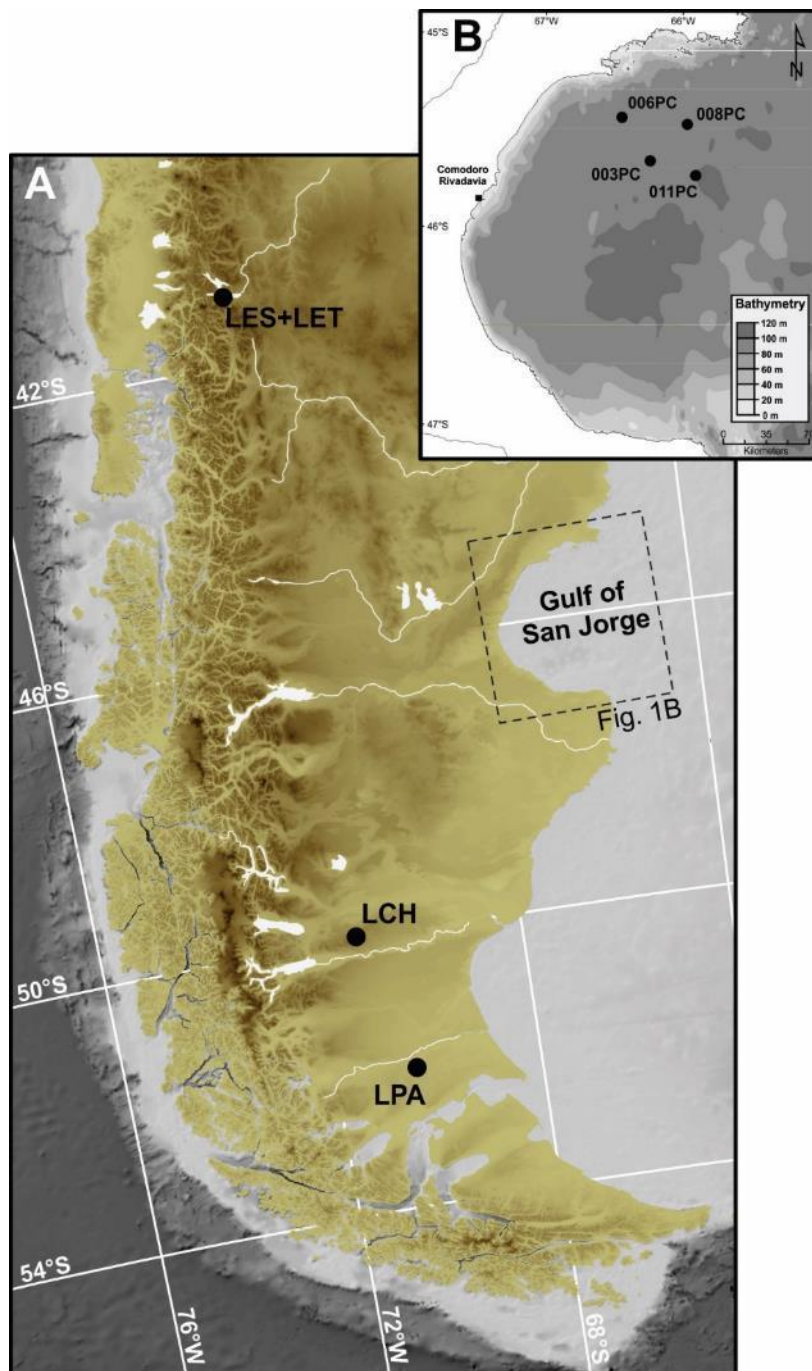


Figure 34: (A) Regional map illustrating the location of the Gulf of San Jorge, as well as the paleomagnetic records discussed in this paper. From north to south, LES: Lake Escondido, LET: Lake El trébol, LCH: Lake Laguna Cháltel, LPA: Lake Laguna Potrok Aike (PASADO and SALSA projects). (B) Bathymetric map of the Gulf of San Jorge with the location of the sedimentary records used in this study

3.5.1 Continuous magnetic measurements

The magnetic measurements were performed at 1-cm intervals on u-channels using a 2G Enterprises™ SRM-755 cryogenic magnetometer and a pulse magnetizer (for the induction of isothermal remanent magnetization, IRM, and saturated isothermal remanent magnetization, SIRM) at the *Institut des sciences de la mer de Rimouski* (ISMER, Canada). In order to reduce the edge effect related to the response function of the cryogenic magnetometer pick-up coils (Weeks et al., 1993), the data from the first and last 4 cm of each U-channel section were masked. The natural remanent magnetization (NRM) was measured and demagnetized by stepwise peak alternating fields (AF) up to 85 mT at 5 mT increments. An AF of 100 mT coupled with a direct current (DC) biasing field of 0.05 mT was implemented to the sample to obtain the anhysteretic remanent magnetization (ARM). The IRM and SIRM were induced by the pulse magnetizer with intensities of 300 and 950 mT, respectively. The u-channel were then measured following progressive AF demagnetization up to 80 mT at 5 mT increments for ARM and IRM, as well as between 0 and 50 mT at 5 mT for SIRM. The volumetric magnetic susceptibility (k_{LF}) was measured at 1-cm intervals using a Bartington point source MS2E online with a GEOTEK Multi-Sensor Core Logger (MSCL).

The Excel spreadsheet developed by Mazaud (2005) was used in order to estimate the paleomagnetic inclination and declination, as well as the associated maximum angular deviation (MAD; Fig. 35) values from the characteristic remanent magnetisation (ChRM) interval using principal component analysis (Kirschvink, 1980). The ChRM was generated with the AF demagnetization data from 10 to 40 mT. In order to correct the non azimuthal orientation during coring, the declinations were corrected to provide a continuous record for each core. MAD values lower than 5° are considered to be optimal for reliable PSV and relative paleointensity studies. In order to determine the RPI from sediments, the intensity of the NRM is normalized by an appropriate magnetic parameter (e.g., ARM, IRM; Tauxe 1993; Stoner & St-Onge 2007). The complete procedure to generate RPI will be developed in the results section. The median destructive fields of the NRM (MDF_{NRM}), which could be used as an indicator of coercivity of the remanence carriers, could not be determined due to a

viscous magnetization acquired after the retrieval of the cores and removable after the first steps of magnetisation (up to 10 mT).

3.5.2 Discrete magnetic measurements

A total of 50 discrete samples were collected in u-channels of the four cores, focused in this study, and measured using an alternating gradient force magnetometer (AGM; MicroMag 2900 from PrincetonMeasurements CorporationTM). The analysis of the hysteresis loops and backfield remanence curves obtained from the AGM were used to estimate the saturation magnetization (M_s), the coercive force (H_c), the saturation remanence (M_{rs}) and the coercivity of remanence (H_{cr}). Those parameters allowed us to determine the coercivity (H_{cr}/H_c) and the remanence (M_r/M_s) ratios commonly employed as magnetic grain size proxies, as well as to establish the magnetic domain state (e.g., Day et al., 1977; Dunlop, 2002a, b).

3.5.3 Chronology

The chronology of the four piston cores used in this study, previously presented by Desiage et al. (in prep.), is based on 22 radiocarbon ages calibrated with the Marine13 calibration curve (Reimer et al., 2013) and a marine regional reservoir correction (ΔR) of 0 (Cordero et al., 2003; Schellmann and Radtke, 2010). Accumulation rates of the sedimentary sequences covered by radiocarbon ages were calculated by Desiage et al. (in prep.) after the construction of age-depth models for each core using the Bayesian statistical approach of the BACON v2.2 package of the R software (Blaauw and Christen, 2011).

3.6 RESULTS

Every core used in this study will be presented in this section with an emphasis on the sediment of units 3 and 4, as these units were used to build the age model. Indeed, no datable material has been found beyond the base of unit 3 (Desiage et al., in prep.).

3.6.1 Magnetic mineralogy, concentration and grain size

The pseudo S-ratio (St-Onge et al, 2003) of lithological units 3 and 4, when treated as a whole, varies between 0.83 and 1 with median values between 0.9 and 0.99 (Table 8). In the other parts of the cores, the pseudo S-ratio are also similar with median values between 0.9 and 0.99 as well. These values generally >0.9 reveal that most of the saturation of the magnetic assemblage is achieved in a 0.3 T field, which is consistent with low coercivity ferrimagnetic minerals, such as magnetite and/or titanomagnetite (Stoner & St-Onge 2007). Moreover, the shape of the hysteresis loops, from samples of the four investigated cores, agree with the typical shape for magnetite (Fig. 36A, B, C and D; Tauxe et al., 1996).

Tableau 8: Minimum (Min.), median and maximum (Max.) values of pseudo S-ratios according to the lithological units of the four sediment cores

Core	Litho. unit*	Pseudo S-ratio		
		Min. value	Median value	Max. value
003 PC	Unit 2	0.84	0.9	0.99
	Unit 3	0.85	0.92	0.94
	Unit 4	0.86	0.91	0.94
006 PC	Unit 3	0.87	0.91	0.94
	Unit 4	0.86	0.9	0.91
008 PC	Unit 1	0.98	0.99	1
	Unit 2	0.98	0.98	0.99
	Unit 3	0.97	0.99	1
	Unit 4	0.85	0.91	1
011 PC	Unit 3	0.92	0.93	0.93
	Unit 4	0.83	0.91	0.93

* = Lithological unit

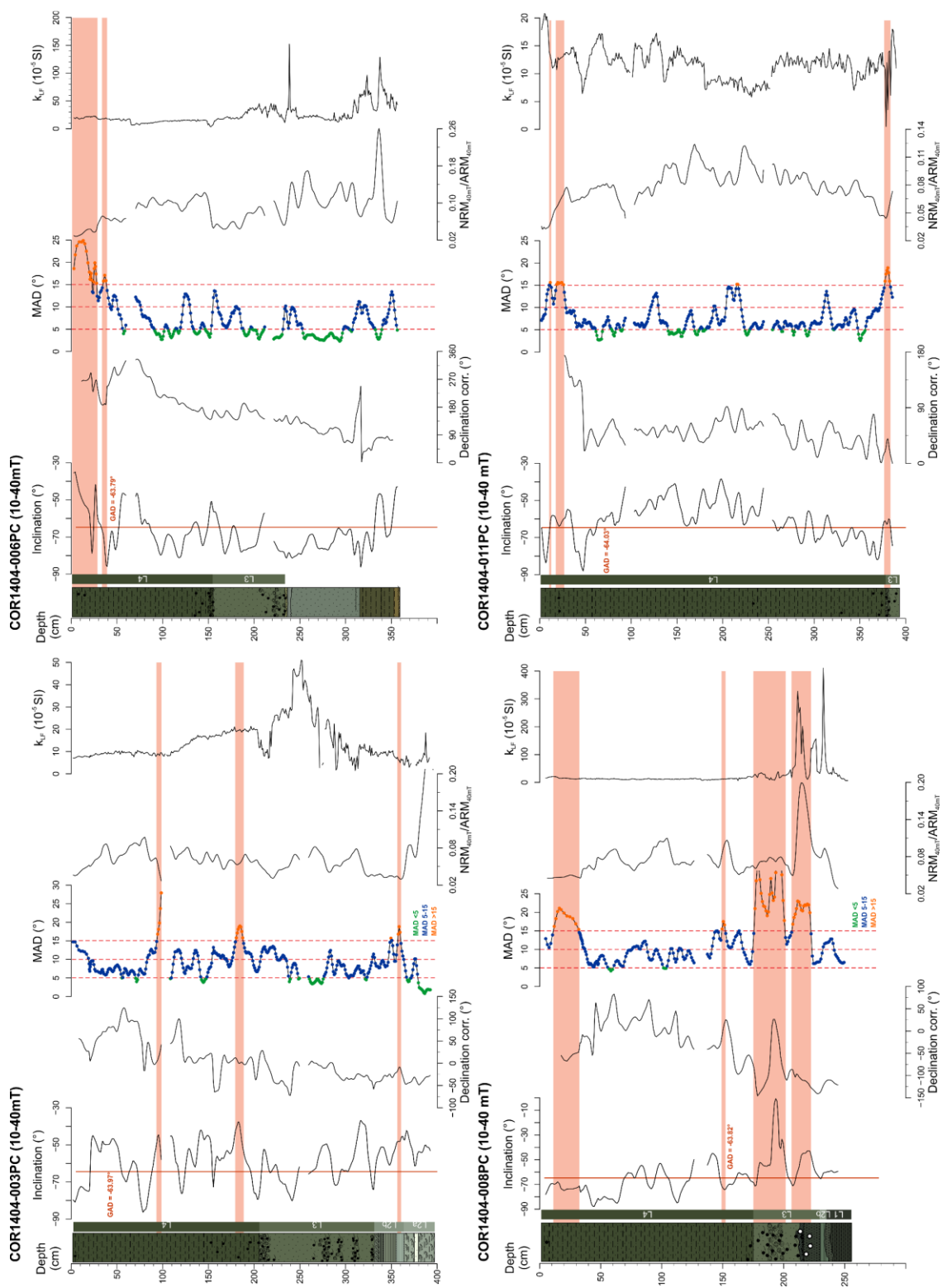


Figure 35: High-resolution downcore variations of the characteristic remanent magnetization (i.e., inclination and corrected declination), MAD values and magnetic properties of cores 003PC, 006PC, 008PC and 011PC. These results are presented with the lithologic descriptions and lithofacies of the four cores. The red vertical line on the inclination graphs depicts the expected inclination from the GAD model for the latitude of the coring sites. The intervals with MAD values $> 15^\circ$ are highlighted in red and the limits of the MAD values used in the stacking method (i.e., 5° , 10° and 15° , see text for details) are indicated with the red dashed lines

According to the coercivity and the remanence ratios, regrouped in the Day plot to predict the domain state of the magnetic grains, the samples seems to be grouped in the pseudo-single domain (PSD) region (Day et al., 1977; Dunlop, 2002a, b). Furthermore, the extensive dispersion of samples in the PSD range does not indicate any grain size clusters between lithological units 3 and 4. Another relevant property to grain size is the Mrs/Ms values; high Mrs/Ms values (i.e., 0.3 to 0.4) could suggest a non negligible proportion of finer magnetic grains compare to coarser PSD titanomagnetite grains, which are usually identified with lower Mrs/Ms values (i.e., 0.1 to 0.3; Day et al., 1977; Dunlop, 2002a, b). The three samples corresponding to the multi domain (MD) region present limited coarser grain layers in unit 1, as well as a very coarse rapidly deposited layer (RDL) in unit 3 of core 008PC. The nature of the RDL, with a potentially higher proportion of MD magnetite grains, has been considered when the stacks were generated. Considering magnetite as the dominant ferrimagnetic mineral, the anhysteretic susceptibility (k_{ARM}) versus the magnetic susceptibility (k_{LF}) diagram also represents a grain-size proxy (King et al., 1983). The absence of a clear magnetic grain size tendency between units 3 and 4 is confirmed by the k_{ARM} vs. k_{LF} diagrams (Fig. 46). The diagrams indicate relatively fine magnetic grain size, with the presence of magnetite grain between 0.1 and 5 μm for unit 3 and between 0.2 and 5 μm for unit 4.

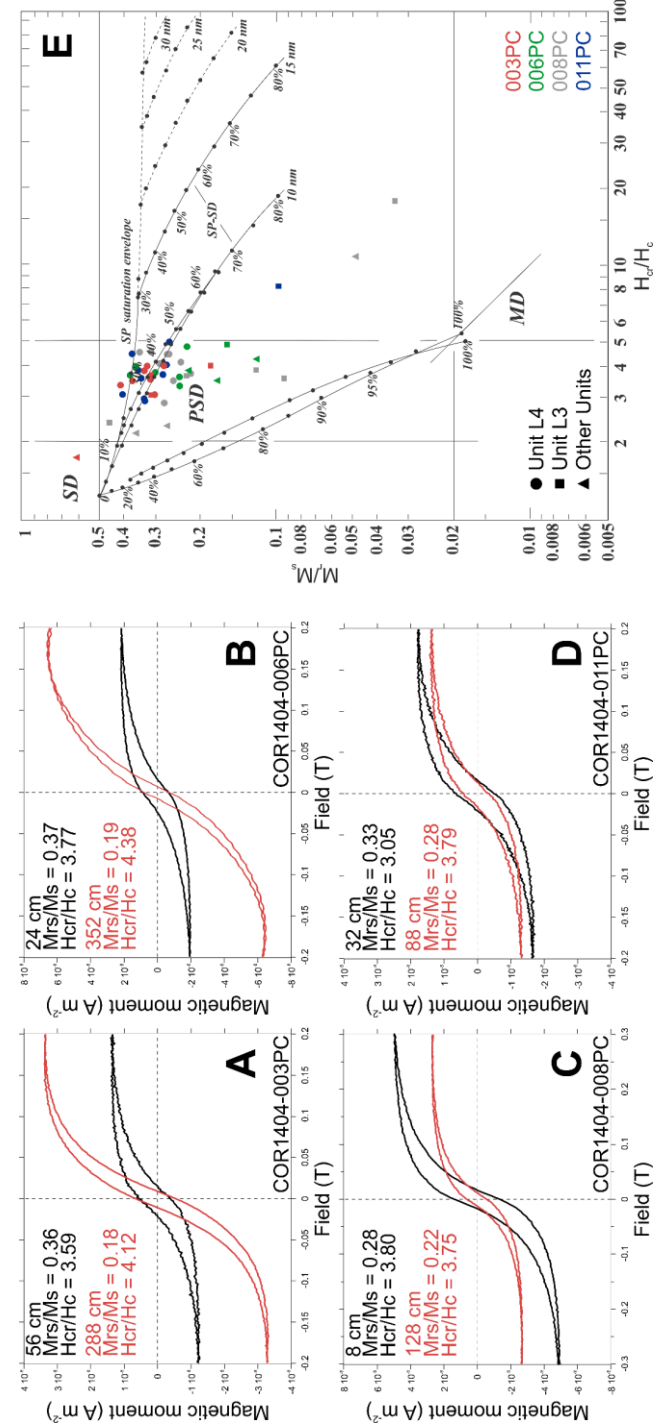


Figure 36: (A), (B), (C) and (D). Hysteresis loops of two typical samples for the cores 003PC, 006PC, 008PC and 011PC, respectively. (E). Day plot (Day et al., 1977) for the discrete samples retrieved in eachu-channel. The mixing reference lines for single and multi-domain (SD and MD) are from Dunlop (2002a, 2002b)

3.6.2 Natural remanent magnetization

The vector end-point diagrams (Fig. 47; Zijderveld, 1967) reveal a stable single-component magnetisation isolated between 10 and 40 mT and identified as characteristic remanent magnetization (ChRM). A significant viscous magnetization, described in almost all samples, was observed, but could be easily removed after 5 or 10 mT demagnetisation. The MAD values are generally between 5 and 15° which is considered as good quality data (Fig. 35; Butler, 1992; Opdyke and Channell, 1996; Stoner & St-Onge 2007). MAD values between 5° and 10° represent ~60 % of the samples. Nonetheless, some layers with MAD values >15° have been identified at the top of cores 006PC, 008PC and 011PC and they are associated to shell rich layers and to a coarse poorly-sorted sand rich layer in core 008PC (Fig. 35; Desiage et al., in prep.). The variations of MAD values within layers of less reliable data have been considered in the construction of the stacks as the stacking method is using the MAD values as a quality factor (see below). In most of the four sediment cores, the average ChRM inclination oscillates around the geocentric axial dipole (GAD) model values of ~64°, which were calculated for the latitudes of the coring sites (Fig. 35). These results testify of well-preserved and coherent paleomagnetic directional records. In core 008PC, significant lower values of inclination are observed from ~175 cm and are once again associated to a shell rich layer which is also related to MAD values >15°.

3.6.3 Relative palaeointensity (RPI) determination

In order to reconstruct the relative paleointensity of the geomagnetic field in sedimentary sequences, the natural remanent magnetisation (NRM) is usually normalized by an appropriate rock-magnetic parameter to remove the factors that potentially affect the natural remanence, such as changes in the magnetic mineralogy, concentration and grain size (Tauxe, 1993). Concentration-dependent parameters such as ARM, IRM or k_{LF} are usually chosen as normalizer. In this study, the latter has not been tested or used as normalizer due to potential interferences of coarse MD grains, diamagnetic and paramagnetic material that influence the k_{LF} . Prior to building and assessing the validity of the RPI proxy, several criteria

must be satisfied (e.g., Levi & Banerjee 1976; Tauxe 1993; Stoner & St-Onge 2007). The natural remanence must be characterized by well-defined, strong and stable SD-PSD component magnetization carried by relatively low coercivity ferrimagnetic minerals such as magnetite in the 1–15 µm grain-size range. According to our results previously mentioned, the magnetic properties of sediments from the archives used in this study satisfy the criteria for RPI reconstruction.

The best normalizer can be determined using two different normalization methods with a selected range of demagnetization as part of the characteristic remanent magnetisation interval. The first one is the widely used average ratio method (e.g., Valet et al., 1998; Channell et al., 2000; Stoner et al., 2003) which does the average of the normalized NRM for an interval of demagnetization steps. In the second method, the slope of the NRM is used versus the normalizer at different demagnetization steps (e.g., Tauxe et al., 1995; Channell et al., 2002; Snowball and Sandgren, 2004). This method is called the pseudo Thellier method or the slope method. In this study, an interval of demagnetization between 10 and 40 mT (7 steps) was used on the four cores. In order to obtain the most reliable RPI reconstruction, the sections with MAD values $>15^\circ$ were not considered to determine the best normalizer.

The correlation coefficients (*r*) associated with the slopes are mostly presenting high values (>0.9) suggesting well-defined slopes. Few exceptions were found on limited sections of 008PC characterized by slightly lower *r* values (between 0.8 and 0.9) (Fig. 37C). The curves depicting the normalization by the slope method for the ARM, as well as curves showing the ratio method for ARM and IRM all present similar tendencies (Fig. 37). However, the ratio method for both normalizers shows more defined changes with pronounced variations. Furthermore, the demagnetization curves ($M/M_{10\text{mT}}$ vs. AF field; Fig. 37A, B, C and D) seems to suggest that the ARM is a better normalizer than the IRM. Indeed, the ARM activates a coercivity spectrum closer to that of the NRM for cores 003PC, 006PC and 008PC. As the selected normalizer must not be correlated with the RPI proxy (Tauxe and Wu, 1990), the correlation between $\text{ARM}_{10-40\text{mT}}$ and $\text{NRM}/\text{ARM}_{10-40\text{mT}}$ have been calculated for each sedimentary sequences (Fig. 37). No significant correlations were observed for cores

003PC, 006PC and 011PC ($r^2 = 0.002, 0.012$ and 0.21 , respectively), whereas in 008PC, the interval containing the units 3 and 4 shows a very low correlation ($r^2 = 0.28$). According to all the evidence presented in this section, the ARM has been selected as the normalizer of the NRM to reconstruct the relative paleointensity in the stack.

3.7 PSV AND RPI STACKS

3.7.1 Stacking method

In order to take into consideration the magnetic and lithologic characteristics inherent to each sedimentary sequence for the reconstruction of the PSV and RPI, two quality factors have been considered: The MAD values and the sedimentation rates. As previously mentioned, the MAD values are usually used to demonstrate the quality of the magnetization by providing a quantitative measurement of the analytical uncertainty of the calculated component magnetization (Stoner and St-Onge, 2007). MAD values ≤ 5 are considered optimal for high-resolution paleomagnetic study and a maximal quality factor of 1 is attributed to those values (Fig. 38; Stoner and St-Onge, 2007). Low-quality factors of 0.1 and 0.01 were attributed to data with MAD values > 15 and ≥ 20 , respectively, which are considered unreliable records for PSV and RPI reconstructions (Butler, 1992; Opdyke and Channell, 1996; Stoner and St-Onge, 2007). Between those three MAD values, the quality factors have been determined using a linear interpolation (Fig. 38).

The second criterion is related to the resolution of paleomagnetic records associated to the sedimentation rates in the archive as well as to the width of the cryogenic magnetometer response functions. As presented by Philippe et al. (2018), the response functions obtained for the magnetometer (i.e., in this study the 2G Enterprises Model 755-R of ISMER; Fig. 39), are used to estimate the sensitivity curve inherent to this magnetometer and thus its capacity to detect high frequency secular variations with u-channel measurements. A small variation of 100 years over 1.5 cm is then artificially generated, and the width of the event is progressively incremented to simulate an increase of the accumulation rate. By increasing

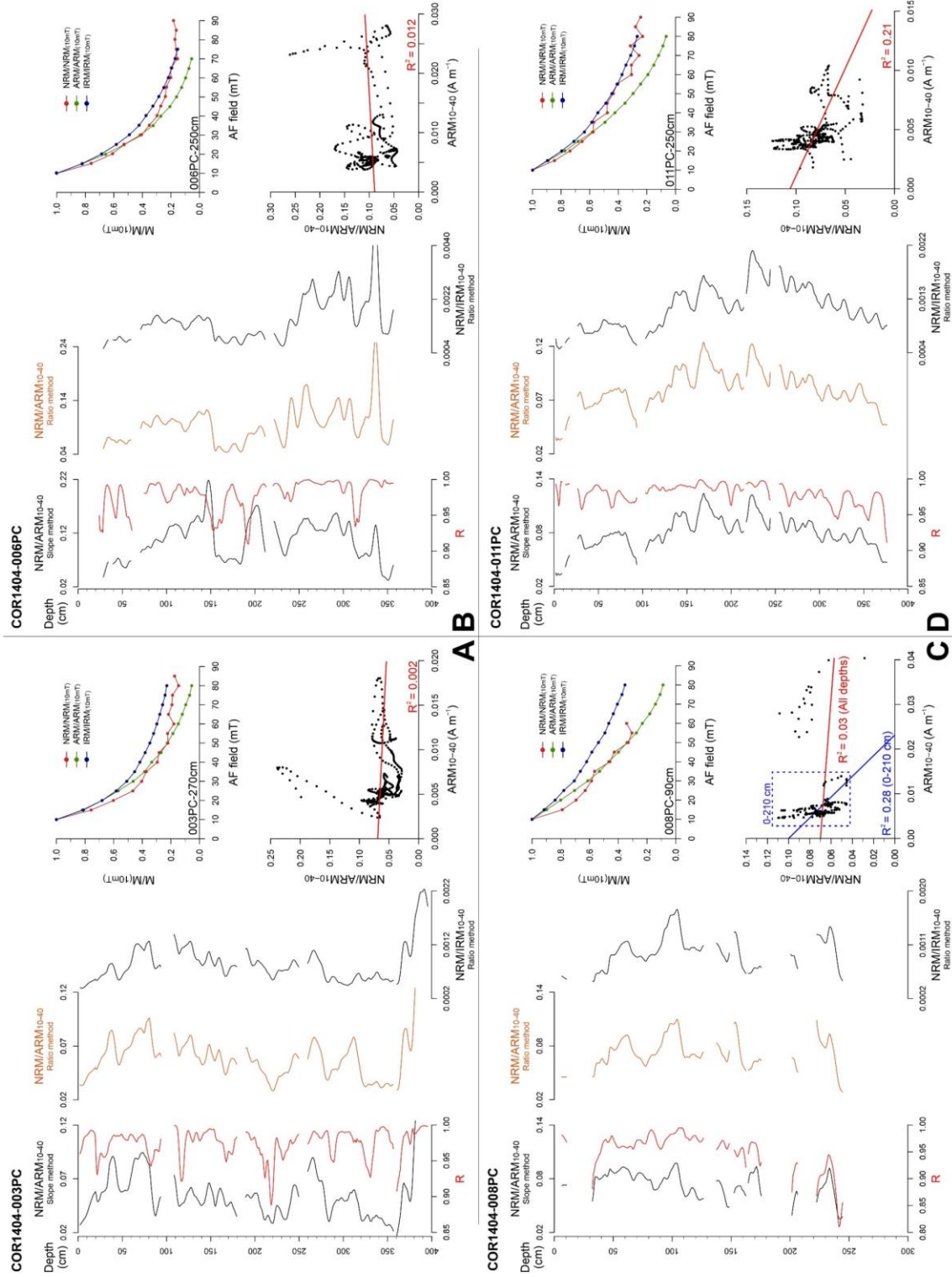


Figure 37: Comparison of the normalized relative paleointensity from the slope method with ARM as normalizer (left), from the average ratios of NRM/ARM (middle) and NRM/IRM (right) at 10-40 mT, coupled with the demagnetization curves for NRM, ARM and IRM (top), as well as the RPI proxy vs. its normalizer with correlation coefficients (bottom). The results are presented for cores 003PC (A), 006PC (B), 008PC (C) and 011PC (D)

the sedimentation rate, it is then possible to calculate, by convolution of the magnetometer response, its sensitivity for the direction (i.e., angular sensitivity) and intensity (i.e., moment sensitivity; Fig. 39). As shown by Philippe et al. (2018), the intensity appears to be more sensitive than the direction for u-channel measurements. The quality factor Q_{Uch} can be read on the sensitivity curve of the magnetometer for the direction or the intensity with values between 0 and 1 (Fig. 39). In both cases, the maximum sensitivity seems to be reached for sedimentation rates above 150 cm ka⁻¹.

The final quality factor, including both the resolution of the paleomagnetic records and the MAD values, is calculated as follows:

$$Q_f = Q_{MAD} \times Q_{Uch}$$

The value of the final quality factor is applied as the weight of each measure for each core used for the stack. Then, the data will be interpolated to generate the stack $S(t)$ according to a predetermine time resolution t (e.g., year, decade or century):

$$S(y) = \frac{\sum_{i=1}^N Q_{fi}(t) \times V_i(t)}{\sum_{i=1}^N Q_{fi}(t)}$$

Where $Q_{fi}(t)$ and $V_i(t)$ represent the final quality factor and the value of inclination, declination or RPI, respectively, of the core i at the time t . N indicate the number of cores used to reconstruct the stack. Furthermore, the standard deviation has been calculated at each stack time (t). For this study, the declination generated for the stack were standardized according to the mean value calculated between 0 and 14 cal ka BP whereas the RPIs were normalized by the maximum value between 0 and 12 cal ka BP due to potential unreliable data related to poor MAD values after 12 cal ka BP in core 008PC.

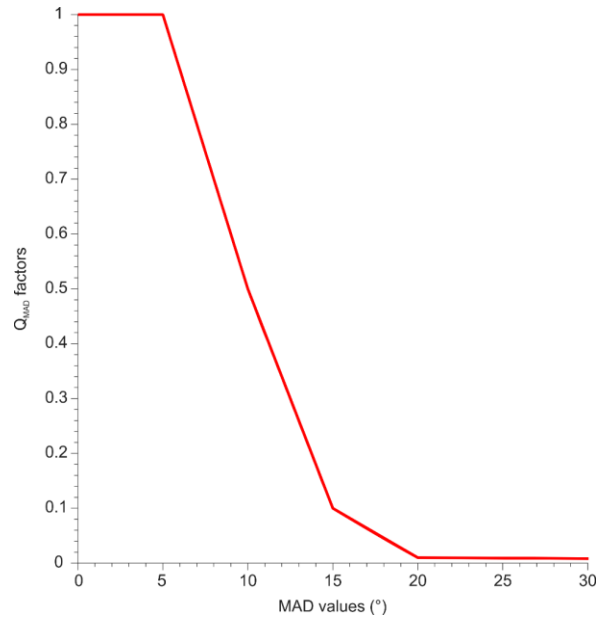


Figure 38: Quality factors used depending on the MAD values for the construction of the PSV and RPI stacks

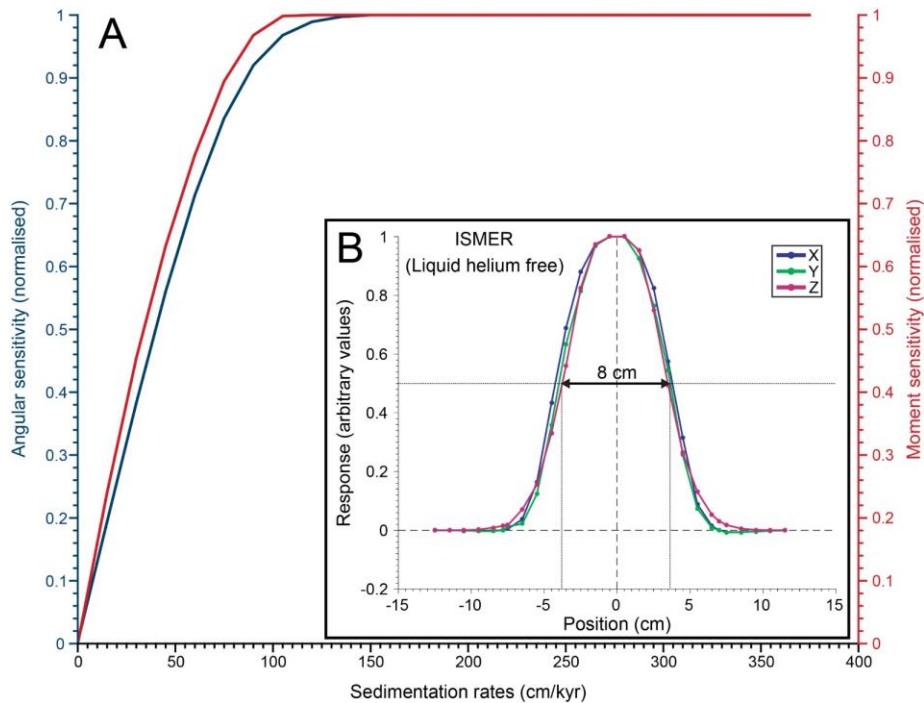


Figure 39: (A). Angular (blue curve) and moment (red curve) sensitivity function of simulated sedimentation rates. (B). Response functions of the 2G Enterprises™ SRM-755 cryogenic magnetometer used in this study at ISMER

3.7.2 PSV and RPI stacks of the GSJ

The created PSV (inclination and declination) and RPI stacks have been plotted and compared to the paleomagnetic records from the GSJ used to build the stacks in order to confirm the reliability of the data as well as the stacking method (Figs. 38 and 39). Overall, several similar swings, peaks and lows of inclination, declination and RPI can be identified in the stacks and the records from the four sediment cores. Prior to ~11.5 cal ka BP and from ~7 cal ka BP, the stacks present well-defined swings and high-resolution variations related to higher deposition rates at the base of 003PC, as well as at the top of cores 008PC and 011PC. Lower sedimentation rates lead to the smoothing of the amplitude and swings of paleomagnetic records as observed between ~11.5 cal ka BP and ~7 cal ka BP (Figs. 38 and 39).

The inclination generated in the stack shows values oscillating around the GAD, with values ranging between -80° and -50°. The relative declination of the stack varies between -75° and 100°. Close to 12.5 cal ka BP, a noticeable inclination and declination low, observed in all records except for 011PC, is well-defined in both stacks (I-G and D-G; Fig. 40 and 41). At the top of the records, the stacks also present a major inclination and declination low (I-A and D-A) identified for all the cores close to 800 cal a BP. Moreover, the declination from all records indicate an increasing trend (D-E), depicted in the stack, and starting with a declination swing at 7 cal ka BP and ending around 5 cal ka BP. The early stage of this variation matched with a significant inclination low shared by all the records and highlighted in the stack around 6.8 cal ka BP (I-E; Fig. 40). The stack of inclination also illustrates several peaks identified in every records (I-F, I-D, I-C and I-B), except for cores 006PC and 008PC in which I-C and I-D, respectively, seem to correspond to core breaks between u-channels. Some distinctive declination swings shared by most of the cores (D-B, D-C, D-D and D-F) can also be identified in the declination stack (Fig. 41). For these last inclination and declination features, the peaks and lows depict slight temporal shifts between the records (e.g., D-D and I-F; Fig. 40 and 41).

Inclination

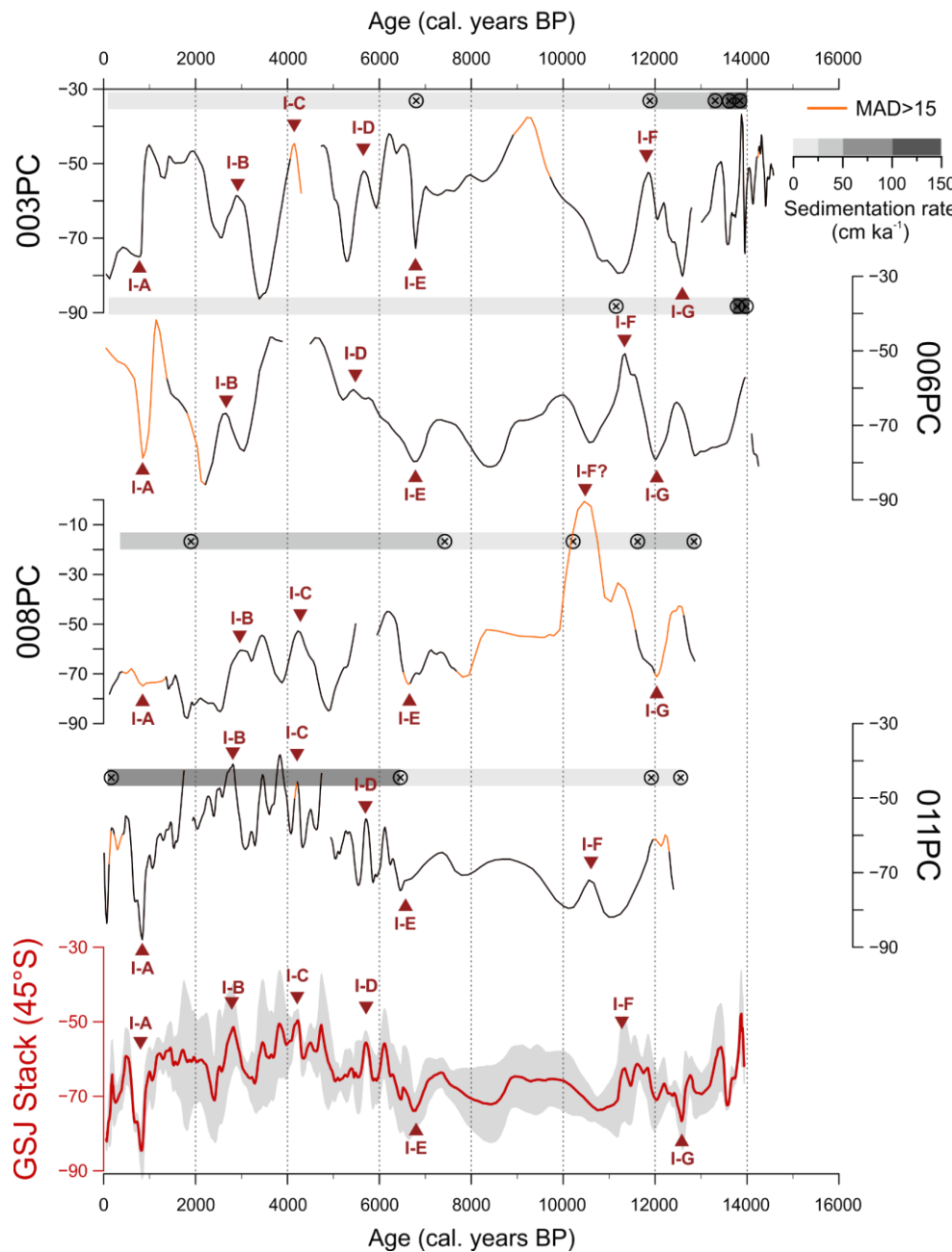


Figure 40: Paleomagnetic inclination profiles of the four sediment cores, as well as the GSJ stacks. Correlative features of paleomagnetic inclination (I-A to I-G) and declination (D-A to D-G) are indicated in red. Calibrated radiocarbon ages used in the age-depth models are illustrated by sun crosses. A gray scale is used to represent the evolution of sedimentation rates in each core. The intervals with MAD values $> 15^\circ$ are delimited with an orange line

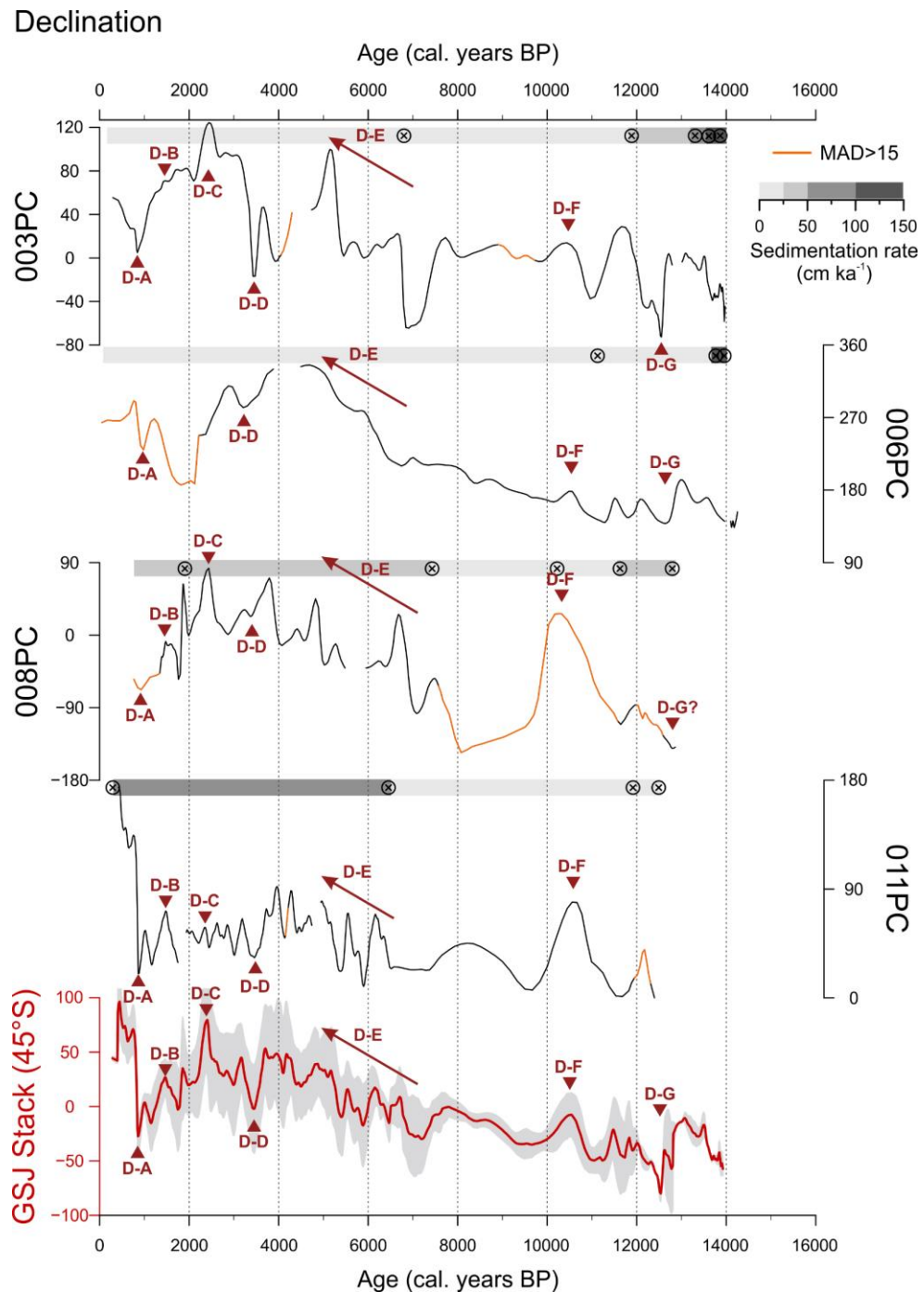


Figure 41: Paleomagnetic declination profiles of the four sediment cores, as well as the GSJ stacks. Correlative features of paleomagnetic inclination (I-A to I-G) and declination (D-A to D-G) are indicated in red. Calibrated radiocarbon ages used in the age-depth models are illustrated by sun crosses. A gray scale is used to represent the evolution of sedimentation rates in each core. The intervals with MAD values $> 15^\circ$ are delimited with an orange line

Contrary to the declination and inclination records, the RPI data present solely one intensity low shared by all the coring sites and transcribed in the stack around ~12 cal ka BP (R-G; Fig. 42). However, a similar general trend, with a peak at ~1.5 cal ka BP (R-A) followed by a significant decrease of intensities until the top of the cores can be observed in all the records and in the stack, except for 008PC in which the peak and the decline of values seem unclear. Between 7 cal ka BP and 3 cal ka BP, the stack of RPIs still indicate significant peaks and swings displayed partially in cores 003PC, 006PC and 008PC and entirely in core 011PC (R-B, R-C, R-D and R-E; Fig. 42). A large swing (R-F) is also perceptible in the lower-resolution interval between ~11.5 cal ka BP and ~7 cal ka BP. As for the directional features, temporal shifts can be observed for several RPI peaks (e.g., R-E and R-F).

Overall, the constructed stacks are in good agreements with the PSV and RPI records from the sedimentary archives retrieved in the GSJ. Indeed, the paleomagnetic data from the cores presents a consistent variability and numerous common features with the stacks. However, as shown by Lisé-Pronovost et al. (2013) for sedimentary archives in the lake Laguna Potrok Aike, the disparity in the amplitude and swings of variations could be related to non-dipolar local features, as well as to the different sedimentation rates and lock-in depths of the different records. The time required to reach the lock-in depth depends on sedimentation rate (Verosub, 1977). Furthermore, some temporal asymmetry of peaks, lows and swings are noticed between the records from the four cores used for the stacks (Figs. 38 and 39). These shifts can be related to uncertainties of the age models of each core possibly due to the disparity of datable material between lithological units as well as to the complexity and the potential strong variability of post-LGM ^{14}C reservoir values in the Atlantic coast of Argentina (Gómez et al., 2008; Schellmann and Radtke, 2010; Desiage et al., in prep.). The progressive marine invasion and flooding of the gulf starting around 15.5 cal ka BP with asynchronous changes of depositional environments between coring sites could have also contributed to the temporal uncertainties (Desiage et al., in prep.). Thus, these results suggest that the stacking method consent to harmonize the slight disparity between the different records. Furthermore, the application of the sedimentation rates as quality factor in the

stacking method seems to be an efficient way to obtain the highest temporal resolution available from different sedimentary archives.

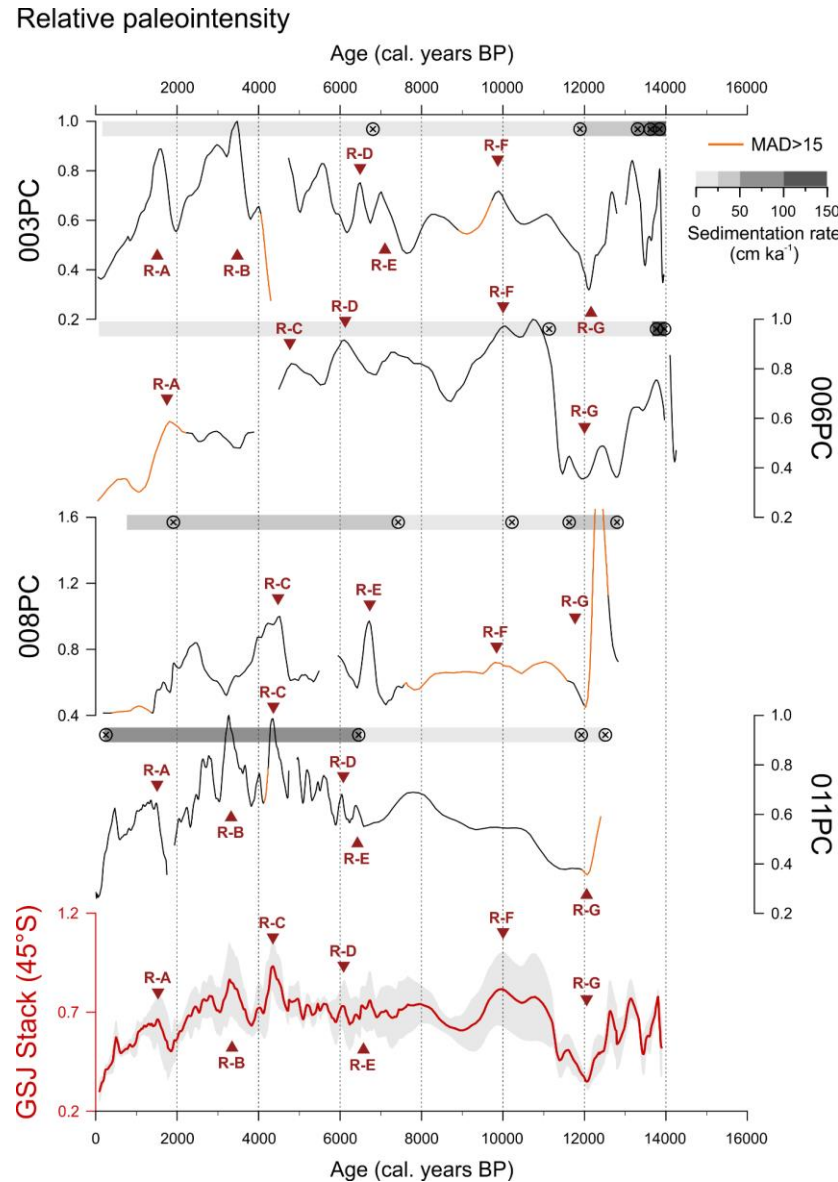


Figure 42: Relative paleointensity profiles of the four sediment cores, as well as the GSJ stack. Correlative features of relative paleointensity (R-A to R-G) are indicated in red. Calibrated radiocarbon ages used in the age-depth models are illustrated by sun crosses. A gray scale is used to represent the evolution of sedimentation rates in each core. The intervals with MAD values $> 15^\circ$ are delimited with an orange line

3.8 DISCUSSION

The high-resolution PSV and RPI stacks from the GSJ have been compared to paleomagnetic data from southern South America, as well as global-scale models to assess the reliability of these new paleomagnetic records and to better define the behavior of the geomagnetic field in this part of the globe. The inclination, declination and relative paleointensity from the GSJ stacks are plotted along with the PSV and RPI records from several Patagonian lakes (Figs. 40 and 41). The curves were obtained from paleomagnetic data of two concomitant lakes located 600 km northwest of the GSJ, Escondido and El Trébol (Gogorza et al., 2002; Irurzun et al., 2006), as well as two other lakes, Laguna Cháltel (Parlermo et al., 2019) located 500 km southwest of the gulf and lake Laguna Potrok Aike (Gogorza et al., 2012; Lisé-Pronovost et al., 2013) where the SALSA and PASADO discrete samples- and u-channel-based paleomagnetic records respectively, were retrieved 600 km southwest of the GSJ. In figures 43, 44 and 45, the PSV and RPI stacks are also presented against the global time-varying spherical harmonic models of the geomagnetic field CALS10k.2 (Constable et al., 2016) and SHA.DIF.14 (Pavón-Carrasco et al., 2014). The SHA.DIF.14 model is calculated using archaeomagnetic and volcanic data only, whereas CALS10k.2 also include lacustrine and marine sedimentary archives.

3.8.1 Gulf of San Jorge PSV stack versus southern South America records

The PSV records from the GSJ stacks and from the Patagonian lakes illustrated in Figures 43 and 44 share several swings, peaks and lows in inclination (i1 to i7) and declination (d1 to d5). The youngest part of the GSJ stack, from ~7 cal ka BP to the present, characterized by well-defined high-frequency variations and related to higher sedimentation rates at the top of cores 008PC and 011PC, reveals the highest number of common directional paleomagnetic features with Patagonian lake records (Fig. 43 and 44). During this period, the inclination of the GSJ presents a similar trend to lakes Escondido and El Trébol, characterized by a major peak at ~6 cal ka BP (i4), but not discernible in the southernmost lake Laguna Potrok Aike records. A significant broad peak (i2) is also identified around 3.3 cal ka BP in

all the records but appeared narrower in both the GSJ and Laguna Cháltel stacks. Moreover, the inclination curve of the GSJ stack significantly corroborates the 4700 yr record variations from Laguna Cháltel (Parlermo et al., 2019) up to the inclination swing observed ~1 cal ka BP (i1; Fig. 43). This significant inclination swing is also present in all the records from the published Patagonian lakes. In the lower resolution interval, the smoothed inclination curve depicts a large swing, with a peak and a through (i5 and i6) which is perceptible either in whole or in part in the records of lakes Laguna Potrok Aike, Escondido and El Trébol.

From ~7 cal ka BP to present, all the inclination records display similar declination swings (e.g., d1, d2 and d3), which are particularly noticeable in the stacks of the GSJ and Laguna Cháltel, as well as in the PASADO record from Laguna Potrok Aike (Fig. 44). Indeed, the records from the northern lakes (Escondido and El Trébol), as well as the younger part of the lake Laguna Cháltel (from ~2.7 cal ka BP), present less detailed and smoother curves due to lower sedimentation rates (Lisé-Pronovost et al., 2013; Parlermo et al., 2019), which makes the delimitation of every peaks and throughs more difficult. However, as previously observed for the inclination, the declination of the GSJ and Laguna Cháltel stacks illustrate comparable trends until ~1 cal ka BP. The declination pattern for the low-resolution interval defined by two swings, d5 and d4 at ~11.5 cal ka BP and ~7 cal ka BP respectively, indicates an apparent concomitance with the curves of northern Patagonia lakes (Escondido and El Trébol) that also have a lower temporal resolution compared to Laguna Potrok Aike (Lisé-Pronovost et al., 2013).

The temporal offset occasionally noticeable among the Patagonian PSV records could be related to uncertainties in the age models, non-dipolar local features, as well as the different lock-in depths of the different records. Comparisons of records retrieved in distant sites and/or with dissimilar depositional environments could exacerbate all these factors (e.g., St-Onge et al., 2003; Lisé-Pronovost et al., 2013). However, the reasonable repeatability and concordance of directional paleomagnetic features between the GSJ stacks and the Patagonian records suggest that the sedimentary archives from the gulf have captured regional geomagnetic dynamics and represents new records to define the regional variability

of the geomagnetic field over the last 14 000 years. Furthermore, the stacking method developed in this paper and using the MAD values and the sedimentation rates as quality factors seems to provide the highest temporal resolution available from the archives used to build the stack.

3.8.2 Global-scale paleomagnetic direction comparison

The long term trend of the GSJ stack as well as the SHA.DIF.14 model display a strong analogy as they share numerous peaks and lows, whereas the CALS10k.2 model only shows the major inclination features which can clearly be identified due to its lower temporal resolution (Fig. 44). Both the SHA.DIF.14 and CALS10k.2 models have in common the characteristic peak at ~6 cal ka BP (i4), as well as the inclination swing close to ~1 cal ka BP (i1), which are both identified in almost all the Patagonian sites used in this study. In the lower temporal resolution interval between ~11.5 and ~7 cal ka BP, the smoothed swings of the GSJ stack, also supported by the trend of the 95% confidence interval, depict common features with the SHA.DIF.14 model (i.e., i5 and i6; Fig. 43). Moreover, the curves of the GSJ stack and the SHA.DIF.14 model present relatively similar patterns for the oldest part of the record between ~14 and ~11.5 cal ka BP. As observed for inclination, the declination of the SHA.DIF.14 and CALS10k.2 models display several common features with the GSJ stack, mainly from ~8 cal ka BP to present, although only the main swings in inclination can be identified in the CALS10k.2 records (Fig. 44). Furthermore, the well-detailed declination curve of the SHA.DIF.14 model corresponds substantially with the variations of the GSJ stack for the interval between ~8 cal ka BP to the present.

Despite a global model not well constrained in the Southern Hemisphere due to the poor density of data in this part of the globe (Pavón-Carrasco et al., 2014), the PSV records of the GSJ stacks coincide significantly with the SHA.DIF.14 model, particularly for the period between ~8 cal ka BP and ~2 cal ka BP. As previously observed by Gogorza et al. (2018) on PSV records from another Patagonian lake (i.e., Carmen Lake), the high-resolution inclination and declination patterns from our stacks and from the SHA.DIFF.14 model are a

Inclination

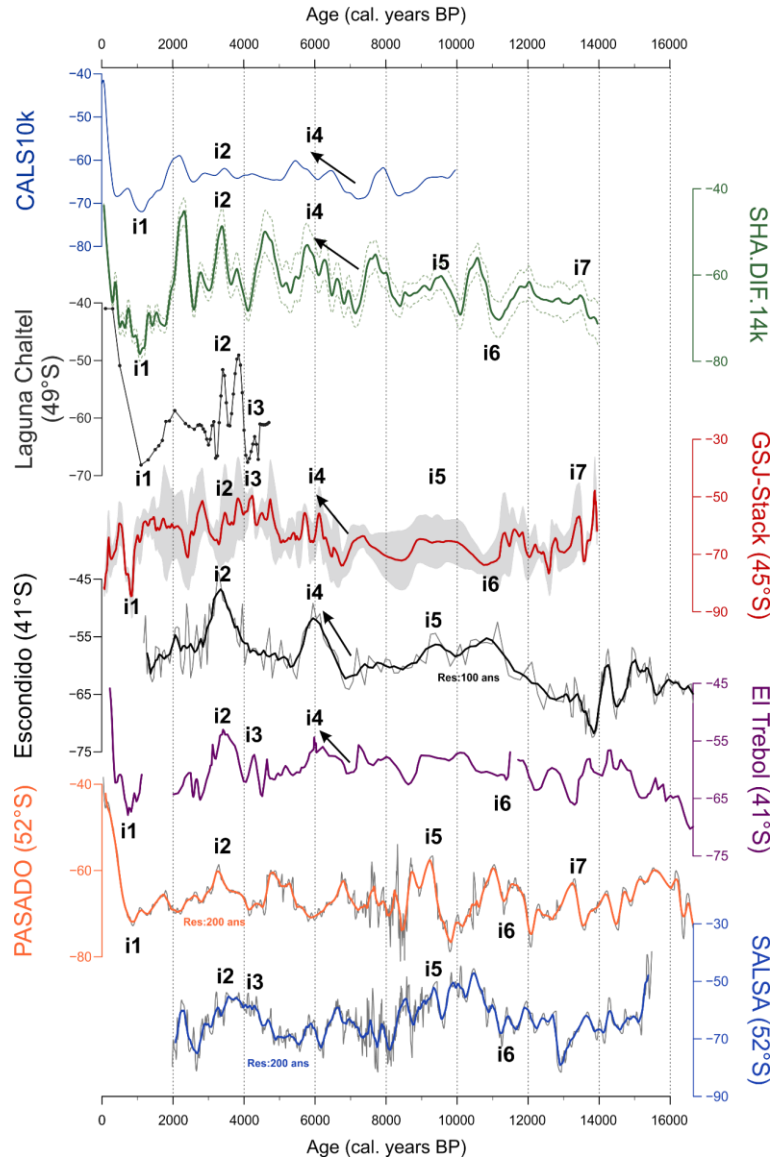


Figure 43: Comparison of paleomagnetic inclination from the GSJ stacks with southern South America paleomagnetic direction and spherical harmonic models. The regional PSV records consist of data from lakes Laguna Cháltel (dark gray; Parlomo et al., 2019), Escondido (black; Gogorza et al., 2002), El trébol (purple; Irurzun et al., 2006) and Laguna Potrok Aike (orange and light blue; PASADO and SALSA projects; Lisé-Pronovost et al., 2013; Gogorza et al., 2012). The models are represented by the CALS10k.2 spherical harmonic model (dark blue; Constable et al., 2016) and the SHA.DIF.14k model (green; Pavón-Carrasco et al., 2014). The gray shading and the dotted green lines indicate the 95% confidence interval of the GSJ stack and the SHA.DIF.14k data, respectively. Correlative features of inclination (i1 to i7) and declination (d1 to d5) are displayed in black

Declination

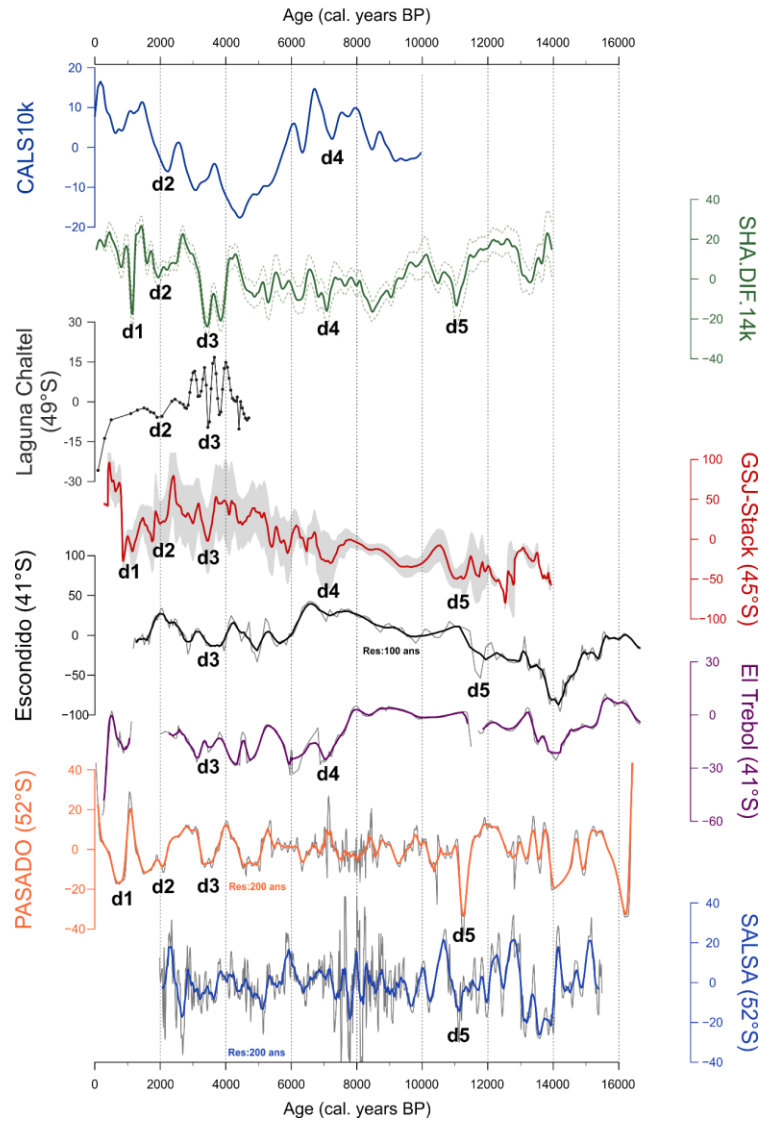


Figure 44: Comparison of paleomagnetic declination from the GSJ stacks with southern South America paleomagnetic direction and spherical harmonic models. The regional PSV records consist of data from lakes Laguna Cháltel (dark gray; Parlermo et al., 2019), Escondido (black; Gogorza et al., 2002), El trébol (purple; Irurzun et al., 2006) and Laguna Potrok Aike (orange and light blue; PASADO and SALSA projects; Lisé-Pronovost et al., 2013; Gogorza et al., 2012). The models are represented by the CALS10k.2 spherical harmonic model (dark blue; Constable et al., 2016) and the SHA.DIF.14k model (green; Pavón-Carrasco et al., 2014). The gray shading and the dotted green lines indicate the 95% confidence interval of the GSJ stack and the SHA.DIF.14k data, respectively. Correlative features of inclination (i1 to i7) and declination (d1 to d5) are displayed in black

better fit in terms of event timing and amplitude compared to other current models (i.e., CALS10k.2). Indeed, the SHA.DIFF.14 model seems to provide a more accurate variability in comparison with the visibly smoother curves of the previous models (Pavón-Carrasco et al., 2014; Goguitchaichvili et al., 2015; Gogorza et al., 2018). Both models being poorly fed by South America records, especially the SHA.DIFF.14 model, the rare non-concordant peaks and swings between the GSJ stacks, the Patagonian records and the models could suggest non-dipolar regional geomagnetic features that are not depicted by the global-scale models (Gogorza et al., 2018; Palermo et al., 2019).

3.8.3 Pattern of RPI variation

In the oldest part of the stack, prior to ~10 cal ka BP, the RPI trends of the GSJ and the Laguna Potrok Aike (PASADO dataset) record depict similarities, for instance the peaks r6 and r5 with limited temporal offset (Fig. 45). From ~6 cal ka BP to ~2 cal ka BP, all the relative paleointensity records from Patagonia display slightly increasing values characterized by several common peaks identified in all the regional curves. In this interval, the RPI stacks from the GSJ and Laguna Cháltel present numerous similarities until ~2.5 cal ka BP which correspond to the beginning of the lowest temporal resolution interval of the lake (Fig. 45; Palermo et al., 2019). Furthermore, most of the relative paleointensity features shown from this period can also be identified in the SHA.DIFF.14 model. However, the trends between the GSJ stack and the SHA.DIFF.14 model are not as well correlated as for the paleomagnetic directions even though the stack and the model present numerous similar features. Over the last ~400 years, the RPI records from the GSJ stack and the lakes Escondido and Laguna Potrok Aike (PASADO dataset) display a substantial decrease that seems to persist until the present (Fig. 45). This significant decrease is also noticeable in the two global-scale SHA.DIFF.14 and CALS10k.2 models (Fig. 45) and it has been previously documented by several archeointensity studies based on South American and African archives (e.g., Hartmann et al., 2011, 2019; Goguitchaichvili et al., 2012, 2015; Osete et al., 2015; Poletti et al., 2016) and used to build global-scale geomagnetic field models (e.g., Pavón-Carrasco et al., 2014; Constable et al., 2016; Campuzano et al., 2019). This

paleomagnetic feature corresponds to the development and the migration toward South America of an area of low field intensity, known as the South Atlantic Anomaly (SAA; Hartman and Pacca, 2009). For the last ca 400 years, the SAA minimum intensity has been moving from Africa to South America to reach its current location in southern Brazil. The development of the SAA is commonly associated to the presence of strong non-dipole features related to a reversed flux patch in the South Atlantic region (Hartman and Pacca, 2009; Terra-Nova et al., 2017 and references therein).

Despite intervals of relatively high MAD values (5° to 15°), which could be considered as not optimal for the reconstruction of relative paleointensity (Stoner and St-Onge, 2007), the variability of the RPI stack from the GSJ is comparable and concordant, for several time intervals, with the southern South American records, as well as with the SHA.DIFF.14 model and to a lesser extent with the CALS10k.2 model. Thus, the stacking method proposed in this study, using the MAD values and sedimentation rates as quality factors, seems to be a promising way to reconstruct multi-archives RPI records by maximizing intervals where the paleomagnetic signal is well-preserved and of high-quality. As previously mentioned in this paper, one of the limits and a source of concern of the stack is related to the uncertainties of the age model as well as the potential differences between age of the sediment deposition and age of the sediment magnetization associated with the lock-in depths (Verosub, 1977). In order to improve the stacking method, the next step could be to use an age-depth modeling approach to estimate an ensemble of potential age depth combinations. This would more likely reflect the incertitude associated with radiocarbon ages calibration and correction as well as the incertitude related to the lock-in depths actions as developed by Reilly et al. (2018).

3.9 CONCLUSIONS

This study presents one of the first high-resolution PSV and RPI marine records from southern South America. The records were reconstructed from four sedimentary archives retrieved in the GSJ and covering the last 14 ka cal BP. The paleomagnetic data of the gulf

Paleointensity

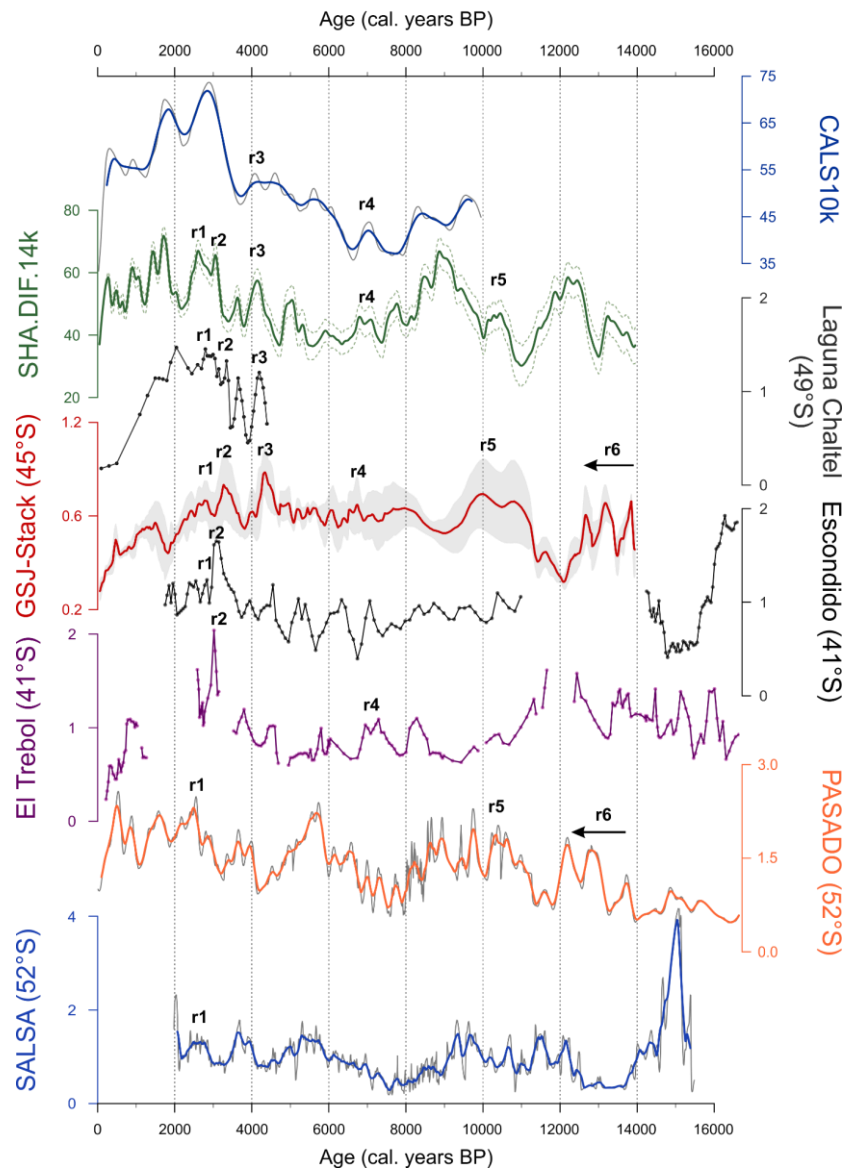


Figure 45: Comparison of relative paleointensity from the GSJ stack with southern South America records and spherical harmonic models. The regional RPI records consist of data from lakes Laguna Cháltel (dark gray; Parlermo et al., 2019), Escondido (black; Gogorza et al., 2002), El trébol (purple; Irurzun et al., 2006) and Laguna Potrok Aike (orange and light blue; PASADO and SALSA projects; Lisé-Pronovost et al., 2013; Gogorza et al., 2012). The models are represented by the CALS10k.2 spherical harmonic model (dark blue; Constable et al., 2016) and the SHA.DIF.14k model (green; Pavón-Carrasco et al., 2014). The gray shading and the dotted green lines indicate the 95% confidence interval of the GSJ stack and the SHA.DIF.14k data, respectively. Correlative features of intensity (r1 to r6) are displayed in black

meet the criteria to reconstruct reliable PSV and RPI records with a strong, stable and single component magnetization carried by low coercivity ferrimagnetic minerals in the PSD range. The PSV and RPI stacks of the gulf have been build using a new stacking approach based on two quality factors, the MAD values and the sedimentation rates in order to respect the magnetic and lithologic characteristics inherent to each sedimentary archive. Introduction of these quality factors in the stacking method allowed to reach the highest quality and temporal resolution available from the archives. Indeed, the paleomagnetic inclination, declination and relative paleointensity of the GSJ stacks support consistent patterns with southern South America lacustrine records, as well as global-scale models of the geomagnetic field. This suggests that the sedimentary archives of the GSJ were able to capture of the regional geomagnetic dynamics.

3.10 ACKNOWLEDGMENTS

The authors would like to sincerely thanks the captain, crew and scientific participants of the COR1404 (MARES and MARGES) expedition on board the R/V Coriolis II. Financial support for MARES and MARGES expeditions was provided by *the Ministerio de Ciencia, Tecnología e Innovación Productiva (MINCyT), Provincia de Chubut and Consejo Nacional de Investigaciones Científicas y Técnicas (CONICET)*. This research was funded by the Natural Sciences and Engineering Research Council of Canada (NSERC) through Discovery grants to G. St-Onge and J.-C. Montero-Serrano and by the Fonds de recherche du Québec – Nature et Technologies (FRQNT) through a team grant to G. St-Onge, J.-C. Montero-Serrano and A. Rochon. We are thankful to Quentin Beauvais for his technical support. The authors would also like to thank Agathe Lisé-Pronovost and Claudia Gogorza for providing paleomagnetic data from Patagonian lakes.

3.11 REFERENCES

- Barletta, F., St-Onge, G., Stoner, J.S., Lajeunesse, P., Locat, J., 2010. A high-resolution Holocene paleomagnetic secular variation and relative paleointensity stack from eastern Canada. *Earth Planet. Sci. Lett.* 298, 162–174.
- Blaauw, M., Christen, J.A., 2011. Flexible paleoclimate age-depth models using an autoregressive gamma process. *Bayesian Anal.* 6, 457–474.
- Butler, R.F., Butler, R.F., 1992. Paleomagnetism: magnetic domains to geologic terranes. Blackwell Scientific Publications Boston.
- Campuzano, S.A., Gómez-Paccard, M., Pavón-Carrasco, F.J., Osete, M.L., 2019. Emergence and evolution of the South Atlantic Anomaly revealed by the new paleomagnetic reconstruction SHAWQ2k. *Earth Planet. Sci. Lett.* 512, 17–26.
- Channell, J.E.T., Mazaud, A., Sullivan, P., Turner, S., Raymo, M.E., 2002. Geomagnetic excursions and paleointensities in the Matuyama Chron at Ocean Drilling Program sites 983 and 984 (Iceland Basin). *J. Geophys. Res. Solid Earth* 107 (B6), 2114.
- Channell, J.E.T., Stoner, J.S., Hodell, D.A., Charles, C.D., 2000. Geomagnetic paleointensity for the last 100 kyr from the sub-antarctic South Atlantic: a tool for inter-hemispheric correlation. *Earth Planet. Sci. Lett.* 175, 145–160.
- Constable, C., Korte, M., Panovska, S., 2016. Persistent high paleosecular variation activity in southern hemisphere for at least 10 000 years. *Earth Planet. Sci. Lett.* 453, 78–86.
- Cordero, R.R., Panarello, H., Lanzelotti, S., Dubois, C.M.F., 2003. Radiocarbon age offsets between living organisms from the marine and continental reservoir in coastal localities of Patagonia (Argentina). *Radiocarbon* 45, 9–15.
- Day, R., Fuller, M., Schmidt, V.A., 1977. Hysteresis properties of titanomagnetites: grain-size and compositional dependence. *Phys. Earth Planet. Inter.* 13, 260–267.
- Desiage, P.-A., Montero-Serrano, J.-C., St-Onge, G., Crespi-Abril, A.C., Giarratano, E., Gil, M.N., Haller, M.J., 2018. Quantifying sources and transport pathways of surface sediments in the Gulf of San Jorge, central Patagonia (Argentina). *Oceanography* 31, 92–103.
- Desiage, P.-A., St-Onge, G., Duchesne, M.J., Montero-Serrano, J.-C., Haller, M.J., In-prep. Late Pleistocene and Holocene evolution of sedimentary environments associated with postglacial transgression in the Gulf of San Jorge, central Patagonia, Argentina.

- Dunlop, D.J., 2002a. Theory and application of the Day plot (Mrs/Ms versus Hcr/Hc) 1. Theoretical curves and tests using titanomagnetite data. *J. Geophys. Res. Solid Earth* 107 (B3), 2056.
- Dunlop, D.J., 2002b. Theory and application of the Day plot (Mrs/Ms versus Hcr/Hc) 2. Application to data for rocks, sediments, and soils. *J. Geophys. Res. Solid Earth* 107 (B3), 2057.
- Gogorza, C.S.G., Irurzun, M.A., Chaparro, M.A.E., Lirio, J.M., Nuñez, H., Bercoff, P.G., Sinito, A.M., 2006. Relative paleointensity of the geomagnetic field over the last 21,000 years BP from sediment cores, Lake El Trébol (Patagonia, Argentina). *Earth, planets Sp.* 58, 1323–1332.
- Gogorza, C.S.G., Irurzun, M.A., Orgeira, M.J., Palermo, P., Llera, M., 2018. A continuous Late Holocene paleosecular variation record from Carmen Lake (Tierra del Fuego, Argentina). *Phys. Earth Planet. Inter.* 280, 40–52.
- Gogorza, C.S.G., Irurzun, M.A., Sinito, A.M., Lisé-Pronovost, A., St-Onge, G., Haberzettl, T., Ohlendorf, C., Kastner, S., Zolitschka, B., 2012. High-resolution paleomagnetic records from Laguna Potrok Aike (Patagonia, Argentina) for the last 16,000 years. *Geochemistry, Geophys. Geosystems* 13, 12.
- Gogorza, C.S.G., Lirio, J.M., Nuñez, H., Chaparro, M., Bertorello, H.R., Sinito, A.M., 2004. Paleointensity studies on Holocene–Pleistocene sediments from lake Escondido, Argentina. *Phys. Earth Planet. Inter.* 145, 219–238.
- Gogorza, C.S.G., Sinito, A.M., Lirio, J.M., Nuñez, H., Chaparro, M., Vilas, J.F., 2002. Paleosecular variations 0–19,000 years recorded by sediments from Escondido Lake (Argentina). *Phys. Earth Planet. Inter.* 133, 35–55.
- Goguitchaichvili, A., Loponte, D., Morales, J., Acosta, A., 2012. The archaeointensity of the Earth's magnetic field retrieved from Pampean ceramics (South America). *Archaeometry* 54, 388–400.
- Goguitchaichvili, A., Morales, J., Schavelzon, D., Vásquez, C., Gogorza, C.S.G., Loponte, D., Rapalini, A., 2015. Variation of the Earth's magnetic field strength in South America during the last two millennia: new results from historical buildings of Buenos Aires and re-evaluation of regional data. *Phys. Earth Planet. Inter.* 245, 15–25.
- Gómez, E.A., Borel, C.M., Aguirre, M.L., Martínez, D.E., 2008. Radiocarbon reservoir ages and hardwater effect for the northeastern coastal waters of Argentina. *Radiocarbon* 50, 119–129.
- Hartmann, G.A., Genevey, A., Gallet, Y., Trindade, R.I.F., Le Goff, M., Najjar, R., Etchevarne, C., Afonso, M.C., 2011. New historical archeointensity data from Brazil:

- Evidence for a large regional non-dipole field contribution over the past few centuries. *Earth Planet. Sci. Lett.* 306, 66–76.
- Hartmann, G.A., Pacca, I.G., 2009. Time evolution of the South Atlantic magnetic anomaly. *An. Acad. Bras. Cienc.* 81, 243–255.
- Hartmann, G.A., Poletti, W., Trindade, R.I.F., Ferreira, L.M., Sanches, P.L.M., 2019. New archeointensity data from South Brazil and the influence of the South Atlantic Anomaly in South America. *Earth Planet. Sci. Lett.* 512, 124–133.
- Irurzun, M.A., Gogorza, C.S.G., Chaparro, M.A.E., Lirio, J.M., Nuñez, H., Vilas, J.F., Sinito, A.M., 2006. Paleosecular variations recorded by Holocene-Pleistocene sediments from Lake El Trébol (Patagonia, Argentina). *Phys. Earth Planet. Inter.* 154, 1–17.
- King, J.W., Banerjee, S.K., Marvin, J., 1983. A new rock-magnetic approach to selecting sediments for geomagnetic paleointensity studies: Application to paleointensity for the last 4000 years. *J. Geophys. Res. Solid Earth* 88, 5911–5921.
- Kirschvink, J.L., 1980. The least-squares line and plane and the analysis of palaeomagnetic data. *Geophys. J. Int.* 62, 699–718.
- Kokot, R.R., 2004. Erosión en la costa patagónica por cambio climático. *Rev. la Asoc. Geológica Argentina* 59, 715–726.
- Korte, M., Brown, M.C., Panovska, S., Wardinski, I., 2019. Robust Characteristics of the Laschamp and Mono Lake Geomagnetic Excursions: Results from Global Field Models. *Front. Earth Sci.* 7, 86.
- Korte, M., Constable, C., Donadini, F., Holme, R., 2011. Reconstructing the Holocene geomagnetic field. *Earth Planet. Sci. Lett.* 312, 497–505.
- Laj, C., Kissel, C., Beer, J., 2004. High resolution global paleointensity stack since 75 kyr (GLOPIS-75) calibrated to absolute values. *Washington DC Am. Geophys. Union Geophys. Monogr. Ser.* 145, 255–265.
- Levi, S., Banerjee, S.K., 1976. On the possibility of obtaining relative paleointensities from lake sediments. *Earth Planet. Sci. Lett.* 29, 219–226.
- Lisé-Pronovost, A., St-Onge, G., Gogorza, C., Haberzettl, T., Preda, M., Kliem, P., Francus, P., Zolitschka, B., Team, T.P.S., 2013. High-resolution paleomagnetic secular variations and relative paleointensity since the Late Pleistocene in southern South America. *Quat. Sci. Rev.* 71, 91–108.
- Lund, S.P., Stoner, J., Lamy, F., 2006. Late Quaternary paleomagnetic secular variation and chronostratigraphy from ODP Sites 1233 and 1234. In: Tiedemann, R., Mix, A.C., Richter, C., Ruddiman, W.F. (Eds.), 2006b. *Proceedings of the Ocean Drilling Program, Scientific Results*, vol. 202.

- Martínez, O.A., Kutschker, A., 2011. The ‘Rodados Patagónicos’ (Patagonian shingle formation) of eastern Patagonia: environmental conditions of gravel sedimentation. *Biol. J. Linn. Soc.* 103, 336–345.
- Mazaud, A., 2005. User-friendly software for vector analysis of the magnetization of long sediment cores. *Geochemistry, Geophys. Geosystems* 6, 1–5.
- Opdyke, M.D., Channell, J.E.T., 1996. Magnetic stratigraphy. Academic press.
- Osete, M.L., Catanzariti, G., Chauvin, A., Pavón-Carrasco, F.J., Roperch, P., Fernández, V.M., 2015. First archaeomagnetic field intensity data from Ethiopia, Africa (1615 ± 12 AD). *Phys. Earth Planet. Inter.* 242, 24–35.
- Palermo, P., Irurzun, M.A., Gogorza, C.S.G., Sinito, A.M., Ohlendorf, C., Zolitschka, B., 2019. Rock-magnetic and paleomagnetic studies on late-Holocene sediments from Laguna Cháltel (Patagonia, Argentina). *J. South Am. Earth Sci.* 90, 204–215.
- Panovska, S., Constable, C.G., Brown, M.C., 2018. Global and regional assessments of paleosecular variation activity over the past 100 ka. *Geochemistry, Geophys. Geosystems* 19, 1559–1580.
- Pavón-Carrasco, F.J., Osete, M.L., Torta, J.M., De Santis, A., 2014. A geomagnetic field model for the Holocene based on archaeomagnetic and lava flow data. *Earth Planet. Sci. Lett.* 388, 98–109.
- Philippe, É.G.H., Valet, J., St-Onge, G., Thevarasan, A., 2018. Are Paleomagnetic Records From U-Channels Appropriate for Studies of Reversals and Excursions? *Geochemistry, Geophys. Geosystems* 19, 4130–4142.
- Poletti, W., Trindade, R.I.F., Hartmann, G.A., Damiani, N., Rech, R.M., 2016. Archeomagnetism of Jesuit Missions in South Brazil (1657–1706 AD) and assessment of the South American database. *Earth Planet. Sci. Lett.* 445, 36–47.
- Reilly, B.T., Stoner, J.S., Hatfield, R.G., Abbott, M.B., Marchetti, D.W., Larsen, D.J., Finkenbinder, M.S., Hillman, A.L., Kuehn, S.C., Heil Jr, C.W., 2018. Regionally consistent Western North America paleomagnetic directions from 15 to 35 ka: Assessing chronology and uncertainty with paleosecular variation (PSV) stratigraphy. *Quat. Sci. Rev.* 201, 186–205.
- Reimer, P.J., Bard, E., Bayliss, A., Beck, J.W., Blackwell, P.G., Ramsey, C.B., Buck, C.E., Cheng, H., Edwards, R.L., Friedrich, M., 2013. IntCal13 and Marine13 radiocarbon age calibration curves 0–50,000 years cal BP. *Radiocarbon* 55, 1869–1887.
- Schellmann, G., Radtke, U., 2010. Timing and magnitude of Holocene sea-level changes along the middle and south Patagonian Atlantic coast derived from beach ridge systems, littoral terraces and valley-mouth terraces. *Earth-Science Rev.* 103, 1–30.

- Snowball, I., Sandgren, P., 2004. Geomagnetic field intensity changes in Sweden between 9000 and 450 cal BP: extending the record of “archaeomagnetic jerks” by means of lake sediments and the pseudo-Thellier technique. *Earth Planet. Sci. Lett.* 227, 361–376.
- St-Onge, G., Stoner, J.S., Hillaire-Marcel, C., 2003. Holocene paleomagnetic records from the St. Lawrence Estuary, eastern Canada: centennial-to millennial-scale geomagnetic modulation of cosmogenic isotopes. *Earth Planet. Sci. Lett.* 209, 113–130.
- Stoner, J.S., Laj, C., Channell, J.E.T., Kissel, C., 2002. South Atlantic and North Atlantic geomagnetic paleointensity stacks (0–80ka): implications for inter-hemispheric correlation. *Quat. Sci. Rev.* 21, 1141–1151.
- Stoner, J.S., St-Onge, G., 2007. Magnetic stratigraphy in paleoceanography: reversals, excursions, paleointensity and secular variation. *Proxies Late Cenozoic Paleoceanogr.* Elsevier 99–137.
- Sylwan, C.A., 2001. Geology of the Golfo San Jorge Basin, Argentina. *Geología de la Cuenca del Golfo San Jorge, Argentina. J. Iber. Geol.* 27, 123–158.
- Tauxe, L., 1993. Sedimentary records of relative paleointensity of the geomagnetic field: theory and practice. *Rev. Geophys.* 31, 319–354.
- Tauxe, L., Mullender, T.A.T., Pick, T., 1996. Potbellies, wasp-waists, and superparamagnetism in magnetic hysteresis. *J. Geophys. Res. Solid Earth* 101, 571–583.
- Tauxe, L., Pick, T., Kok, Y.S., 1995. Relative paleointensity in sediments: A pseudo-Thellier approach. *Geophys. Res. Lett.* 22, 2885–2888.
- Tauxe, L., Wu, G., 1990. Normalized remanence in sediments of the western equatorial Pacific: relative paleointensity of the geomagnetic field? *J. Geophys. Res. Solid Earth* 95, 12337–12350.
- Terra-Nova, F., Amit, H., Hartmann, G.A., Trindade, R.I.F., Pinheiro, K.J., 2017. Relating the South Atlantic Anomaly and geomagnetic flux patches. *Phys. Earth Planet. Inter.* 266, 39–53.
- Valet, J., 2003. Time variations in geomagnetic intensity. *Rev. Geophys.* 41.
- Verosub, K.L., 1977. Depositional and postdepositional processes in the magnetization of sediments. *Rev. Geophys.* 15, 129–143.
- Violante, R.A., Paterlini, C.M., Marcolini, S.I., Costa, I.P., Cavallotto, J.L., Laprida, C., Dragani, W., Chaporri, N.G., Watanabe, S., Totah, V., 2014. The Argentine

continental shelf: morphology, sediments, processes and evolution since the Last Glacial Maximum. Geol. Soc. London, Mem. 41, 55–68.

Weeks, R., Laj, C., Endignoux, L., Fuller, M., Roberts, A., Manganne, R., Blanchard, E., Goree, W., 1993. Improvements in long-core measurement techniques: applications in palaeomagnetism and palaeoceanography. *Geophys. J. Int.* 114, 651–662.

Zijderveld, J.D.A., 2013. AC demagnetization of rocks: analysis of results, in: Developments in Solid Earth Geophysics. Elsevier, pp. 254–286.

3.12 SUPPLEMENTARY MATERIAL (FIGURES)

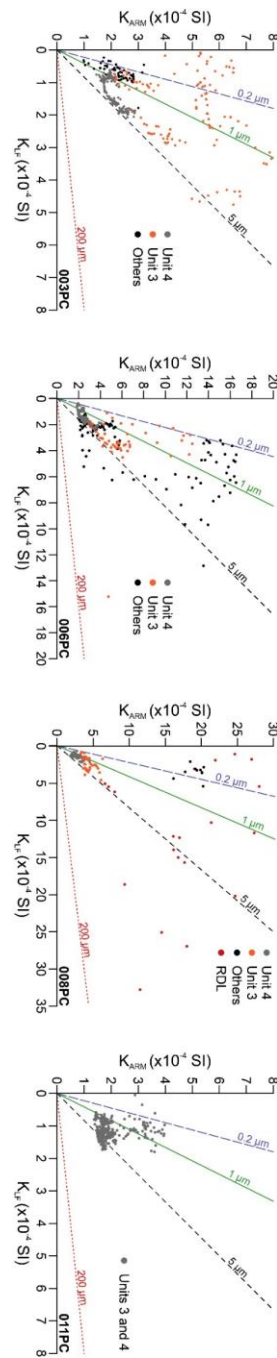


Figure 46: Anhysteretic susceptibility (k_{ARM}) vs. magnetic susceptibility (k_{LF}) biplot (King et al., 1983) used as a grain-size proxy of magnetite for the samples of cores 003PC, 006PC, 008PC and 011PC

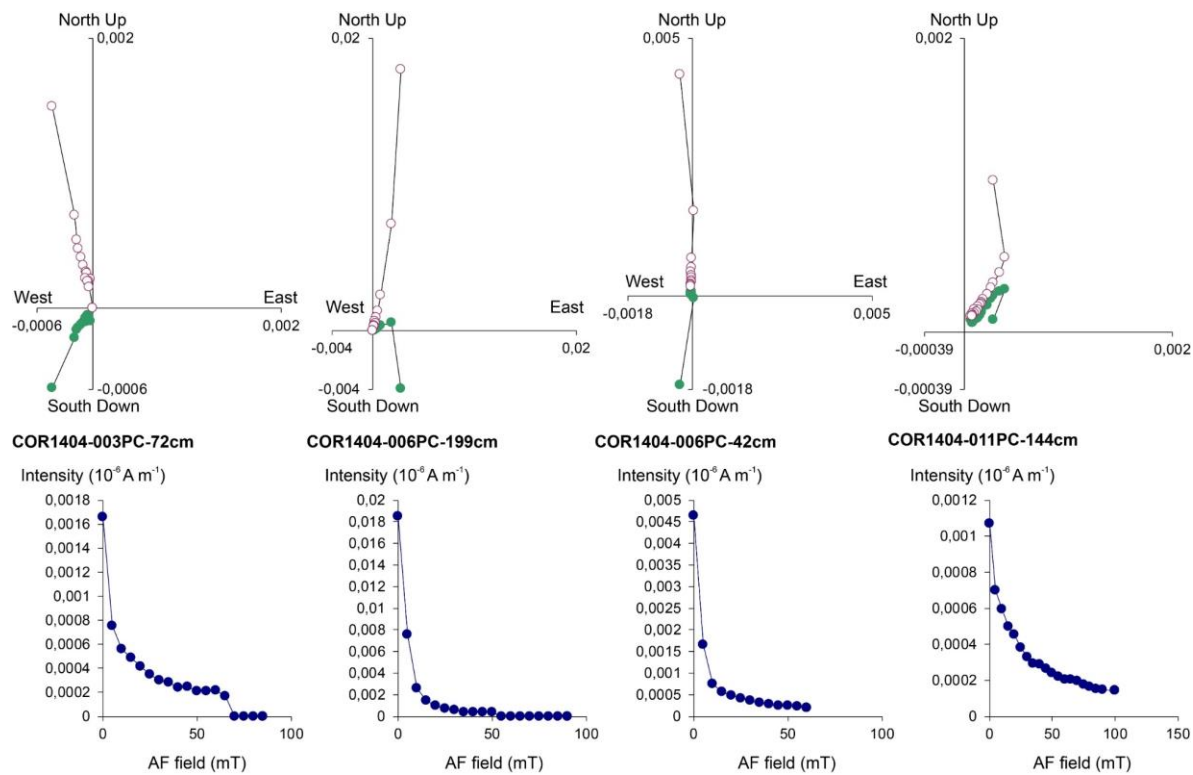


Figure 47: Vector end-point diagrams (Zijderveld, 1967) of representative samples retrieved from the four sediment cores used in this study

CONCLUSION GÉNÉRALE

L'étude d'enregistrements sédimentaires et géophysiques du golfe de San Jorge a permis de saisir l'objectif général de cette thèse, soit de reconstituer la dynamique sédimentaire et géomagnétique ainsi que les variations du niveau marin dans le secteur central de la Patagonie au cours de la dernière transgression marine. Cet objectif a été atteint à partir de divers outils méthodologiques développés pour répondre à chacun des objectifs spécifiques de ce projet de thèse. Dans cette section seront présentées les principaux résultats et conclusions de ces objectifs spécifiques suivie d'une discussion sur certaines limites de l'étude et diverses perspectives de recherche pour poursuivre les travaux réalisés dans le cadre de cette thèse.

Objectif 1 : Sédimentation contemporaine

Dans ce premier chapitre, les propriétés granulométriques, minéralogiques et géochimiques des sédiments de surface ont été utilisées afin de répondre au premier objectif qui était de déterminer les sources et les mécanismes de transport à l'origine de la sédimentation contemporaine dans le golfe de San Jorge. Les résultats de cette étude ont, notamment, mis en évidence un assemblage minéralogique dominé par les plagioclases, les quartz et les argiles. La forte proportion de plagioclases et de quartz confirme la prépondérance de la signature volcanique andine et extra-andine dans les sédiments de Patagonie, ce qui a précédemment été mis en évidence par plusieurs études dans cette région (e.g., Gaiero et al., 2007; Bertrand et al., 2012). L'influence du volcanisme andin est également mise de l'avant dans notre recherche à la suite de l'identification de téphras rhyolitiques dans les sédiments de surface et possiblement associés aux plumes de cendres générées par des éruptions rhyolitiques dans les Andes (i.e., le volcan Chaitén). L'analyse des argiles a également mis en lumière un assemblage minéralogique fortement dominé par

la smectite qui a une origine régionale et qui est transportée dans le golfe par des apports éoliens et des apports côtiers locaux (i.e., érosion et ruissellement).

Si les propriétés minéralogiques et géochimiques présentent une certaine homogénéité, l'analyse des échantillons de surface a permis de mettre en évidence l'existence, dans le golfe, de trois régions où la provenance et les conditions de sédimentation diffèrent sensiblement. Ainsi le secteur littoral au nord du GSJ constitue un environnement érosif principalement alimenté par des apports côtiers enrichis en quartz et plagioclases. La vaste région centrale du GSJ, caractérisée par des conditions plus calmes, présente une influence prédominante des apports océaniques et externes au golfe, et dans une moindre mesure des apports de poussières. Dans le secteur au large du golfe, au niveau de la partie sud-ouest, la composition des sédiments, notamment enrichie en illite et chlorite, est conditionnée par les apports océaniques externes au GSJ. En effet, les courants marins qui remontent le plateau continental vers le Nord depuis le passage de Drake contribuent à alimenter le golfe et le plateau continental argentin en illite et chlorite originaires du sud de la Patagonie ainsi que de l'Antarctique.

Finalement, en l'absence de cours d'eau majeurs et pérennes dans le golfe, nos résultats présentent de nombreux facteurs susceptibles d'alimenter les eaux du GSJ en particules terrigènes. Ces facteurs peuvent être rassemblés en trois catégories : (1) Les apports océaniques et externes au GSJ qui regroupent principalement les sédiments du plateau continental transportés par les courants; (2) Les apports des rives du golfe qui incluent, notamment, l'érosion et le ruissellement; (3) Les apports éoliens avec le transport de poussières par les vents d'ouest. A l'aide du programme SedUnMixMC, qui permet de quantifier la contribution de chaque source à partir des données minéralogiques (Andrews et Eberl, 2012), notre étude des échantillons terrestres et marins associés à ces trois catégories suggère que 50% des sédiments de surface du GSJ proviennent des apports océaniques, 40% des apports côtiers locaux et 10% des apports éoliens. Les travaux réalisés au cours de ce chapitre de thèse ont ainsi permis de décrire et caractériser les sédiments de surface du GSJ afin de déterminer les mécanismes qui gouvernent la sédimentation contemporaine dans cette région.

Objectif 2 : Stratigraphie et variations du niveau marin

Le chapitre 2 de cette thèse a permis de reconstituer la stratigraphie tardi-Quaternaire du golfe de San Jorge et de documenter les variations du niveau marin dans la région au cours de la transgression marine en s'appuyant sur l'interprétation de lignes géophysiques et sur l'analyse d'archives sédimentaires prélevées dans le golfe, couplées à la reconstruction de modèles d'âge établis à l'aide de 24 datations radiocarbonées. À partir de l'analyse multi-traceurs de 5 carottes sédimentaires, quatre unités lithologiques ont été identifiées dans la séquence de sous-surface du GSJ. De plus, le traitement développé pour les lignes sparker lors de cette thèse a permis de faciliter l'interprétation des données et ainsi identifier cinq unités sismiques, incluant le socle acoustique, dans la succession sommitale de la séquence sédimentaire au large du GSJ. En l'absence de datation, les analyses sismiques et lithologiques des données, couplées aux nombreuses études lithostratigraphiques conduites dans le secteur continental du bassin du golfe de San Jorge (e.g., Bellosi, 1990; Nullo et Combina, 2002; Paredes, 2002), suggèrent que la surface du socle acoustique pourrait correspondre à des unités sédimentaires déposées au cours de l'Oligocène tardif et du Miocène (Fig. 48A). La surface de cette unité, qui est caractérisée par des sédiments indurés identifiés à la base des carottes sédimentaires 001PC et 008PC, témoigne d'une ou plusieurs périodes de bas niveau marin mises en lumière par la présence d'une troncature d'érosion incisée laissant apparaître des vallées et des chenaux. L'interprétation de trois unités sismiques observées uniquement dans ces dépressions suggère la présence de dépôts de remplissage de vallées qui se seraient déposés sous différentes conditions hydrodynamiques (unités S1, S2 et S3 ; Fig. 48A). Le fond des vallées semble être rempli par des dépôts fluviatiles et comblé par la suite avec des dépôts possiblement associés à des conditions plus calmes telles que des environnements lagunaires ou certains milieux estuariens. Ces résultats mettent en évidence l'existence d'un système de paléodrainage associé à des périodes de bas niveau marin dans le golfe et oblitéré par des sédiments lors de phases de transgression ou de haut niveau marin subséquentes.

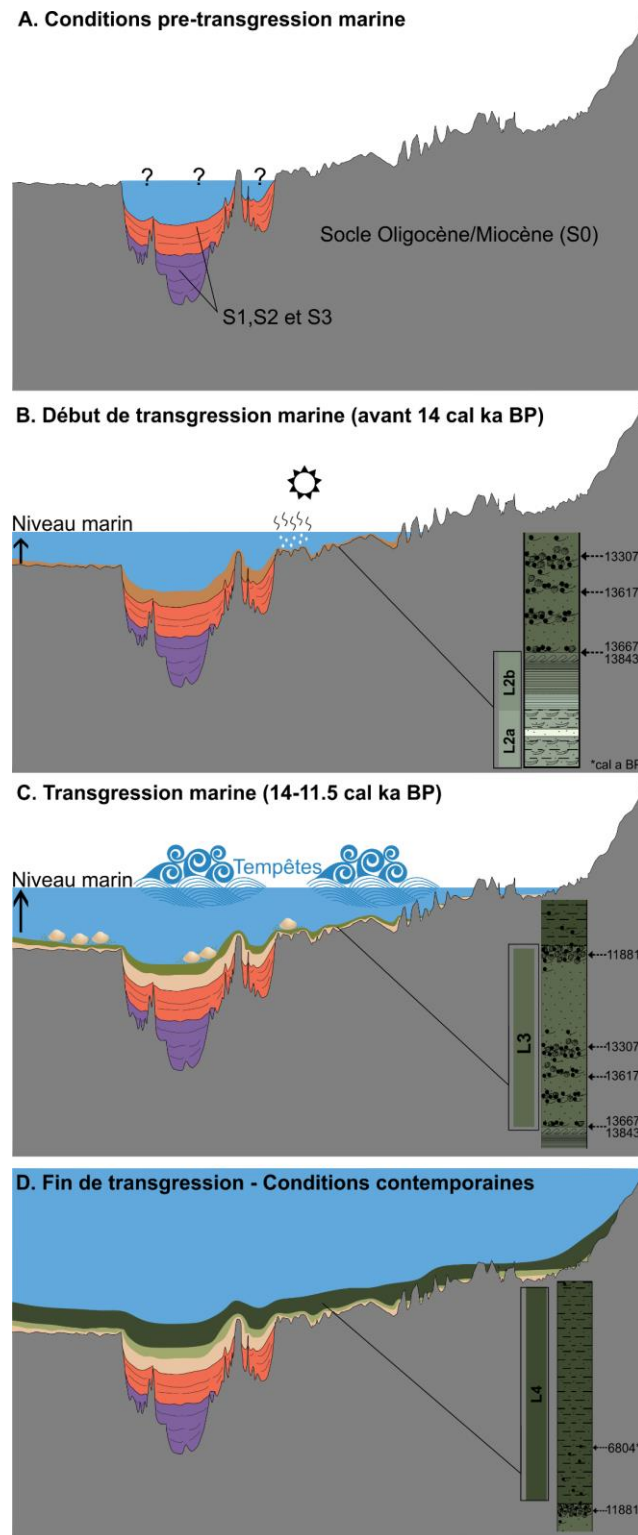


Figure 48: Modèle schématique présentant l'évolution des environnements sédimentaires au centre du golfe de San Jorge depuis la dernière transgression marine

Les âges radiocarbone obtenus dans cette étude ne permettent malheureusement pas de confirmer ou d’infirmer le début de l’invasion marine dans le golfe entre 15.5 et 15 cal ka BP comme proposé par Ponce et al. (2011). Cependant, les interprétations lithologiques des unités sédimentaires à la base des carottes sédimentaires suggèrent l’existence d’environnements intertidaux avant 14 cal ka BP, avec, notamment, des dépôts riches en gypse (unités L2a et L2b ; Fig. 48B). À la suite de l’élévation du niveau marine, une sédimentation associée à la zone subtidale ce serait développé et maintenu entre ~14 cal ka BP et ~11.5 cal ka BP avec des conditions qui pourraient avoir permis l’enregistrement d’événements extrêmes et abruptes tel que des ondes de tempête (unité L3 ; Fig. 48C). Finalement, un environnement hémiplégique ce serait mis en place dans le centre du GSJ au cours d’une période de transition avant ~7 cal ka BP (unité L4 ; Fig. 48D). L’évolution entre la sédimentation intertidale et subtidale pourrait être associée à une montée rapide du niveau marin comme le montre le changement lithologique abrupt entre leurs unités respectives couplé à une augmentation rapide et distincte des ratios élémentaires Ti/Ca et Rb/Sr. Cet évènement semble concorder avec un épisode de brusque augmentation du niveau des mers associé à une intense décharge glaciaire, l’impulsion de fonte 1A (MWP-1A). Finalement, notre étude, supportée notamment par les variations des ratios élémentaires Ti/Ca et Rb/Sr, suggère que la sédimentation dans le GSJ a été profondément conditionnée par l’augmentation du niveau marin depuis le début de la transgression marine jusqu’au milieu de l’Holocène. Les travaux réalisés au cours de ce chapitre de thèse ont ainsi permis de décrire la lithostratigraphie de sous-surface du GSJ afin de documenter l’évolution des environnements sédimentaires associée aux variations du niveau marin.

Objectif 3 : Reconstitution paléomagnétique

Dans ce troisième chapitre, les données paléomagnétiques provenant de 4 archives sédimentaires du GSJ et assemblées à l’aide d’une nouvelle méthode de compilation ont permis de reconstituer les variations du champ magnétique au centre de la Patagonie au cours des 14 000 dernières années. Cette étude propose une nouvelle méthodologie de sommation des données paléomagnétiques (*stacking*) des différentes archives sédimentaires basée sur

l'utilisation des vitesses de sédimentation ainsi que des valeurs de déviation angulaire maximum (MAD) comme facteurs de qualité. Les résultats présentent des enregistrements magnétiques avec une aimantation forte et stable portée essentiellement par des grains PSD. Les nouvelles données de PSV et RPI ont été comparées à des reconstitutions paléomagnétiques provenant d'archives sédimentaires de lacs situés au nord et au sud de la Patagonie (i.e., les lacs Escondido, El Trébol, Laguna Cháltel et Laguna Potrok Aike) et à des modèles dipolaires globaux (CALS10k.2 et SHA.DIF.14). Dans l'ensemble, les données du GSJ présentent de nombreux éléments de corrélation avec les données régionales, notamment avec les enregistrements du lac Laguna Cháltel pour les derniers 5 cal ka BP, et avec le modèle global SHA.DIF.14 qui est construit à partir de données archéomagnétiques et volcaniques. De plus, ces nouveaux enregistrements paléomagnétiques présentent une diminution marquée de la paléointensité relative au cours des 400 dernières années, également observées par plusieurs reconstitutions régionales et globales, qui semble témoigner de l'enregistrement de l'anomalie magnétique de l'Atlantique Sud (SAA) dans les sédiments du GSJ. L'ensemble de ces résultats confirment la conformité et la qualité des enregistrements paléomagnétiques dans le GSJ.

La nouvelle méthode de sommation développée dans ce chapitre semble ainsi permettre d'optimiser les enregistrements paléomagnétiques en fournissant la meilleure qualité et la plus haute résolution de données parmi les archives sédimentaires disponibles. Cette méthode et les critères de qualité qu'elle intègre pourraient-être utilisés à l'avenir pour les reconstitutions paléomagnétiques locales basées sur plusieurs archives sédimentaires ainsi que pour les reconstitutions régionales des variations du champ magnétique terrestre à l'image de l'étude réalisée par Barletta et al. (2010) pour l'est du Canada.

Perspectives

Comme il a été résumé au cours de la conclusion des différents chapitres de cette thèse, ce projet a notamment permis de caractériser la sédimentation contemporaine et de documenter la chronologie et l'évolution des environnements sédimentaires dans le golfe liées à la transgression marine. Cependant la limite principale de ces résultats est la disparité

géographique des données disponibles dans le GSJ. En effet, l'ensemble des longues carottes sédimentaires, susceptibles de retrancrire l'histoire océanographique et géologique de la région, ont été prélevées dans le secteur central du golfe tandis que les lignes sismiques à haute-résolution se concentrent essentiellement dans la moitié nord du GSJ. Cette architecture d'échantillonnage issue des missions MARGES et MARES en 2014 s'explique par plusieurs raisons : la quasi-absence de publications et de données sur les sédiments de surface et de sous-surface dans le GSJ et plus généralement dans cette partie du plateau continental qui auraient facilité la sélection de secteurs clés lors de la campagne d'échantillonnage; la limitation des relevées géophysiques dans la moitié sud du GSJ en l'absence de certaines autorisations régionales; et finalement la nécessité d'optimiser les deux semaines de temps navire disponible pour sonder la plus grande surface possible. Les résultats de cette thèse ont ainsi soulevé plusieurs questionnements et pistes de réflexion, présentées ci-après, qui pourraient s'appuyer sur les données disponibles ou nécessiteraient de nouvelles campagnes d'échantillonnages dans la région du GSJ.

Dans le chapitre 2, l'observation de vallées et chenaux incisées a permis de mettre en évidence l'existence d'un système de paléodrainage sans pouvoir en fournir une caractérisation et une classification détaillée. Une campagne géophysique spécifique avec un quadrillage serré de lignes à haute-résolution, à l'image de ce qui est fait sur de nombreux plateaux continentaux (e.g., Nordfjord et al., 2005; Menier et al., 2006; Bae et al., 2018), pourrait permettre de documenter avec précision ces structures. Ainsi, l'existence d'un système de drainage centripète dans le golfe comme suggéré par Violante et al. (2014) et appuyé par nos résultats pourrait être confirmé ou infirmé. De nouvelles données pourraient également permettre de mieux identifier l'évolution et le remplissage de ces vallées qui sont intrinsèquement liée à l'histoire glaciaire et aux variations du niveau marin dans la région. De plus, la taille significative des vallées identifiées dans le nord du golfe suggère le développement d'un réseau de drainage conséquent formée sur de longue période de temps alors qu'à l'actuel aucun bassin versant ne connecte directement le golfe (Hernández et al., 2017). En effet, les rivières Deseado et Chico longent les plateaux à l'ouest du golfe pour se diriger vers le sud et le nord, respectivement. Si la rivière Deseado rejoint l'océan Atlantique

à quelques dizaines de kilomètres au sud du golfe, il apparaît peu probable que l'embouchure actuelle de cette rivière ai pût former ces chenaux. Ceci est d'autant plus plausible étant donné la configuration au sud-est du golfe définie par une remontée de la bathymétrie et une absence de vallée incisée dans ce secteur, comme discuté dans le chapitre 2. L'étude de l'origine de ces chenaux et leurs associations avec des structures géomorphologiques et hydrologiques sur le continent pourrait ainsi permettre de documenter et de discuter de l'histoire des écoulements glaciaires au centre de la Patagonie.

Les résultats présentés dans le cadre de cette thèse ont suggéré que la montée du niveau marin a fortement conditionnée la sédimentation terrigène dans le golfe, comme le montre les ratios Ti/Ca et Rb/Sr élevés, entre le début de l'Holocène et ~7 cal ka BP. Cependant au cours de la période couverte par les archives sédimentaires, de nombreux mécanismes climatiques et environnementaux, que nous n'avons pas encore étudiés au cours de ce projet, sont susceptibles d'avoir influencé les sources et les processus sédimentaires dans la région du GSJ. En effet, depuis le LGM, le débit et la morphologie des rivières en Patagonie ont été modifiés (McCulloch et al., 2000; Kokot, 2004; Isla et al., 2015) et le transport éolien au sud de l'Amérique du Sud réduit (Haberzettl et al., 2009; Sugden et al., 2009). C'est pourquoi, à partir du cadre minéralogique et géochimique développé lors du premier chapitre pour les sédiments de surface ainsi que de la chronostratigraphie présentée dans le chapitre 2, les propriétés minéralogiques (fraction totale et argileuse) et géochimiques des carottes sédimentaires prélevées dans le golfe pourraient permettre de documenter les variations des conditions climatiques et océanographiques au centre de la Patagonie. L'évolution des sources et des mécanismes de transport de sédiment dans GSJ au cours de l'Holocène pourraient également être retracées et quantifiées avec l'analyse des propriétés minéralogiques à l'image de ce qui a été réalisé dans le chapitre 1. Les analyses ayant déjà été effectuées sur les sédiments des carottes au cours de ma thèse, ces perspectives constituent de possibles futurs collaborations avec mon directeur Guillaume St-Onge et mon co-directeur Jean Carlos Montero Serrano.

RÉFÉRENCES BIBLIOGRAPHIQUES

- Andrews, J.T., Eberl, D.D., 2012. Determination of sediment provenance by unmixing the mineralogy of source-area sediments: the “SedUnMix” program. *Mar. Geol.* 291, 24–33.
- Aravena, J., Luckman, B.H., 2009. Spatio-temporal rainfall patterns in southern South America. *Int. J. Climatol.* 29, 2106–2120.
- Bae, S.H., Kong, G.S., Lee, G.S., Yoo, D.G., Kim, D.C., 2018. Incised channel morphology and depositional fill of the paleo-Seomjin River in the continental shelf of the South Sea, Korea. *Quat. Int.* 468, 49–61.
- Barletta, F., St-Onge, G., Stoner, J.S., Lajeunesse, P., Locat, J., 2010. A high-resolution Holocene paleomagnetic secular variation and relative paleointensity stack from eastern Canada. *Earth Planet. Sci. Lett.* 298, 162–174.
- Bellosi, E., 1990. Formación Chenque: Registro de la transgresión patagoniana (Terciario medio) de la cuenca de San Jorge, Argentina, in: Actas 11 Congreso Geológico Argentino, San Juan. pp. 57–60.
- Bertrand, S., Hughen, K.A., Sepulveda, J., Pantoja, S., 2012. Geochemistry of surface sediments from the fjords of Northern Chilean Patagonia (44–47° S): Spatial variability and implications for paleoclimate reconstructions. *Geochim. Cosmochim. Acta* 76, 125–146.
- Bini, M., Zanchetta, G., Ribolini, A., Salvatore, M.C., Baroni, C., Pappalardo, M., Isola, I., Isla, F.I., Fucks, E., Boretto, G., 2017. Last Interglacial Sea-level highstand deduced from notches and inner margins of marine terraces at Puerto Deseado, Santa Cruz Province, Argentina. *Geogr. Fis. e Din. Quat.* 40, 29–39.
- Blott, S.J., Pye, K., 2001. GRADISTAT: a grain size distribution and statistics package for the analysis of unconsolidated sediments. *Earth Surf. Process. Landforms* 26, 1237–1248.
- Bout-Roumazeilles, V., Cortijo, E., Labeyrie, L., Debrabant, P., 1999. Clay mineral evidence of nepheloid layer contributions to the Heinrich layers in the northwest Atlantic. *Palaeogeogr. Palaeoclimatol. Palaeoecol.* 146, 211–228.
- Bout-Roumazeilles, V., Riboulleau, A., Châtelet, E.A., Lorenzoni, L., Tribouillard, N., Murray, R.W., Müller-Karger, F., Astor, Y.M., 2013. Clay mineralogy of surface sediments as a tool for deciphering river contributions to the Cariaco Basin (Venezuela). *J. Geophys. Res. Ocean.* 118, 750–761.
- Campos, E.J.D., Mulkherjee, S., Piola, A.R., de Carvalho, F.M.S., 2008. A note on a mineralogical analysis of the sediments associated with the Plata River and Patos Lagoon outflows. *Cont. Shelf Res.* 28, 1687–1691.
- Cavallotto, J.L., Violante, R.A., Hernández-Molina, F.J., 2011. Geological aspects and evolution of the Patagonian continental margin. *Biol. J. Linn. Soc.* 103, 346–362.
- Cavallotto, J.L., Violante, R.A., Parker, G., 2004. Sea-level fluctuations during the last 8600 years in the de la Plata River (Argentina). *Quat. Int.* 114, 155–165.

- Constable, C., Korte, M., Panovska, S., 2016. Persistent high paleosecular variation activity in southern hemisphere for at least 10 000 years. *Earth Planet. Sci. Lett.* 453, 78–86.
- Coronato, A.M.J., Coronato, F., Mazzoni, E., Vázquez, M., 2008. The physical geography of Patagonia and Tierra del Fuego. *Dev. Quat. Sci.* 11, 13–55.
- Creer, K.M., Valencio, D.A., Sinito, A.M., Tucholka, P., Vilas, J.F.A., 1983. Geomagnetic secular variations 0–14 000 yr BP as recorded by lake sediments from Argentina. *Geophys. J. Int.* 74, 199–221.
- Crémer, J.F., Long, B., Locat, J., Desrosiers, G., 2000. Application de la tomodensitométrie al'étude de la densité des sediments et la caractérisation des structures sédimentaires: Exemple des sediments déposés dans le Saguenay après la crue de juillet 1996. *Proc. Can. Geotechn. Soc.* 1, 153–159.
- Crespi Abril, A.C., Montes, A.M.I., Williams, G.N., Carrasco, M.F., 2016. Uso de sensores remotos para la detección de eventos de transporte eólico de sedimentos hacia ambientes marinos en Patagonia. *Meteorologica* 41, 33–47.
- Day, R., Fuller, M., Schmidt, V.A., 1977. Hysteresis properties of titanomagnetites: grain-size and compositional dependence. *Phys. Earth Planet. Inter.* 13, 260–267.
- de Mahiques, M.M., Tassinari, C.C.G., Marcolini, S., Violante, R.A., Figueira, R.C.L., da Silveira, I.C.A., Burone, L., e Sousa, S.H. de M., 2008. Nd and Pb isotope signatures on the Southeastern South American upper margin: Implications for sediment transport and source rocks. *Mar. Geol.* 250, 51–63.
- Dietze, E., Hartmann, K., Diekmann, B., IJmker, J., Lehmkühl, F., Opitz, S., Stauch, G., Wünnemann, B., Borchers, A., 2012. An end-member algorithm for deciphering modern detrital processes from lake sediments of Lake Donggi Cona, NE Tibetan Plateau, China. *Sediment. Geol.* 243–244, 169–180.
- Dormy, E., Valet, J., Courtillot, V., 2000. Numerical models of the geodynamo and observational constraints. *Geochemistry, Geophys. Geosystems* 1.
- Duchesne, M.J., Bellefleur, G., Galbraith, M., Kolesar, R., Kuzmiski, R., 2007. Strategies for waveform processing in sparker data. *Mar. Geophys. Res.* 28, 153–164.
- Eberl, D.D., 2003. User guide to RockJock-A program for determining quantitative mineralogy from X-ray diffraction data. US Geological Survey. Open-File Rep. 03-78.
- Elmore, A.C., Thunell, R.C., Styles, R., Black, D., Murray, R.W., Martinez, N., Astor, Y., 2009. Quantifying the seasonal variations in fluvial and eolian sources of terrigenous material to Cariaco Basin, Venezuela. *J. South Am. Earth Sci.* 27, 197–210.
- Fernández, M., Carreto, J.I., Mora, J., Roux, A., 2005. Physico-chemical characterization of the benthic environment of the Golfo San Jorge, Argentina. *J. Mar. Biol. Assoc. United Kingdom* 85, 1317–1328.
- Fitzgerald, M.G., Mitchum Jr, R.M., Uliana, M.A., Biddle, K.T., 1990. Evolution of the san jorge Basin, Argentina (1). *Am. Assoc. Pet. Geol. Bull.* 74, 879–920.
- Fleming, K., Johnston, P., Zwart, D., Yokoyama, Y., Lambeck, K., Chappell, J., 1998. Refining the eustatic sea-level curve since the Last Glacial Maximum using far- and intermediate-field sites. *Earth Planet. Sci. Lett.* 163, 327–342.

- Gaiero, D.M., Brunet, F., Probst, J.-L., Depetris, P.J., 2007. A uniform isotopic and chemical signature of dust exported from Patagonia: Rock sources and occurrence in southern environments. *Chem. Geol.* 238, 107–120.
- Gaiero, D.M., Depetris, P.J., Probst, J.-L., Bidart, S.M., Leleyter, L., 2004. The signature of river-and wind-borne materials exported from Patagonia to the southern latitudes: a view from REEs and implications for paleoclimatic interpretations. *Earth Planet. Sci. Lett.* 219, 357–376.
- Gaiero, D.M., Probst, J.-L., Depetris, P.J., Bidart, S.M., Leleyter, L., 2003. Iron and other transition metals in Patagonian riverborne and windborne materials: geochemical control and transport to the southern South Atlantic Ocean. *Geochim. Cosmochim. Acta* 67, 3603–3623.
- Gamboa, A., Montero-Serrano, J., St-Onge, G., Rochon, A., Desiage, P., 2017. Mineralogical, geochemical, and magnetic signatures of surface sediments from the Canadian Beaufort Shelf and Amundsen Gulf (Canadian Arctic). *Geochemistry, Geophys. Geosystems* 18, 488–512.
- Gogorza, C.S.G., Irurzun, M.A., Chaparro, M.A.E., Lirio, J.M., Nuñez, H., Bercoff, P.G., Sinito, A.M., 2006. Relative paleointensity of the geomagnetic field over the last 21,000 years BP from sediment cores, Lake El Trébol (Patagonia, Argentina). *Earth, planets Sp.* 58, 1323–1332.
- Gogorza, C.S.G., Irurzun, M.A., Sinito, A.M., Lisé-Pronovost, A., St-Onge, G., Haberzettl, T., Ohlendorf, C., Kastner, S., Zolitschka, B., 2012. High-resolution paleomagnetic records from Laguna Potrok Aike (Patagonia, Argentina) for the last 16,000 years. *Geochemistry, Geophys. Geosystems* 13, 12.
- Gogorza, C.S.G., Irurzun, M.A., Orgeira, M.J., Palermo, P., Llera, M., 2018. A continuous Late Holocene paleosecular variation record from Carmen Lake (Tierra del Fuego, Argentina). *Phys. Earth Planet. Inter.* 280, 40–52.
- Gogorza, C.S.G., Irurzun, M.A., Lirio, J.M., Nuñez, H., Chaparro, M., Bertorello, H.R., Sinito, A.M., 2004. Paleointensity studies on Holocene–Pleistocene sediments from lake Escondido, Argentina. *Phys. Earth Planet. Inter.* 145, 219–238.
- Gogorza, C.S.G., Sinito, A.M., Lirio, J.M., Nuñez, H., Chaparro, M., Vilas, J.F., 2002. Paleosecular variations 0–19,000 years recorded by sediments from Escondido Lake (Argentina). *Phys. Earth Planet. Inter.* 133, 35–55.
- Gogorza, C.S.G., Sinito, A.M., Ohlendorf, C., Kastner, S., Zolitschka, B., 2011. Paleosecular variation and paleointensity records for the last millennium from southern South America (Laguna Potrok Aike, Santa Cruz, Argentina). *Phys. Earth Planet. Inter.* 184, 41–50.
- Gogorza, C.S.G., Sinito, A.M., Tommaso, I.D., Vilas, J.F., Creer, K.M., Nuñez, H., 2000. Geomagnetic secular variations 0–12kyr as recorded by sediments from Lake Moreno (southern Argentina). *J. South Am. Earth Sci.* 13, 627–645.
- Goguitchaichvili, A., Loponte, D., Morales, J., Acosta, A., 2012. The archaeointensity of the Earth's magnetic field retrieved from Pampean ceramics (South America). *Archaeometry* 54, 388–400.

- Goguitchaichvili, A., Morales, J., Schavelzon, D., Vásquez, C., Gogorza, C.S.G., Loponte, D., Rapalini, A., 2015. Variation of the Earth's magnetic field strength in South America during the last two millennia: new results from historical buildings of Buenos Aires and re-evaluation of regional data. *Phys. Earth Planet. Inter.* 245, 15–25.
- Grousset, F.E., Biscaye, P.E., Revel, M., Petit, J.-R., Pye, K., Joussaume, S., Jouzel, J., 1992. Antarctic (Dome C) ice-core dust at 18 ky BP: Isotopic constraints on origins. *Earth Planet. Sci. Lett.* 111, 175–182.
- Guilderson, T.P., Burckle, L., Hemming, S., Peltier, W.R., 2000. Late Pleistocene sea level variations derived from the Argentine Shelf. *Geochemistry, Geophys. Geosystems* 1.
- Haberzettl, T., Anselmetti, F.S., Bowen, S.W., Fey, M., Mayr, C., Zolitschka, B., Ariztegui, D., Mauz, B., Ohlendorf, C., Kastner, S., 2009. Late Pleistocene dust deposition in the Patagonian steppe-extending and refining the paleoenvironmental and tephrochronological record from Laguna Potrok Aike back to 55 ka. *Quat. Sci. Rev.* 28, 2927–2939.
- Hagelund, R., Levin, S.A., 2017. SEG-Y r2. 0: SEG-Y revision 2.0 Data Exchange format. Society of Exploration Geophysicists.
- Heirtzler, J.R., 2002. The future of the South Atlantic anomaly and implications for radiation damage in space. *J. Atmos. Solar-Terrestrial Phys.* 64, 1701–1708.
- Hernández, M.A., González, N., Hernández, L., 2017. Hydrogeology of a Large Oil-and-Gas Basin in Central Patagonia: San Jorge Gulf Basin, Argentina. Springer.
- Irurzun, M.A., Gogorza, C.S.G., Sinito, A.M., Chaparro, M.A.E., Nuñez, H., Lirio, J.M., 2008. Paleosecular variations 12–20 Kyr as recorded by sediments from Lake Moreno (southern Argentina). *Stud. Geophys. Geod.* 52, 157–172.
- Irurzun, M.A., Gogorza, C.S.G., Torcida, S., Lirio, J.M., Nuñez, H., Bercoff, P.G., Chaparro, M.A.E., Sinito, A.M., 2009. Rock magnetic properties and relative paleointensity stack between 13 and 24 kyr BP calibrated ages from sediment cores, Lake Moreno (Patagonia, Argentina). *Phys. Earth Planet. Inter.* 172, 157–168.
- Isla, F.I., Espinosa, M., Iantinos, N., 2015. Evolution of the Eastern flank of the North Patagonian Ice Field: The deactivation of the Deseado River (Argentina) and the activation of the Baker River (Chile). *Zeitschrift für Geomorphol.* 59, 119–131.
- Isla, F.I., Iantinos, N., Estrada, E., 2002. Playas reflectivas y disipativas macromareales del Golfo San Jorge, Chubut. *Rev. la Asoc. Argentina Sedimentol.* 9, 155–164.
- Kilian, R., Lamy, F., 2012. A review of Glacial and Holocene paleoclimate records from southernmost Patagonia (49–55 S). *Quat. Sci. Rev.* 53, 1–23.
- Kirschvink, J.L., 1980. The least-squares line and plane and the analysis of palaeomagnetic data. *Geophys. J. Int.* 62, 699–718.
- Kokot, R.R., 2004. Erosión en la costa patagónica por cambio climático. *Rev. la Asoc. Geológica Argentina* 59, 715–726.
- Korte, M., Constable, C., Donadini, F., Holme, R., 2011. Reconstructing the Holocene geomagnetic field. *Earth Planet. Sci. Lett.* 312, 497–505.

- Korte, M., Constable, C.G., 2005. The geomagnetic dipole moment over the last 7000 years—new results from a global model. *Earth Planet. Sci. Lett.* 236, 348–358.
- Lemoine, J.-M., Capdeville, H., 2006. A corrective model for Jason-1 DORIS Doppler data in relation to the South Atlantic Anomaly. *J. Geod.* 80, 507–523.
- Lim, D.I., Jung, H.S., Choi, J.Y., Yang, S., Ahn, K.S., 2006. Geochemical compositions of river and shelf sediments in the Yellow Sea: grain-size normalization and sediment provenance. *Cont. Shelf Res.* 26, 15–24.
- Lisé-Pronovost, A., St-Onge, G., Gogorza, C., Haberzettl, T., Preda, M., Kliem, P., Francus, P., Zolitschka, B., Team, T.P.S., 2013. High-resolution paleomagnetic secular variations and relative paleointensity since the Late Pleistocene in southern South America. *Quat. Sci. Rev.* 71, 91–108.
- Lund, S.P., Stoner, J., Lamy, F., 2006. Late Quaternary paleomagnetic secular variation and chronostratigraphy from ODP Sites 1233 and 1234. In: Tiedemann, R., Mix, A.C., Richter, C., Ruddiman, W.F. (Eds.), 2006b. *Proceedings of the Ocean Drilling Program, Scientific Results*, vol. 202.
- Maher, B.A., 2007. Environmental magnetism and climate change. *Contemp. Phys.* 48, 247–274.
- Matano, R.P., Palma, E.D., Piola, A.R., 2010. The influence of the Brazil and Malvinas Currents on the southwestern Atlantic shelf circulation. *Ocean Sci.* 6, 983–995.
- McConnell, J.R., Aristarain, A.J., Banta, J.R., Edwards, P.R., Simões, J.C., 2007. 20th-Century doubling in dust archived in an Antarctic Peninsula ice core parallels climate change and desertification in South America. *Proc. Natl. Acad. Sci.* 104, 5743–5748.
- McCulloch, R.D., Bentley, M.J., Purves, R.S., Hulton, N.R.J., Sugden, D.E., Clapperton, C.M., 2000. Climatic inferences from glacial and palaeoecological evidence at the last glacial termination, southern South America McCulloch, R. D., Bentley, M. J., Purves, R. S., Hulton, N. R. J., Sugden, D. E., & Clapperton, C. M. (2000). Climatic inferences from gl. *J. Quat. Sci.* 15, 409–417.
- Menier, D., Reynaud, J.-Y., Proust, J.-N., Guillocheau, F., Guennoc, P., Bonnet, S., Tessier, B., Goubert, E., 2006. Basement control on shaping and infilling of valleys incised at the southern coast of Brittany, France.
- Montero-Serrano, J.C., Bout-Roumazeilles, V., Tribouillard, N., Sionneau, T., Riboulleau, A., Bory, A., Flower, B., 2009. Sedimentary evidence of deglacial megafloods in the northern Gulf of Mexico (Pigmy Basin). *Quat. Sci. Rev.* 28, 3333–3347.
- Montes, A., Rodríguez, S.S., Domínguez, C.E., 2017. Geomorphology context and characterization of dunefields developed by the southern westerlies at drying Colhué Huapi shallow lake, Patagonia Argentina. *Aeolian Res.* 28, 58–70.
- Nordfjord, S., Goff, J.A., Austin Jr, J.A., Sommerfield, C.K., 2005. Seismic geomorphology of buried channel systems on the New Jersey outer shelf: assessing past environmental conditions. *Mar. Geol.* 214, 339–364.
- Nullo, F.E., Combina, A.M., 2002. Sedimentitas terciarias continentales, in: Congreso Geológico Argentino. pp. 245–258.

- Palermo, P., Irurzun, M.A., Gogorza, C.S.G., Sinito, A.M., Ohlendorf, C., Zolitschka, B., 2019. Rock-magnetic and paleomagnetic studies on late-Holocene sediments from Laguna Cháltel (Patagonia, Argentina). *J. South Am. Earth Sci.* 90, 204–215.
- Palma, E.D., Matano, R.P., 2012. A numerical study of the Magellan Plume. *J. Geophys. Res. Ocean.* 117.
- Palma, E.D., Matano, R.P., Piola, A.R., 2008. A numerical study of the Southwestern Atlantic Shelf circulation: Stratified ocean response to local and offshore forcing. *J. Geophys. Res. Ocean.* 113.
- Panovska, S., Constable, C.G., Brown, M.C., 2018. Global and regional assessments of paleosecular variation activity over the past 100 ka. *Geochemistry, Geophys. Geosystems* 19, 1559–1580.
- Paredes, J.M., 2002. Asociaciones de facies y correlación de las sedimentitas de la Formación Chenque (Oligoceno-Mioceno) en los alrededores de Comodoro Rivadavia, Cuenca del Golfo San Jorge, Argentina. *Rev. la Asoc. Argentina Sedimentol.* 9, 53–64.
- Parker, G., Paterlini, M.C., Violante, R., 1997. El fondo marino.
- Parker, G., Violante, R.A., Paterlini, C.M., Costa, I.P., Marcolini, S.I., Cavallotto, J.L., 2008. Las secuencias depositacionales del Plioceno-Cuaternario en la plataforma submarina adyacente al litoral del este bonaerense. *Lat. Am. J. Sedimentol. basin Anal.* 15, 105–124.
- Paruelo, J.M., Beltran, A., Jobbagy, E., Sala, O.E., Golluscio, R.A., 1998. The climate of Patagonia: general patterns and controls on biotic. *Ecol. Austral* 8, 85–101.
- Pavón-Carrasco, F.J., Osete, M.L., Torta, J.M., De Santis, A., 2014. A geomagnetic field model for the Holocene based on archaeomagnetic and lava flow data. *Earth Planet. Sci. Lett.* 388, 98–109.
- Petschick, R., Kuhn, G., Gingele, F., 1996. Clay mineral distribution in surface sediments of the South Atlantic: sources, transport, and relation to oceanography. *Mar. Geol.* 130, 203–229.
- Pierce, J.W., Siegel, F.R., 1979. Suspended particulate matter on the southern Argentine shelf. *Mar. Geol.* 29, 73–91.
- Pinto, O., Gonzalez, W.D., Pinto, I., Gonzalez, A.L.C., Mendes, O., 1992. The South Atlantic magnetic anomaly: three decades of research. *J. Atmos. Terr. Phys.* 54, 1129–1134.
- Piola, A.R., Matano, R.P., 2001. Brazil and Falklands (Malvinas) currents. *Ocean Curr. A Deriv. Encycl. Ocean Sci.* 35–43.
- Ponce, J.F., Rabassa, J., Coronato, A., Borromei, A.N.A., 2011. Palaeogeographical evolution of the Atlantic coast of Pampa and Patagonia from the last glacial maximum to the Middle Holocene. *Biol. J. Linn. Soc.* 103, 363–379.
- Prospero, J.M., Ginoux, P., Torres, O., Nicholson, S.E., Gill, T.E., 2002. Environmental characterization of global sources of atmospheric soil dust identified with the Nimbus 7 Total Ozone Mapping Spectrometer (TOMS) absorbing aerosol product. *Rev. Geophys.* 40, 2–31.
- Pye, K., 2015. Aeolian dust and dust deposits. Elsevier.

- Rabassa, J., 2008. Late cenozoic glaciations in Patagonia and Tierra del Fuego. *Dev. Quat. Sci.* 11, 151–204.
- Ramos, V.A., Haller, M.J., 2002. Evolución tectónica. *Geol. y Recur. Nat. St. Cruz* 165–174.
- Razik, S., Govin, A., Chiessi, C.M., von Dobeneck, T., 2015. Depositional provinces, dispersal, and origin of terrigenous sediments along the SE South American continental margin. *Mar. Geol.* 363, 261–272.
- Reimer, P.J., Bard, E., Bayliss, A., Beck, J.W., Blackwell, P.G., Ramsey, C.B., Buck, C.E., Cheng, H., Edwards, R.L., Friedrich, M., 2013. IntCal13 and Marine13 radiocarbon age calibration curves 0–50,000 years cal BP. *Radiocarbon* 55, 1869–1887.
- Ribolini, A., Aguirre, M., Baneschi, I., Consoloni, I., Fucks, E., Isola, I., Mazzarini, F., Pappalardo, M., Zanchetta, G., Bini, M., 2011. Holocene beach ridges and coastal evolution in the Cabo Raso bay (Atlantic Patagonian coast, Argentina). *J. Coast. Res.* 27, 973–983.
- Rostami, K., Peltier, W.R., Mangini, A., 2000. Quaternary marine terraces, sea-level changes and uplift history of Patagonia, Argentina: comparisons with predictions of the ICE-4G (VM2) model of the global process of glacial isostatic adjustment. *Quat. Sci. Rev.* 19, 1495–1525.
- Schellmann, G., Radtke, U., 2010. Timing and magnitude of Holocene sea-level changes along the middle and south Patagonian Atlantic coast derived from beach ridge systems, littoral terraces and valley-mouth terraces. *Earth-Science Rev.* 103, 1–30.
- Singer, B.S., 2014. A Quaternary geomagnetic instability time scale. *Quat. Geochronol.* 21, 29–52.
- St-Onge, G., Ferreyra, G.A., 2018. Introduction to the special issue on the Gulf of San Jorge (Patagonia, Argentina). *Oceanography* 31, 14–15.
- St-Onge, G., Mulder, T., Francus, P., Long, B., 2007. Continuous physical properties of cored marine sediments. *Proxies Late Cenozoic Paleoceanogr.* Elsevier 63–98.
- Stoner, J.S., Laj, C., Channell, J.E.T., Kissel, C., 2002. South Atlantic and North Atlantic geomagnetic paleointensity stacks (0–80ka): implications for inter-hemispheric correlation. *Quat. Sci. Rev.* 21, 1141–1151.
- Stoner, J.S., St-Onge, G., 2007. Magnetic stratigraphy in paleoceanography: reversals, excursions, paleointensity and secular variation. *Proxies Late Cenozoic Paleoceanogr.* Elsevier 99–137.
- Stuiver, M., Reimer, P.J., 1993. Extended ^{14}C data base and revised CALIB 3.0 ^{14}C age calibration program. *Radiocarbon* 35, 215–230.
- Sugden, D.E., McCulloch, R.D., Bory, A.J.-M., Hein, A.S., 2009. Influence of Patagonian glaciers on Antarctic dust deposition during the last glacial period. *Nat. Geosci.* 2, 281–285.
- Sylwan, C.A., 2001. Geology of the Golfo San Jorge Basin, Argentina. *Geología de la Cuenca del Golfo San Jorge, Argentina. J. Iber. Geol.* 27, 123–158.
- Tauxe, L., 2010. Essentials of paleomagnetism. Univ. of California Press.
- Tauxe, L., 1993. Sedimentary records of relative paleointensity of the geomagnetic field: theory and practice. *Rev. Geophys.* 31, 319–354.

- Tauxe, L., Mullender, T.A.T., Pick, T., 1996. Potbellies, wasp-waists, and superparamagnetism in magnetic hysteresis. *J. Geophys. Res. Solid Earth* 101, 571–583.
- Thió-Henestrosa, S., Martín-Fernández, J.A., 2005. Dealing with compositional data: the freeware CoDaPack. *Math. Geol.* 37, 773–793.
- Violante, R.A., Parker, G., 2004. The post-last glacial maximum transgression in the de la Plata River and adjacent inner continental shelf, Argentina. *Quat. Int.* 114, 167–181.
- Violante, R.A., Paterlini, C.M., Marcolini, S.I., Costa, I.P., Cavallotto, J.L., Laprida, C., Dragani, W., Chapor, N.G., Watanabe, S., Totah, V., 2014. The Argentine continental shelf: morphology, sediments, processes and evolution since the Last Glacial Maximum. *Geol. Soc. London, Mem.* 41, 55–68.
- Viscosi-Shirley, C., Mammone, K., Pisias, N., Dymond, J., 2003. Clay mineralogy and multi-element chemistry of surface sediments on the Siberian-Arctic shelf: implications for sediment provenance and grain size sorting. *Cont. Shelf Res.* 23, 1175–1200.
- Xu, K., Milliman, J.D., Li, A., Liu, J.P., Kao, S.-J., Wan, S., 2009. Yangtze-and Taiwan-derived sediments on the inner shelf of East China Sea. *Cont. Shelf Res.* 29, 2240–2256.
- Zanchetta, G., Bini, M., Isola, I., Pappalardo, M., Ribolini, A., Consoloni, I., Boretto, G., Fucks, E., Ragagni, L., Terrasi, F., 2014. Middle-to late-Holocene relative sea-level changes at Puerto Deseado (Patagonia, Argentina). *The Holocene* 24, 307–317.
- Zanchetta, G., Consoloni, I., Isola, I., Pappalardo, M., Ribolini, A., Aguirre, M., Fucks, E., Baneschi, I., Bini, M., Ragagni, L., 2012. New insights on the Holocene marine transgression in the Bahía Camarones (Chubut, Argentina). *Ital. J. Geosci.* 131, 19–31.

